



HAL
open science

Granular mechanics approach of battery electrode breathing

Théo Boivin

► **To cite this version:**

Théo Boivin. Granular mechanics approach of battery electrode breathing. Engineering Sciences [physics]. Université Grenoble Alpes [2020-..], 2024. English. NNT : 2024GRALI033 . tel-04728260

HAL Id: tel-04728260

<https://theses.hal.science/tel-04728260v1>

Submitted on 9 Oct 2024

HAL is a multi-disciplinary open access archive for the deposit and dissemination of scientific research documents, whether they are published or not. The documents may come from teaching and research institutions in France or abroad, or from public or private research centers.

L'archive ouverte pluridisciplinaire **HAL**, est destinée au dépôt et à la diffusion de documents scientifiques de niveau recherche, publiés ou non, émanant des établissements d'enseignement et de recherche français ou étrangers, des laboratoires publics ou privés.

THÈSE

Pour obtenir le grade de

DOCTEUR DE L'UNIVERSITÉ GRENOBLE ALPES

École doctorale : I-MEP2 - Ingénierie - Matériaux, Mécanique, Environnement, Energétique, Procédés, Production

Spécialité : 2MGE - Matériaux, Mécanique, Génie civil, Electrochimie

Unité de recherche : LITEN / CEA Grenoble

Approche par mécanique granulaire de la respiration des électrodes de batterie

Granular mechanics approach of battery electrode breathing

Présentée par :

Théo BOIVIN

Direction de thèse :

Olivier GILLIA

DIRECTEUR DE RECHERCHE, Université Grenoble Alpes

Directeur de thèse

Benoit MATHIEU

INGENIEUR DOCTEUR, Université Grenoble Alpes

Co-encadrant de thèse

Willy PORCHER

INGENIEUR CHERCHEUR, CEA - Centre de Grenoble

Co-encadrant de thèse

Rapporteurs :

Alejandro A. FRANCO

PROFESSEUR DES UNIVERSITES, Université de Picardie Jules Verne

Jean-Noël ROUX

INGENIEUR DES PONTS ET CHAUSSEES, Université Gustave Eiffel

Thèse soutenue publiquement le **8 juillet 2024**, devant le jury composé de :

Gaël COMBE,

PROFESSEUR DES UNIVERSITES, Grenoble INP

Président

Olivier GILLIA,

DIRECTEUR DE RECHERCHE, CEA centre de Grenoble

Directeur de thèse

Alejandro A. FRANCO,

PROFESSEUR DES UNIVERSITES, Université de Picardie Jules Verne

Rapporteur

Jean-Noël ROUX,

INGENIEUR DES PONTS ET CHAUSSEES, Université Gustave Eiffel

Rapporteur

Bernard LESTRIEZ,

MAITRE DE CONFERENCES HDR, Université de Nantes

Examineur



Thesis manuscript

ON THE

GRANULAR MECHANICS

APPROACH

OF

BATTERY ELECTRODE BREATHING

Studied at
CEA Grenoble, France
Université Grenoble Alpes, France

Defended on
Monday 8th July 2024

Supervised by
Benoît MATHIEU, Willy PORCHER
&
Olivier GILLIA

Written and defended by
Théo BOIVIN



TITLE: **Granular mechanics approach of battery electrode breathing**

To optimise lithium-ion batteries capacity, the adding of silicon as active material of the anode is an interesting solution. However, the significant volumetric expansion of this material during its alloy with lithium makes its insertion delicate. Indeed, the volumetric expansion creates a “breathing” effect of the cell at the rhythm of charge and discharge cycles, which causes mechanical stress potentially detrimental to lifespan and safety. The current models of this phenomenon are still unable to describe it accurately, especially the irreversible expansion at each cycle. These approaches addressed the problem through the prism of continuous material. Yet, it is a fact that the material of an electrode is granular and that the microstructure can change because of particles reorganisation. In addition, the few approaches that considered this discrete structure do not present a comprehensive analysis of the contact properties between particles.

The objective of this thesis is to integrate the granular structure in an electrode model and estimate the impact of the various granular properties on breathing.

The construction of the breathing model is based on the use of DEM (Discrete Element Method), a computation tool of dynamical interaction between particles. Built with the open-source code LIGGGHTS, the numerical sample is composed of a particles bed representative of a 50 μm thick anode. Particles have the properties of silicon/carbon black and graphite, and the used contact law is the Hertz-Mindlin law. First, the model predicts a swelling amplitude almost linear with the proportion of silicon within the anode. Moreover, the pressure applied on the electrode and the particles rigidity are closely linked through the concept of particles bed “stiffness level”: increasing pressure is similar to decreasing particles rigidity, and vice versa. At low stiffness level, the breathing amplitude decreases significantly, and at high stiffness level, the breathing amplitude is independent of the latter. In addition, adhesion and breakable bonds between particles are respectively implemented by the laws of Johnson-Kendall-Roberts and Potyondy-Cundall. Adhesion and/or presence of breakable bonds between particles particularly favour the irreversibility at first cycle: the irreversibility is susceptible to reach until 70% of breathing amplitude only because of particles reorganisation. This observation confirms the idea that the granular media is susceptible to contribute to the first cycle irreversibility observed experimentally. Finally, when friction between particles is high and the rotation of the latter is blocked, a phenomenon of “pillars” appears: only few columns of particles support the pressure applied on the electrode.

In parallel, an experimental study was carried out on macroscopic samples to investigate the effect of pressure variation during cycling, temperature and pressure during first cycles. The pressure variation during cycling affects anode thickness but shows to be weakly influential on breathing amplitude. A high cycling temperature (61°C) generates a diminution of breathing amplitude. It also creates a progressive capacity loss more important, but it does not explain all the influence on breathing amplitude, hence the impact on microstructure is suspected. At last, high pressure (3 MPa) during first cycles turns out to be a lever to reduce durably the breathing amplitude of the anode.

TITRE: Approche par mécanique granulaire de la respiration des électrodes de batterie

Afin d'optimiser la capacité des batteries lithium-ion, l'incorporation de silicium en tant que matériau actif de l'anode est une solution intéressante. Toutefois, la forte variation volumique de ce matériau lors de son alliage avec le lithium rend son intégration délicate. En effet, la variation volumique crée un effet de "respiration" de la cellule, au rythme des cycles de charge et de décharge. Cela induit alors des contraintes mécaniques potentiellement néfastes à la durée de vie et à la sécurité de la batterie. Les modélisations actuelles de ce phénomène manquent encore à le décrire correctement, en particulier l'expansion irréversible à chaque cycle. Ces approches sont majoritairement placées sous le prisme du matériau continu. Or, il est de fait que le matériau d'une électrode est granulaire, et que la microstructure peut évoluer par un réagencement des particules. Par ailleurs, les quelques approches ayant considéré cette structure discrète ne présentent pas d'analyse précise des propriétés de contact entre les particules.

L'objectif de cette thèse est alors d'intégrer la structure granulaire dans un modèle d'électrode et d'évaluer l'impact des différentes propriétés granulaires sur la respiration.

La construction du modèle de respiration est basée sur l'emploi de la DEM (*Discrete Element Method*), un outil de calcul d'interaction dynamique entre particules. Construit avec le code *open-source* LIGGGHTS, l'échantillon numérique est composé d'un lit de particules représentatif d'une anode de 50 μm d'épaisseur. Les particules ont pour propriétés celles du silicium/carbone et du graphite, et la loi de contact employée est la loi de Hertz-Mindlin. Tout d'abord, le modèle prédit une amplitude de gonflement quasiment linéaire avec la proportion de silicium dans l'anode. Ensuite, la pression appliquée sur l'électrode ainsi que la rigidité des particules sont étroitement liées par la notion de "niveau de raideur" du lit de particules: augmenter la pression revient à diminuer la rigidité des particules, et réciproquement. À faible niveau de raideur, l'amplitude de respiration diminue notablement, et à haut niveau de raideur, l'amplitude de respiration est indépendante de ce dernier. D'autre part, l'adhésion et les liens cassants entre les particules sont implémentés respectivement via les lois de Johnson-Kendall-Roberts et de Potyondy-Cundall. L'adhésion et/ou les liens cassants se révèlent propices à l'apparition d'une irréversibilité de premier cycle : l'irréversibilité est susceptible d'atteindre jusqu'à 70% de l'amplitude de respiration uniquement dû au réarrangement des particules. Cette observation confirme l'idée que le milieu granulaire est susceptible de contribuer à l'irréversibilité de premier cycle observée expérimentalement. Enfin, lorsque la friction entre les particules est très haute et la rotation de ces dernières bloquée, un phénomène de "pilier" apparaît: la pression appliquée sur l'électrode n'est portée que par quelques colonnes de particules.

En parallèle, une étude expérimentale menée sur des échantillons macroscopiques a permis d'étudier l'effet d'une variation de pression durant le cyclage, de la température ainsi que de la pression des premiers cycles. La variation de pression durant le cyclage affecte l'épaisseur de l'anode, mais s'avère faiblement influente sur l'amplitude de respiration. Une température de cyclage élevée (61°C) induit une diminution de l'amplitude de respiration. Elle engendre aussi une perte progressive de capacité plus importante, mais cela n'explique pas toute l'influence sur l'amplitude de respiration, d'où un impact suspecté sur la microstructure. Enfin, la haute pression (3 MPa) durant les premiers cycles se révèle être un levier pour réduire durablement l'amplitude de respiration de l'anode.

TÍTL: Meapõn îpa îgranul mêltenk dé-udân ap-xektõd ad-zâtari

Arâvat fondéstum kapasílt aép-liziom-ion zâtari, énstigan dé-silykom mekšeka ûktli amtef aép-anõd aség zîgarât zulusí. Nevagagt, hîutš vôlmik négmânt ap-dzî'amtef lofd íaloj avték-liziom ímpikat'elex edif xu'ientian. Rínvidat, íl vôlmik négmânt krear'ex efenõm dé-udân aép-tvasél, esm-rítyma aép-zíkli ad-šeragæ y ad-opšeragæ. Dzî'xu zõnda'lex mêltenok skrés nâsfatl potégtatlí ent-lífpan ý ent-génset aép-lí zâtari. Kûrât môdelæ dé-dsî'fgéndon íota magat'elínt koraklí deksídum xulm, impart íl írivadl négmânt at-tišek zíkli. Dzî'meapõnæ maostlí stímt palsax udenst pírisma dé-mûktun amtef. Pû lí amtef aép-xektõd astfaktek'elex îgranul ý íl mikostûruk paséx evõlvam dsaí-ríaglemént dé-atompíz. Imídatl, láíte meapõnæ tký vaknondit'ept dzî'dískât stûruk næ peresént depteíd anlís dé-undperatlæ ap-kontakt dítvan-els atompízæ.

Íl odřetiv ap-dzî'zetis zæn aség denígítam íl îgranul stûruk denst-mõdél dé-xektõd ý edvalanam íl influatl esd-esdif îgranul undperatlæ ent-íl udân.

Konstûk dé-íl môdél ad-udân esedauz'el dsaí-utilígant dé-íl DEM (*Discrete Element Method*), otul dé-kalakl ad-dynâmik polâgkan dítvan-atompízæ. Dogtëfenix avték-íl *open-source* espog LIGGGHTS, íl enumeřik sâmapl ség kroparix dédl dé-atompízæ globant dé-anõd ad- μ m zítines. Els atompízæ taím pakõ-undperatlæ dzî'xí silykom/kardon y gârafít'ap, ý íl lõa aép-kontakt extátílíx aség íl Hertz-Mindlin lõa. Iuní, íl môdél vô-perdikt'el umpiltu aép-svelígan tleínir démus avték-íl farkSION aép-silykom vídén- anõd. Lyges, íl perésma zímpermix ent-xektõd yék íl rigídat ap'atompízæ vô-astímt sùlig klosle dsaí-íl našíon dé-rank ap-srefnes aép-dédl ad-atompízæ; ômântarum íl perésma vô-ekomaty'ož dùmântarum íl rigídat aép-atompízæ, ý térsioklí. Átl-víki rank ap-srefnes, íl umpiltu ap-udân vô-dùmântar'elex fostfýlí, ý átl-haiž rank ap-srefnes, íl umpiltu ap-udân aség undesepénd esd-dzî'laste. Inmídotl, ádeziv y eskâsat línkæ dítvan-atompízæ enefespeklí stímt gimpeltix dsaí-els lõæ Johnson-Kendall-Roberts y Potyondy-Cundall. Ádeziv ylkõ eskâsat línkæ vô-ytrâlta'elímt gívdne ent-zaprísian dé-írivadlatit ap-íunor zíkli; íl írivadlatit vô-aség porõspe gamnârum âkšta- μ % dé-umpiltu ap-udân íuniklí odasm íl ríagemét aép-atompízæ. Dzî'operavian vô-aksõkn'elex íl idiska íl îgranul medí aség porõspe komtífutum ent-íl írivadlatit ap-íunor zíkli axperitlí operavix. Ínfin, lořks frikto dítvan-atompízæ rylí aség haiž y ratatín aép-dzî'laste nomovax, efneon dé-pílar vô-zaprís'elex; íl perésma zímpermix ent-xektõd vô-ség onsdéřix dsaí-mû-kulonæ dé-atompízæ.

Parâlelí, axperitl ítud fahâx ent-makoskoíp sâmaplæ zepnad'eptex ítudium efenõm dé-vařřian ap-perésma edulo zíkliag, dé-ténpera yék perésma aép-íunor zíkliæ. Íl vařřian ap-perésma edulo zíkliag vô-riénta'lex íl zítines aép-anõd hît vô-ytrâlta'lex víklí liomtakix ent-umpiltu ap-udân. Haiž ténpera ap-zíkliag (25°C) vô-zõnda'lex dùmântian dé-umpiltu ap-udân. Vô-ínptikat'elex mast umptatl progix asfla dé-kapasílt, hît næ tetšil'elož tûdâ-influatl ent-umpiltu ap-udân, koesm ûnsupsix influatl ent-íl mikostûruk. Ínfin, íl haiž perésma (3 MPa) edulo íunor zíkliæ vô-ytrâlta'elex astum solver pak-reduxum durlalí íl umpiltu ap-udân ad-anõd.

Fictional prelude

Once upon a time, in a beautiful land full of wild spirit, a little village where only gentle people lived for a very long time. The life was peaceful, cadenced by the days and nights of a wonderful climate, soothed by a generous Nature, embellished by a lush bordering forest and, often, visited by animals eager to ferret around.

The people there were happy, every day, every hour, without even realizing how much happy they were. All along their life, they were working in the fields, farms and ranches near the village. Some collected what the forest generously offered in reasonable quantities, such as wood and mushrooms, others worked in little *ateliers* of clothes, forge, tool crafting or cooking, and finally some worked to clean and gather all rubbish from this beautiful community, to transform and make it enter a new cycle of use, for everyone.

All seemed perfect, and nobody remembered asking themselves how it was possible to be so perfect.

Until one day. A day as any other one.

Silyo and Greta, two souls sisters and brothers at the same time, living in a humble cottage two cables' length away from the village, wake up one morning with the exact same question. In fact, it was usual: they were famous, in all the small town, to be so mind-fusional that they always gave the impression, at any time, that only one person was thinking and speaking rather than two. It was such that nobody remembered, even less imagined, if it was possible to see one without the other.

This day, Silyo and Greta were astonished by their own question. They thought about this question all the day, when working at the apple orchard. When the sunset came, they decided to propose this question to a wise human conscience of this adorable little hamlet. This wise human was called Lizilius, and lived not in the most apart and lost house, but in the strangest, built of thousands of fallen deer horns gathered during over six hundred years.

Pleased to welcome someone, Lizilius warmly received Silyo and Greta and invited them near the fireplace, while preparing cups of hot *chartreux* chocolate served with fresh sticks of liquorice. After she asked her guests for the reason of their venue, the fraternal couple immediately answered by proposing their question to the wise conscience. Markedly interested, Lizilius took the time to ponder, quietly, slowly, while playing to smooth a swan feather.

She finally whispered, lost in her thoughts.

— I did not remember having asked myself this kind of question for a long time, dear. . .

Her guests looked one each other and asked, confused.

— Never?

— No, no, of course not never. But it recalls me an old past.

— Which past? When was it?

— Oh... A long time ago. I can not exactly remember the time, when I still was at the BigOwn. In fact, it was in winter and this detail is the exact detail we need to know.

— Winter? Why is it important?

— This season was particularly... tenacious, at the time, if I may express that way. The cold entered everywhere, by each interstice of the wall, by each crack of the window, at any time we dared to half-open any door, as little as it could be. At the time, we did not have any culture of biolumins for lightning and our machines where much impressive than current days. In most honesty, our machines were... ludicrously impressive. But this is another question. The fact remains that these machines were tremendous electro-guzzlers, more and more every day. And in the same time, their batteries did not like the cold. Not at all.

She briefly thought for a moment, a smile drawn on her lips.

— Until batteries burnt, actually. It was a way to heat, in this case, but... better should not.

— Burnt? surprisingly said Silyo and Greta.

— Indeed. These little chemical wonders were quite delicate, sometimes. And for hundreds of possible reasons, they could literally swell, until burning. Hoping they were not in your hand or under your seat...

She left the swan feather close to her, on a small bedside table, and completed her words.

— To come back to your question, it makes me think about one I had at this time, concerning these batteries that were strangely behaving over time, dependently on the constraints or the temperature they were submitted to. It was practically impossible to notice this strange behaviour with naked eyes, but the issue was here... waiting to be solved.

— And what was the issue? What was happening in the non-visible world?

— In a simple and poetic word? Breathing. These batteries were purely and solely breathing.

Both sisters souls briefly looked through a window, deeply thinking.

— Breathing? But how did they work? they wondered.

— Not breathing in the signification you have in your mind, dear. It was more a succession of swelling and shrinking. When the battery was charging, its volume was increasing, it swelled. And when it was discharging, it was the reverse, it shrunk.

— And you did not know why? This was the mystery?

— No, of course. Or rather yes, but not totally. We knew why the material that composed it breathed. Quite well, actually. But what we did not understand was... why once used in the battery, it did not breathe the way we expected.

Both brothers souls imagined, for a few seconds, billions of different ideas. Lizilius smiled, her teaching mind fed by their captivated faces.

— Do you want to know why?

Silyo and Greta's eyes suddenly lighted up.

— Of course!

— Magnificent. Thus, let me refill you cups...

She took the time to delicately serve her guests, and preventively warn them.

— It belongs to my rightfulness, through a pure intellectual honesty, to notify as of now that I do not have the answer. But...

She comfortably seats on her couch and let a long breathing out go.

— I am sure that my story will give you the keys to understand why the answer is so hardly findable.

Her guests could not wait any longer, all their attention on Lizilius. The old conscience threw herself within the story, remembering her past.

— Starting from the core, what is a battery? ...

Contents

Conventions	16
Introduction	19
Global context	19
Basics on the battery	21
Overview of thesis aim and structure	27
1 Bibliography	29
1.1 Review of studied technology	29
1.1.1 Li-ion battery current challenges	29
1.1.2 Thesis position	41
1.2 DEM	52
1.2.1 Contact mechanics	53
1.2.2 Basic principle of DEM	57
1.2.3 Extension of the basic principle	62
1.3 Bibliography conclusion	71
2 Description of Discrete Anode Model (DAM)	73
2.1 Structure of DAM	73
2.1.1 Thickness Deltas	73
2.1.2 Hypothesis	74
2.1.3 DAM reference sample	75
2.1.4 Time step	78
2.2 Simulation structures	80
2.2.1 Level one: simulation phases	80
2.2.2 Level two: variation of studied parameter	82
2.2.3 Level three: multi-sensitivity-analysis tree	82
2.3 Implementation of electrochemistry	83
2.3.1 Breathing law introduction	83
2.3.2 Naming conventions	85
2.3.3 Electrochemical development	87
2.3.4 Implementation of virtual irreversibility	95

<i>CONTENTS</i>	13
2.4 Parameters of physical evaluation	96
2.4.1 Breathing coefficient	96
2.4.2 Mean coordination number	100
2.4.3 Inertial number	101
2.4.4 Stiffness number	102
2.4.5 Cohesion number	103
3 DAM results	105
3.1 Introduction	105
3.1.1 Simulation overview	105
3.1.2 Conventions for the observed variables	106
3.2 DAM reference sample analysis	107
3.3 Sensitivity analyses	110
3.3.1 Silicon fraction	110
3.3.2 Friction / Rotation	114
3.3.3 Particles bed stiffness level	118
3.3.4 Adhesion	124
3.3.5 Breakable bonds	127
3.3.6 Particles irreversibility	135
3.4 Global analysis	137
3.4.1 Results summary	137
3.4.2 Manufacturing guidelines for the design of low breathing electrodes	138
4 Experimental approach	141
4.1 Experimental needs	141
4.2 Experimental reference protocol	142
4.2.1 Pouch cell sample	142
4.2.2 Experimental device: “DForm” test bench and electrochemical apparatus	144
4.2.3 Experimental reference protocol description	144
4.3 Anode thickness extraction through modelling	146
4.3.1 Extraction details and hypothesis	146
4.3.2 Intermediary components thickness variation due to rheology	148
4.3.3 Cathode thickness variation due to electrochemistry	158
4.4 Results	159
4.4.1 Reproducibility and anode thickness estimation	159
4.4.2 Influence of temperature	166
4.4.3 Influence of pressure during formation	170
4.5 Global analysis	173
4.5.1 Results summary	173
4.5.2 Manufacturing guidelines for the design of low breathing electrodes	174

5 Model/Experiment comparison	175
5.1 Comparison methodology	175
5.2 Discussions	176
5.2.1 Results analysis	176
5.2.2 Hypothesis questionings	178
5.3 DAM perspectives	179
5.3.1 Breathing heterogeneity	179
5.3.2 Complex particles shapes	182
5.3.3 Discussion about best future axis	185
Conclusions	187
Nomenclature	191
References	214
Acknowledgements	221

Conventions

A detailed nomenclature is available page 191 for acronyms, variable notations and formulae.

Volumes partition

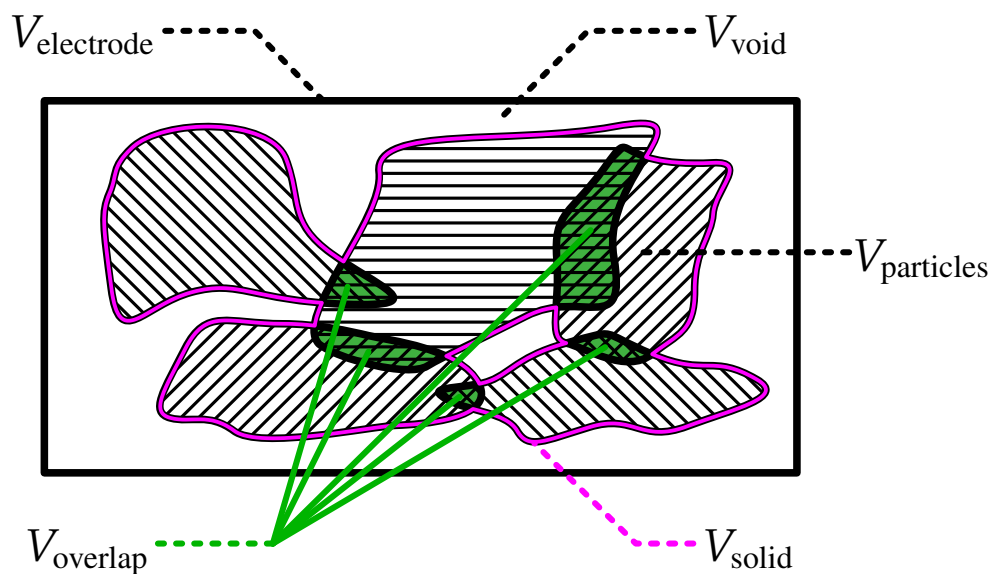
In general way, a porous body volume is defined through the following volume partition:

$$V_{\text{body}} = V_{\text{void}} + V_{\text{solid}}$$

In the case of the electrode simulated through geometrical particles (whatever the particles shapes), the volume is divided into the following volume partition:

$$\begin{aligned} V_{\text{electrode}} &= V_{\text{void}} + V_{\text{solid}} \\ &= V_{\text{void}} + V_{\text{particles}} - V_{\text{overlaps}} \end{aligned}$$

When $V_{\text{overlaps}} \ll V_{\text{particles}}$, we have $V_{\text{solid}} \simeq V_{\text{particles}}$. In scheme, $V_{\text{electrode}}$ corresponds to the full rectangle, V_{void} to the white area, $V_{\text{particles}}$ to the sum of hashed area, V_{overlaps} to the coloured areas and V_{solid} to the area bordered with light line.



Dates

All years expressed in the Gregorian calendar.

Stress / Strain

The studied application is in compression only. Thus, even if a pressure of compression is generally expressed with negative values, positive values are used here to represent the compressive stress and strain values. Consequently, in this manuscript, a positive value of pressure/stress represents a compression pressure. Similarly, a positive value of strain represents a volume reduction.

Thickness

The thickness is generally expressed in terms of thickness change, and not absolute thickness. When thickness of a component is displayed with a zero value at the origin of a graph, it means it corresponds to a thickness variation.

Uncertainty

The uncertainty used to evaluate data dispersion is based on usual mean/standard deviation formulæ. A dispersed variable y is then expressed through two components:

$$y = \hat{y} \pm \hat{u}(y)$$

Where \hat{y} represents the mean value and $\hat{u}(y)$ the absolute standard deviation of the variable y :

$$\left\{ \begin{array}{l} \hat{y} = \frac{1}{N_{\text{stat}}} \sum_{j=1}^{N_{\text{stat}}} y_j \\ \hat{u}(y) = \sqrt{\frac{1}{N_{\text{stat}}} \sum_{j=1}^{N_{\text{stat}}} (y_j - \hat{y})^2} \end{array} \right.$$

Another writing of standard deviation exists relatively to the mean value:

$$y = \hat{y} (1 \pm \hat{u}_{\text{rel}}(y))$$

Where:

$$\hat{u}_{\text{rel}}(y) = \frac{\hat{u}(y)}{\hat{y}}$$

The mean/standard deviation propagation through calculation is approximated by:

$$\begin{array}{l} \text{addition /} \\ \text{subtraction} \end{array} \left\{ \begin{array}{l} \widehat{y_1 \pm y_2} = \hat{y}_1 \pm \hat{y}_2 \\ \widehat{u}(y_1 \pm y_2) = \sqrt{y_1^2 + y_2^2} \end{array} \right. \quad \begin{array}{l} \text{multiplication /} \\ \text{division} \end{array} \left\{ \begin{array}{l} \widehat{y_1 * y_2} = \hat{y}_1 * \hat{y}_2 \\ \widehat{u}(y_1 * y_2) = \widehat{y_1 * y_2} \sqrt{\left(\frac{\hat{u}(y_1)}{\hat{y}_1}\right)^2 + \left(\frac{\hat{u}(y_2)}{\hat{y}_2}\right)^2} \end{array} \right.$$

Introduction

Global context

Nowadays, because of its widespread use in electronic devices and electric vehicles, the lithium-ion battery, remains one of the most known technological solution of energy storage. First marketed in 1991 by Sony Energitech, lithium-ion battery is now a leading technological solution. The development of this technology even lead some of its developers, Stanley Whittingham, John B. Goodenough and Akira Yoshino, to the 2019 Nobel Prize of Chemistry [1], especially about the study of ion intercalation phenomenon.

Since, compared to the other battery technologies such as Lead-acid, Nickel-Cadmium (NiCd) or Nickel-metal hydride (NiMH), the advantages offered by lithium-ion battery has been predominant, with a great energetic density, good longevity (life cycles), good charging/discharging efficiency, low maintenance required, very low of memory effect, low auto discharge phenomenon and noticeable power [2]–[4]. Nevertheless, it does have its disadvantages, like the risks of heating or even fire provoked by an internal short-circuit [5] and still presents many issues in terms of stability, charging, thermal management, recycling and safety [6]. In addition, this technology consumes unevenly distributed and critical materials across the world, such as lithium, copper or cobalt. Even rare-earths metals, that are ironically not rare, are subject to China’s quasi-monopoly, which can imply geopolitical and commercial conflicts [7]–[9].

Speaking of the general overview of the current issue with energy, it is now clear that the energy present a key role in the global warming. The sixth report of the IPCC (International Panel on Climate Change) [9], [10] emphasizes a global reduction of use of fossil energies responsible for 86% of worldwide CO₂ emissions. In this global change, the electrification reveals a major place, where the batteries have a role to play not as a key solution but as part of a global diversification of technologies. Indeed, Fig. 1 reveals the main and most opportunities proposed by the sixth report of IPCC to scale up climate action. Solar and wind reveal to be at the top, as in terms of cost as in efficient greenhouse gas reduction. Of course, this intermittent sources of energy are closely linked with energy storage technologies. However, the current stage of battery as energy storage enables a high viability in terms of costs, as the report specifies:

«

Electricity from photovoltaic and wind is now cheaper than electricity from fossil sources in many regions, electric vehicles are increasingly competitive with internal combustion engines, and large-scale battery storage on electricity grids is increasingly viable.

» — Sixth report of IPCC (2023) [10]

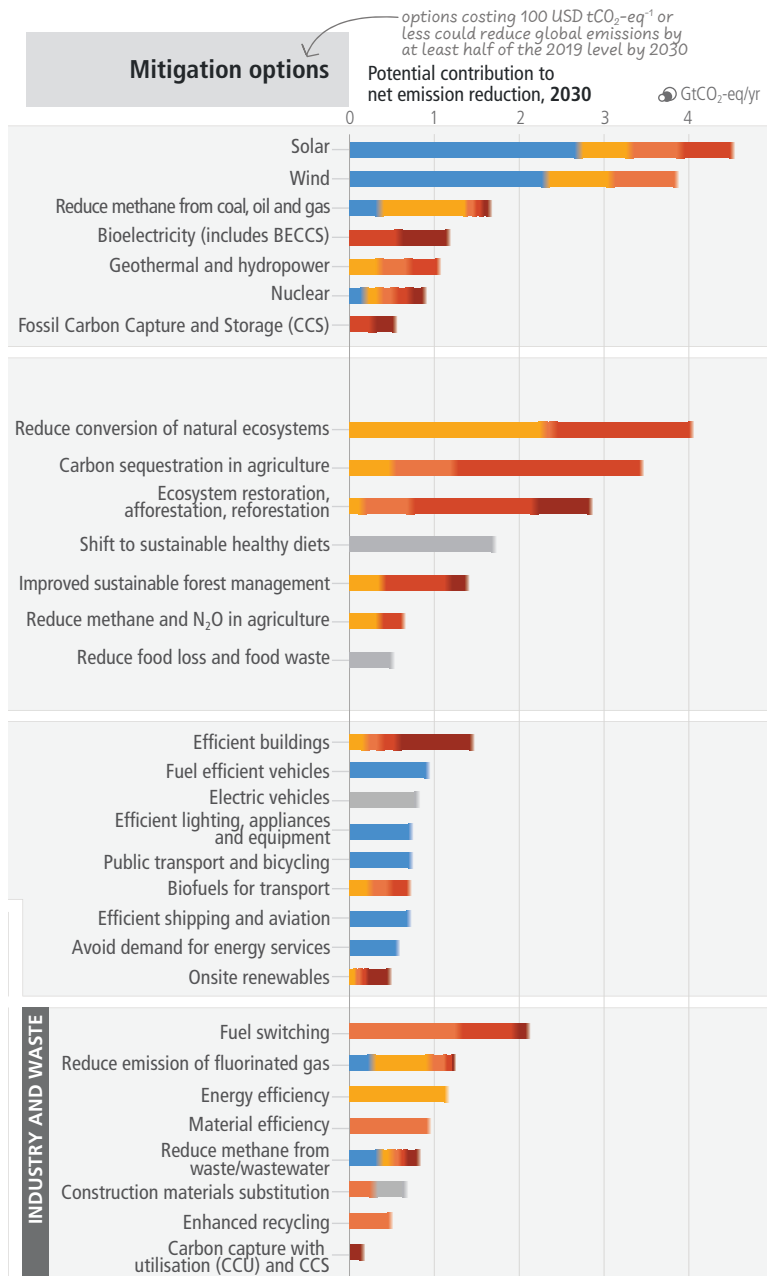


Figure 1: Mitigation opportunities for scaling up climate action, in terms of greenhouse gas reduction and cost. Extracted from sixth report of IPCC (2023) [10], Figure SPM.7 ^a.

^a © International Panel on Climate Change. Open access.

In addition, considering a strategy of non-single technology resolution in the great energy debate, the issues of the lithium-ion battery also concern the electric vehicles, the field in which this technology is particularly considered as a storage solution. This is why when we talk about the lithium-ion battery issues, we generally talk about its exploitation for electric vehicles, in which the disadvantages are particularly revealed (autonomy, security, financial and environmental cost, etc.).

As an obvious way in this period of Ecological Transition, the main issue tackled by the transition to electric vehicles are the greenhouse gas emissions. In this sense, in the report of the E4T Project of the ADEME, Le Berr

et al. (2018) [11] estimate the most relevant evolutions of electric vehicles by the year 2030, in order to minimize the environmental impact. Of course, this study also takes into account the actual vehicles manufacturing, one of the most polluting life part of the electric vehicles. The conclusions are particularly interesting, and non-necessarily intuitive. For example, the use of full electric or hybrid buses for collective transport is strongly efficient in terms of greenhouse gas emission reduction. However, the Plug-in Hybrid Electric Vehicle shows to be more effective compared to the Batteries Electric Vehicles, thanks to the sizing of the batteries more adapted for a daily use. Finally, long distant goods transports still favour the diesel or natural gas engines, mainly because of financial reasons but also because of thermal engine that competes with the electrical technology (due to the high energetic density of the petrol).

In their report, dealing with the place of electric vehicles in the automobile market for the next decade, Juton & Le Berr (2020) [7] estimate the place of electric vehicles (hybrid systems included) in car market of 5.3%, with a total of 5 million electric vehicle on the road globally, which represent 0.5% of the total light vehicles (2020 figures). Even if these vehicles are still marginal, the cost reduction, the public power, the governmental investments and the attractive concurrence gradually introduced by Tesla lead to a global strategic reorientation of car manufacturers to the electrification of their vehicles. In French market, electric vehicles represented 15.1% of the total sales in 2020, and Juton & Le Berr estimate they will reach 79.8% by 2035. Moreover, China today remains the market leader with more than 2 million electric vehicles, twice as much as in Europe or United-States. In the same way, Hache *et al.* (2018) [12] evaluates the evolution of lithium resource under the constraints engendered by the electric automotive development. They suggest the global stock can reach between 60 and 200 million electric vehicles by 2030, depending on the political scenario, with a required production of lithium comprised between 1,000 and 1,700 kilotons (5 kgLi/vehicle hypothesis). Furthermore, with a aim of enriching the energy mix of renewable energies and its storage devices, the idea of exploiting electric vehicles as mobile storage batteries is gradually considered [2], [13].

In any case, because the challenges of the electric vehicles development are closely related to the lithium-ion batteries' ones, the overview of the required improvement can be based on the introducing list of major electric vehicles points of Sauvant-Moynot *et al.* (2020) [14]: cost, safety, specific energy, specific power, charging speed and life cycles.

In this context, this thesis aims to address mechanical behaviours of the lithium-ion battery that can generate safety issues and accelerated aging.

Basics on the battery

Before entering any discussion about the battery, it is noteworthy to clearly state and define what is a “**battery**”, the technology at the core of this manuscript. A precise way to designate what we will call “battery” all along this manuscript would be an “**reversible electrochemical accumulator**”, by excluding the category of “flow batteries”. By definition, an “**accumulator**” is an energy storage device (whatever the form of the energy: mechanical, thermal, chemical, electrical, etc.) and an “**electrochemical**” reaction refers to reciprocal transformation between electrical energy (electric charges movement) and chemical energy (potential stored by substances provided or captured during a transformation to another substance). The “**reversible**” term presents

one of the core interests of this manuscript. Indeed, through divergences of use, the term “battery” designates an electrochemical accumulator that is reversible or not. The term “battery” can also designate an assembly of batteries. In the latter case, some will prefer to talk about a “cell battery”. As a French speaker, the confusion is all the more important concerning the real definitions, due to the French terms “*batterie*” that designates only an assembly, “*pile*” an irreversible battery and “*pile rechargeable*” a reversible battery, sometimes called “*accumulateur*”. . . Hence, stating a clear definition is obviously necessary.

In this manuscript, the term “**battery**” designates a unique electrochemical accumulator able to effectuate the conversion between chemical energy and electrical energy, possibly in both directions but non-simultaneously. The definition of this manuscript also excludes the “flow battery” that is based on the liquid flow of electrolyte solution.

To better understand the composition of a battery, an interesting axis is to look at its past. Many pioneer inventors introduced systems of “capacitors banks” generally based on assemblies of jars. Ewald Jürgen von Kleist introduced the “Leyden jar” in 1745, a precursor form of the condenser [15], closely followed by Johann Heinrich Winkler, Daniel Gralath but also Benjamin Franklin with only one year apart each (1746, 1747 and 1748 respectively). Even if he did not invent it, the latter one, Benjamin Franklin, is known to be the first to use the term “electrical battery” [16]. Some precursor forms of the battery were even older. The oldest discussed remnant of battery is the “Baghdad battery”, a 2000-year-old ceramic pot discovered in 1936 in Khu jut Rabu, a village closed to the Iraqi capital Baghdad [17]. Even if it contained the major components of a battery and was capable of producing voltages from 0.8 to nearly 2 V, its real use as a battery is still discussed today [18], and its remains were unfortunately lost during the Iraq war in 2003 [19].

However, the current history often presents another actor at the origin of the battery. In 20th of March 1800, as a key date in battery history, Alessandro Giuseppe Antonio Anastasio Volta sent a letter to the Rt. Hon. Sir Joseph Banks of the Royal Society, presenting his new invention based on the work of his predecessors [20], [21] (translated from French):

«

The apparatus to which I allude, and which will, no doubt, astonish you, is only the assemblage of a number of good conductors of different kinds arranged in a certain manner. Thirty, forty, sixty, or more pieces of copper, or rather silver, applied each to a piece of tin, or zinc, which is much better, and as many layer of water, or any other liquid which may be a better conductor, such as salt water, detergent, &c. or pieces of cardboard, skin, &c. well soaked in these liquids; such layer interposed between every pair or combination of two different metals in an alternate series, and always in the same order of these three kinds of conductors, are all that is necessary for constituting my new instrument, which, as I have said, imitates the effects of the Leyden jar, or of electric batteries.

» — Volta (1800) [21]

Volta consequently presented an astonishingly simple assembly that has remained the fundamental structure of a battery for centuries, until nowadays. Indeed, where Volta describes “*pieces of copper, or rather silver*”, we currently talk about a “positive electrode”; where he describes “*a piece of tin, or zinc*”, we think about a “negative electrode”; and when he describes “*pieces of cardboard, skin, &c. well soaked in these liquids*” (salt water, detergent, etc.), we guess in this description a separator soaked with electrolyte.

Consequently, we are meeting here three main components:

- The cathode
- The anode
- The separator

An important detail to have in mind is the shapes of these components. It is easy to imagine three major blocks aligned and connected, forming the shape of the battery. In fact, each of these components is a thin layer alternatively organised with others and rolled into different ways, generally in cylindrical shape or “pouch” (flat) shape. Moreover, in the today’s batteries, the cathode and the anode are thin layers of mixed “**active material**” and other additives coated on one current collector layer each. By “active material”, we talk about material that stores or release the energy. Generally, the collector is in aluminium for the cathode and in copper for the anode. As an illustration, Fig. 2 presents a schematic view of a cylindrical battery: cathode (+ aluminium collector), anode (+ copper collector) and separator are layers rolled along the cylindrical axis. As a first order of magnitude, their thicknesses are several tens of micrometers. Both anode and cathode are separated by a separator and each one is connected to a different terminal via its respective collector. To obtain such a structure, the battery needs several manufacturing steps, as schemed in Fig. 3 for only one layer. Initially as the form of dried powders, the cathode or anode materials are mixed with solvents. It forms a liquid slurry, also called “ink”, coated on the collector (3.①). The resulting wet layer is dried through a heating process in an oven (3.②) and then calendered under a roll to compact the material 3.③. All the different layers are then rolled, the battery assembled and filled with the electrolyte that impregnates the layers (3.④), giving the final battery in its protective can (3.⑤).

Since its introduction in 1800 by Volta, the fundamental structure of the battery remained the same, though it knew many improvements. These improvements were mainly brought through the use of new materials for its compounds. In particular, when we talk about the ions travelling across the separator, the nature of these ions depends on the material the battery is made of. In this thesis, the type of battery addressed is the one already introduced above: the “**lithium-ion battery**”, also called “**Li-ion battery**” (or “**LIB**”).

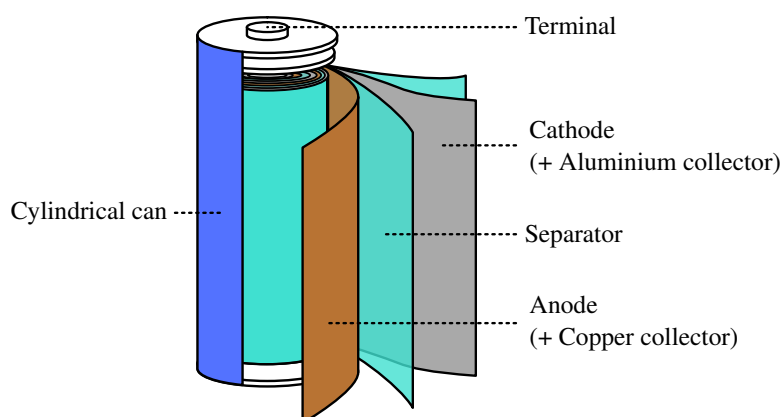


Figure 2: 3D scheme of cylindrical battery. Cathode (+ aluminium collector), anode (+ copper collector) and separator are thin layers rolled within a container. Cathode and anode are connected to different terminals (only one shown here) via the collectors.

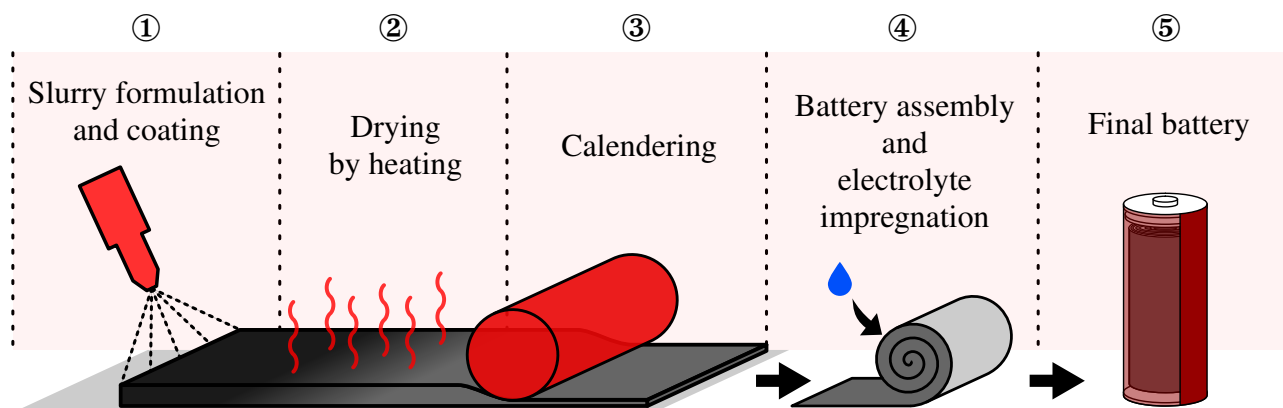


Figure 3: Scheme of battery manufacturing process (only one layer displayed, cathode or anode) — ①): The cathode or anode powder is mixed with solvents in a slurry and coated on the collector. ②) The wet layer is dried through a heating process in an oven. ③) The dried layer is calendered under a roll to compact the material. ④) The different layers are rolled, the battery assembled and filled with the electrolyte that impregnates the layers. ⑤) The final battery is contained in its protective can (cylindrical here).

Concerning its intrinsic functioning, a Li-ion battery has no any other objective than creating a flux of electrons within an electrical circuit, as schemed in Fig. 4. This flux of electrons is made through the connection of parallel “redox reactions”, one reaction of “reduction” that receives electrons and another one of “oxidation” that releases electrons. The current goes in and out through two terminals (half-transparent rectangles in Fig. 4). Each one of these terminals is then connected to an electrode through a current collector, “**electrode**” being the generic name of cathode or anode. Hence, to distinguish if an electrode is a cathode or an anode, we have to look at the electrochemical reaction that occurs at its surface. By definition, the “**cathode**” (left electrodes in Fig. 4) is an electrode where the reaction of reduction occurs and an “**anode**” (right electrodes in Fig. 4) where the reaction of oxidation occurs. Rigorously, the names of both electrodes would have to interchange depending on the use of the battery (charge or discharge), but for the sake of naming convention, the action of reference is the discharge. As a direct consequence, during the discharge, the anode releases the electrons and the cathode receives them. Thus, the anode is the “negative” electrode and the cathode the “positive” electrode. In more simple terms, the anode is the electrode that stores the electrons for a future practical use. Of course, this connection through the terminals is not enough for the parallel redox reactions. When electrons are released by the reduction reaction, some ions are also released, their nature depending on the battery type (lithium ions in the case of Li-ion battery). Rather than going through the circuit, they cross the third main component, the microporous “**separator**”, impermeable to electrons but not to ions (central rounded rectangles in Fig. 4). Consequently, the charge and discharge process creates a displacement of atoms within the battery, alternating between cathode and anode. More particularly, when ions travels across the separator, from an electrode to another, it is stored within the destination electrode. In proper terms, the storing of lithium within an electrode is called “**lithiation**”, and the reverse phenomenon “**delithiation**”.

The lithiation and delithiation phenomena, obviously, make necessary the travelling of ions through the electrode material, which imposes a certain microstructure. When we talk about the electrode material, we do not talk about a perfect monocrystalline material composed of one layer, but a material composed of multiple

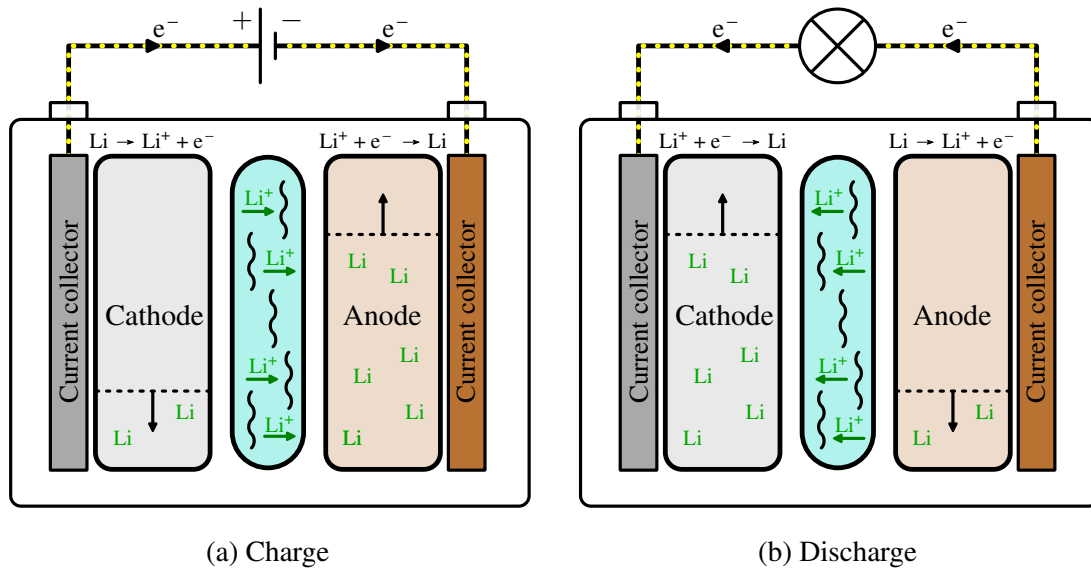


Figure 4: Basic functional scheme of a battery. During charge (a), lithium ions transfer from cathode to anode through the separator (central rounded rectangles), whereas electrons goes through the electrical circuit. During discharge (b), the reverse occurs.

particles and aggregates. To illustrate this, the anode cross-section in Fig. 5a, extracted from Lory *et al.* (2020) [22], reveals the anode as an assembly of complex-shaped particles and flakes packed on a unique layer. The light grey particles are made of silicon-carbon composite and the dark grey particles are made of graphite. The black and white parts represents the inter-particles cavities. Moreover, Fig. 5b schemes the different components of this microstructure. The particles that store or release the ions are, as introduced above, the “**active material**” (AM) particles. In the surrounding cavities, some material called “**carbon-binder domain**” (CBD) particles are composed of additives that ensure the cohesion of active material particles and their conductivity. The material used to glue the active material particles is called “**binder**”. The extra void volume (also called “**pore volume**”), filled with electrolyte, is essential to ensure the diffusion of lithium ions within the electrode, so that they can reach all the particles of the layer. When the electrode material is charged, the lithium ions enter the electrode, travel through the pore volume until lithiating an active Li material particle. When the electrode material is discharged, the reverse occurs.

In direct consequence of this basic fundamental functioning, the exchange of ions between cathode and anode during charge or discharge is an exchange of mass. If the battery does not leak, we may think about the conservation of the mass: the mass of lithium within the battery always remains the same. However, we must strictly distinguish the mass from another physical quantity: the volume. As we can imagine, the exchange of ions imposes a restructuring of electrodes inner materials. This aspect is fundamental for the development of this thesis.

The mass is conserved, but not necessarily the volume.

To enter the subject with a playful metaphor, let us consider the travelling ions as clothes, and each electrode material as a people owing a bag to store the clothes. Let consider that the absolute mass of the clothes does not change. Now, let imagine that the first person is particularly fastidious and always take the time to fold any piece of clothing to optimize the volume it takes, and the second person is, at the opposite, especially messy

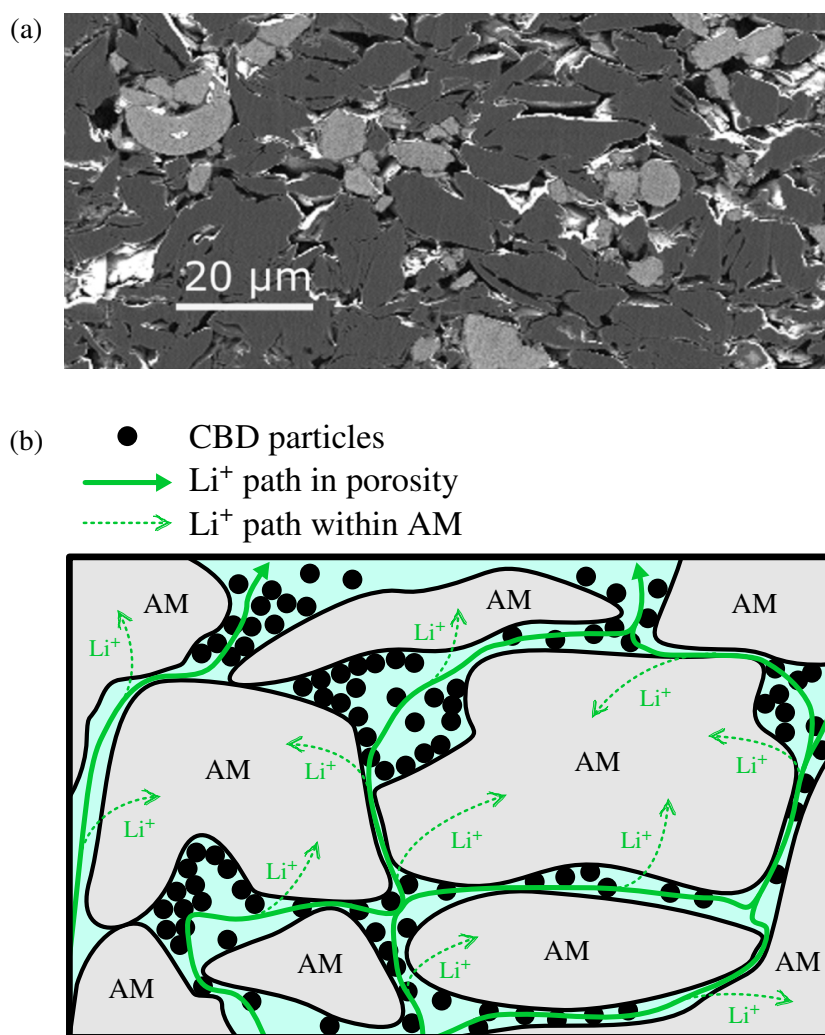


Figure 5: Illustration of granular structure of electrode material — **a)** Cross-section of a pristine anode composed of silicon-carbon composite (light grey particles) and graphite (dark grey particles). Observed by scanning electron microscopy. Extracted from Lory et al. (2020) [22], Figure 1^a. **b)** Scheme of electrode material microstructure (lithiation). It is mainly composed of active material (AM) particles glued together by carbon-binder domain (CBD) particles. The CBD particles (simplified as spheres for readability) are composed of binder and conductive additives that ensure the electrical conductivity between particles. Lithium ions travels in the electrolyte that fills the pore cavities (path as thick solid arrows) and lithiate the AM particles (path as thin dashed arrows) on all the electrode layer. The reverse paths occur for delithiation.

^a © Journal of The Electrochemical Society. Reproduced under charge-free nature of reuse. IOP Publishing Ltd, all rights reserved.

and always tidy the clothes by rolling and throwing them in the bag. As you can imagine, if the first person gives to the second one all the content of his or her bag, the final volume of both bags will be higher than at the beginning, even if the mass of clothes did not change. With this image in mind, this is the same for materials: during an alloy with lithium, the atomic reorganisation changes from a material to another. Then, any battery presents two electrodes composed of materials necessarily different to ensure an electrochemical potential, and these electrodes exchange ions. As a direct consequence, it is most likely that the volume variation of these materials does not compensate each other, because when one increase, the other does not necessarily decrease in the exact opposite way. In other words, the total battery volume variation is most likely to vary during the

charge or the discharge. Both charge/discharge phases will present opposite behaviours: if the volume increases during charge, it decreases during discharge, and vice versa. With other terms, the battery can alternately swell and shrink.

The term “swelling” is a commonly used term in literature to describe this phenomenon. However, this term seems incomplete because it forgets the half of this phenomenon. In this optic, to include both swelling and shrinking behaviours, Olivier Gillia, the PhD advisor of this thesis, proposed to call it “**breathing**”, as he used this term when studying the breathing of metal hydrides [23].

Overview of thesis aim and structure

An internal breathing of the electrode placed in its rigid container can generate more or less important variation of pressure. On one hand, this variation of pressure may constitute a safety issue. Indeed, any crack of the container could imply the contact of lithium with humidity, which is known to create a highly exothermic reaction. On the other hand, the internal pressure variation can generate accelerated fractures of active material microstructure, and then an accelerated diminution of conductivity and/or capacity. As it is further detailed in bibliography (see Chapter 1), one of the current challenge is to better understand the breathing behaviour of the battery electrode. The final goal of such a knowledge will be the design of electrode material that mechanically absorb its own breathing. The term “mechanically” is important, because this thesis focuses on the mechanics of the breathing. More particularly, it considers the active material as a granular structure. Thus, the main objective of this thesis is to understand the role of the granular structure in the breathing behaviour. The main strategy is a progressive analysis of the granular parameters likely to influence the breathing, in order to detect which parameters can be possible levers to influence the breathing during material design. Chapter 1 details the state-of-the-art about battery breathing studies, in order to detail why this thesis objective has been stated. It also introduces the DEM (Discrete Element Method), the main simulation tool used in this thesis. Chapter 2 details the discrete model of electrode used in this thesis, and Chapter 3 presents the associated results, through a succession of sensitivity analyses. Chapter 4 presents a series of experimental measurements to complete the breathing knowledge, more precisely about the influence of temperature and pressure. Finally, Chapter 5 presents a comparison between discrete model and experimental results in order to define the eventual axis of modelling accuracy improvement.

Chapter 1

Bibliography

1.1 Review of studied technology

1.1.1 Li-ion battery current challenges

1.1.1.a State-of-the-art of Li-ion battery

The current standard needs in terms of power and energy require an important optimisation, as for the voltage and current it has to provide as for the capacity weight or volume density. However, many phenomena occur within a battery, and some are responsible for gradual internal damaging [2], [5], [24]–[26]. For example, the breathing of the material creates compressive stress within the material, engendering fractures of inner-particles and then loss of conductivity. Moreover, the Solid Electrolyte Interphase (SEI), *i.e.* an accumulation of decomposition product at the interface with electrolyte and electrode material, implies lithium loss or limited diffusivity of ions, reducing capacity and increasing current resistance [26].

The description of the electrochemical failure mechanisms is complex and not the subject of this thesis. However, the improvement of Li-ion battery is twined with the understanding of these failure mechanisms that create capacity loss, short lifespan and even safety issues [4], [25], [27]. Moreover, it is known that an intrinsic correlation exists between mechanics and electrochemistry [26], [27], starting with the existence of internal volume changes that engender hardly predictable pressure changes and material fractures.

Nowadays, a highly regarded solution to improve battery capacities is adding silicon in the anode material. Most batteries anode are composed of graphite, a cheap and common material that reveals a capacity of 372 mAh/g [4], [25], [28]–[30]. The use of silicon is attractive because of its high energy density of around 4,200 mAh/g [29], [31]–[34], with a more realistic and practical value at room temperature of around 3,580 mAh/g [4], [28], [29], [35], [36]. As an important solution for capacity improvement, silicon could help in improving today's energy densities mainly based on graphite material, from 160~260 Wh/kg / 450~730 Wh/L to 275~320 Wh/kg / 750~900 Wh/L by 2030 (electrode level, more detailed figures are given in Table 1.1) [4]. This solution is rooted in the liquid-electrolyte-based lithium-ion batteries generation, whereas other solutions are seriously considered today such as solid-state lithium batteries and non-lithium based batteries (mainly sodium), even if many challenges remain [26], [37]–[39]. In this context, the current battery technology requires further development of classical liquid-electrolyte-based solution.

	2020	2030	2050		2020	2030	2050
	Gravimetric energy density (Wh/kg)				Volumetric energy density (Wh/L)		
Pack level	90~180	190~230	>250	Pack level	250~400	450~550	>600
Cell level	160~260	275~320	>350	Cell level	450~730	750~900	>1000

Table 1.1: Orders of magnitude of lithium-ion battery energy densities (gravimetric and volumetric, pack level and cell level). Compiled values for 2020 and estimated values for 2030 and 2050. Data extracted from Armand *et al.* (2020) [4], Table 3.

More centred to the current work, this thesis is located at the continuation of a previous thesis, by Delphine Vidal (2021) [40]. With a mainly experimental approach, Delphine Vidal’s work addressed the impact of mechanical stress on performances and cyclability of a lithium cell containing silicon. By joining macroscopic measurement of lithium cell thickness and X-ray microtomography, Delphine Vidal’s work provided a rich understanding on the way batteries containing silicon behave, in terms of structure change during charge and discharge cycles. This predecessor thesis often referred to “particles rearrangement” in order to explain some phenomena of irreversibility. Nevertheless, her approach did not enable her to clarify this aspect. As a result, the current thesis aims to establish the continuity of these questions of “particles rearrangement”. The main objective of the thesis is discussed in Section 1.1.2.a.

1.1.1.b Key technological issue

Silicon presents a major drawback: during lithiation, the atomic reorganisation leads to a drastic macroscopic volume change. Using atomic force microscopy, Beaulieu *et al.* (2003) [41], [42] studied silicon lithiation until the maximum crystallographic stage, revealing an approximate volume change of 310% (4.1 times the delithiated material volume). The resulting volume variation is displayed in Fig. 1.1, where two particular scans reveal a silicon sample thickness varying from around 240 nm to 850 nm. In practice, the swelled stage at 310% is never reached and the battery context conditions (in temperature, pressure, etc.) limits the macroscopic volume change to around 280%. By comparison, the graphite present a maximum of 10% volume change [30], [35], [43], [44]. Inevitably, this mechanical behaviour is undesirable when it comes to ensure safe and long-life batteries and directly linked to the questionings about inner failure mechanisms of battery. For this reason, many researches aimed to understand the breathing of electrode containing silicon, in order to find how to control it from a manufacturing perspective.

— As a brief parenthesis, silicon is never introduced directly as a raw material within the graphite anode and always encapsulated in a composite, because of a strong reactivity with usual electrolytes. Several composite types exist, but the most commonly used are the oxygen-based (SiO_x) or carbon-based (Si/C) composite, the latter being the one used in this thesis. For a better clarity, because these materials are often introduced in this manuscript, it is proposed to note “Si/C” or “CSI” for silicon-carbon composite and “Gr” for graphite. In order to avoid any confusion with silicon carbide, the designation “SiC” is avoided in this manuscript. —

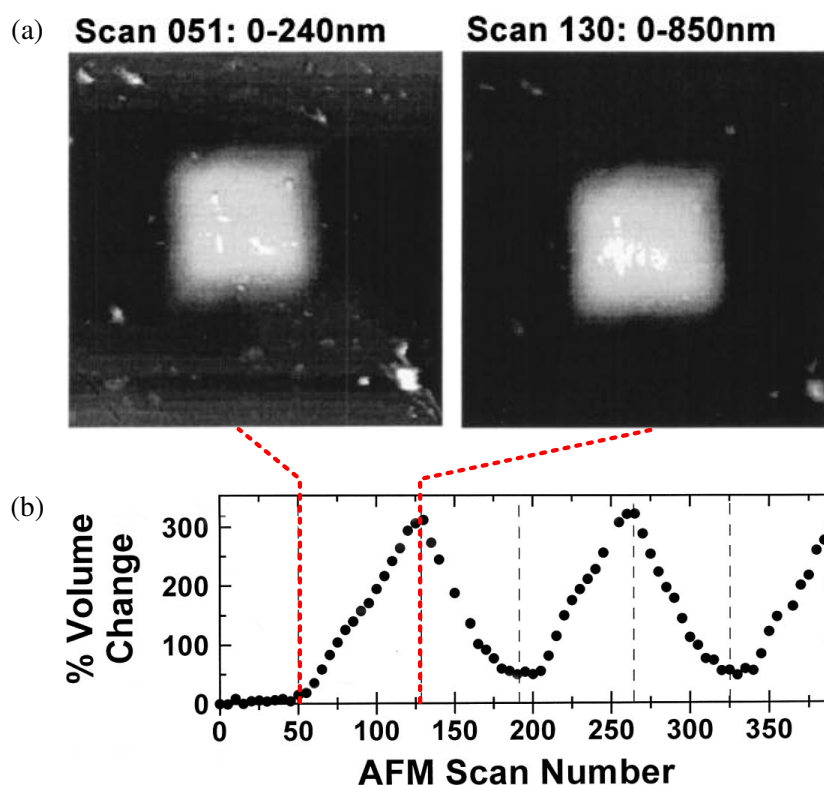


Figure 1.1: Measurement of amorphous silicon structure change during lithiation/delithiation — **a)** Patterned silicon sample observed with in-situ atomic force microscopy (AFM). **b)** Volume of silicon tower shown as a function of AFM scan number. Adapted from Beaulieu *et al.* (2003) [42], Figure 9 & 10 ^a.

^a © Journal of The Electrochemical Society. Reproduced under charge-free nature of reuse. IOP Publishing Ltd, all rights reserved.

1.1.1.c Review of experimental studies on electrode breathing

The electrode breathing is already addressed in literature and many approaches are experimental. In this sense, Table 1.2 lists the experimental approaches that explain the breathing behaviour, detailing the techniques used (with the associated scale: particles or electrode), the studied parameter susceptible to impact the breathing and noticeable conclusions directly or indirectly linked to the breathing. The present section enters in details of these references, before developing a more general analysis of experimental approaches.

Li *et al.* (2017) [45] made *in situ* swelling measurement of NMC-Si/C-Gr electrodes using scanning electron microscopy, revealing a final amount of swelling at the end of life of around 56%. More singular, Wen *et al.* (2017) [46] carried out an *in operando* measurement of the volume change using Archimedes effects by recording the change of buoyancy of a cell plunged in water. They demonstrated that the binder type had a noticeable impact on swelling (eventual reduction of around 30%), but the very low amount of volume expansion ($\sim 1\%$) is as debatable as the fact they do not clearly define the volume change ratio.

Closer to the methods used in this thesis, Müller *et al.* (2019) [47] used a spring-based press device to measure the thickness evolution at controlled pressure, through three regimes of compression: “uncompressed”, “flexible” (constant pressure and variable thickness) and “fixed” (variable pressure and constant thickness). Their development misses an important definition about the “fixed” compression, where the pressure necessarily varies over time. They associate a value of pressure to this compression, by stating it as “average pressure”,

Reference	Measurement technique	Studied parameter impacting breathing	Noticeable conclusion(s)
Li <i>et al.</i> (2017) [45]	Scanning electron microscopy *	–	End-of-life thickness change: 56% of initial thickness.
Wen <i>et al.</i> (2017) [46]	Byouancy change of cell in water	Binder type	Reduction of 30% of volume change by using the right type.
Müller <i>et al.</i> (2019) [47]	Spring-based press	Pressure regime during cycling	High pressure (0.84 MPa) with variable thickness: microstructure porosity erased. Low average pressure (0.08 MPa) with constant thickness: microstructure similar to uncompressed cell.
Zhao <i>et al.</i> (2017) [48]	Surface laser scan	Adhesive contaminant	Generates local change of breathing behaviour (swelling during discharge)
Petz <i>et al.</i> (2021) [49]	X-ray tomography *	Current tab position	When placed within the roll, generates inhomogeneous lithiation (eventually breathing)
Yao <i>et al.</i> (2019) [50]	X-ray diffraction *	Lithiation distribution between Si and Gr	Its variability along charge/discharge explains the breathing shape of Si/Gr anode
Berhaut <i>et al.</i> (2019) [51]	Synchrotron X-ray *	C-rate	Charge: limited impact. Discharge: limits the internal lithium exchange between Si and Gr (eventual impact on breathing shape)
Vidal <i>et al.</i> (2021) [40], [52]	Step-motor-based press	Pressure during cycling	Reduces breathing amplitude and porosity
von Kessel <i>et al.</i> (2023) [53]	Air-pressure-based press	Pressure during cycling	Reduces breathing amplitude

Table 1.2: Review of experimental studies of electrode breathing. The technique used can be either at particles scale (noted with an asterisk “*”) or at electrode scale (by default, without asterisk). This summary focuses on the studied parameters with eventual influence on breathing and/or microstructure.

without defining what the average is based on (spatial on cell surface? Temporal on all the cycles? Statistical on several samples?). It is supposed that the average is temporal on the whole cycle. When it comes to their results, Fig. 1.2 presents three scans of post-cycled Si/C anodes submitted to these three regimes. They reveal a clear influence on anode microstructure, especially for flexible compression at high pressure that almost erased the particle structure. Strangely enough, the anode at fixed compression reached a microstructure similar to uncompressed anode, despite the increasing pressure during cycling. Some inhomogeneities in pressure distribution on the surface of the cell compressed at fixed pressure were also revealed, likely to influence the capacity loss according to the authors. Through their work, Müller *et al.* (2019) [47] found optimum configurations to obtain the lowest capacity fading with an average pressure (0.08 MPa) for constant-thickness and middle pressure (0.42 MPa) for constant pressure.

As a complementary approach about lithiation inhomogeneities, Zhao *et al.* (2019) [48] focused on the heterogeneity of swelling using a laser-scanning device on the surface of the cell. As displayed in Fig. 1.3a, the cell presented some swelling spots on the surface that strangely appeared during the discharge (when the

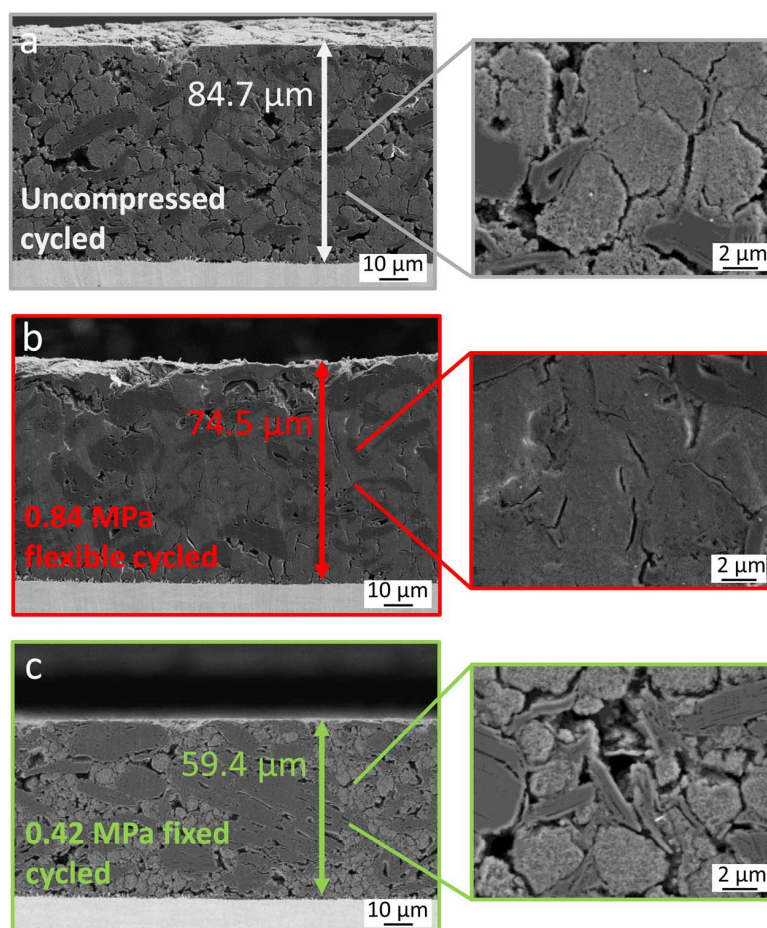


Figure 1.2: Cross-sections in two different magnifications of the Si/C anodes harvested from cells cycled, observed with scanning electron microscopy — **a)** Uncompressed cell. **b)** Cell under 0.84 MPa “flexible compression” (constant pressure and variable thickness). **c)** Cell under 0.42 MPa “fixed compression” (variable pressure and constant thickness). The pressure is given as an “average value”, but the “average” definition is missing in referenced paper. Extracted from Müller *et al.* (2019) [47], Figure 4^a.

^a © Journal of The Electrochemical Society. Open access.

cell is expected to shrink, not to swell). They correlated this swelling spots with the presence of adhesive-like contaminant (certainly from glue used in the cell manufacturing). Hence, this result demonstrates how a layer with different adhesive properties can present diverging swelling behaviour. In a comparable objective, Petz *et al.* (2021) [49] used X-ray micro-computed tomography to measure the inner-heterogeneity swelling of 34 18650-type (cylindrical) cells. They showed that the current tabs (conductive tabs connecting current collectors to terminals) can have an impact on lithiation only through the position they have within the cell. As an example, Fig. 1.3b draws four samples, where left sample had a tab inside the roll radius and right samples had tabs on rolls centre and border. The lithiation is clearly impacted, through a characteristic “half-moon” of lower lithiation present around the tab within the roll radius (left samples), whereas the tabs placed in centre and borders (right samples) generated a more homogeneous lithiation. It was also shown that the tabs within the roll radius presented better performances in terms of C-rate (speed of charge/discharge referenced to the cell capacity), so a compromise between performance and cell ageing emerges from this study. The authors did

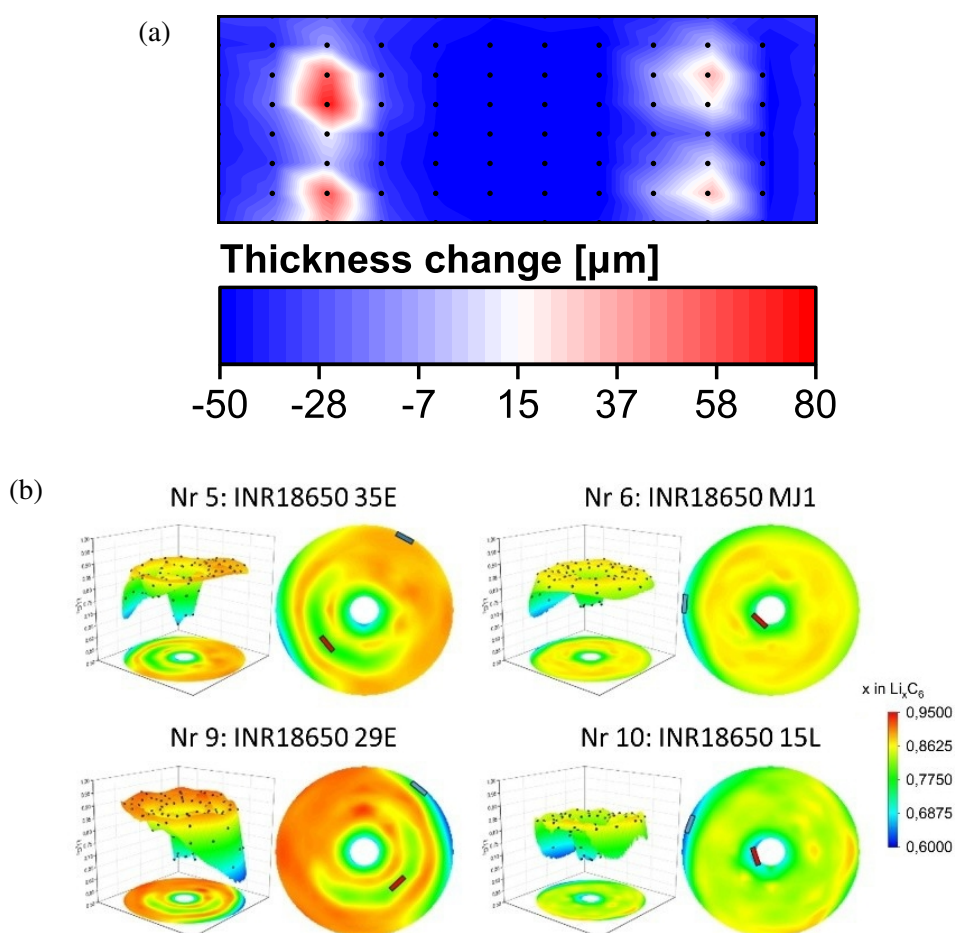


Figure 1.3: Measurements of breathing/lithiation heterogeneities — **a)** Normalized cell thickness distribution change during the IC discharge (top view). Adapted from Zhao *et al.* (2019) [48], Figure 2 ^a. **b)** Lithium concentration in graphite anode of different 18650-type cells (top views), observed X-ray diffraction. Adapted from Petz *et al.* (2021) [49], Figure 2 ^b.

^a © Journal of The Electrochemical Society. Open access.

^b © Batteries & Supercaps. Open access.

not discuss the electrodes breathing itself, or even the variation of stress within the cell, but this inhomogeneity of lithiation is certainly another source of breathing inhomogeneity, comparable to the observations of Zhao *et al.* (2019) [48].

As a way to detect optimal cell use, using an *operando* energy dispersive X-ray diffraction, Yao *et al.* (2019) [50] studied the evolution of lithiation distribution in Si/C and Gr during charge and discharge, in order to catch the best cycling windows. As an illustration, Fig. 1.4 plots both component capacity and potential (VS lithium) of graphite and silicon during lithiation (left half part) and delithiation (right half part). Concerning the lithiation, the lithium storage was silicon-only during the 1→0.2V range (1.4.①) and around 60%silicon/40%graphite during the 0.2→0.01V range (1.4.②). For delithiation, the lithium release was mainly from graphite during the 0.01→0.23V (1.4.③) range and mainly from silicon during the 0.23→1V range (1.4.④). This observation is really useful to estimate the potential range where the volume variation occurs, and then to understand the shapes of volume variation curves during charge and discharge. Berhaut *et al.* (2019) [51] confirmed these observations using a synchrotron wide-angle and small-angle X-ray to analyse *in-situ* lithiation and delithiation phases of both anode materials. They also analysed the influence of C-rate. The influence of C-rate on lithiation distribution between Si and Gr is limited during charge, but during discharge, lower C-rate generates internal exchange of lithium between Si and Gr.

Besides, similarly to the work of Müller *et al.* (2019) [47] presented above, a common way to assess the thickness variation is to use a controlled loading system, in order to pilot the pressure applied on pouch cell (constant or variable load). This method was used by Delphine Vidal in her thesis. Indeed, Vidal *et al.* (2021) [40], [52] used a set-up where the spring/screw system is replaced by a monitored *operando* compression con-

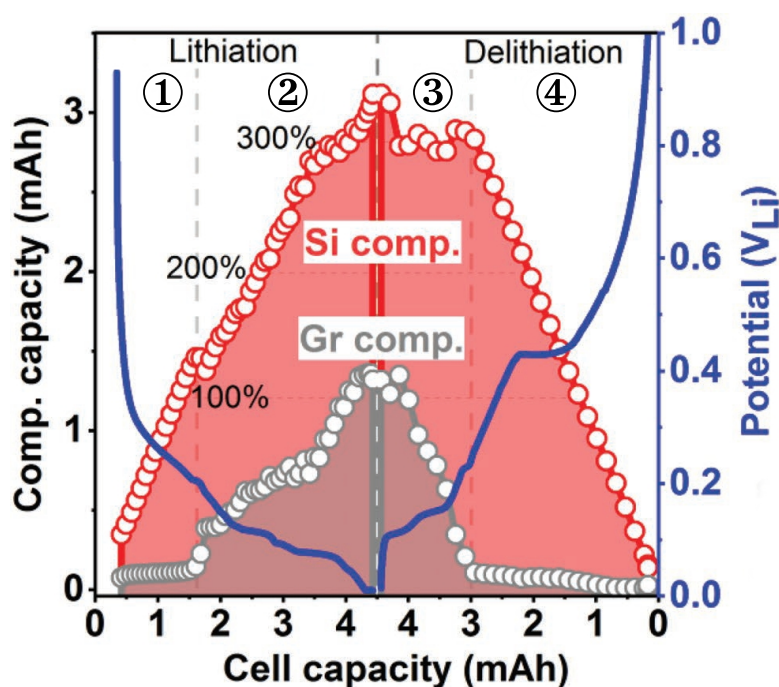


Figure 1.4: Capacity and potential (VS lithium) of graphite and silicon components in Si/Gr electrode during lithiation and delithiation. Percentages are the estimated expansions of silicon particles. Adapted from Yao *et al.* (2019) [50], Figure 4^a.

^a © Advanced Energy Materials. Reproduced under charge-free nature of reuse. John Wiley & Sons (Wiley), all rights reserved.

trolled through a step motor. The experimental approach revealed an asymmetric volume variation between charge and discharge, but also an irreversible porosity increase when pressure on cell was too low. They precisely quantified the variation of thickness of pouch cells, more especially during cell formation cycles. By “formation cycles”, the terms refer to the first cycles of a fresh cell. As an illustration, Fig. 1.5 displays the measurement of thickness change of a NMC622 / Si/C/Gr pouch cell containing 6.5wt% of silicon within active material, during its formation cycles. It was supposed that the measured variation was mainly generated by anode breathing (this aspect is discussed in this manuscript, in Section 4.3.1), so the percentage in right axis presents the relative thickness variation based on the initial anode thickness (48 μm). As we can see, the thickness variation is really high compared to the initial anode thickness, until 23.3% at the highest plotted point. Relatively to the initial full pouch cell thickness (360 μm), it represents a thickness change of around 3.1% (value not displayed on graph). This graph also introduces two important features: the swelling amplitude (dashed arrows) and the irreversibility (solid arrows). Their evolution over time, cycle after cycle, is problematic due the variable stress they generate during the cell life. This aspect is discussed in more detail in Section 1.1.2.a, but also globally in this manuscript as it constitutes a key feature to assess the breathing. To conclude the section on experimental studies, von Kessel *et al.* (2023) [53] proposed an air-pressure-based press to study the cell expansion but also some material parameters, revealing the high proportion of volume expansion due to SiO_x and the clear impact of pressure on reversible volume expansion (changing pressure from 0.1 to 2 MPa generates a 34% decrease of volume expansion). In the same scope as Vidal *et al.* (2021) [40], [52], they also presented a complete multiscale coupled electro-mechanical model, and their clear subdivision of the problem scales (atomic, particle, electrode, cell and housing, displayed in Fig. 1.6) is an excellent frame to expose the core question of this thesis, exposed in Section 1.1.2.a.

The review of these experimental approaches gives us interesting clues to understand the electrode breathing, as Table 1.2 introduced above summarises. As we can see, mostly looking at the studied parameters, studies

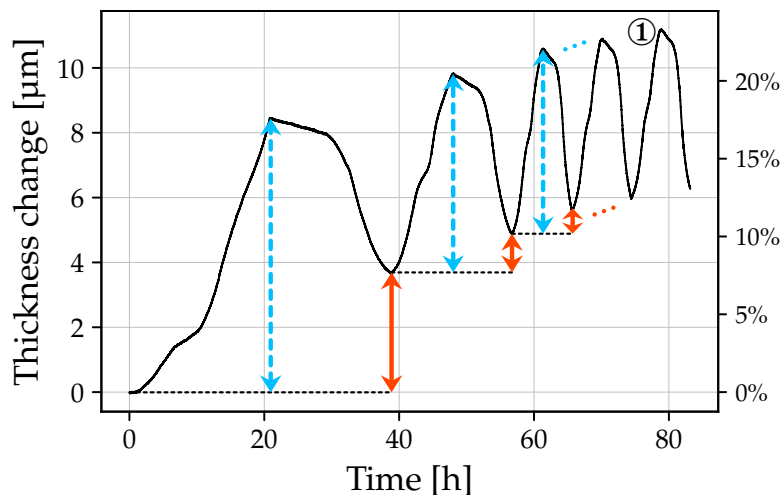


Figure 1.5: Operando thickness change measurement on a NMC622 / Si/C/Gr pouch cell with 6.5wt% of silicon in anode active material (cycled at 0.5 MPa and 22°C). The percentage on the right axis is the relative thickness change, based on the initial anode thickness (48 μm). Dashed arrows represent the swelling amplitude of the breathing and the solid arrows the irreversibility of the breathing. Data extracted from Vidal *et al.* (2021) [40], Figure III-6 (pouch cell A72).

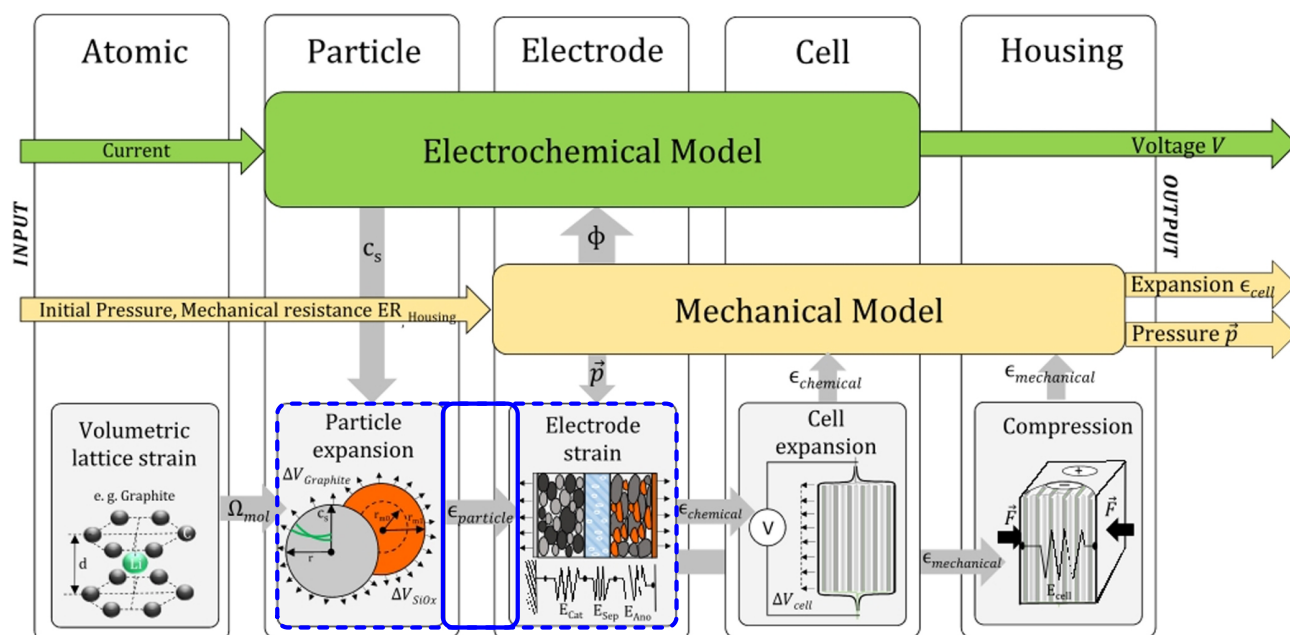


Figure 1.6: Scheme of workflow and structure of the multiscale electrochemical-mechanical model. Thick dashed rectangle designates both scales related to this thesis. Thick solid rectangle locates the objective of this thesis: breathing transfer from particles scale to electrode scale (see Section 1.1.2.a). Adapted from von Kessel *et al.* (2023) [53], Figure 2^a.

^a © Journal of The Electrochemical Society. Reproduced under charge-free nature of reuse. IOP Publishing Ltd, all rights reserved.

have focused on electrode use conditions (C-rate, pressure during cycling), manufacturing artefacts (adhesive contaminant, current tab position) and electrochemical properties of Si and Gr (lithiation distribution). The latter parameter (lithiation distribution), is really useful to understand the breathing shape at electrode scale. However, it is not a key parameter to control the breathing, because it is imposed by electrochemical laws. Concerning the electrode use conditions (C-rate, pressure during cycling) are partially interesting from a manufacturing perspective, because they are related to the capacity and packing design. However, their evident dependency to conditions out of the manufacturing process limits the breathing controllability through electrode design. In fact, the manufacturing artefacts, and more precisely the adhesive contaminant study by Yao *et al.* (2019) [50], reveals an interesting feature in terms of breathing controllability. Indeed, this study reveals that, considering a given electrode composed with a material supposed homogeneous, local change of adhesion within the material causes significant change of its breathing behaviour. This observation is important to address the breathing controllability through a mechanical perspective, the electrochemical aspect being quite imposed by the use conditions and the electrochemistry itself. In that respect, the literature already addressed the breathing behaviour through modelling.

1.1.1.d Review of modelling studies on electrode breathing

In literature, the electrode breathing is less addressed through modelling than experiment. As a summary, Table 1.3 lists all the cited references, the type of model used, the studied parameter and noticeable conclusions. This section reviews these references before discussing more generally about the eventual unexplored axis.

Reference	Model dimension	Studied parameter	Noticeable conclusion(s)
Pereira <i>et al.</i> (2019) [54]	1D	Silicon fraction	Existence of optimal value to obtained enhanced capacity (considering fixed casing constraint).
Chen <i>et al.</i> (2019) [55]	P2D	Silicon fraction	Existence of optimal value to obtained enhanced capacity (considering fixed casing constraint).
Mai <i>et al.</i> (2019) [56]	P2D	–	Necessity to take into account electrode breathing in models to obtain accurate capacity.
Zhang <i>et al.</i> (2021) [57]	1D	–	Important coupling between electrochemical behaviour and mechanical deformation.
Sauerteig <i>et al.</i> (2018) [58]	1D	Pressure during cycling	Linked to the electrochemistry by reducing pore volume and then ions' diffusivity.
Vidal <i>et al.</i> (2021) [40], [52]	1D	–	Good breathing amplitude but divergent breathing slopes compared to experimental, and no irreversibility captured.
Pegel <i>et al.</i> (2022) [59]	1D	–	Importance of considering void volume variation to obtain accurate breathing behaviour.
Gomadam & Weidner <i>et al.</i> (2005) [60]	3D	Swelling coefficient	Induces greater discharge capacity.

Table 1.3: Review of modelling studies of electrode breathing (all electrochemical-mechanical coupled models) — 1D: mono-dimensional, P2D: pseudo-two-dimensional.

Pereira *et al.* (2019) [54] used a coupled electrochemical-mechanical model to predict the volume change of a cell, through an equivalent Fick's law of porosity and strain for cathode and anode (active layers). They also took into account the mechanical contribution of inactive layers (current collectors, separator and foam packing). By imposing different “cut-off” pressures, *i.e.* standard design limitations (0.25 and 0.5 MPa), they searched for optimal amount of silicon to introduce within anode to improve capacity, simultaneously respecting these packing limitations. Through this approach, they revealed that a judicious balance of silicon fraction and initial porosity could lead to a 59% capacity improvement compared to traditional graphite anode. On their side, Chen *et al.* (2022) [55] used an electrochemical-mechanical model with coupled pseudo-2D and mechanical laws. Their results are consistent with the conclusions of Pereira *et al.* (2019) [54], revealing that casing constraints had a significant impact on cell structure, as opposite to electrochemical behaviours that showed to be poorly affected, as illustrated in Fig. 1.7, where the anode capacity is analysed from 550 to 1,250 mAh/g by varying the Si/C weight fraction. On the left graph (Fig. 1.7a), the cell voltage presents a slight variation induced by anode capacity, only at low state of charge (between 0 and 0.5), whereas on the right graph, the volume variation notably increases with anode capacity (from 4.4% to 10.5%). By introducing a similar notion of “casing constraint” (this time in terms of volume variation cut-off, at 6 and 10%), this work

also underlines the importance of judicious choice of silicon fraction within the anode. It indeed constitutes a compromise point between casing design and required capacity. Moreover, Mai *et al.* (2019) [56] also used a coupled electrochemical-mechanical pseudo-2D model to investigate the behaviour of a silicon-based cell, at both particles and electrode levels. If their equation of porosity/strain variation is really close to Pereira *et al.* (2019) [54]. They underlined the importance of taking into account the electrodes' deformation in models, otherwise it could lead to over-prediction of accessible capacity or energy.

Besides, Zhang *et al.* (2021) [57] considered a mono-dimensional model by a combination of layers with different strains/porosities, demonstrating that mechanical deformation and electrochemical behaviour are connected in a non-negligible way. Sauerteig *et al.* (2018) [58] already used this multi-layer approach through an uniaxial elastic model, by evaluating the deformation of the porous structures only. They demonstrated that the mechanical pressure on the cell is closely linked to the electrochemistry, due to impact on pore volume and then ions' diffusivity. Finally, Pegel *et al.* (2022) [59] also considered the material as a porous one. As schemed in Fig. 1.8, they took into account the void volume variation, and distinguished the respective influence of both SiO_x and graphite in layer structure. They observed that considering in the model the swallowing of the initial large volume expansion of SiO_x by pore volume lead to a very good fit with experiment.

Taking a step back, the previous approaches follow a wide-spread conventional methodology to model the cell breathing, based on a mono-dimensional or pseudo-two-dimensional consideration of electrode. In all these approaches, the consideration of void volume, generally introduced via the porosity, seems highly relevant to model accurately the electrode breathing. Actually, Gomadam & Weidner (2005) [60] already modelled the volume change of porous electrodes by studying the effect of a new-introduced parameter, the "swelling coefficient g ", that is also interesting to introduce our fundamental problematic. Basically, the volume partition of a porous electrode is composed of two terms:

$$V_{\text{electrode}} = V_{\text{solid}} + V_{\text{void}} \quad (1.1)$$

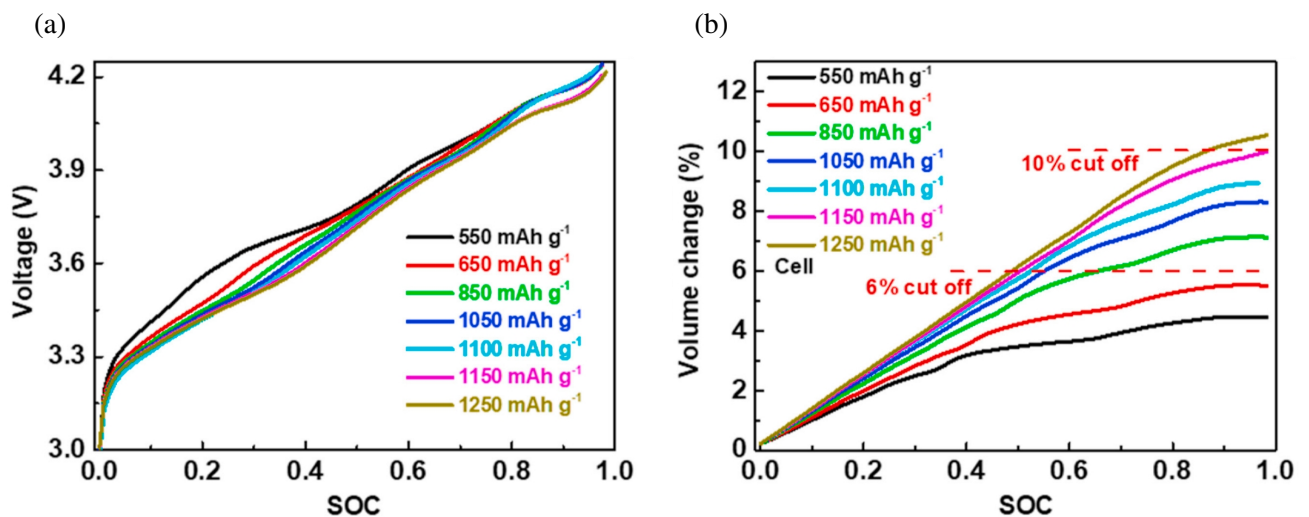


Figure 1.7: Influence of Si/C composite anode capacity (by varying the Si/C weight fraction) — **a**) Influence on cell voltage (electrochemical aspect). **b**) Influence on cell volume variation (mechanical aspect). SOC: State-Of-Charge. Adapted from Chen *et al.* (2022) [55], Figure 6 ^a.

^a © Journal of Power Sources. Reproduced under charge-free nature of reuse. Elsevier B.V., all rights reserved.

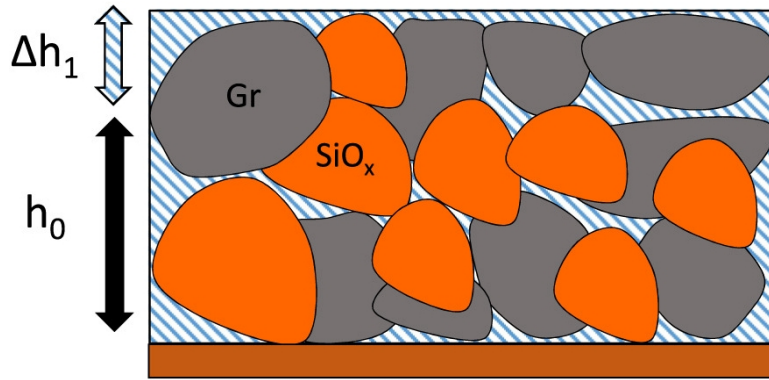


Figure 1.8: Scheme of anode thickness change due to particles (Gr and SiO_x) and porous volumes. Extracted from Pegel et al. (2022) [59], Figure 7^a.

^a © Journal of Power Sources. Reproduced under charge-free nature of reuse. Elsevier B.V., all rights reserved.

Where, as a first approach, we consider the “void” as “everything that do no constitute particles” (electrolyte, binder, additives, etc.). Consequently, when it comes to the variation of this volume, it comes:

$$\Delta V_{\text{electrode}} = \Delta V_{\text{solid}} + \Delta V_{\text{void}} \quad (1.2)$$

Adapted to this volume change partition, the swelling coefficient of Gomadam & Weidner is defined as:

$$g = \frac{\Delta V_{\text{electrode}}}{\Delta V_{\text{solid}}} \quad (1.3)$$

Thus, it describes the proportion of void filling within the electrode: $g = 0$ means that all the solid material volume change is transferred to the void volume (the total electrode volume being constant) and $g = 1$ means that all solid material volume change is transferred to the total electrode volume (the void volume being constant). This number is of major interest for this thesis.

Strangely enough, Gomadam & Weidner (2005) [60] used the swelling coefficient as an input parameter, whereas it is more intuitive to consider it as an evaluating parameter. Indeed, from a manufacturing perspective, the way to set this parameter is hard to imagine.

With a step back on all these references, Table 1.3 offers an overview of the current modelling approaches of breathing modelling. Compared to experiment review in Table 1.2, it is clear that the modelling studies are less oriented to parameters that influence breathing. As we can see, when a studied parameter is defined and analysed sensitively, the conclusions mainly address the electrochemical performances, not the breathing. The breathing is considered in these studies, but not with the aim of finding which parameter is susceptible to reduce it. Furthermore, most of these approaches are mono-dimensional or pseudo-two-dimensional. From a mechanical perspective, considering a material composed of particles that can reorganise in space, these dimensions may be too restrictive. This is this idea of particles space reorganisation that led to the formulation of this thesis.

1.1.2 Thesis position

1.1.2.a Discussion on current studies and core question

All the modelling approaches introduced in previous section considered the void volume within electrode using a key word: “**porosity**”. As a recall, the material that composes the electrode is granular and composed of multiple particles and aggregates glued together by the binder. Then, between these particles, some “void” volume is present. Of course, this void volume is filled with electrolyte, and it is hard to estimate in what extent this liquid generates mechanical resistance. The fact remains that the granular structure implies several questions in terms of mechanics, more precisely in terms of breathing transmission. Indeed, coming back to the scale illustration of von Kessel *et al.* (2023) [53] displayed in Fig. 1.6, the most difficult part in modelling the breathing is the question of scale (thick rectangle Fig. 1.6, illustrated in Fig. 1.9a): how is the breathing of particles transferred to the electrode scale? Does the fact that particles can eventually move relatively each other can impact the breathing at electrode scale? In the thesis of Vidal (2021) [40], several questionings were asked concerning the impact of the granular media on the breathing, mostly to understand phenomena hardly explainable via continuous models. More precisely, Fig. 1.5 shows two important observable features: the “**swelling amplitude**” (dashed arrows) and the “**irreversibility**” (solid arrows) of the breathing. These features, whose definitions are detailed in Section 2.1.1 and largely exploited in this manuscript, are precisely the ones that raised suspicions about the influence of granular media on electrode breathing. Furthermore, in their conclusion, von Kessel *et al.* (2023) [53] clearly indicates the needs in understanding better how the electrodes behave mechanically:

«

The understanding and modeling of the mechanical properties of composite anodes with silicon and high-nickel cathodes should be enhanced and modeled based on physics.

» — von Kessel *et al.* (2023) [53]

As a consequence, the current knowledge about electrode breathing should be modelled to a greater extent. Facing this huge amounts of modelling studies that take into account the granular structure only through evaluation of void volume, here comes an interesting sentence: what if the breathing behaviour was less a matter of porosity than a matter of contact? Indeed, let us consider the following thought exercise: by considering a given particles bed (for example, the one of Fig. 1.9a). If we keep the exact same contact point and reduce the “non-touching volume” of the particles, as in Fig. 1.9b, admitting that these contact points (little squares) does not change significantly all along the breathing, the amount of porosity will be different, but the forces network (dashed lines) and so the final global thickness is likely to remain the same. Of course, this perspective is certainly reductive, and many phenomena can interfere in this simplification, starting with the reorganisation of this new particles bed that will, necessarily, change the forces network and porosity. However, it does not change the main idea proposed here: the porosity should not be seen as a causative parameter, but only as an evaluating one. Instead, the particles are organised because of micro-phenomena that occurs at the levels of the contacts between each other, and this engenders a resulting porosity. Hence, to obtain a better comprehension on the transfer of particles breathing to the electrode scale, searching in the physics of particles contact is certainly a relevant way to explore, as an echo to one of the conclusions of Delphine Vidal’s work:

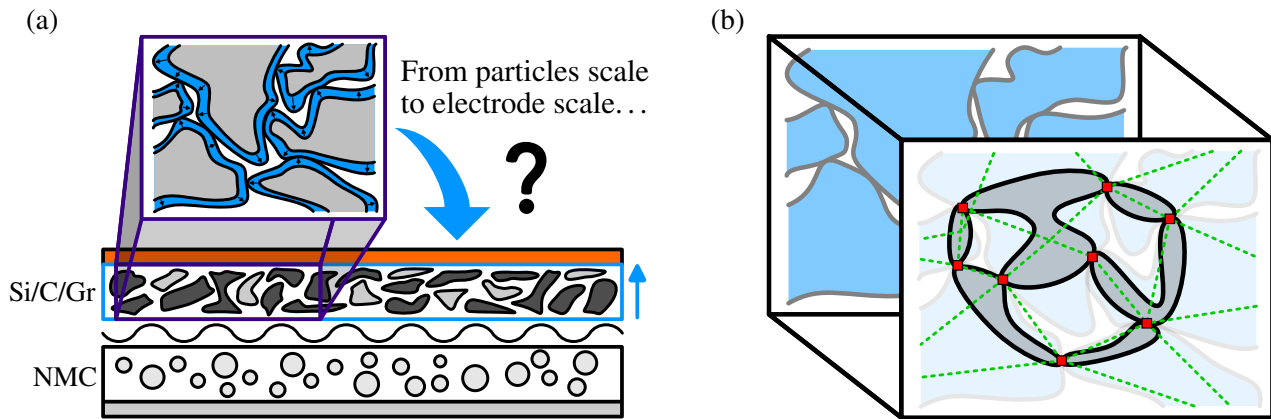


Figure 1.9: Scheme of thesis main problematic reflections — **a)** Issues in modelling the real transfer of breathing from particles scale to electrode scale. **b)** Simplification of the contact network to its unique points of contact.

«

Finally, a more elaborated model, maybe considering spherical particles [...], could provide a more precise evaluation of the porosity and tortuosity of the anode. The study of the mechanical stresses at particle level might also provide significant insights to understand and limit the swelling at electrode level.

» — Vidal (2021) [40]

Hence, the objective of this thesis is to introduce the granular structure within a breathing model of the electrode and to analyse the influence of contact properties on the breathing. This approach aims to explore how the granular media is susceptible to absorb or generate void volume, more or less depending on the granular properties. With a more concrete perspective, the goal is to detect the eventual granular parameters that can be used by a battery manufacturer to obtain an electrode that breaths more reversibly and/or with a lower amplitude. This objective can be summarised with the following “core question”:

To what extent the granular properties of an electrode considered as a discrete particulate structure have an influence on its breathing behaviour?

To our knowledge, the study of inter-particles contact to assess the porous electrode breathing was made by only one paper: Gudmundson & Larsson (2020) [61]. They considered an isotropic distribution of equal-size particles and the associated contact points, to extrapolate a local analysis to the whole particles bed. To make the local analysis, they established an analytical model based on laws of contact mechanics, with an evaluation of forces and pressure at the level of contacts. Their results revealed that the local pressure at contact points between particles was able to reach large amount of stress, from 1 to 6 GPa. By taking into account plasticity, they also noticed that this plastic deformation primarily occurs during the first cycle, which is coherent with experimental observations where significant differences appear between the first cycle and the following ones. As they state, the advantage of their method is to quickly evaluate the influence of the governing contact parameters. In this sense, they oppose their method to discrete element simulations that present higher uncertainties concerning the contact properties, but a more efficient description of microstructure. In this manuscript, it is

proposed to develop the complementary approach mentioned by Gudmundson & Larsson, in other words to consider the electrode as an assembly of particles and to evaluate the evolution of its microstructure during breathing. To consider this granular structure, the chosen tool is the DEM, often used in literature.

1.1.2.b Review of modelling studies on battery using DEM

This section does not aim to detail DEM, an entire section being already dedicated to this task (Section 1.2). Instead, it mainly aims to review the studies that have already used DEM to model battery. The objective is to evaluate what DEM has been used for in the battery field, in order to evaluate the accuracy of this tool to model battery mechanical behaviour. As a first summary, Table 1.4 lists all the cited references, the contact laws used, the related mechanical phase of the battery (drying, calendaring or cycling) and noticeable conclusions. This section details the related references before a global discussion on these approaches.

Briefly, as the acronym of “Discrete Element Method”, DEM is a dynamics tool of mechanical interaction between particles that enables, for its most common use, the dynamic flow of a granular media such as sand, seeds or pills. It has often proved to efficiently compute the behaviour of granular media, through a large panel of applications in many different fields, such as agribusiness [74]–[76], nano-mechanics [77], [78], grinding process [79], screening process [80] or wearing flow [81], [82]. In fact, the “discrete structure” aspect of the core question stated above has already been considered by many researchers for the study of electrodes. Liu *et al.* (2011) [62] were precursors by using DEM in a mechanical discrete study of an electrode (though for electrolyser technology, not for battery), simulating the microstructure of a porous composite electrode during a sintering process. They used the sample displayed in Fig. 1.10, where pore volumes were introduced through

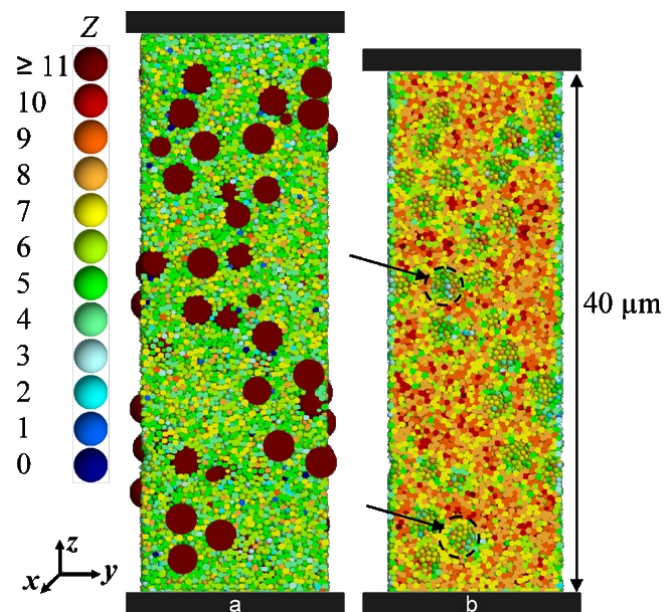


Figure 1.10: Discrete microporous electrode sample during sintering. Colours indicate the number of contacts for each particle. Arrows indicate examples of initial positions of “pore formers” (big particles), removed just before the sintering — *a*) Sample before sintering. *b*) Sample after sintering. Adapted from Liu *et al.* (2011) [62], Figure 1^a.

^a © Journal of Power Sources. Reproduced under charge-free nature of reuse. Elsevier B.V., all rights reserved.

Reference	Contact law(s)	Mechanical phase	Noticeable conclusion(s)
Liu <i>et al.</i> (2011) [62]	BM	Sintering	Introduce pore formers improves ions diffusion.
Zhu <i>et al.</i> (2018) [63]	Hz + JKR	–	Inter-particle sliding and particle deformation are the main mechanism governing the plastic behaviour of anode material.
Sangrós Giménez <i>et al.</i> (2018) [64]	Hz + PC	Calendering	DEM is able to model accurately the mechanical response of anode material.
Sangrós Giménez <i>et al.</i> (2019a) [65]	Hz + PC + Th	Calendering	Calendering pressure reduces the elastic response of the electrode.
Schreiner <i>et al.</i> (2021) [66]	Ed + PC	Calendering	Normal stiffness, tangential stiffness and critical normal stress (considering particles contact) are the most influential parameters.
Forouzan <i>et al.</i> (2016) [67]	Hz + LJ	Drying	Higher electrode coating speed improves their microstructure by reducing the required solvent.
Ngandjong <i>et al.</i> (2021) [68]	Hz + LJ + SJKR	Calendering	Leads to an increase of electronic conductivity, ionic resistance and tortuosity.
Lombardo <i>et al.</i> (2021) [69]	Hz + LJ	Calendering	High drying rate generates heterogeneous distribution of active material along electrode thickness.
Lombardo <i>et al.</i> (2022) [70]	Hz + LJ	Calendering	Calendering at the half of initial electrode thickness gives the best electrochemical compromise (considering electronic conductivity over tortuosity).
Xu <i>et al.</i> (2023b) [71]	Hz + SJKR + PC	Calendering	Inner-particles bonds break non-linearly as a function of compression degree. Bonds breakage can occur even at lowest calendering pressure.
So <i>et al.</i> (2021a) [72] *	Hz + TL	Calendering / Cycling	High calendering pressure limits internal cracks during breathing.
So <i>et al.</i> (2022b) [73] *	Hz + TL	Calendering / Cycling	Due to lithium diffusion, high C-rates generate heterogeneous lithiation within the active material particles. It also partially explains particles breathing irreversibility.

Table 1.4: Review of modelling studies on battery using DEM. Breathing behaviour is approached in references noted with an asterisk “*” — **Hz:** Hertz (non-linear elasticity due to spherical contact), **JKR:** Johnson, Kendall & Roberts (adhesion), **SJKR:** simplified JKR (lighter formulation of JKR adhesion theory), **PC:** Potyondy & Cundall (breakable bond), **Th:** Thornton (plasticity), **LJ:** Lennard-Jones (inter-atomic potential), **BM:** Bouvard & McMeeking (sintering contact at high temperature) **Ed:** Edinburgh (elasto-plastic adhesion), **TL:** Tomas & Luding (plasticity).

“pore formers” (big dark particles) removed just before the sintering. They demonstrated that the introduction of pore formers had a positive effect on the ions’ diffusion, quite beneficial even if some exchange area has been lost. Similarly, more focused on the anode material itself (without considering a precise manufacturing process), Zhu *et al.* (2018) [63] predicted the mechanical properties of a pure graphite anode submitted to a compacting pressure. They concluded that inter-particle sliding and particle deformation were the main deformation mechanisms governing the plastic behaviour of the anode material.

Beyond these approaches, it turns out that the study of electrode mechanical behaviour during fabrication process using DEM was recently of major interest. Through a rich series of papers, Sangrós Giménez *et al.* (2018-2020) [64], [65], [83], [84] made a huge work of DEM application on batteries, for several purposes: predicting the mechanical response during calendaring process in 2018 and 2019 [64], [65], evaluating the impact of calendaring process on ionic behaviour around particles in 2019 [83] and modelling the electrical network through particles in 2020 [84]. By this approach, they demonstrated the ability of DEM to simulate the micro-mechanics of an electrode and the non-negligible impact of calendaring process on electrochemistry. As examples, Fig. 1.11a presents the comparison between nanoindentation experimental measurement on an electrode material sample and DEM simulation, the discrete model reproducing quite accurately the plastic response. On its side, Fig. 1.11b plots different specific elastic recoveries as a function of calendaring pressure. It demonstrates a reduction of elasticity with the increase of calendaring pressure, except for lower values of pressure (explained by the authors by a load maybe not high enough to reach elastic regime of active material particles, the deformation being dictated by plastic binder particles). In the same scope, Schreiner *et al.* (2020) [85] introduced their own discrete model with bonded particles and tested it through the analysis of stress and number of bounds. Then, Schreiner *et al.* (2021) [66] made a sensitivity study on the inter-particles parameters

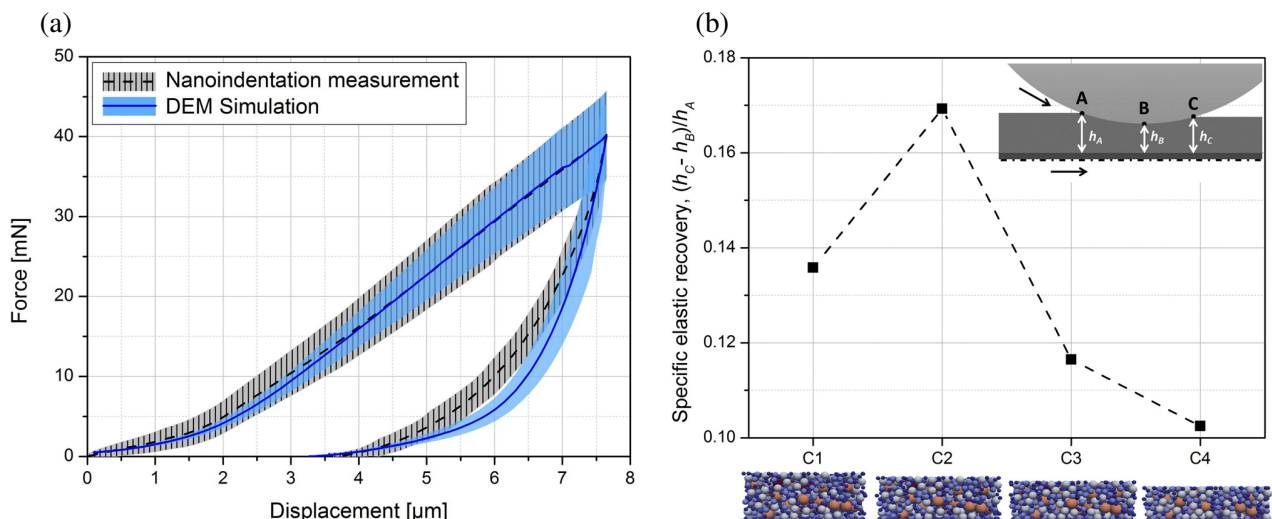


Figure 1.11: Mechanical response of granular cathode during calendaring process — **a)** Force-displacement curves (experimental and DEM simulation) of a nanoindentation. Adapted from Sangrós Giménez *et al.* (2018) [64], Figure 7^a. **b)** Specific elastic recovery as a function of calendared structure (C1, C2, C3 and C4 respectively calendared at 19, 43, 73 and 159 MPa). Extracted from Sangrós Giménez *et al.* (2019a) [65], Figure 8^b.

^a © Advanced Powder Technology. Reproduced under charge-free nature of reuse. Elsevier B.V. and The Society of Powder Technology Japan, all rights reserved.

^b © Powder Technology. Reproduced under charge-free nature of reuse. Elsevier B.V., all rights reserved.

to construct a model of electrode, showing that normal stiffness, tangential stiffness and critical normal stress are the most influential parameters during calendering. Focusing on the fabrication step preceding calendering, Forouzan *et al.* (2016) [67] predicted the microstructure formation during the coating and drying step of manufacturing process. They modelled the electrode as an ensemble of active material (AM) and carbon-binder domain (CBD, binder and conductive additives) particles. To simulate the slurry, *i.e.* the presence of liquid solvent around particles, they used a force derived from Lennard-Jones potential between particles. Using this approach, they demonstrated that the coating of electrodes at higher speed was a possible way to improve their microstructure, because of the reduction of required solvent that avoids, after drying, an eventual excessive porosity.

Furthermore, the whole electrode fabrication process (slurry, drying and calendering) is at the core of the ARTISTIC project (from European Research Council, N°772873) [86] that gave birth to many studies using DEM to address the electrode microstructure. In particular, Ngandjong *et al.* (2017) extended the work of Forouzan *et al.* (2016) [67] to include material properties, fabrication method and electrochemical performance in a unique framework. Ngandjong *et al.* (2021) [68] used this tool to analyse the effect of calendering process on electrochemical properties, detecting that the calendering leads to an increase of electronic conductivity, ionic resistance and tortuosity. Afterwards, Lombardo *et al.* (2020-2022) [69], [70], [87] paid a particular attention on drying and calendering, based on the same methodology to simulate slurry. They indeed presented a whole-fabrication process simulation workflow, from slurry, drying to calendering. In 2020 [87], they characterised the coarse grained molecular dynamics with force fields, the same mesoscale simulation technique used by Ngandjong *et al.* (2021) [68], introducing an optimised workflow to reduce the time of manual force fields optimization that, originally, could last several months. In 2021 [69], they applied the developed workflow to the drying and calendering processes, with a drying speed depending on the position along the electrode thickness. As schemed in Fig. 1.12a, the drying is simulated through the size reduction of carbon-domain particles, at different shrinking speeds depending on the layer part (bottom, centre, or top). As plotted in Fig. 1.12b, the drying rate seems to mostly influence the active material volume fraction, lowering its value in the bottom zone and increasing it in the top zone. Thus, a higher drying rate tends to generate more heterogeneous distribution of active material along electrode thickness. Finally, in 2022 [70], they also focused on the impact of calendering on electrochemical performances, with a specific attention on organic-based sodium-ion cell. As plotted in Fig. 1.12c, the ratio of effective electronic conductivity over tortuosity is increasingly influenced by the compression degree. Therefore, an optimal calendering target to obtain the best electrochemical compromise is to compress at the half of initial electrode thickness. Still in the ARTISTIC project, Xu *et al.* (2023a) [88] extended and tested the model of Lombardo *et al.* (2021) [69] by subdividing active material particles into clusters of sub-particles (as schemed in Fig. 1.13a), based on shapes measured with X-ray computed tomography measurements. Then, Xu *et al.* (2023b) [71] introduced laws of breakable bond (light links in Fig. 1.13a) within active material clusters to analyse the cracking phenomena. They noticed a discrepancy of porosity compared to experimental Fig. 1.13b that was mostly explained by the limitation of elastic contact model used to capture the electrode plastic behaviour. However, Fig. 1.13c clearly reveals that inner-particles bonds break non-linearly as a function of compression degree, and that bonds breakage can occur even at lowest calendering pressure.

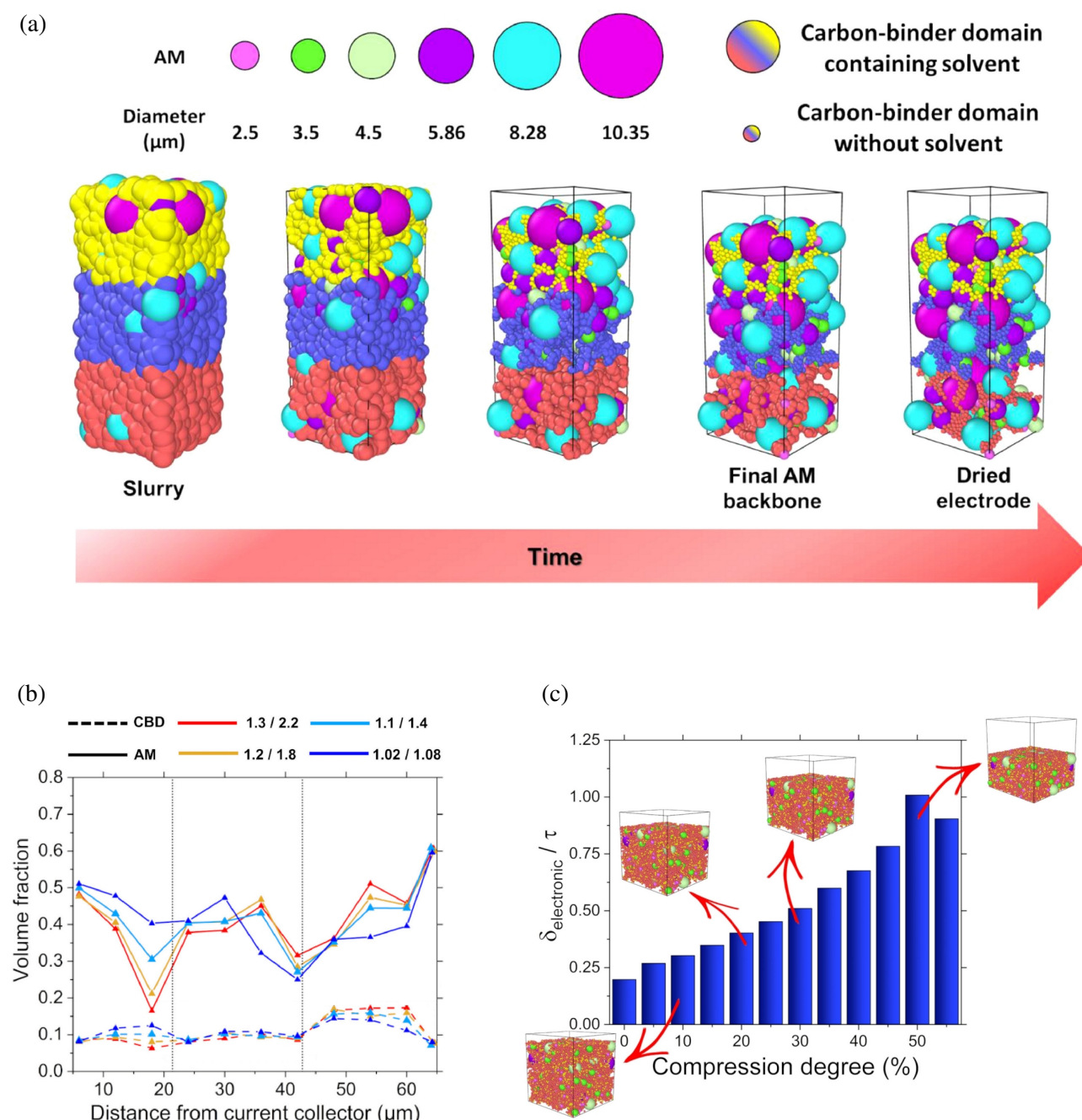


Figure 1.12: DEM model simulating drying process, including active material (AM) and carbon-binder domain (CBD) particles — **a**) 3D representations of dried electrode: CBD particles are divided into three groups (from bottom to top). Top group dries at higher rate than bottom group. **b**) Evolution of volume fractions (AM and CBD) as a function of electrode thickness for different drying rates (based on shrinking velocities \dot{d} of different electrode parts). Each pair of drying rate is defined with two ratios: $\dot{D}_{\text{centre}}/\dot{D}_{\text{bottom}}$ and $\dot{D}_{\text{top}}/\dot{D}_{\text{bottom}}$. Adapted from Lombardo et al. (2021) [69], Figure 4^a. **c**) Normalized ratio of electrode effective electronic conductivity ($\delta_{\text{electronic}}$) and tortuosity factor τ as a function of electrode degree of compression. Extracted from Lombardo et al. (2022) [70], Figure 3^b.

^a © Energy Storage Materials. Open access.

^b © Batteries & Supercaps. Open access.

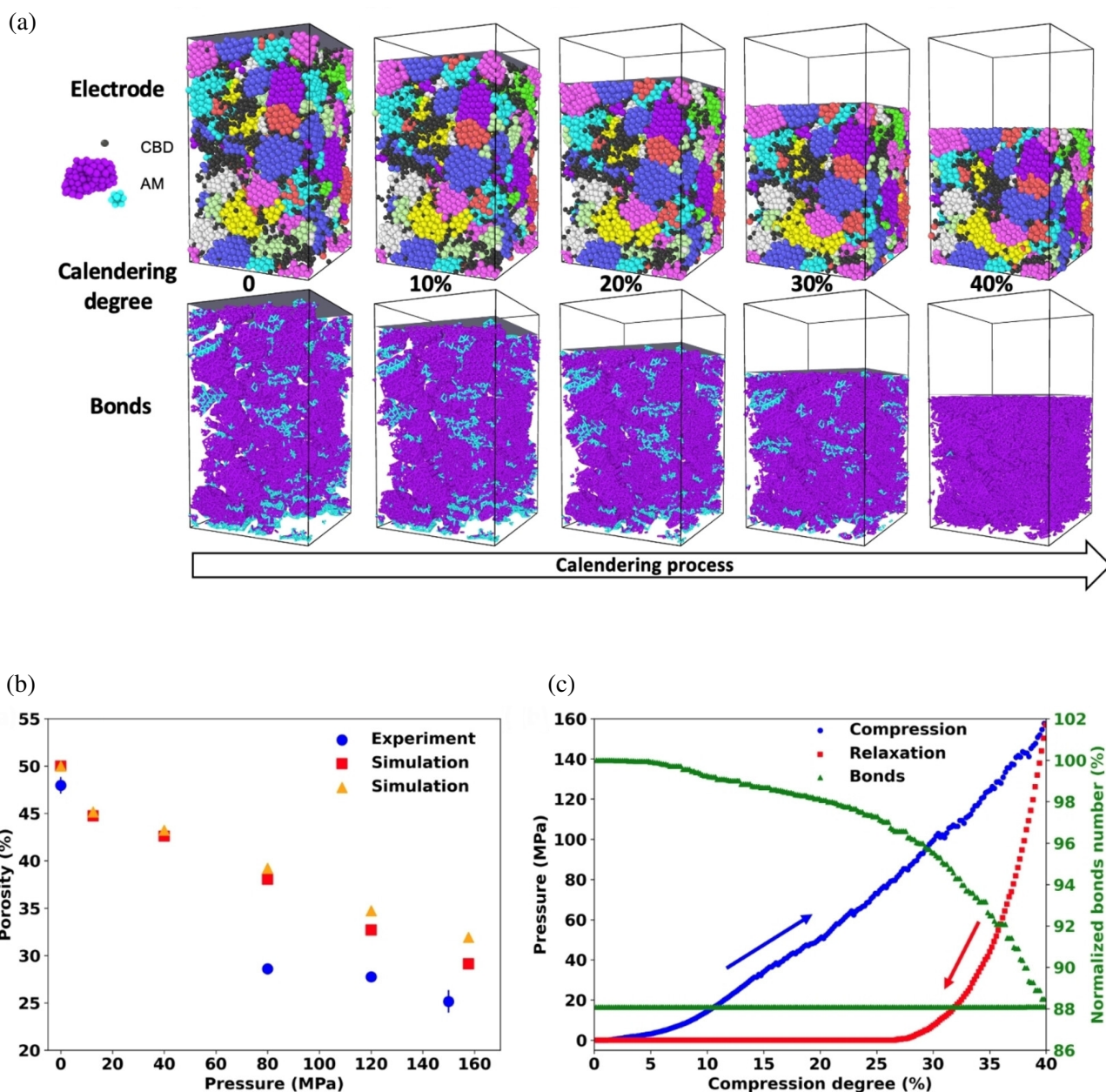


Figure 1.13: DEM model simulating calendering process (until 150 MPa), including active material (AM) and carbon-binder domain (CBD) particles — **a**) 3D representations of calendered electrode. Top row: particles. Bottom row: particles bonds. CBD: Carbon-Binder Domain. AM: Active Material. **b**) Comparison of porosity (model/experimental) at different calendering pressures. Triangle simulation markers: porosity calculated based on microstructure meshing. Square simulation markers: porosity calculated based on theoretical material volume. **c**) Pressure and proportion of broken bonds as a function of compression degree (reduced thickness). Adapted from Xu et al. (2023) [71], Figure 3 & 4^a.

^a © Batteries & Supercaps. Open access.

Despite all these models using DEM, the electrode breathing was rarely approached with this technique. To our knowledge, one of the closest approach is the one of Charlas (2013) [89] who used a discrete model to simulate the mechanical behaviour of metal hydride for hydrogen storage, this technology is also particularly confronted to material breathing. He observed that using spherical particles does not enable to obtain the same initial density, with comparison to experiment. This aspect introduces the difficulties to realise complex electrode microstructure using only spherical particles. As presented above, these difficulties have been already well studied in the ARTISTIC project, by modelling complex shapes of particles by clusters of sub-particles.

So far, the closest approach to model electrode breathing has been made through a rich series of papers from So *et al.* (2021-2022) [72], [73], [90]–[92]. They indeed used DEM to study reorganisation of all-solid-state lithium-ion batteries electrode microstructure during breathing, but also the resulting impact on electrochemical performances. They initially started in 2021 [72] with a 2D approach, by implementing a Hertzian contact law (detailed in Section 1.2.1.a) joined to a plastic deformation law, in order to simulate a cohesive contact created by high compressive force. More simply than in ARTISTIC project, they simulated the manufacturing process (slurry, drying and calendaring) through a simple rainfall/compression of particles. As schemed in Fig. 1.14a, the active material (big dark particles) are embedded in a mixture of solid electrolyte (little particles). After five breathing cycles, the particles bed fragmentation differs depending on maximum state of charges (8% and 24%) and fabrication pressures (100 and 200 MPa): the electrode calendered at high pressure presents a more compacted bed than at low pressure. Furthermore, at low calendaring pressure, the increase of maximum state of charge creates many internal cracks, which underlines the impact of calendaring step on microstructure during the cycling. Still in 2021 [90], they extended the model to the third dimension and mainly paid attention to the calendaring step, as schemed in Fig. 1.14b: the active materials particles and solid electrolyte clusters are generated in a tall simulation box and rainfall, then compressed at different pressure levels. In 2022, while presenting the complete development of Hertzian-plastic contact model [91] and proposing a method to replace active material single particles by coated clusters of sub-particles [92], they studied the electrode breathing by taking into account the lithium diffusion within the active material sub-particles [73]. As illustrated in Fig. 1.14c, active material (coloured particles) is initially delithiated, then it lithiates until a predefined content of lithium has been charged ($SOC = 1$) which increases the global cell volume, then it delithiates until the same amount of lithium is discharged. As it can be seen, the final volume is higher than at initial state. This is mainly explained by the inhomogeneous delithiation of active material due to diffusion limitation (lithiation gradient in final state of Fig. 1.14c). This inhomogeneous lithiation and delithiation is highly enhanced by a higher C-rate, which consequently generates faster inner damaging of active material. Indeed, as plotted in Fig. 1.14d, the increase of C-rate accelerates the damage (evaluated via the remaining number of inter-particles bonds). On the opposite, Fig. 1.14e demonstrates that the pressure applied on the cell poorly affects the internal cracks appearance.

First, this list ensures the efficiency of DEM in modelling the microstructure of the electrode. In addition, when it comes to electrode mechanical behaviour, this table quickly reveals that most of the studies focused on the manufacturing scope. They generally analysed the mechanical behaviour during the calendaring process to evaluate its impact on electrochemistry, but not on the breathing itself. In fact, most studies did not address the breathing, only by So *et al.* (2021-2022) [72], [73], [90]–[92] did. Moreover, the latter did not address the

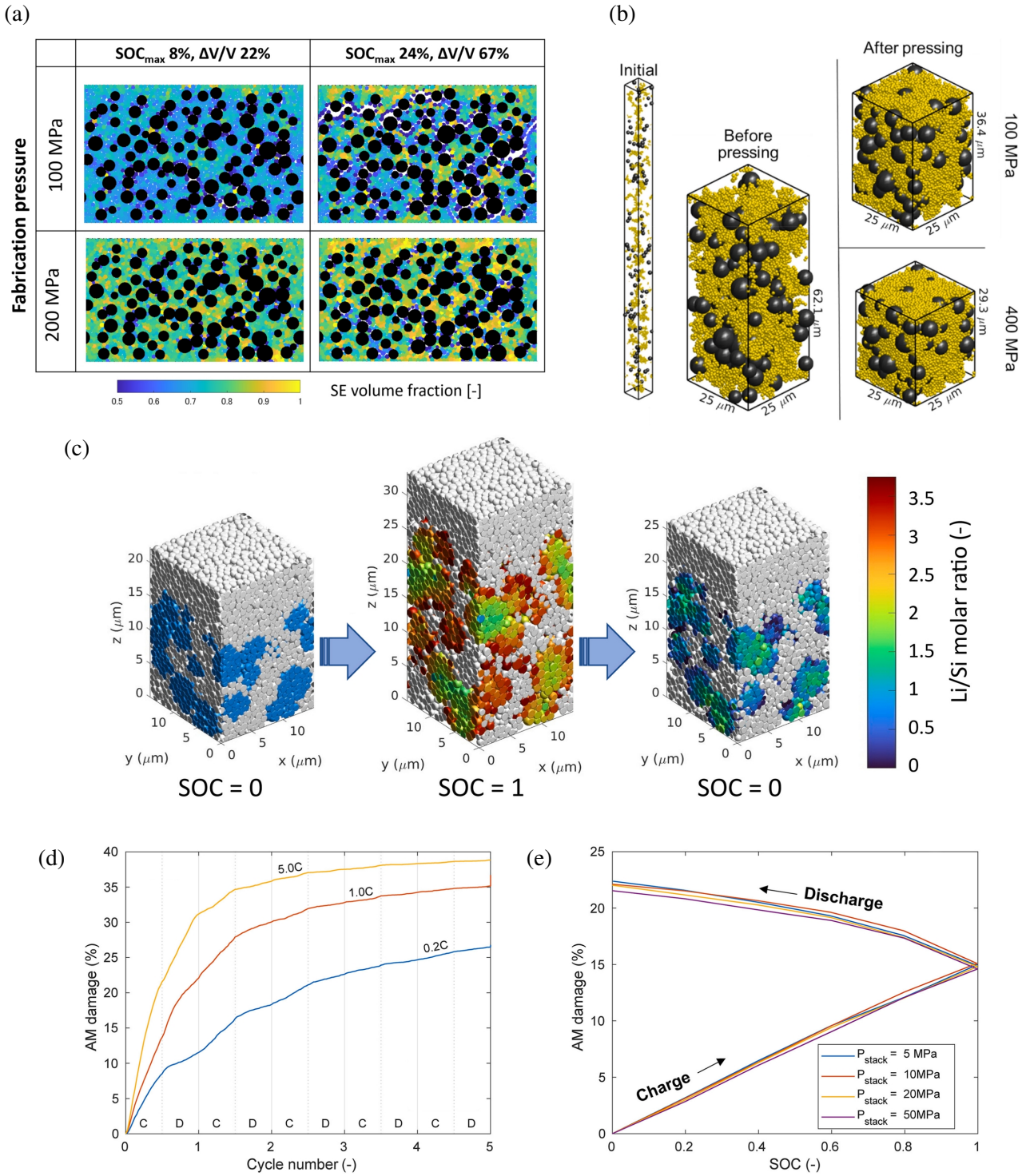


Figure 1.14: DEM model of all-solid-state lithium electrode — **a**) 2D electrode structures after five cycles for different fabrication pressures and maximum states of charge. Volume fraction is computed locally, based on polygonal volume from Voronoi tessellation with neighbour particles. Adapted from So et al. (2021a) [72], Figure 7^a. **b**) 3D initial distribution of active material (big dark particles) and solid electrolyte (clusters of little light particles), with two different calendaring pressures (100 and 400 MPa). Adapted from So et al. (2021b) [90], Figure 3^b. **c**) Distribution of molar ratio x in Li_xSi in active material and volume variations (1C and 10 MPa). **d, e**) Active material damage as a function of C-rates and cycles (**d**), and pressure and state of charge (**e**). Damage based on number of bonds. Adapted from So et al. (2022c) [71], Figure 5^b.

^a © Journal of The Electrochemical Society. Reproduced under charge-free nature of reuse. IOP Publishing Ltd, all rights reserved.

^b © Journal of Power Sources. Reproduced under charge-free nature of reuse. Elsevier B.V., all rights reserved.

breathing from a volume transfer perspective. They mainly focused on the internal phenomena, at the particles level, without considering the transfer of volume variation from particles to electrode scale. Furthermore, they did not enter precisely in the understanding of inter-particles contact and did not focus on the issue of breathing amplitude and irreversibility. Hence, as a particularly close approach, this thesis aims to address these aspects.

1.1.2.c Position of thesis in state-of-the-art

As a global summary of all that have been developed in the previous subsections, we can picture three main observations of the current state-of-the-art linked to the core question, schematised in Fig. 1.15:

- The electrode breathing has already been well studied experimentally, with many different techniques, at different scales (a), as summarised in Table 1.2.
- The electrode breathing was also studied through some models. However, there is a lack of microstructure and inter-particles contacts consideration to really understand the volume variation transfer from particles to electrode scale (b), as summarised in Table 1.3.
- DEM has proven to be an efficient tool to model microstructure behaviour, and it has been even already well-used to study Li-ion batteries (c), as summarised in Table 1.4.

This thesis consequently aims to be at the crossroads of these three fields: using DEM to better understand the role of the granular microstructure and inter-particles contacts properties in the breathing. In the particular case of the silicon-based anode, the final goal is to determine which granular properties are susceptible to be

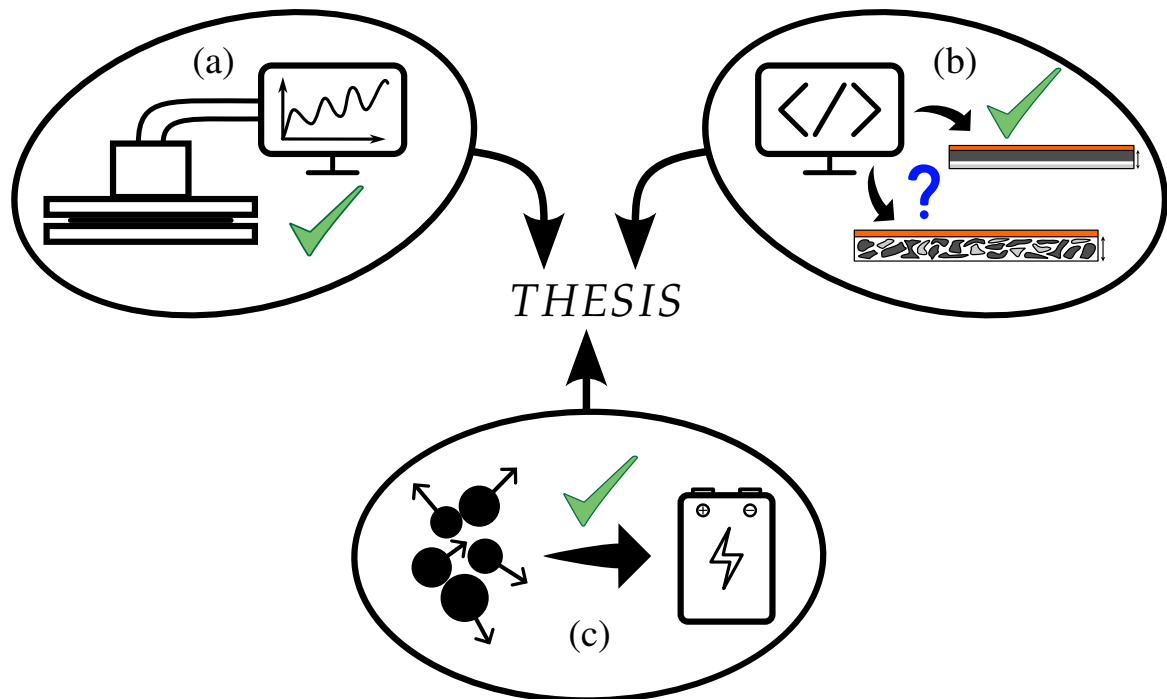


Figure 1.15: Position of the thesis in current state-of-the-art: the breathing is already well studied experimentally (a), also computationally but with lack of discrete microstructure consideration (b), and the DEM tool has been already well-used to study battery microstructure (c).

exploited during manufacturing to reduce mechanically the breathing, thanks to the exploitation of void volume. The granular properties can be silicon fraction, friction, particles rotation, pressure on the electrode, particles rigidity, adhesion or breakable bonds between particles. However, even if it composes the main technique used in this thesis, DEM is completed by other tools, going from macroscopic experimental measurements to electrochemical modelling, without forgetting an important part of rheology, *i.e.* the mechanical study of materials that deform under stress.

For this purpose, the second section of the present chapter (Section 1.2) details the contact laws used in this manuscript. Chapter 2 develops the complete numerical model based on DEM of this thesis, called “DAM”, more precisely its geometrical characteristics, the strategy of sensitivity analysis, the implemented breathing laws of particles and the different parameters used to evaluate the results. Chapter 3 presents the results of DAM sensitivity analyses and quantifies the impact of the studied parameters on breathing, mainly in terms of swelling amplitude and irreversibility. Chapter 4 presents the experimental work that has been carried out to complete the work of Delphine Vidal, more precisely by introducing a rheological model built to extract the anode thickness from experimental samples and detailing the methodology and results. Finally, Chapter 5 presents a cross-comparison of model and experimental approaches, in order to identify the promising future leads in breathing modelling improvement.

1.2 DEM

As introduced in Section 1.1.2.b, “DEM” is the acronym for “Discrete Element Method” or, at the origin, “Distinct Element Method”. DEM can be defined as a computation technique for dynamical interaction between solid particles that move into space. In a simple question: how to compute the dynamics of two particles, *i.e.* their trajectories over time? An intuitive answer would be the application of the Newton’s Second Law, highly efficient when it comes to compute trajectories with velocities much lower than the velocity of light. But a key question appears at the instant these particles touch each other. What happens when two particles with given shapes, moving with given velocities and directions, meet the surface of the other one? What happens when contact occurs between these particles? This physical phenomenon particularly complexifies the dynamics resolution, even more if the considered system is composed of thousands or even millions of particles.

To solve this computational challenge, an answer can be found in the famous paper “*A discrete numerical model for granular assemblies*” by Cundall & Strack (1979) [93]. By their work, they introduced a simple principle, summarized in two sentences:

«

The distinct element method is based upon the idea that the time step chosen may be so small that during a single time step disturbances cannot propagate from any disc further than its immediate neighbours. Then, at all times the resultant forces on any disc are determined exclusively by its interaction with the discs with which it is in contact.

» — Cundall & Strack (1979) [93]

Where “discs” refer to 2D particles. The principle consequently states that, mechanically, a sufficiently small discretisation of time able any complex system of many particles to be treated at the level of the particle itself, and then to simplify the problem to an ensemble of simple dynamics equations. The complex system is reduced to its smallest piece. This is how a flow of thousands or even millions of particles can be computed with basic dynamics tools.

However, this does not answer the real question about the contact between particles. How to consider the dynamical reaction of this contact? In fact, this question raises the intrinsic link of DEM with the area of contact mechanics.

1.2.1 Contact mechanics

1.2.1.a Introduction to Hertzian contact

It is quite difficult to fix a key date on the origin of contact mechanics. If we had to go back in time in its history, certainly we would stop at 1676. This is at this date Robert Hooke stated its famous solution about the linear-elasticity. He published this result in 1678, in his book “*Potentia Restitutiva, Or of Spring Explaining the Power of Springing Bodies*” [94], under a Latin citation: “*Ut tensio, sic vis*”, which can be literally translated by “*As the extension, so the force*”, more precisely “*The force of any springy body is in the same proportion with the extension*”. This result described the linear-elasticity, introducing a basic mechanical behaviour of a material comparable with a spring, nowadays named as a Hookean material.

The Hooke’s Law is today expressed as the linear equation between the stress and the strain:

$$\sigma = \varepsilon E \quad (1.4)$$

Where σ the stress and, E is the Young modulus and ε the strain of the material.

Afterwards, it is necessary to wait almost a century and half, before another famous name of mechanics, Charles Augustin de Coulomb, published its work in his book “*Théorie des machines simples, en ayant égard au frottement de leurs parties et à la roideur des cordages*” [95] (“*Theory of simple machines, having regard to the friction of their pieces and the stiffness of the ropes*”) in 1821. In this volume, he presented the results that gave birth to the Coulomb’s Law of mechanics. Taking place during the friction between two solids, the simplified equation stipulate a linear evolution of the normal force and the tangential force of the contact. This law stipulates that, at the static state the tangential force is bounded by the normal force via the static coefficient of friction μ_s :

$$\|\vec{F}_t\| < \mu_s \|\vec{F}_n\| \quad (1.5)$$

In addition, at the dynamic state, the tangential force is directly proportionally related to the normal force via the dynamic coefficient of friction μ_d :

$$\|\vec{F}_t\| = \mu_d \|\vec{F}_n\| \quad (1.6)$$

Where, generally, both friction coefficients are approximated as equal ($\mu_s = \mu_d = \mu$).

Even if it is also from the same author, this law of mechanics should not be confused with the Coulomb's Law of electrostatic, which evaluates the force of electrical interaction between two electrically charged particles. By default, in this treatise, the "Coulomb's Law" refers to the mechanical law and not to the electrostatic one.

Finally, as another key date in contact mechanics history, we have to wait only a few decades. Factually speaking, we practically all know the person considered, today, as a key pioneer in contact mechanics, because he is none other than Heinrich Rudolph Hertz, mainly known for its essential discoveries in electromagnetic waves. It is by mutual agreement that its work introduced the first base of contact mechanics, by presenting a classical contact model. During its doctorate of physics under, Hertz needed to solve the deformation of two spherical bodies pressed one against the other. Thus, he solved mathematically this issue in 1880 during the Christmas holidays, and described his results in his article "*Ueber die Berührung fester elastischer Körper*" [96], published in the journal *De Gruyter* in 1882 [97].

The major problem solved by this model is that, despite the linear reaction of the material as dictated by the Hooke's Law, the contact area is non-linear, provoking a non-linear evolution of the reaction force as a function of the overlap between both spheres. This phenomenon is provoked by the unequal repartition of the pressure on the surface of the contact area, is drawn in Fig. 1.16a. Furthermore, this case is also applied for a single sphere in contact with a half-space (where the latter can be seen as a sphere with an infinite radius). The most noticeable result Hertz presented in his article is certainly the definition of the pressure distribution, page 12 (167), defined as follows with the original notation:

$$P(r) = \frac{3F}{2\pi} \frac{\sqrt{a^2 - r^2}}{a^3} \quad (1.7)$$

Where P represents the pressure (noted Z_z in [96]) and F the total force of interaction (noted p in [96]). The elegance of this equation is the mathematical respect of one particular condition fixed at the beginning of the article, page 5 (160), based on the fundamental link between force and pressure:

«

Lastly the integral $\int Z_z ds$, taken over the part of the surface which is bounded by the curve of pressure, must be equal to the given total pressure, which we shall call p .

» — Hertz *et al.* (1896) [98], page 150

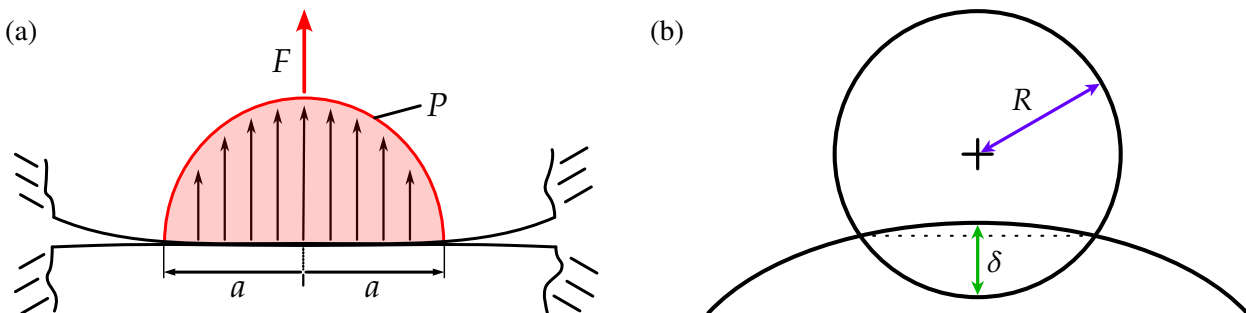


Figure 1.16: Basic schemes of Hertzian contact — **a)** Hertzian pressure distribution. **b)** Overlap with spheres of different sizes.

Mathematically, the “total pressure” certainly refers to the total force applied between the two spheres/sphere and half-space. Indeed, if we apply Eq. (1.7) to the pressure distribution proposed by Hertz on the surface of contact, it gives, after integration:

$$\int_0^a P dS = F \quad (1.8)$$

Indirectly, by this work that constitute only parentheses in his doctorate, Hertz established the major field of contact mechanics that, nowadays, is commonly used in DEM. Nevertheless, in order to award the right recognition, it must be reminded that many researchers contemporary to Hertz also played an important role for the development of this theory, such as Joseph Valentin Boussinesq with his theory of potentials in “*Application des potentiels à l’étude de l’équilibre et du mouvement des solides élastiques*” (“*Application of potentials to the study of equilibrium and movement of elastic solids*”) in 1885 [99] or Augustus Edward Hough Love in “*A treatise on the mathematical theory of elasticity*” in 1892 [100]. Even if the equation proposed by Hertz remains a fundamental mathematical equation for the DEM, it is still imperfect to represent the full phenomenon of solid contact. According to Johnson in his 1958 PhD note [101], the Hertz theory that does not take into account the adhesion can present discrepancies in reality, especially about boundary conditions and for very low values of load. In this sense, Boussinesq had already found a solution for the distribution of pressure of normal surface traction.

Despite this, one of the most interesting results of Hertz, at the origin of the pressure distribution and reintroduced by Johnson (1958) [102], [103] and Johnson *et al.* (1971) [102], is the relationship between the contact radius a and the load applied F :

$$a^3 = \frac{3}{4} E^* R^* F \quad (1.9)$$

Where E^* and R^* are contact-pair defined:

$$E^* = \left(\frac{1 - \nu_i^2}{E_i} + \frac{1 - \nu_j^2}{E_j} \right)^{-1} \quad (1.10)$$

$$R^* = \frac{R_i R_j}{R_i + R_j} \quad (1.11)$$

Where R_i , E_i and ν_i are respectively the radius, the Young’s modulus and the Poisson’s ratio of the sphere i (and likewise for the sphere j). Another important result of Hertz’s work, reintroduced in the well-known book “*Contact Mechanics*” by Johnson (1985) [104], also presented in the “*Introduction to Contact Mechanics*”, Johnson (1992) [105], is the basic equation of the overlap δ linked to the contact radius a by:

$$a = \sqrt{R^* \delta} \quad (1.12)$$

Where the overlap δ is roughly schematised in the Fig. 1.16b. It gives the final expression of the normal force between both spheres:

$$F = \frac{4E^* \sqrt{R^*} \delta^3}{3} \quad (1.13)$$

Or similarly:

$$F = \frac{4E^*a^3}{3R^*} \quad (1.14)$$

We finally find here the non-linear behaviour of the force: $F \propto \delta^{\frac{3}{2}}$. This consequence is certainly the major point revealed by Hertz's work about the interaction of two elastic spheres in contact: even if the physical interaction is fundamentally linear, as described by the Hooke's Law, the geometry of the spheres presents a nonlinear reaction.

1.2.1.b Application of Hertzian contact to DEM: the Hertz-Mindlin law

To our knowledge, Thornton & Randall (1988) [106] were the first to establish the link between the work of Hertz on elastic spheres interpenetration presented in Section 1.2.1 and DEM, while Cundall's team were extending DEM to the third dimension [107]–[110]. Thornton & Randall even went further in their approach, because they also introduced an important feature in the tangential expression, based on the work on Mindlin (1949) and Mindlin & Deresiewicz (1953): the micro-slips. This phenomenon occurs when the two elastic surfaces are submitted two tangential forces, but without slipping. Mindlin & Deresiewicz demonstrated that “micro-slips” happen in an annulus surface around the contact point, engendering a tangential accumulation with a history effect (dependent to the path made in the past). For this reason, the contact law merging both Hertz and Mindlin theories, commonly used nowadays, is often called the “*Hertz-Mindlin contact law*”. Because this law is at the heart of the DEM model used in this thesis, it is reduced to “**HM law**” in this manuscript.

Of course, these researches were not the only ones that made DEM the tool we use today. Bardet & Huang [111] demonstrated the influence of contact couples on the global behaviour of a particles bed, by fixing the particles' rotation. Tsuji *et al.* (1992-1993) [112], [113] were precursor in the use of DEM in practical application, more precisely by using it to simulate a plug flow of particle within a pipe. Thornton (1997) [114] introduced a first form of elasto-plastic contact when studying the coefficient of restitution of collisional particles, demonstrating that a Hertz-based contact law shows a linear force-displacement law after the elastic limit is reached. Vu-Quoc & Zhang (1999) [115], [116] presenting an elasto-plastic normal force-displacement law and an improved tangential force-displacement for HM law. By completing the Mindlin & Deresiewicz solution by the more rigorous approach of Maw *et al.* (1976) [117] who extended the theory to a higher number of cases, Di Renzo & Di Maio [118] compared the classical linear law of DEM with the HM law, showing that the HM law brought surprisingly limited improvement compared to the linear law, being even worst if the Mindlin theory was implemented without slipping. A year latter, Di Renzo & Di Maio (2005) [119] presented an improvement of the HM law without slip in order to propose a form as simple yet effective that takes into account Mindlin & Deresiewicz theory. Finally, Zhu *et al.* (2006) [120] made an impressive state-of-the-art of the DEM summarizing the existing contact laws of contact forces and torques, but also many other dynamics features such as inter-particle cohesive forces, particle-fluid interaction forces or methods of macroscopic stress computation.

As we saw in Table 1.4, the Hertz contact law is widely used in literature to model electrode mechanical behaviour. The main advantage of this law is its link with rheological properties of particles. In original Cundall & Strack (1979) [93] paper, the contact law is linear and is set through parameters such as stiffness or damping

factor. On its side, the Hertz law takes into account the non-linearity of contact due to spherical shape, and the parameters involved are more conventional and interpretable, such as Young's modulus or Poisson's ratio. For this reason, the Hertz law was chosen for this thesis.

1.2.2 Basic principle of DEM

1.2.2.a Main constitutive equations

As a brief convention statement, DEM knew much evolution these last decades, and many researchers developed their own codes and vector conventions. For this thesis, the chosen code was LIGGGHTS, an open-source code based on the Molecular Dynamics code LAMMPS, introduced by Kloss *et al.* (2011-2012) [121], [122], with the current public version 3.8.0 [123]. Thus, the conventions for vectors orientation presented in this manuscript are the ones implemented in LIGGGHTS code.

The fundamental strategy of DEM, whatever its form, is to solve the Newton's Second Law of Motion, based on the work of Isaac Newton published in 1687 in his book "*Philosophiae naturalis principia mathematica*" ("*Mathematical Principles of Natural Philosophy*") [124]. As a side note, the original statement is located on page 12, under the section "*Axiomata Sive Leges Motus*", Lex I. Thus, by considering a spherical particle i with mass m_i and radius R_i (and deduced moment of inertia J_{Δ_i}), two major dynamics equations come, respectively on translation and rotation:

$$\begin{cases} m_i \vec{a} = \sum_k \vec{F}_k \\ J_{\Delta_i} \vec{\alpha} = R_i \sum_k \vec{F}_k \end{cases} \quad (1.15)$$

Where \vec{F}_k represents the inter-particles forces of contact, \vec{a} and $\vec{\alpha}$ represent respectively the translational and angular accelerations. These equations are only true by supposing the following Set of Hypothesis 1.A:

- (i) The mass of the particle is constant.
- (ii) The gravity and other friction forces are supposed negligible compared to forces of contact.
- (iii) The torque is only due to the contact forces.
- (iv) The deformation is sufficiently small to keep the contact point approximately at a distance R_i of the particle center (so that the torque is expressed with R_i)

Basically, to solve the dynamics equations, the core of the resolution lies in the definition of the forces of contact. But how are these forces defined? First, by considering a unique contact between two particles i and j , the force can be expressed as the composition of two forces: the normal force and the tangential force ($\vec{F}_{j \rightarrow i, n}$ and $\vec{F}_{j \rightarrow i, t}$ in Fig. 1.17a). Generally speaking, most of DEM approaches are generalisable to these two fundamental constitutive equations:

$$\begin{cases} \vec{F}_n = k_n \delta_n - \eta_n \vec{v}_n \\ \vec{F}_t = \begin{cases} -k_t \delta_t - \eta_t \vec{v}_t, & \text{if } k_t \delta_t < \mu_s F_n \\ -\mu_d F_n \frac{\delta_t}{\delta_t}, & \text{if } k_t \delta_t \geq \mu_s F_n \end{cases} \end{cases} \quad (1.16)$$

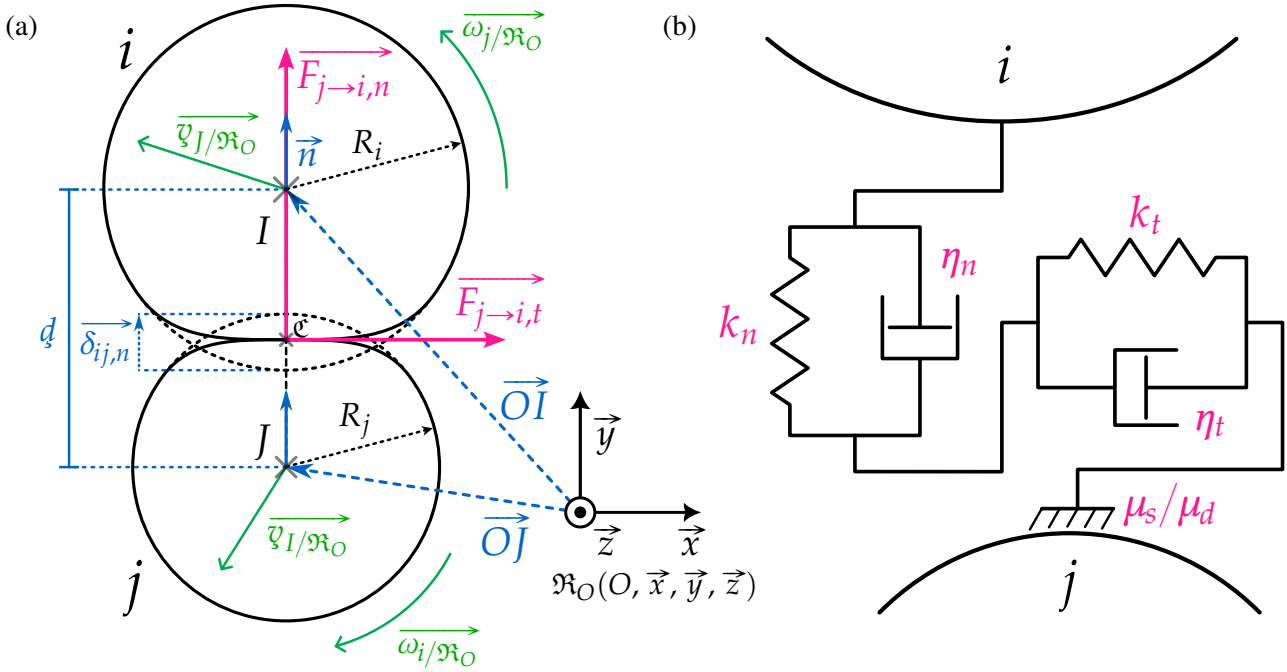


Figure 1.17: DEM scheme of particles mechanical contact — **a)** Pair-particles parameters. **b)** Normal/Tangential parameters.

Where we have to read two main techniques, as illustrated in Fig. 1.17b:

- Each force is a “spring/dashpot” composition: an “elastic” component introducing the overlap and a “damping” component introducing the velocity
- The tangential force is restrained to the normal force through a friction criterion

Of course, depending on the approach, the formulation can differ. For example, the damping is sometimes removed (η_n and η_t set to zero) under the assumption it is useless, because it simulates an energy loss that is already set through the friction criterion. Furthermore, as introduced before, the friction can be reduced to a single friction coefficient ($\mu_s = \mu_d = \mu$). Finally, the signs within the equations are highly dependent to the vector orientation convention.

Concerning the “normal” and “tangential” notions, the literature lacks some mathematical developments. For example, many sources refer to the tangential velocity (\vec{v}_t), but few precisely describe their mathematical expression, summarizing their definition to literal explanations, generally “tangential component of the relative velocity” [64], [78]–[82], even in LIGGGHTS original paper itself [122]. It is not particularly false, but the non-intuitive properties of the tangential velocity can be confusing. To find proper mathematical expressions of these velocities, it is necessary to make a detour in specialized DEM articles, firstly to Cundall & Strack’s 1979 historical paper [93] (page 51, equation 13) where the expression is developed under a 2D approach, Brilliantov *et al.* (1996) [125] and Silbert *et al.* (2001) [126] works, finally to a more recent paper from Zabulionis *et al.* (2012) [127] (page 268, equations 8–11), where the tangential component is specifically studied. This is precisely the latter expression that correspond to the one implemented in LIGGGHTS, with the same vector convention. Hence, let us develop these components to see obtain a clearer view of the mathematics.

Let us divide the terms into two main groups: “dynamic” and “material”. “**Dynamic terms**” refer to the terms that are spatially defined and used for dynamics computation, such as the overlap/velocity terms of the main constitutive equations in Eq. (1.16), δ_n , ϑ_n , δ_t and ϑ_t , respectively the normal overlap, the normal velocity, the tangential overlap and the tangential velocity. “**Material terms**” refer to the terms associated to material properties, such as the spring/damping/friction terms of the main constitutive equations in Eq. (1.16), k_n , η_n , k_t and η_t , respectively the normal stiffness, the normal damping factor, the tangential stiffness and the tangential damping factor.

1.2.2.b Dynamic terms

A particle of reference i is considered for the application of Newton’s Second Law, interacting with a particle j , with I and J the respective centres of both particles and R_i and R_j the respective radii. In a given benchmark \mathfrak{R}_O , we consider the respective translational velocities $\overrightarrow{\vartheta}_{I/\mathfrak{R}_O}$ and $\overrightarrow{\vartheta}_{J/\mathfrak{R}_O}$ and angular velocities $\overrightarrow{\omega}_{i/\mathfrak{R}_O}$ and $\overrightarrow{\omega}_{j/\mathfrak{R}_O}$. In addition, vectors \overrightarrow{OI} and \overrightarrow{OJ} respectively define the positions of particle i and j in \mathfrak{R}_O .

A major vector that define the “normal” direction is the normal vector \vec{n} defined by:

$$\vec{n} = \frac{\overrightarrow{OI} - \overrightarrow{OJ}}{d} \quad (1.17)$$

Where the distance between particles’ centres is directly defined through $d = \|\overrightarrow{OI} - \overrightarrow{OJ}\|$. This is the unit vector that defines the direction of the both centres of particles, from J to I . Hence, this fundamental convention is used in this study, but it must be kept in mind that the other convention (from I to J) can be found in literature, as in Cundall & Strack (1979) [93] or in Tsuji *et al.* (1992) [112].

Finally, this enables us to define the overlap, more precisely the normal overlap between both particles:

$$\delta_n = R_i + R_j - d \quad (1.18)$$

It should be noted, moreover, that a negative value of the overlap corresponds to the distance between particles surfaces, and a positive value corresponds to the overlap of geometrical contact. Directly, the condition of contact between two particles is then determined by the sign:

$$\begin{cases} \delta_n \geq 0 \longrightarrow \text{contact} \\ \delta_n < 0 \longrightarrow \text{no contact} \end{cases} \quad (1.19)$$

Then, its vectorial form is defined based on the normal unit vector:

$$\vec{\delta}_n = \delta_n \vec{n} \quad (1.20)$$

Finally, considering the particles’ interaction, the most important velocity is the relative velocity of both particles, beyond the velocities of these particles in the benchmark \mathfrak{R}_O . Consequently, we define the following velocity of the particle i relative to the particle j :

$$\overrightarrow{\vartheta}_{I/J} = \overrightarrow{\vartheta}_{I/\mathfrak{R}_O} - \overrightarrow{\vartheta}_{J/\mathfrak{R}_O} \quad (1.21)$$

The normal velocity comes:

$$\vec{v}_n = \left(\vec{v}_{I/J} \cdot \vec{n} \right) \vec{n} \quad (1.22)$$

The tangential velocity requires more complex development. Indeed, we must keep in mind that the tangential velocity is useful only at the contact point, *i.e.* \mathcal{C} in Fig. 1.17a, and it has to consider the relative movement of both surfaces. To do so, the sliding is considered, defined thanks to a “dual point” \mathcal{C} that owns two velocities: the speed of the contact point of the particle i and the speed of the contact point of the particle j . Hence, the sliding velocity of the contact point \mathcal{C} is defined by the difference of the velocities at this point:

$$\vec{v}_{\text{sliding}} = \vec{v}_{\mathcal{C}\in i} - \vec{v}_{\mathcal{C}\in j} \quad (1.23)$$

Moreover, the velocities at contact points can be deduced directly from translational and angular velocities thanks to classic relationship of points in a solid in motion:

$$\begin{cases} \vec{v}_{\mathcal{C}\in i} = \vec{v}_{I/\mathfrak{R}_O} + \vec{\mathcal{C}I} \wedge \vec{\omega}_{i/\mathfrak{R}_O} \\ \vec{v}_{\mathcal{C}\in j} = \vec{v}_{J/\mathfrak{R}_O} + \vec{\mathcal{C}J} \wedge \vec{\omega}_{j/\mathfrak{R}_O} \end{cases} \quad (1.24)$$

Where $\vec{\omega}_{i/\mathfrak{R}_O}$ and $\vec{\omega}_{j/\mathfrak{R}_O}$ are the respective angular velocities of particles i and j in the benchmark \mathfrak{R}_O . By defining the point of contact \mathcal{C} as the centre of the overlap (which is geometrically fully acceptable but more questionable when particles have really different rigidities), we can also note:

$$\begin{cases} \vec{\mathcal{C}I} = \left(R_i - \frac{\delta_n}{2} \right) \vec{n} \\ \vec{\mathcal{C}J} = - \left(R_j - \frac{\delta_n}{2} \right) \vec{n} \end{cases} \quad (1.25)$$

Then, by injecting Eq. (1.25) in Eq. (1.24), and Eq. (1.24) in Eq. (1.23), and thanks to Eq. (1.21), it comes:

$$\vec{v}_{\text{sliding}} = \vec{v}_{I/J} + \vec{n} \wedge \left(\left(R_i - \frac{\delta_n}{2} \right) \vec{\omega}_{i/\mathfrak{R}_O} + \left(R_j - \frac{\delta_n}{2} \right) \vec{\omega}_{j/\mathfrak{R}_O} \right) \quad (1.26)$$

However, this does not constitute the final formula of the wanted velocity, because it includes a normal part. Consequently, it is necessary to consider the tangential part of this expression, with reference to the normal unit vector \vec{n} , to obtain the final form. Then, the “tangential velocity” implemented in LIGGGHTS is defined as:

$$\vec{v}_t = \vec{v}_{I/J} - \left(\vec{v}_{I/J} \cdot \vec{n} \right) \vec{n} - \left(\left(R_i - \frac{\delta_n}{2} \right) \vec{\omega}_{i/\mathfrak{R}_O} + \left(R_j - \frac{\delta_n}{2} \right) \vec{\omega}_{j/\mathfrak{R}_O} \right) \wedge \vec{n} \quad (1.27)$$

Finally, the tangential overlap is defined iteratively from the time of first contact between particles, in order to implement a simplified form of “micro-slips” as described by Mindlin theory. The vector can be more precisely written with an iterative form:

$$\vec{\delta}_t = \vec{\delta}_t^h \quad (1.28)$$

Where h is the time step index. At each time step, it is possible to define a tangential displacement which corresponds to the update of tangential overlap with the infinitesimal displacement induced \vec{d} by the tangential velocity:

$$\vec{d}_t^h = \vec{\delta}_t^{h-1} + \vec{v}_t^h \Delta t \quad (1.29)$$

Nevertheless, this vector does not match with the wanted result. Due to the relative movement of particles, the tangential overlap $\vec{\delta}_t$ that was tangential at step $h - 1$ is not necessarily tangential any more at step h . Consequently, at step h , the tangential displacement \vec{d}_t^h can have a normal component, which is not wanted in the model. Thus, tangential overlap $\vec{\delta}_t^h$ is defined, at each step h , as the tangential displacement reduced of the normal component define by the normal unit vector at step h :

$$\vec{\delta}_t^h = \vec{d}_t^h - \left(\vec{d}_t^h \cdot \vec{n}^h \right) \vec{n}^h \quad (1.30)$$

Which gives:

$$\vec{\delta}_t^h = \vec{\delta}_t^{h-1} + \vec{v}_t^{h-1} \Delta t - \left(\left(\vec{\delta}_t^{h-1} + \vec{v}_t^{h-1} \Delta t \right) \cdot \vec{n}^h \right) \vec{n}^h \quad (1.31)$$

And for the initial value (when the contact begins): $\vec{\delta}_t^0 = \vec{0}$.

1.2.2.c Material terms

Material terms link the main constitutive equations to the intrinsic properties of the particles. As we saw, originally, these terms were self-defined, and the use of any DEM model was made by setting directly their values. As a consequence, the assembly of particles was governed through five parameters (both stiffnesses, both damping factors and friction coefficient), eventually different from a particle to another. In this thesis, it was chosen to use the HM law, simply called “*Hertz model*” in LIGGGHTS. In other words, the material parameters were not set through raw values of stiffness and damping factor. Instead, these parameters were set through equations, all these equations being positive and defined by:

$$\begin{cases} k_n = \frac{2}{3} k'_n \\ \eta_n = -\beta \sqrt{\frac{10}{3} k'_n m^*} \\ k_t = k'_t \\ \eta_t = -\beta \sqrt{\frac{10}{3} k'_t m^*} \end{cases} \quad (1.32)$$

Where:

$$\begin{cases} k'_n = 2E^* \sqrt{R^* \delta_n} \\ k'_t = 8G^* \sqrt{R^* \delta_t} \end{cases} \quad (1.33)$$

Notably, we find again the expression of Hertz theory in the normal stiffness k_n , coming back to the normal Hertzian force described in Eq. (1.13).

Moreover, the pair equivalent mass and bulk modulus are defined as:

$$m^* = \frac{m_i m_j}{m_i + m_j} \quad (1.34)$$

$$G^* = \left(\frac{2(2 - \nu_i)(1 + \nu_i)}{E_i} + \frac{2(2 - \nu_j)(1 + \nu_j)}{E_j} \right)^{-1} \quad (1.35)$$

Finally, β is a negative damping coefficient related to the restitution coefficient e through:

$$\beta = \frac{\ln(e)}{\sqrt{\ln(e)^2 + \pi^2}} \quad (1.36)$$

Where the restitution coefficient, as described by Kuwabara & Kono (1987) [128], is the ratio of relative velocities of two colliding particles before and after the collision, giving a positive value between zero and one. It can represent several loss phenomena such as remaining vibrations, plastic deformations, fractures or inner viscosity.

1.2.3 Extension of the basic principle

1.2.3.a Introduction to attraction

All that has been introduced in previous section constitutes the core of the DEM equations used in this thesis. However, it is possible to add features to this core in order to implement additional phenomena. For example, the previous DEM equations only deal with repulsive interaction of particles. However, as we previously saw, the particles that compose electrode are glued together, mainly via the binder substrate or indirect gluing phenomena due to presence of electrolyte. Consequently, considering supplementary laws to implement attraction, or in other word “stickiness”, seems highly relevant. More precisely, there are two main ways to approach the stickiness: reversibly (the particles can attract even after the loss of a contact) and irreversibly (once the contact of a particles pair is lost, the attraction is also lost).

The reversible stickiness can be called “**adhesion**” (Fig. 1.18a) and the irreversible one the “**breakable bond**” (Fig. 1.18b).

1.2.3.b Adhesion: the JKR law

The adhesion remains a complex reaction and behind this term are hidden several physical and chemical phenomena (van der Waals forces, Coulombic forces, additional adhesive substances, capillary adhesion, junctions due to elastic/plastic deformations, etc.). Moreover, the physics of adhesion met a really rich development during the last century.

In historical literature, it is a inconceivable to miss out the pioneering work of Bowden & Tabor (1950) [129], in their book “*The Friction and Lubrication of Solids*”, where they present in particular sensitive experiments to measure the forces of adhesion of non-lubricated metals. The proof of these forces was hardly found only for soft metals, and the question remained opened for harder materials. In this optic, Johnson (1958) [101] brought in his note an analytic explanation, joining Hertz and Boussinesq theories, thus finding the presence

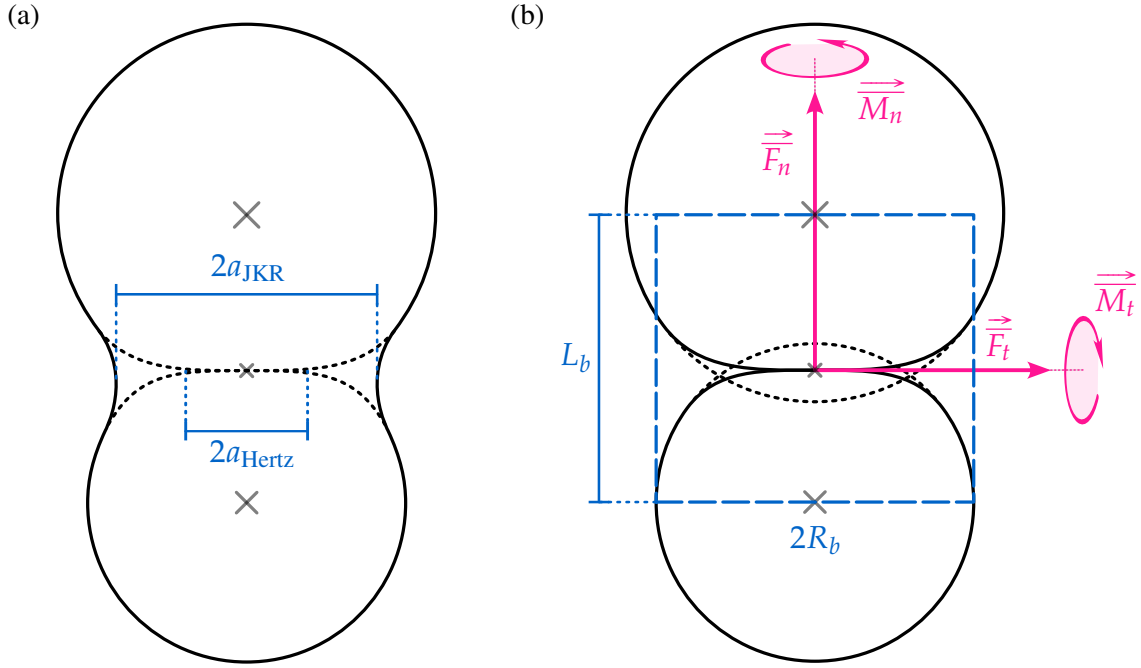


Figure 1.18: DEM scheme of particles stickiness models — **a)** Adhesion model scheme: the contact neck was observed higher than the Hertzian radius and gave birth to the JKR theory of adhesion. **b)** Breakable bond model scheme: a virtual bond is considered in parallel to the HM law and adds supplementary normal/tangential forces and torques.

of an infinite traction at the edge of the contact area of both solids. However, this mathematical result still remained unrealistic for highly stiff material that cannot deform enough and, consequently, present area of contact lower than the one predicted by Hertz theory. However, the problem is still more complex, and for more deformable materials, the behaviour seems reversed. Indeed, in 1968 and 1969, during the doctorate work using respectively smooth rubber spheres and glass spheres respectively, Roberts and Kendall found contact areas between bodies notably larger than those predicted by Hertz theory when the load was tending to zero. For this reason, Johnson, Kendall and Roberts worked on a theory to explain this phenomenon, giving birth to the well-known JKR theory of adhesion, in Johnson *et al.* (1971) [102] (schematised in Fig. 1.18a). They astonishingly showed that the force of adhesion was independent of the elastic moduli of the materials, through a simple equation that describes the load of spheres separation, *i.e.* the maximum force of adhesion (also called “pull-of force”):

$$F_{\text{JKR}} = \frac{3}{2}\pi R^* \Delta\xi \quad (1.37)$$

Where $\Delta\xi$ is the surface energy per unit contact area (including both surfaces).

Nevertheless, it would be unwise to limit the historical context with these names. In fact, the so-called work of Johnson had been already tackled almost forty years earlier. Bradley (1932) [130] demonstrated experimentally the proportionality between the adhesion force and equivalent diameter. He also proposed the expression of surface energy for a single surface, giving birth to the following expression of adhesive force:

$$F_{\text{Bradley}} = 4\pi R^* \xi \quad (1.38)$$

— In parentheses, specific attention should be paid on a common mistake about the surface energy: depending on the source, this physical quantity can be expressed for a single surface (ξ) or for the interfacial contact ($\Delta\xi$). Maugis & Pollock (1984) [131] defined the Dupré energy that introduces surface energies of both solids (ξ_1 and ξ_2) and the interfacial energy (ξ_{12}):

$$\Delta\xi = \xi_1 + \xi_2 - \xi_{12} \quad (1.39)$$

A common simplification is the equality between both surface energies ($\xi_1 = \xi_2$) joined to the zeroing of the interfacial-energy ($\xi_{12} \simeq 0$), so that $\Delta\xi = 2\xi$. Consequently, a coefficient 2 can appear in an equation across different sources. Because of this subtlety, the inevitable happened: compared to the others, Maugis & Pollock (1984) [131] let appear a wrong factor 2 due to the use of Dupré energy that is interfacial. It is then proposed here to call the interfacial surface energy $\Delta\xi$ the “**work of adhesion**” and to use W as an equivalent notation of $\Delta\xi$ ($W = \Delta\xi$). —

Coming back to History, Derjaguin (1934) [132] was the first to study the effect of contact deformation, and to do so, he introduced the so-called Derjaguin approximation that simplify the force profile calculation between colloidal particles thanks to a discretisation of the spherical shape, which finally gave the final expression that confirmed Bradley’s result:

$$F_{\text{Derjaguin}} = 4\pi R^* \left(\xi_{13} - \frac{1}{2}\xi_{11} \right) \quad (1.40)$$

Where Derjaguin distinguishes sub-terms of surface energy (ξ_{13} and ξ_{11}).

One year after the publication of JKR theory, Dahneke (1972) [133] proposed another theory that took into account the repulsion due to elastic flattening, by improving the Bradley’s work and correcting with experimental data from Derjaguin and its colleagues of 1968. He criticized the analysis made in the latter work that justified a quadratic evolution of the adhesive force, and not linear as the theory dictated.

As it can be imagined, after the publication of the JKR theory in 1971 and the work of Dahneke in 1972, Derjaguin and his colleagues answered three years later, as a clarification of many discrepancies in the recent publications concerning the adhesive force expression. As a result, Derjaguin *et al.* (1975) [134] maintained the original expression, giving birth in their turn to the DMT theory (Derjaguin, Muller and Toporov):

$$F_{\text{DMT}} = 2\pi R^* W \quad (1.41)$$

They also harshly criticised the approach of Dahneke by underlining a wrong equality between molecular repulsive forces and normal elastic stress, the use of old knowledge and also his bad interpretation of they work. Facing this “intellectual duel”, as a humble experimentalist mind, Tabor (1977) [135] established a clear and neutral comparison of both JKR and DMT theories, by reformulating them with single solid surface energies:

$$\begin{cases} F_{\text{JKR}} = 3\pi R^* \xi \\ F_{\text{DMT}} = 4\pi R^* \xi \end{cases} \quad (1.42)$$

Where $\Delta\xi$ has been replaced by surface energy ξ . The major result that have been kept in mind, as a physical compromise between JKR and DMT theories, is the Tabor limit defined by:

$$\tilde{\Theta}_{\text{Tabor}} = \frac{E \zeta^{\frac{3}{2}}}{R^{\frac{1}{2}} \Delta\xi} \quad (1.43)$$

Where ζ is the equilibrium separation between atoms (also called ‘‘inter-atomic spacing’’). This number evaluates the competition of surfaces roughness, between by the higher asperities (compressive forces that separate the surfaces) and lower asperities (adhesion forces that hold the surfaces). Thus, Muller *et al.* (1980) [136] analytically demonstrated this result and found a similar dimensionless parameter. Afterwards, Maugis (1992) [137] introduced an additional model for transition between both JKR and DMT theories, based on the work of Dugdale (1960). This is finally Greenwood (1997) [138] and Jonhson & Greenwood (1997) [139] that stated a final conclusion to this long intellectual debate by stating another definition of Tabor limit through:

$$\tilde{\Theta}_{\text{Greenwood}} = \left(\frac{R^* W^2}{E^{*2} \zeta^3} \right)^{\frac{1}{2}} \quad (1.44)$$

And a global summary:

$$\left\{ \begin{array}{ll} \tilde{\Theta}_{\text{Greenwood}} \leq 0.2 & \rightarrow \text{Bradley-Derjaguin curve} \\ 2 \leq \tilde{\Theta}_{\text{Greenwood}} < 3 & \rightarrow \text{Intermediary Maugis (1992) model} \\ 3 \leq \tilde{\Theta}_{\text{Greenwood}} & \rightarrow \text{JKR curve} \end{array} \right. \quad (1.45)$$

Today, the consensus for DMT-JKR transition is preferably fixed for the range of [0.1, 5] [137], [140], [141]. Beyond this pure theory of adhesion, when it comes to the DEM application, the literature seems to have simplified the approach of hybrid model by ignoring the Bradley-Derjaguin equation. Most of the models currently used for adhesion are JKR, or simplified JKR models. This monopole of JKR theory is maybe explained by the range of availability of Bradley-Derjaguin equation that remains extremely particular, mainly adapted for large separation of particles, placing JKR theory as a more polyvalent model. Moreover, in the considered problem of the thesis, it is relevant to establish the approximate value of $\tilde{\Theta}_{\text{Greenwood}}$ to evaluate the right theory to use. For example, by taking the material properties that minimize the expression of $\tilde{\Theta}_{\text{Greenwood}}$, summarised in Table 1.5, we obtain $\tilde{\Theta}_{\text{Greenwood}} \simeq 5.5$. The value is not particularly high, but according to the criteria dictated by Greenwood (1997) [138], it is more relevant to use the JKR theory for the anode model. Nevertheless, in absolute way, this value more belongs to the DMT-JKR developed by Maugis (1992) [137], but looking at the Figure 10 of this work proves that the air-gap profile with this value of $\tilde{\Theta}_{\text{Greenwood}}$ is close to the JKR profile. Thus, it is assumed that the DEM model closely follows a JKR profile, so the JKR model is preferred for the studied case to avoid the complexity of Maugis analytical approach.

The fact remains that the problem is not solved yet. Indeed, in practice, the application of JKR theory is more complicated than a component added to the normal force of a contact between two particles. To better understand this complexity, let us go back to the original formulation of JKR theory, in Johnson *et al.* (1971) [102]. In their system of equations (17), they established the following equation:

Variable	R	W	E	ν	ζ
Unit	μm	J/m^2	GPa	–	\AA
Value	1	0.5	50	0.3	1
Source	Table 2.1	[142]	Table 2.1	Table 2.1	[143]

Table 1.5: Values for computation of Tabor limit of studied system. Sources referring to Table 2.1 are detailed in Chapter 2.

$$F_{\text{ap}}^2 - 2F_{\text{ap}}(F + 3\pi WR^*) + F^2 = 0 \quad (1.46)$$

Where F_{ap} is the apparent Hertz load between particles and F the real applied load the particles are subjected to. To understand how a load can be “apparent”, it must be reminded the reason of JKR team for creating this theory: the apparent contact radius (a_{JKR} in Fig. 1.18a) was revealed to be higher than radius predicted by Hertz theory (a_{Hertz} in Fig. 1.18a). Consequently, the real radius is larger than in Hertz theory, and as Maugis & Pollock (1984) [131] said, the force required to obtain a given radius is lower than in Hertz theory. This is why a given contact radius is associated to a force that can be calculated through Hertz theory, a force that is however “apparent” and not applied in reality.

To find the real load F applied between particles, it is necessary to solve the previous equation, via a classical second degree polynomial resolution on the variable F :

$$F = F_{\text{ap}} - \sqrt{6\pi F_{\text{ap}} WR^*} \quad (1.47)$$

As it was said, it is possible to consider the apparent load as a classical Hertzian force (defined through Eq. (1.14)), which gives:

$$F_n = \frac{4E^* a_{\text{JKR}}^3}{3R^*} - \sqrt{8\pi WE^* a_{\text{JKR}}^3} \quad (1.48)$$

And where, if adhesion is neglected ($W = 0$), the load comes back to the original form of Hertz theory, as defined in Eq. (1.13). This form, or at least the adhesive term, is a common result that is introduced in many papers (Maugis & Pollock (1984) [131], Chokshi *et al.* (1993) [144], Parteli *et al.* (2014) [145], Coetzee (2020) [146]), but the demonstration is rarely developed. Facing the result of Eq. (1.48), we can observe that it is impossible to apply this formula to the problem and solve it thanks to geometrical and rheological properties. Indeed, according to Coetzee (2020) [146] and Thornton (2015) [140]:

$$\delta_n = \frac{a_{\text{JKR}}^2}{R^*} - \sqrt{\frac{4\pi W a_{\text{JKR}}}{E^*}} \quad (1.49)$$

Where, once again, neglecting the adhesion leads to the original Hertzian radius defined by Eq. (1.12). The non-linear relationship demonstrates the difficulty to compute the contact radius, and by consequence the normal force, directly from dynamic parameters. To improve computation, the adhesion model used in LIGGGHTS uses a lookup table of pre-computed values, as proposed by Marshall (2009) [147].

Finally, the computation of the tangential component of contact force is the same as the HM law. However, an issue can appear concerning the friction criterion. Indeed, this adhesion model can present a normal state of equilibrium between both particles even if they are in contact, *i.e.* the normal force component is null. The classical friction criterion defined in the main constitutive equation Eq. (1.16) would consequently lead to a null tangential component. This question was already tackled by Thornton (1991) [148], who defined an extended surface energy dependent friction criterion:

$$k_t \delta_t < \mu(F_{n,\text{spring}} + 2F_{\text{JKR}}) \quad (1.50)$$

The model defined through Eqs. (1.37) and (1.48) to (1.50), able to come back to the whole HM law only by setting $W = 0 \text{ J/m}^2$, is then called the “**JKR law**” in this manuscript. The LIGGGHTS version of this model is the user-made code developed by Eidevåg *et al.* (2019) [141], introduced in [149]. The version used in this thesis is the version available in the “Flexible Fibers” version proposed by Schramm [150].

1.2.3.c Breakable bond: the PC law

The breakable bond model is built on a simplified spring/dash-pot modelling of an inter-particle bond. The technique was originally introduced by Potyondy & Cundall (2004) [151], in order to model cracks mechanisms within rocks. It consists in keeping the original contact law (in our case, the HM law) and adding in parallel a supplementary law that simulates the presence of a virtual bond (dashed rectangle in Fig. 1.18b). To do so, this law creates additional forces added in parallel to main contact forces defined through Eq. (1.16). The forces and the associated torques are incrementally defined by:

$$\begin{cases} \overrightarrow{\Delta F_n} = K_n S_b \overrightarrow{\Delta \chi_{i/j,n}} \\ \overrightarrow{\Delta F_t} = K_t S_b \overrightarrow{\Delta \chi_{i/j,t}} \\ \overrightarrow{\Delta M_n} = K_t J_{\Delta^2 b} \overrightarrow{\Delta \theta_{i/j,n}} \\ \overrightarrow{\Delta M_t} = \frac{1}{2} K_n J_{\Delta^2 b} \overrightarrow{\Delta \theta_{i/j,t}} \end{cases} \quad (1.51)$$

Where $\overrightarrow{\Delta \chi_{i/j}}$ and $\overrightarrow{\Delta \theta_{i/j}}$ are the increments of relative displacements, respectively translational and angular. More complete approaches even proposed the consideration of a damping component of these parallel forces. For example, Guo *et al.* (2013a,b) [152], [153] implemented a damping reaction through a damping coefficient η . However, considering the quasi-static state studied here (this aspect is discussed in Section 2.4.3 and for a reason of simplicity, the damping reaction was set to zero ($\eta = 0 \text{ N.s/m}$)).

Generally speaking, each bond is created with given length L_b , radius R_b , Young’s modulus E_b . The length L_b (also called “equilibrium distance”) is defined as the initial distance between particles at the creation of the bond. As for R_b , it is defined as a ratio of the minimum radius of both particles. Indeed, Potyondy & Cundall (2004) [151] proposed the ratio Y (between 0 and 1) to reduce the size of the bond, *i.e.* $R_b = Y \min(R_1, R_2)$. Considering the studied case, because the particles of electrode are entirely mixed in a mixture of binder, it was decided to select the highest radius of the bond, *i.e.* $Y = 1$, as schematised in Fig. 1.18b.

These parameters finally give the necessary terms previously introduced in Eq. (1.51)

$$\left\{ \begin{array}{l} R_b = \min(R_1, R_2) \\ S_b = \pi R_b^2 \\ J_{\Delta^2 b} = \frac{1}{2} \pi R_b^4 \\ K_n = \frac{E_b}{L_b} \\ K_t = \frac{E_b}{2L_b(1 + \nu_b)} \end{array} \right. \quad (1.52)$$

After its creation, the bond influences the contact forces until it breaks. More precisely, the presence of the bond is determined by two criteria, respectively tensile and shear, defined by the following formulae:

$$\left\{ \begin{array}{l} \sigma = \frac{\overline{F}_n}{S_b} + 2 \frac{\overline{M}_n R_b}{J_{\Delta^2 b}} < \sigma_{\max} \\ \tau = \frac{\overline{F}_t}{S_b} + \frac{\overline{M}_t R_b}{J_{\Delta^2 b}} < \tau_{\max} \end{array} \right. \quad (1.53)$$

If at least one of the criteria defined in Eq. (1.53) is not respected anymore, the bond is irreversibly broken and its forces and torques are removed from dynamics computation. As a particular case, it is noteworthy that if at least one of the maximum values of shear and tensile criteria is null ($\sigma_{\max} = 0$ Pa or $\tau_{\max} = 0$ Pa), all the bonds of the particles bed are immediately lost and then the model immediately comes back to the classical law used, in our case the HM law.

It is proposed here to call this model the “**PC law**”. It was implemented in LIGGGHTS through the work of Schramm *et al.* (2019) [154], initially in [155] (today deprecated). The version used in this thesis is also the one proposed by Schramm [150].

1.2.3.d Illustration of sticky laws

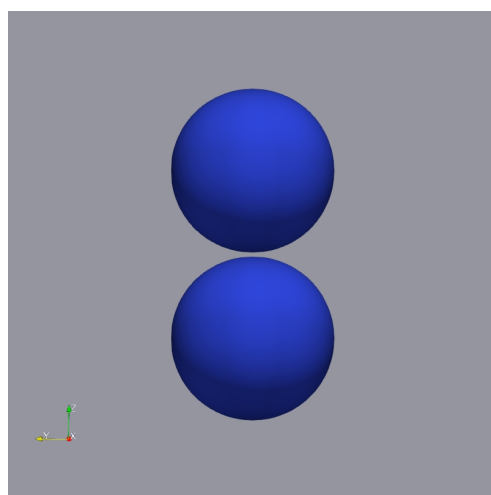
Even if they are quite different, these two sticky laws share a common point: they present a stable equilibrium point in their force-displacement curve at the opposite of the HM law. A stable equilibrium point is defined, when plotting the force as a function of the overlap, as a positive derivative slope at the intersection of the curve with the zero of force axis. Indeed, in this case, increasing the overlap creates a repulsive force and decreasing the overlap creates an attractive force, engendering a convergence to the equilibrium point.

To better illustrate what both JKR and PC laws bring to the contact model, let us see a little example focused on the normal direction of a particles pair. Let us consider a particles pair z-axis oriented, with same radii of 1 μm (see Fig. 1.19a). The bottom particle is frozen in space and the top one is moved with controlled velocity along the z-axis. The curves then display the force-displacement curve.

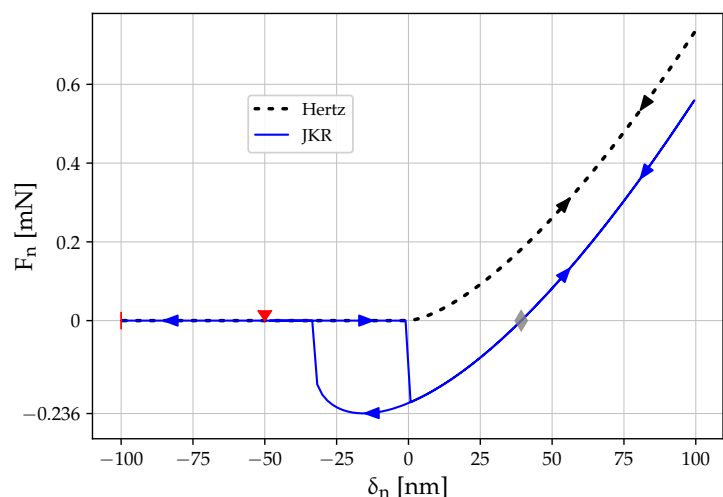
The test for JKR law consists in an initial distance between particles ($\delta_{n,\text{init}} = -50$ nm), followed with an overlapping move ($\dot{v}_z < 0$ $\mu\text{m}/\mu\text{s}$, until $\delta_n = 100$ nm) and finally a detaching move ($\dot{v}_z > 0$ $\mu\text{m}/\mu\text{s}$, until $\delta_n = -100$ nm), as plotted in Fig. 1.19b. Set with a work of adhesion 100 J/m^2 , the JKR law begins when

particles surfaces meet ($\delta_n = 0$ mN) and immediately creates an attractive force ($F_n < 0$ mN) whose evolution is similar to a Hertz law. In consequence, a stable equilibrium overlap appears (grey diamond that presents a positive derivative slope) and the particles, if not submitted to any other external force, can endlessly remain in contact. At the opposite, the Hertz law presents an unstable equilibrium point (point (0,0) of force-displacement curve), due to the null slope of its derivative. The noticeable value of the JKR curve is of course the pull-of force, as defined by Eq. (1.37). By applying this formula with $R = 1 \mu\text{m}$ and $\Delta\xi = W = 100 \text{ J/m}^2$, we get a value of around 0.236 mN. Thus, Fig. 1.19b elegantly demonstrates the sense of this value: it corresponds to the minimum amount of traction force required to detach both particles (lowest point of JKR solid curve). The advantage of the JKR law is to introduce a permanent attractive force and, first, reversible. Indeed, after the loss of contact (brief rupture after the lowest point of JKR solid curve), the force scheme is able to begin again.

When it comes to the PC law, the test must be more diversified to capture its real characteristic. Indeed, the equilibrium point of JKR law is unique for each pair values of radii and work of adhesion, but this is not the case for the PC law: the equilibrium point also depends on the initial distance between particles at the creation of the bond. Let us take the same example, with the same succession of two moves (overlapping and detaching) but with two different initial overlaps when the bond is created: the particles are already overlapped (“In” case, $\delta_{n,\text{init}} = 50 \text{ nm}$) and the particles are not in geometrical contact (“Out” case, $\delta_{n,\text{init}} = -50 \text{ nm}$). Let us also fix a maximum stress value such that the bond never breaks ($\sigma_{\text{max}} = \tau_{\text{max}} \rightarrow \infty$). Fig. 1.20a clearly shows two different equilibrium points (grey diamonds) and we then distinguish two cases. When the bond is created with an initial overlap of particles (“In” case), the equilibrium point verifies the following condition: $0 < \delta_{n,\text{equ}} < \delta_{n,\text{init}}$. When the bond is created with an initial space between particles (“Out” case), the equilibrium is directly defined: $\delta_{n,\text{equ}} = \delta_{n,\text{init}}$. In other words, as long as it is present, the bond keeps the memory of the initial bond length (through the value L_b). Thereby, the force evolves linearly when the particles are not in geometrical contact ($\delta_n < 0 \mu\text{m}$) and quadratically when they are overlapped. Another



(a) Particles pair



(b) Force-displacement curve Hertz/JKR

Figure 1.19: Simple test for JKR law illustration — **a)** Particle pair for sticky laws’ illustration: bottom particle is frozen in space, top particle is velocity controlled. **b)** Force-displacement curve: $\blacktriangledown \rightarrow$ initial overlap, $\blacklozenge \rightarrow$ equilibrium overlap, $| \rightarrow$ final overlap

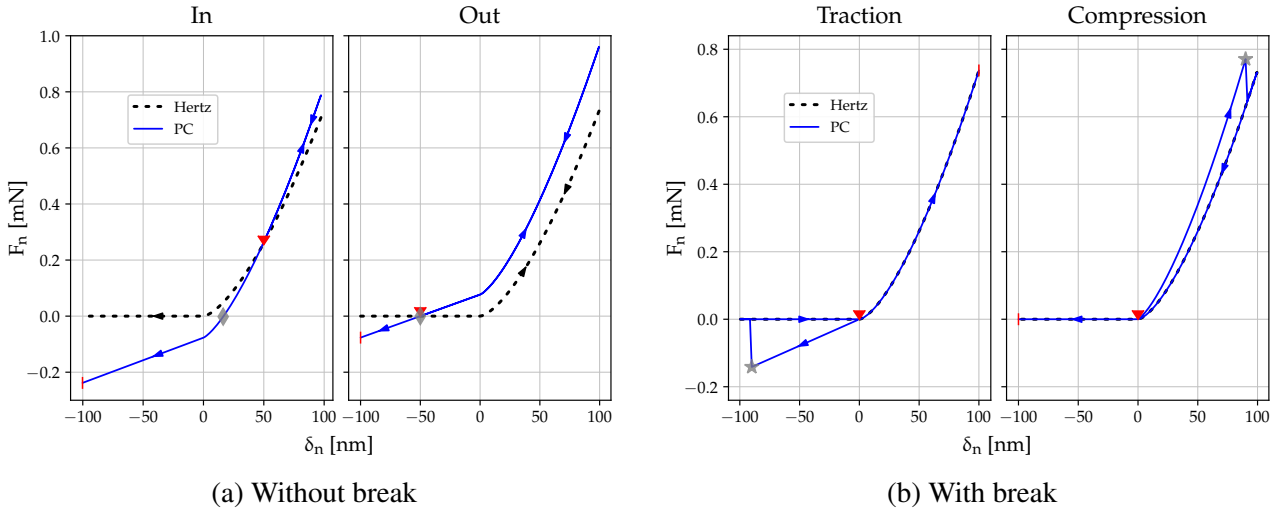


Figure 1.20: Simple test for PC law illustration: $\blacktriangledown \rightarrow$ initial overlap (bond creation), $| \rightarrow$ final overlap, $\blacklozenge \rightarrow$ equilibrium overlap, $\star \rightarrow$ bond break — **a)** Force-displacement curve without break: the "In" case begins with an initial overlap of 50 nm, the "Out" case begins with an initial distance between surfaces of 50 nm. **b)** Force-displacement curve with break: the "Traction" case pulls on the bond and the "Compression" case pushes on the bond.

important feature to have in mind is the ability of the bond to break as in traction as in compression. In this sense, Fig. 1.20b draws the force-displacement curves of two symmetric cases, where the bond is created with a null initial overlap ($\delta_{n,\text{init}} = 0 \mu\text{m}$), with a maximum stress value lowered enough to make the bond break. In the "Traction" case, the particles are detached first and in the "Compression" case, the particles are overlapped first. In both cases, the bond is broken at the same overlap but differentiated by its sign (grey stars, $\delta_{n,\text{break}} \simeq 100 \text{ nm}$). After the break, the force-displacement curve comes back to the classical Hertz law (black dotted line). Furthermore, when the break occurs, this is a one way step: this specific particles pair now follows the HM law, without presenting any sticky behaviour any more. The stickiness is then irreversible.

This is what characterises most both JKR and PC laws: able to implement a sticky behaviour of particles, they are complementary by their reversibility. The JKR law is more inclined to simulate the gluing effect of a liquid or a viscous glue (electrolyte, undried binder) and the PC law is more relevant in simulating rigidified glue or inter-blocked particles (dried binder, merged particles).

1.3 Bibliography conclusion

All the bibliographic work presented above is, first, a review on the “why” of this thesis, built on the core question that we would rather recall: “*Do discrete structure contact properties of an electrode have an influence on its breathing behaviour?*”. We used the general term “electrode”, but we have to remind that the studied case is the Si/C/Gr anode. Nevertheless, the reasoning will be quite applicable to other types of electrodes, or even other technologies, as long as the system is composed of a layer of packed particles that breathe cyclically and notably enough to engender important mechanical consequences.

In this chapter, we mainly took the time to describe a selection of DEM methods and theories, the ones that are the most efficient in the resolution of the core question. However, the development in this manuscript does not only focus on this tool, as a succession of DEM simulations. A major part of the content also covers some experimental validations joined to a rheological approach to improve mechanical measurements of electrode breathing (see Chapter 4).

As for now, the next chapter enters the details about the DEM model of this thesis: the “**Discrete Anode Model**”.

Chapter 2

Description of Discrete Anode Model (DAM)

2.1 Structure of DAM

The “DAM” (Discrete Anode Model) is a proposal for a first approach to build a breathing anode model with mechanical discrete consideration. The global protocol consists in exploring the parameters that dictate the contact behaviour, more precisely their role in the breathing behaviour at the scale of the electrode. The development of this protocol is the point of Section 2.2. Beforehand, it is important to precisely describe what we are looking for through the DAM, and what we are able to measure within a DEM tool.

2.1.1 Thickness Deltas

The key features of DAM exploration have already been introduced previously, discussed in the thesis position in Section 1.1.2 and drawn in Fig. 1.5. Both features are the swelling amplitude and irreversibility of the breathing. Fig. 2.1 presents a schematic view of these quantities, with the swelling amplitude in dashed arrow and the irreversibility in solid arrow. The important detail to have in mind is the cycle-referencing: each Δ is based on the initial value of the associated breathing cycle, thus the reference changes at each cycle. Mathematically, for a given cycle n , these quantities are expressed by:

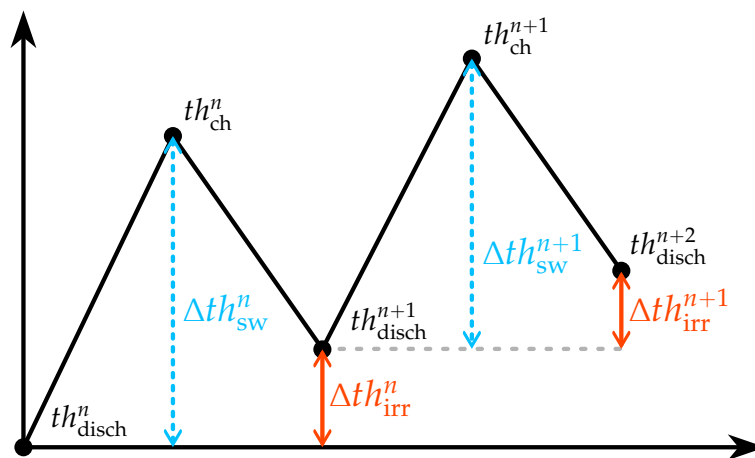


Figure 2.1: Scheme of principal quantities of DAM evaluation: swelling amplitude (dashed arrows) and irreversibility (solid arrows).

$$\begin{cases} \Delta t h_{sw}^n = t h_{ch}^n - t h_{disch}^n \\ \Delta t h_{irr}^n = t h_{disch}^{n+1} - t h_{disch}^n \end{cases} \quad (2.1)$$

2.1.2 Hypothesis

As a recall, the objective is to understand in what an extent the granular media influences the breathing behaviour. As a result, the construction of the DAM has to ensure that any variation of swelling amplitude and irreversibility comes from the granular media itself and not from any other source, in order to avoid as many interpretation biases as possible. It is consequently built on following Set of Hypothesis 2.A:

- (i) **The particles are supposed spherical.** In reality, the structure is close to the cross-section in Fig. 5a displaying the non-spherical shape of real particles. Despite this fact, for computation efficiency and model simplification purposes, the particles are simplified as simple spheres. The granular structure is detailed in Section 2.1.3.a.
- (ii) **The particles material properties are supposed constant.** It is shown in literature that active materials present material properties dependent on state of lithiation [53], [156]–[163]. These properties are simplified as constant values in Section 2.1.3.b.
- (iii) **The mechanical resistance of liquid electrolyte present in pore volume is neglected.** The mechanics of solid particles are supposed much significant than the mechanical action of electrolyte. This is useful to simplify the mechanics of sample presented in Section 2.1.3.
- (iv) **The anode layer is simplified as a mix of Si/C and Gr particles,** then modelled particles exclude carbon-binder domain particles. The granular structure is detailed in Section 2.1.3.a.
- (v) **The particles breathe reversibly with constant swelling amplitude.** More as a condition than a hypothesis, this is necessary to ensure that any captured variation of swelling amplitude or irreversibility does not come from particles themselves. This aspect is treated in the development of breathing laws of particles, in Section 2.3.3.
- (vi) **The inertia of particles is supposed negligible compared to the packing force network,** because of slow cycling. It is technically impossible to simulate breathing using the real cycle period, so this period must be shortened. However, it is necessary to ensure that shortening this time does not create inertial effect that generate false breathing behaviour, in other words that the force network still predominate the particles' inertia. This aspect is further explained in Section 2.4.3.
- (vii) **The electrode breathing occurs only along the thickness axis (edge effect neglected).** This is required to match with experimental practice. Indeed, measurements treat thickness and not volume, through a breathing that occurs only along one axis. The boundary conditions in lateral directions are thus periodic (detailed in Section 2.1.3.a).
- (viii) **Top and bottom “plates” that compress the particles bed are supposed flat and not deformable.** In practice, particles are compressed between two layers: the separator and the copper collector. These surfaces are modelled by two “plates” (introduced in Section 2.1.3.a). In practice, both surfaces may present some local deformations, but the latter are neglected in the model.

2.1.3 DAM reference sample

The whole point of the chosen strategy (detailed in the following Section 2.2) is to start from a well known DAM reference sample. This reference sample is defined through two main aspects: structure and material properties.

2.1.3.a Structure

Because no regular pattern or periodicity is observed experimentally in the anode structure (as in Fig. 5a), the particles bed organisation should follow a heterogeneous enough particle-size distribution (mathematical function that defines the relative amount of particles as a function of size, in mass or in volume), in order to avoid any crystallisation of the packing. To this end, five different sizes for each component (Si/C and Gr) were extracted from anode particle-size distribution provided by Umicore (details about particle-size distribution not provided in this manuscript for confidential reasons). Afterwards, the total size of the reference sample was set based on the extracted radii, by following a common rule of representative elementary volume in DEM: it should be at least ten times higher than the highest particle size. As a result, the final particles' template of reference sample counts 1.360 particles, whose radii are comprised between 5.25 and 15.25 μm . All these conditions finally give the final sizes of the sample displayed in Fig. 2.2 where we can distinguish three parts:

- The particles bed composed of a mix of Si/C and Gr particles
- The top plate
- The bottom plate

In this sample, the boundaries in x and y directions are periodic, which means that each particle going out on one side goes in on the opposite. The size along these directions was set such that the representative

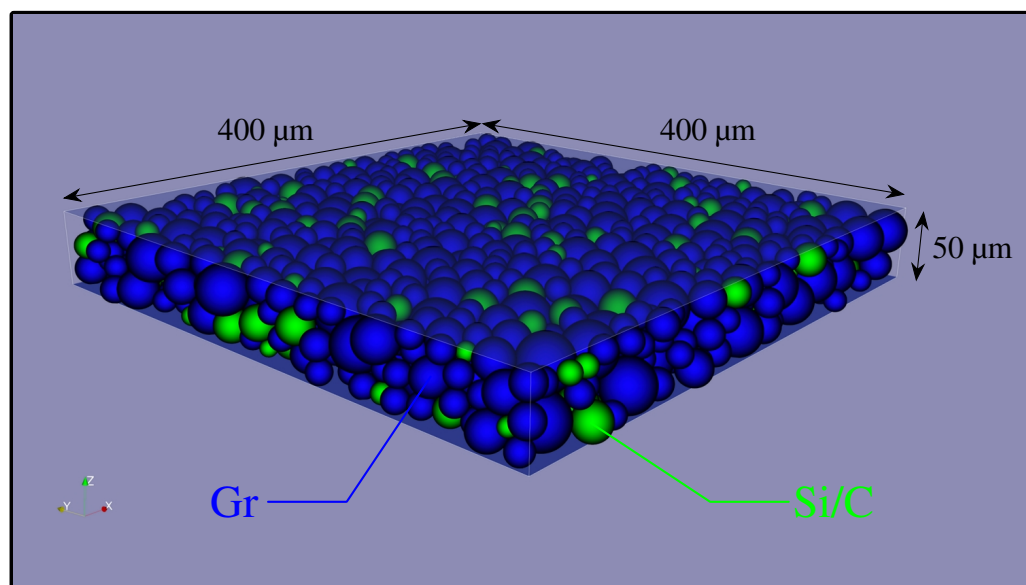


Figure 2.2: Picture of DAM reference sample: particles bed composed of Si/C (in lighter colour) and Gr (in darker colour), between the fixed bottom plate and the moving top plate (in half transparent). Dimensions: $400 \times 400 \times 50 \mu\text{m}$. Boundaries along x and y : periodic. Mass proportion of Si in Si/C/Gr: 5w%.

elementary volume rule is respected, giving the final dimensions of $400 \times 400 \times 50 \mu\text{m}$. Concerning the mass proportions, the weight fraction of silicon within Si/C/Gr total mass of 5wt% (A_{Si}) and the fraction of silicon in Si/C particles is 50wt% (B_{Si}). The convention of these notations (A_{Si} and B_{Si}) are developed in Section 2.3.2.b.

Finally, based on the work of Sangrós Giménez *et al.* (2018) [65], the particles bed is calendered under a range of pressure of 40~60 MPa (6.4~9.6 N considering the DAM reference sample surface). During cycling, the particles bed is submitted to a constant pressure based on experimental practice: the **reference pressure** (P_{ref}) of **0.3 MPa**. This value has been chosen because, in practical applications, it is a compromise to obtain the best mechanical/electrochemical conditions. The details about the calendering and cycling phases are presented in Section 2.2.1.

All the structure parameters are recapitulated in Table 2.1.

2.1.3.b Material properties

The DAM reference sample is set with a basic Hertz-Mindlin law, whose advantage is to reduce the number of parameters to fundamental rheological parameters. As supposed in Hyp. 2.A.ii (page 74), these properties are simplified as constants. Concerning densities, ρ_{Gr} is extracted from literature, whereas ρ_{CSi} is based on silicon and carbon densities from Astrova *et al.* (2020) [164], through the relationship:

$$\rho_{\text{CSi}} = \frac{m_{\text{Si}} + m_{\text{C}}}{V_{\text{Si}} + V_{\text{C}}} = \frac{\rho_{\text{Si}} \rho_{\text{Gr}}}{B_{\text{Si}} \rho_{\text{C}} + \rho_{\text{Si}}(1 - B_{\text{Si}})} \quad (2.2)$$

For Young's moduli, the values for graphite and silicon/carbon composite are based on literature. The silicon/carbon composite is hard to estimate due to many divergences, as summarised in Fig. 2.3a. Firstly, the resources on Si/C composite itself are less common than pure silicon. Secondly, the pure silicon (ranges with point ends in Fig. 2.3b) reveals to be highly dependent on the state of lithiation, varying from 160 GPa at a delithiated state to 5 GPa to highest lithiation state. This obviously questions the Hyp. 2.A.ii (page 74) which supposes that material properties of particles are constant and will maybe constitute an axis for future improvement of DEM electrode model. In addition, the Si/C composite (ranges with diamond ends in Fig. 2.3b) is generally softer than the pure silicon, with values varying from 0.5 to 14.7 GPa measured experimentally. The range of Song *et al.* (2021) [165], much higher, is obtained by model optimisation to minimise failure mechanism. As a compromise, a Young's modulus of 45 GPa was chosen for the DAM reference sample. Concerning the plates, the material properties of copper have been chosen, as it is the material of the anode collector. No research priority was made for Poisson's ratio and coefficient of restitution, as Sangrós Giménez *et al.* (2018) [64] already tested that they have a minor impact on the force displacement curve of a packed particles bed.

Concerning the friction coefficient, the value was much harder to estimate. First, finding a precise figure for the materials of the DAM reference sample is quite unlikely. Besides, by searching values for materials close to the current model remains difficult, due to the divergence of observations in literature. First, a noticeable difference of practice exist between the studies on material (ranges with point ends in Fig. 2.3b) and studies using DEM (ranges with diamond ends Fig. 2.3b). Conventionally, it seems that DEM domain allows to explore much larger ranges of values for the coefficient of friction, certainly because it is often seen as an

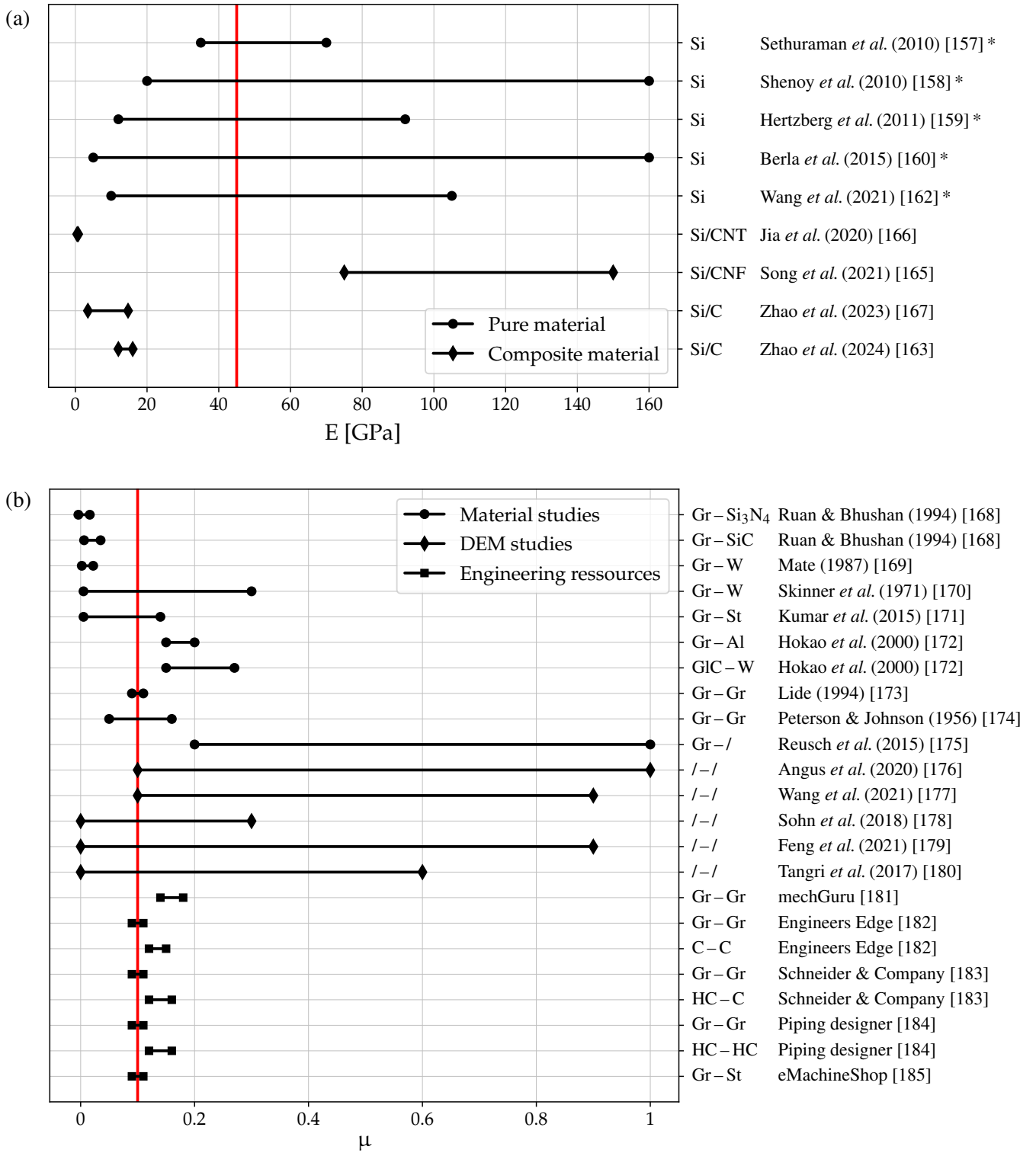


Figure 2.3: Review of material properties. Vertical thick lines represent the values chosen for DAM reference sample — **a)** Review of Young's modulus values for silicon (pure and composite). Young's moduli obtained in references with asterisk "*" are dependent to the state of lithiation of silicon. CNT: Carbon Nanotubes, CNF: Carbon Nanofibers. **b)** Review of friction coefficient values for materials close to DAM reference sample components. Gr: Graphite, Al: Alumina, St: Steel, W: Tungstene, C: Carbon, GIC: Glassy Carbon, HC: Hard Carbon, Gl: Glass.

energetic control parameter, rather than a number with a physical meaning (the material pairs are not even not detailed in cited references). Finally, the engineering websites [181]–[185] also provides values converging between 0.1 and 0.2. Finally, a most interesting question made by Ruan & Bhushan (1994) [168], Mate (1987) [169], Skinner *et al.* (1971) [170] and Kumar *et al.* (2015) [171] (five top lines in Fig. 2.3b) is the about the scale consideration, and especially the very low values measured at microscopic scale (until 0.005). Skinner *et al.* (1971) [170] specified that the difference of their values with previous work “*probably lies in the scale of the experiments*” and “*regions of the surface were selected [...] to be of high perfection*”. In that sense, Ruan & Bhushan (1994) [168] ask the exact question we are facing: “*Why is the atomic-scale coefficient of friction of graphite so small compared with its macroscopic counterpart?*”. Their conclusion goes in the same direction: the surface orientation has an important role in the frictional behaviour and a ploughing mechanism may be at the origin of higher values for macroscopic measurements. Facing all these discrepancies, it was decided to choose for the reference sample a value that globally fit the best all these references, *i.e.* $\mu = 0.1$.

All the material properties are summarised in Table 2.1.

2.1.4 Time step

When it comes to incremental calculation over time, the choice of the time step is the first question met before any computation. This is particularly the case for the anode that present little particles (1 to 10 μm) and long phenomenon period (several hours), giving birth to tremendous amount of time steps to compute. This is why it is necessary to choose the time step wisely. In a general way, the methodology is to choose a time step corresponding to a fraction of a “critical time step”, this value being physically determined by the problem. To quantify precisely this value, Otsubo *et al.* (2014) [192] listed three main approaches to calculate the critical time step:

- The oscillation period of a spring/mass system with a single degree of freedom
- The characteristic time of Rayleigh wave speed
- The Gerschgorin’s theorem based approach

The first definition was used by Cundall & Strack (1979) [93] who met the computational issue, especially with the restrained computing capacity of their 250 Ko memory cored minicomputer. This critical time step was defined by considering the simple case of single degree-of-freedom system of a mass m connected to ground by a spring of stiffness k . Afterwards, Hart *et al.* (1988) [110] detailed this time step in order to minimise it, through the formulation:

$$\Delta t_{c,\text{Cundall}} = 2\sqrt{\frac{m_{\min}}{2k_{\max}}} \quad (2.3)$$

Where m_{\min} is the minimum particle mass and k_{\max} the maximum particle stiffness. However, this definition is not immediately meaningful in a DEM model based on Hertz-Mindlin law. In fact, the definition of critical time step for the Hertzian model is more controversial. This is why the approach considering the characteristic time of Rayleigh wave speed is also considered, as proposed by Thornton & Randall (1988) [106]. In their case, they consider the three existing types of wave motion that occur at contact between particles: dilational (or compressional or pressure) wave, distortional (or shear) wave and Rayleigh (or surface) wave. By using the study of Miller & Pursey (1955) [194], where it is concluded that for a single-element radiator on

Type	Parameter	Notation	Value	Source
Structure	Dimensions	–	400 × 400 × 50 μm	Representative elementary volume condition
	Calendering thickness	th_{cal}	50 μm	Experimental practice
	Total number of particles	N_{part}	1,360	Experimental practice
	Radii range	–	5.25 ~ 15.25 μm	Umicore ^a
	Calendering pressure range	–	40 ~ 60 MPa	[64], [68], [71], [85]
	Cycling pressure	P_{ref}	0.3 MPa	Experimental practice
	Si weight fraction in Si/C/Gr	A_{Si}	5wt%	Experimental practice
	Si weight fraction in Si/C	B_{Si}	50wt%	Experimental practice
Material	Si/C density	ρ_{CSi}	2.07 g/cm ³	[164]
	Gr density	ρ_{Gr}	2.22 g/cm ³	[64], [186]
	Plates density	ρ_{walls}	8.96 g/cm ³	[173], [187]
	Si/C Young's modulus	E_{CSi}	45 GPa	Fig. 2.3a
	Gr Young's modulus	E_{Gr}	15 GPa	[186], [188]–[190]
	Plates Young's modulus	E_{walls}	130 GPa	[187], [191]
	Poisson's ratio	ν	0.3	[63], [64], [189]
	Friction coefficient	μ	0.1	Fig. 2.3b
	Coefficient of restitution	e	0.25	[64], [65]
	/	Time step	Δt	2 ns
/	Contact law	HM	–	Section 1.2.1.b

^a Details about particle-size distribution not provided in this manuscript for confidential reasons.

Table 2.1: Parameters of DAM reference sample.

contact with a semi-infinite solid, the Rayleigh waves account for 67.4% of the radiated energy in comparison with compressional waves (6.9%) and shear waves (25.8%), Thornton & Randall then assumed that all the energy were transmitted by the Rayleigh waves, finally opting for its characteristic time. By adapting it to minimise with the problem settings, this time is defined as:

$$\Delta t_{c,\text{Thornton}} = \frac{\pi R_{\text{min}}}{0.1631 v_{\text{max}} + 0.8766} \sqrt{\frac{2\rho_{\text{min}}(1 + \nu_{\text{min}})}{E_{\text{max}}}} \quad (2.4)$$

Finally, Otsubo *et al.* (2014) [192] also rigorously criticised these approaches, introducing another time step definition based on Gerschgorin's theorem, similar to Cundall critical time step:

$$\Delta t_{c,\text{Otsubo}} = \sqrt{\frac{m_{\text{min}}}{k_{\text{max}} C N_{\text{max}}}} \quad (2.5)$$

Where CN_{\max} is the maximum coordination number, *i.e.* the maximum number of contacts per particle. They specified that the Rayleigh wave speed approach was valid only at low stress levels ($CN < 15$). To replace this criterion, they advised to use the approach based on Gerschgorin's theorem, with a recalculation of critical time increment during simulation, in order to optimize calculation and, consequently, avoid unnecessary waste of resource and energy. Ramírez-Aragón *et al.* (2018) [193] presented a rich test protocol to test different critical time steps. Even though, they precised that any method to find an optimal value of time step is not universal. As a consequence, it is always necessary to study each problem separately. Considering the DAM that uses a Hertz-Mindlin law and a set of particle-size distribution/Young's moduli/pressure not high enough to reach the critical coordination of 15 delimited by Otsubo *et al.* (2014) [192], it was decided to use the Rayleigh wave-based definition, *i.e.* Eq. (2.5).

The value used for the DAM reference sample is then equal to 2 ns (see Table 2.1), which correspond to 32,5% of $\Delta t_{c, \text{Thornton}}$.

2.2 Simulation structures

As introduced in the beginning of this chapter, the main objective is to determine the ability of the DAM parameters to reproduce the observed experimental behaviours. But what are these parameters, and why choosing some rather than others? An important step has been to consider the parameters of the tool and to estimate their relevancy in the battery context. For example, the coefficient of restitution, defined as the ratio of the relative velocities before and after collision of two particles, is not really relevant in a particles bed, especially when considering the Hyp. 2.A.vi (page 74) (quasi-statistic particles bed). Compared to it, the friction coefficient seems much more susceptible to play a role in the particles' reorganisation, as it prevents more or less the particles to move. The main process applied to the DAM is consequently to focus on the parameters that are battery context coherent and that were detected to be the most influential on the breathing of the anode. As a result, the strategy used in this manuscript is a standard succession of sensitivity analyses, starting systematically from a defined example (that we will call "DAM reference sample"), in order to analyse the influence of different parameters. The details about the studied parameters are developed in Chapter 3.

In this aim, a multi-level process of analysis has been especially designed for the DAM. All the points of the current section is to describe how:

- a single simulation is composed (Section 2.2.1)
- multiple simulation compose a unique sensitivity series (Section 2.2.2)
- multiple sensitivity series compose a statistical analysis (Section 2.2.3)

2.2.1 Level one: simulation phases

In the previous sections, we mainly addressed the particles bed itself, but not how it is generated. In practice, several methods exist in DEM to generate a particles bed. For the DAM, the choice of the particles bed generation was inspired from the electrode manufacturing itself. In reality, it involves mixing the particles in a solvent, coating this slurry onto a current collector, evaporating the solvent in an oven and then calendaring

it between two rolls. To match with this practical process, three main phases are finally defined for a given DAM simulation, as represented in Fig. 2.4 (three last images):

- The “**calendering phase**”
- The “**relaxation phase**”
- The “**cycling phase**”

The Calendering phase consists in randomly generating the particles (based on a given particle size distribution), letting them rain without friction on the bottom plate and compressing them with the top plate until it reaches the calendering thickness th_{cal} (equal to the value in Table 2.1). The number of particles was chosen such that the resulting calendering pressure is between 40 and 60 MPa (range based on Sangrós Giménez *et al.* (2018), [64]). The Relaxation phase consists in letting the particles bed relax until the total force on the top plate reaches at a given pressure. The Cycling phase consists in making particles breath periodically and maintaining the pressure constant via a PID (Proportional–Integral–Derivative) controller adapting the top plate displacement. The input pressure of the PID depends on the simulation itself (equal to P_{ref} by default, unless otherwise specified).

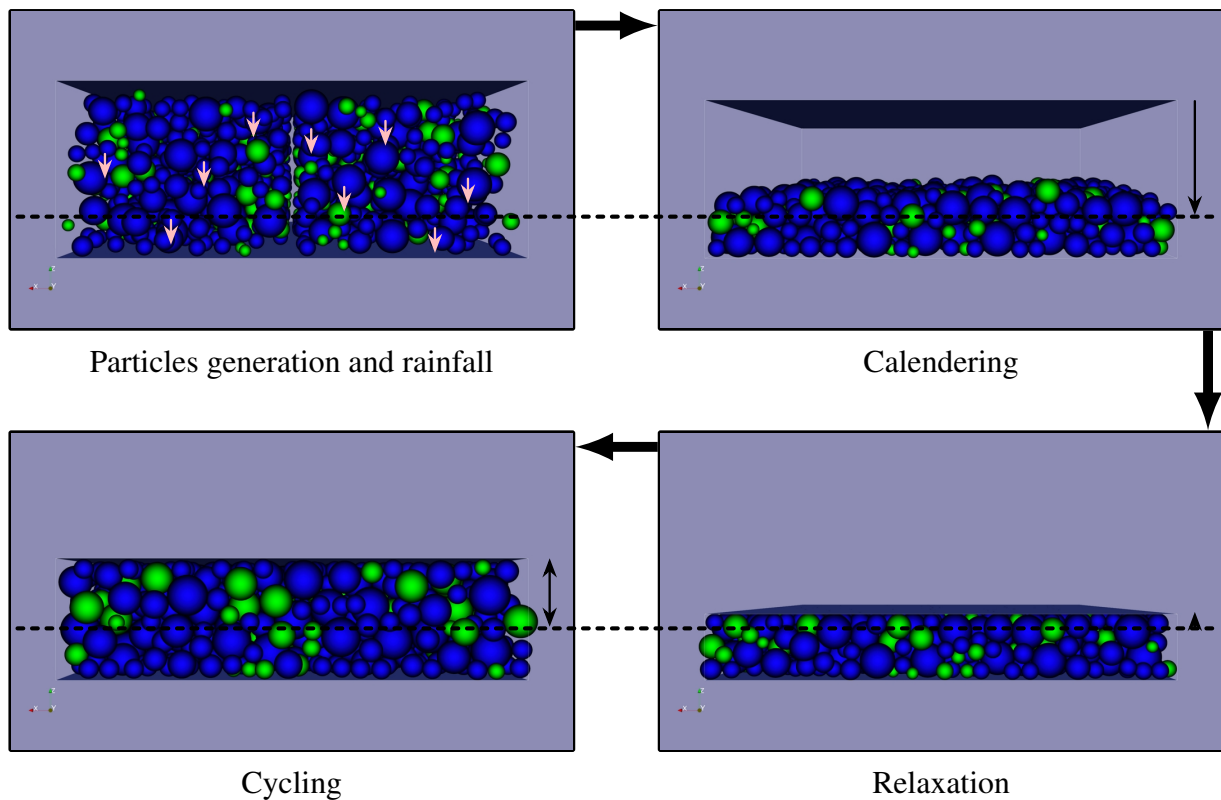


Figure 2.4: Phases of a simulation. From start to end: generation of particles and rainfall, **calendering** (compression at th_{cal} , horizontal dashed line), **relaxation** (relaxation of particles bed and stabilisation at input pressure), **cycling** (breathing of particles). Dashed line represents the calendering thickness (th_{cal}).

2.2.2 Level two: variation of studied parameter

The basic strategy of a sensitivity analysis consists in applying a set of N_{values} different values for the studied parameter on the DAM reference sample. Thus, N_{values} simulations are necessary, and each simulation is differentiated from others by the value of the studied parameters. This set of simulations is called a “**sensitivity series**”. However, an important aspect should be underlined: depending on the studied parameter, the instant when this parameter is set can change. It means that, for example, when the parameter is set at the middle of all simulations, the results must be identical during the first half. In our case, the studied parameter can be set during the particles’ generation, just before the relaxation, or just after. This gives birth to three types of sensitivity series, differentiated by their “fork” structure, as represented in Fig. 2.5. Each is defined by a different instant at which the sensitivity analysis parameter is set:

- The “**pre-calendering**” series (setting before calendering phase, at the beginning of simulation)
- The “**pre-relaxation**” series (setting between calendering and relaxation phases)
- The “**post-relaxation**” series (setting between relaxation and cycling phases)

2.2.3 Level three: multi-sensitivity-analysis tree

Despite the sensitivity analysis of a given parameter, the initial particles distribution presents a non-negligible statistical dispersion. In this optic, a systematic statistical analysis was carried out by multiplying the sensitivity analysis (“fork” structure) N_{draws} times in order to create a “**statistical series**”, as schemed in Fig. 2.6. At each “fork” structure (a, b, c, etc.), the randomness of particles generation is changed in order to create a different bed that still match the particle-size-distribution but with a different initial positions. As a result, a global statistical series is composed of $N_{\text{draws}} \times N_{\text{values}}$ simulations, where N_{draws} has been fixed to 10. Finally, the final quantity displayed for results is obtained by a branch-to-branch statistical merging, converted to a mean/standard deviation pair. By posing $\bar{i} \in \llbracket 1, N_{\text{values}} \rrbracket \equiv \llbracket 1, 2, 3, \dots \rrbracket$ the index of the studied parameter

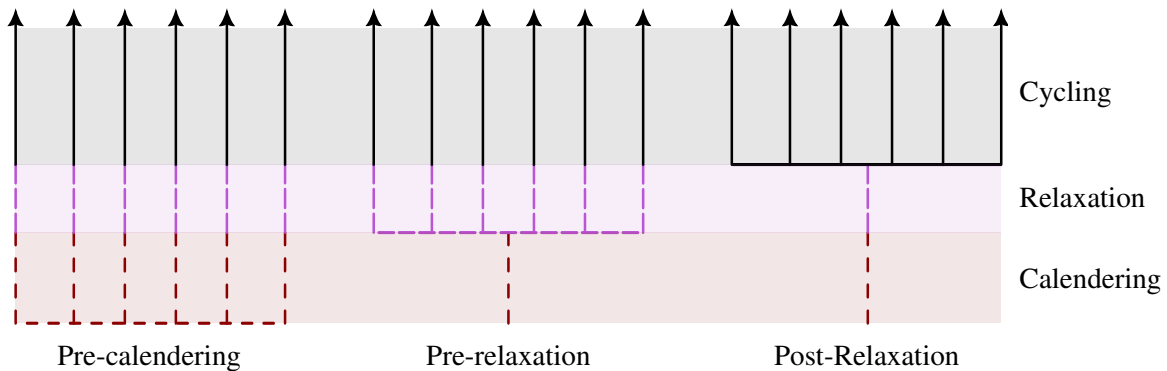


Figure 2.5: Scheme of simulation “fork” structure configurations. Each arrow represent a simulation: the orientation gives the time direction — *Pre-calendering*: setting of studied parameter before calendering phase, *Pre-relaxation*: setting of studied parameter between calendering and relaxation phases, *Post-relaxation*: setting of studied parameter between relaxation and cycling phases.

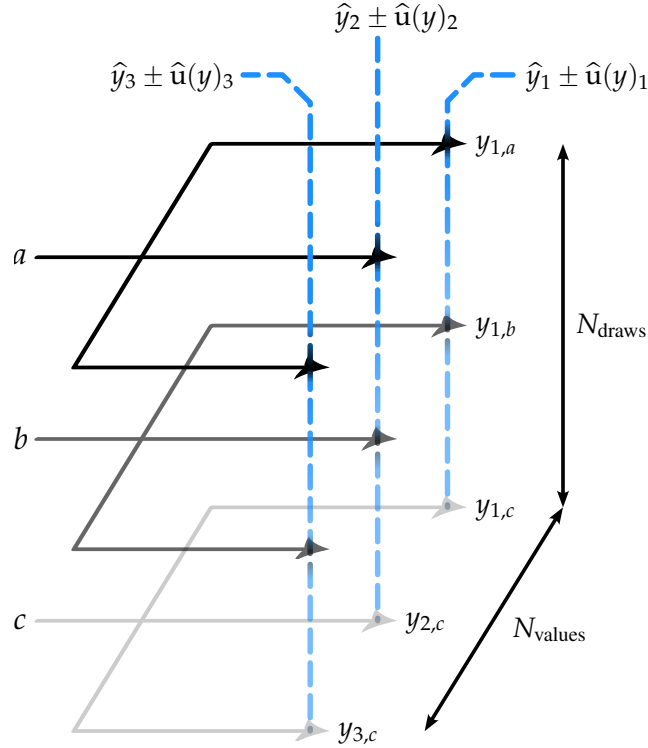


Figure 2.6: Scheme of multi-sensitivity-analysis tree for statistical analysis. N_{values} calculations done by varying a physical parameter, N_{draws} sensitivity series done by varying the initial random particle distribution.

(number subscripts in Fig. 2.6) and $\bar{j} \in \llbracket 1, N_{draws} \rrbracket \equiv \llbracket a, b, c, \dots \rrbracket$ the index of the sensitivity analysis (letter subscripts in Fig. 2.6), it means:

$$y_{\bar{i}} = \hat{y}_{\bar{i}} \pm \hat{u}(y_{\bar{i}}) \quad (2.6)$$

Where $\hat{y}_{\bar{i}}$ represents the mean value and $\hat{u}(y_{\bar{i}})$ the absolute uncertainty of the variable $y_{\bar{i}}$. They are more precisely defined through the standard mean/standard deviation formulæ:

$$\left\{ \begin{array}{l} \hat{y}_{\bar{i}} = \frac{1}{N_{draws}} \sum_{\bar{j}=1}^{N_{draws}} y_{\bar{i},\bar{j}} \\ \hat{u}(y_{\bar{i}}) = \sqrt{\frac{1}{N_{draws}} \sum_{\bar{j}=1}^{N_{draws}} (y_{\bar{i},\bar{j}} - \hat{y}_{\bar{i}})^2} \end{array} \right. \quad (2.7)$$

2.3 Implementation of electrochemistry

2.3.1 Breathing law introduction

2.3.1.a Definition

We still have to keep in mind that, despite the description of the anode microstructure through DEM, the electrochemistry remains at the core of the studied technology. By consequence, the implementation of electrochemistry within the DAM is necessary. To come back at the core of the subject, which is breathing of the

particles, we then have to find a way to establish breathing laws of particles based on electrochemical perspectives. More precisely, from a DEM perspective, a “breathing law” is an equation that evaluates, at each time step, the volume of a given particle. Of course, from an electrochemical perspective, the volume is lithium content dependent and this is the main point of the following electrochemical development.

To develop this, let us state the Set of Hypothesis 2.B:

- (i) **The material of a particle is pure and homogeneous:** each Si/C particle is composed of silicon and carbon black only and each Gr particle is composed of graphite only. Consequently, the swelling of Si/C follows a mixture law of silicon (Si) swelling and carbon black (C) swelling.
- (ii) **All the particles are at the equilibrium potential:** the potential of each particle is equal to all other particles potential.
- (iii) **The lithiation of particles bed is homogeneous:** all particles lithiate and delithiate synchronously, without any delay due to position.
- (iv) **The carbon of Si/C composite is electrochemically passive:** only silicon and graphite lithiate and delithiate due to the negligible capacity of carbon. Consequently, the carbon black (C) breathing is null.
- (v) **Galvanostatic charge and discharge:** the anode is charged and discharged at constant current.
- (vi) **The active materials (Si and Gr) are supposed fully delithiated at the initial time.**

Now, let us consider a material λ that represents Si/C or Gr. By supposing Hyp. 2.B.i (page 84), the electrochemical equation of this particle would be the same as any other one of same material, but not necessarily their volume. It is then reasonable to generalise the volume of this particle to a dimensionless volume that we will call “**relative volume**”, defined as:

$$v_{\lambda}(t) = \frac{V_{\lambda}(t)}{V_{\lambda_0}} \quad (2.8)$$

Similarly, for the particular case of a spherical particle, we can define a “**relative diameter**”:

$$d_{\lambda}(t) = \frac{D_{\lambda}(t)}{D_{\lambda_0}} \quad (2.9)$$

In this case, due to cubic relationship, both breathing laws are directly equivalent:

$$d_{\lambda} = \sqrt[3]{v_{\lambda}} \quad (2.10)$$

Both v_{λ} and d_{λ} relative parameters are then strictly positive numbers whose value is equal to 1 at $t = 0$ s. This constitutes a good point to start the building of our first law: the linear breathing law.

2.3.1.b Linear breathing law

The linear breathing law consists in considering at least one of the relative parameters v_{λ} and d_{λ} linear over the time. For our case, it is more relevant to consider the volume as linear, due to Hyp. 2.B.v (page 84) of charge/discharge constant current. Moreover, a linear function of breathing is nothing else than a triangular function whose period and amplitude values are adapted to fit the problem. Thus, it comes:

$$v_{\lambda}(t) = v_1 + v_2 \text{tri}_F(t) \quad (2.11)$$

Where tri_F is the triangular signal of period F and amplitude 1 and:

$$\begin{cases} v_{\lambda}(0) = 1 = v_1 \\ v_{\lambda}\left(\frac{F}{2}\right) = v_{\lambda,\max} = v_1 + v_2 \end{cases} \implies \begin{cases} v_1 = 1 \\ v_2 = v_{\lambda,\max} - 1 \end{cases} \quad (2.12)$$

So it finally gives the final form:

$$v_{\lambda}(t) = 1 + 2(v_{\lambda,\max} - 1) \left| \frac{t}{F} - \left[\frac{t}{F} + \frac{1}{2} \right] \right| \quad (2.13)$$

Where $v_{\lambda,\max}$ is the maximum value of v_{λ} . The computation for the relative diameter is then directly obtain through:

$$d_{\lambda}(t) = \sqrt[3]{1 + 2(v_{\lambda,\max} - 1) \left| \frac{t}{F} - \left[\frac{t}{F} + \frac{1}{2} \right] \right|} \quad (2.14)$$

On one hand, as it is further explained in Section 2.4.3, the value of the period is physically meaningless and can be reduced as long as the dynamics remain quasi-static. On the other hand, the estimation of $v_{\lambda,\max}$ is much harder to estimate precisely and require deeper electrochemical perspective. To do so, the following sections develop the home-made model used to compute the complete electrochemical breathing law, from which we can derive the value of $v_{\lambda,\max}$.

2.3.2 Naming conventions

2.3.2.a Capacity

The capacity of a battery indicates the amount of current a battery can supply over time. It can be expressed absolutely (Ah) or specifically in weight or volume (Ah/kg or Ah/m³). For reasons of clarity, the notation Q is used to designate an absolute capacity (Ah) and the notation C for a specific weight capacity (Ah/kg).

2.3.2.b Material designations and weight fractions

The definition of a weight fraction necessarily goes with the definition of a mass of reference (denominator mass of the fraction). In order to use a clean mathematical notation for equations, it is proposed to state the following convention of a weight fraction variable name: an upper case Greek letter that corresponds to a defined group of materials (denominator mass), then a subscript lower case Greek letter that corresponds to the concerned material (numerator mass). Thus, different definitions of weight fraction can rise from this convention, depending on the group of material. Here, the particles of the DAM are restrained to the following materials: silicon, carbon black and graphite. It means that the mass of all other components (binder, electrolyte, etc.) are not considered in weight fractions. We can define these following combinations of weight fraction:

- α and A are related to all studied material (Si, C, Si/C or Gr)
- β and B are related to silicon composite materials (Si or C)
- γ is related to active materials (Si or Gr)
- λ is related to silicon composite and graphite (Si/C or Gr)

In these notations, we have to read:

- $\alpha \in \{\text{Si, C, CSi, Gr}\}$, A is composed by Si + C + Gr
- $\beta \in \{\text{Si, C}\}$, B is composed by Si + C
- $\gamma \in \{\text{Si, Gr}\}$
- $\lambda \in \{\text{Si/C, Gr}\}$

By extension of these notations, we define two main types of weight fraction: the “global weight fraction” (Si/C/Gr mass at denominator) and the “composite weight fraction” (Si/C mass at the denominator).

The “global weight fraction” is then defined by:

$$A_\alpha = \frac{m_\alpha}{m_{\text{Si}} + m_{\text{C}} + m_{\text{Gr}}} = \frac{m_\alpha}{m_A} \quad (2.15)$$

And the “composite weight fraction” by:

$$B_\beta = \frac{m_\beta}{m_{\text{Si}} + m_{\text{C}}} = \frac{m_\beta}{m_B} \quad (2.16)$$

As it was detailed in Table 2.1, we have for the DAM reference sample $A_{\text{Si}} = 5\text{wt}\%$ and $B_{\text{Si}} = 50\text{wt}\%$. These definitions give an interesting condition on A_{Si} and B_{Si} , because:

$$A_{\text{Si}} = \frac{B_{\text{Si}}}{1 + \frac{m_{\text{Gr}}}{m_{\text{Si}} + m_{\text{C}}}} \implies \frac{m_{\text{Gr}}}{m_{\text{Si}} + m_{\text{C}}} = \frac{B_{\text{Si}}}{A_{\text{Si}}} - 1 \quad (2.17)$$

Hence, to respect the positiveness of the mass ratio, we necessarily have:

$$A_{\text{Si}} \leq B_{\text{Si}} \quad (2.18)$$

When $A_{\text{Si}} = B_{\text{Si}}$, the anode is in full Si/C composition (no graphite at all).

2.3.2.c Volume fractions

Using the same logic, some equations developed in the following sections require equivalent fraction but in volume, noted here with a supplementary V in superscript. Using the same structure of Eq. (2.15), we get the volume fraction of Si/C in Si/C/Gr:

$$A_{\text{CSi}}^V = \frac{V_{\text{CSi}}}{V_{\text{Si}} + V_{\text{C}} + V_{\text{Gr}}} = \frac{V_{\text{CSi}}}{V_{\text{CSi}} + V_{\text{Gr}}} = \frac{1}{1 + \frac{\rho_{\text{CSi}} m_{\text{Gr}}}{\rho_{\text{Gr}} m_{\text{CSi}}}} \quad (2.19)$$

And by using Eq. (2.17), it comes:

$$A_{\text{CSi}}^V = \frac{1}{1 + \frac{\rho_{\text{CSi}}}{\rho_{\text{Gr}}} \left(\frac{B_{\text{Si}}}{A_{\text{Si}}} - 1 \right)} \quad (2.20)$$

2.3.2.d Lithium content

Usually noted x , the “**lithium content**” (or “Li content”, also called “lithium concentration”) is a positive number that designates, for a given active material (here, Si or Gr), the atomic ratio of lithium within this material. For the silicon, the proportion is defined by the formula Li_xSi and the amount of lithium can reach a theoretical amount of $x = 4.4$ [29], [31], [32], [42]. Of course, this value remains theoretical and reaching it requires specific experimental conditions. It mainly constitutes here a physical point of reference independent of temperature. For the graphite, the proportion is defined by the formula Li_xC_6 , and the theoretical maximum stated by electrochemical is $x = 1$ [31]. Consequently, the ranges of Li are:

$$\begin{cases} 0 \leq x \leq 4.4 = x_{\text{Si,max,theory}} & \text{in } \text{Li}_x\text{Si} \\ 0 \leq x \leq 1 = x_{\text{Gr,max,theory}} & \text{in } \text{Li}_x\text{C}_6 \end{cases} \quad (2.21)$$

Here, the “C” of Li_xC_6 represents the carbon of graphite (and not carbon black of Si/C composite). The advantage of lithium content is its direct link to the component capacity. Indeed:

$$\text{Li}_{x_\gamma} \gamma_{y_\gamma} \implies \frac{J_{\text{Li}}}{x_\gamma} = \frac{J_\gamma}{y_\gamma} \implies J_{\text{Li}} = \frac{x_\gamma J_\gamma}{y_\gamma} \quad (2.22)$$

Because one atom of lithium represents one electronic charge stored, the total weight capacity is given by:

$$C_\gamma = \frac{J_{\text{Li}} e^- \Lambda}{m_\gamma} = \frac{x_\gamma J_\gamma e^- \Lambda}{y_\gamma m_\gamma} = \frac{x_\gamma e^- \Lambda}{y_\gamma \eta_\gamma} \quad (2.23)$$

Where e^- is the elementary charge, Λ the Avogadro constant and η_γ the molar mass of the material γ (Si or Gr). Hence, considering the following constants:

- $e^- = 1.602\,176\,634 \times 10^{-19}$ C, [195]
- $\Lambda = 6.022\,140\,76 \times 10^{23}$ mol⁻¹, [195]
- $\eta_{\text{Si}} = 28.085$ g/mol, [196] (average value)
- $\eta_{\text{Gr}} = \eta_{\text{C}} = 12.106$ g/mol, [197] (average value)

And considering the maximum theoretical lithium contents fixed by Eq. (2.21), the maximum theoretical capacities that silicon and graphite can store are respectively:

$$\begin{cases} C_{\text{Si,max,theory}} \simeq 4\,199 \text{ mAh/g} \\ C_{\text{Gr,max,theory}} \simeq 369 \text{ mAh/g} \end{cases} \quad (2.24)$$

Which well represent the values presented in Section 1.1.1.

2.3.3 Electrochemical development

2.3.3.a Relative volume as a function of lithium content

When it comes to the relationship between volume and lithium content for silicon and graphite, the works of Dahn, Beaulieu, Louli *et al.* are generally the first references met in literature, already reintroduced by

Vidal (2021) [40]. The paper of Louli *et al.* (2017) [30] is certainly the most complete approach of breathing, proposing a model to calculate the volume expansion of a full cell (including positive electrode), starting from electrochemical properties of electrodes components. For this work, they used previous data generated by the team over the years.

More precisely, the data for silicon was extracted from Beaulieu *et al.* (2003) [42] where is reported the volume change of various active material films (crystalline aluminium, crystalline tin, amorphous silicon, and silicon/tin compound), revealing an almost linear evolution of the relative volume as a function of the lithium content. Moreover, the data for graphite are extracted from Dahn (1991) [198], where the author focuses on the phases of Li_xC_6 for a lithium content x going from 0 to 0.5. Finally, the data for graphite for the second half lithium content range (until full lithiated) come from a previous work, Dahn *et al.* (1990) [199].

Exploring further the literature, many other references exist about this type of data. Unfortunately, they mostly explore the silicon behaviour, and not the graphite, and the results are not perfectly consistent with each other. Above all, they reveal a higher complexity than a simple linearity of volume expansion. For example, Jerliu *et al.* (2014) [32] made an *in-operando* neutron reflectometry observation on an amorphous silicon film, galvanostatically lithiated (at constant current) and for two different thicknesses. They observed a clear linear evolution of relative volume, with initial size independence, with divergent values from Louli *et al.* (for $x_{\text{Si}} = 1.7$: Louli *et al.* $\rightarrow v_{\text{Si}} \simeq 1.98$, Jerliu *et al.* $\rightarrow v_{\text{Si}} \simeq 2.5$). In addition, Huang & Zhu (2011) [31] approached the issue by using molecular orbital theory. They found a similar swelling behaviour than in Beaulieu *et al.* (2003) [42], with a short plateau at the initiation of the charge ($x_{\text{Si}} < 0.8$) followed by an almost linear relative volume. However, Beaulieu *et al.* (2013) [42] results plotted in Huang & Zhu (2011) [31] do not fit with the values of the original paper, which is questionable. Dong *et al.* (2019) [29] focused on the observation of spherical particles of silicon using synchrotron X-ray imaging for different size of particles. They showed similar variations of diameters with Beaulieu *et al.* (2003) [42] results, but with inconsistent values (for $x_{\text{Si}} = 3.2$: Louli *et al.* $\rightarrow v_{\text{Si}} \simeq 3$, Dong *et al.* $\rightarrow v_{\text{Si}} \simeq 2.32$). They also noticed post-charge particle growth, even during delithiation, and most importantly an influence of the initial particle size on the relative volume (the smaller the particle, the less it swells). Recently, Schmidt *et al.* (2020) [44] precisely observed the volume expansion of silicon using *in-operando* neutron reflectometry during a potentiostatic lithiation (constant potential) of an Si active layer, obtaining a maximum relative volume of 3.25 for a Li content of 3.1 (2.91 for Louli *et al.* at this Li content), at a potential of 0.06 V. They especially noticed a non-linear evolution, in contrast to galvanostatic lithiation. About graphite, Qi *et al.* (2010) [188] used a computation method to study the influence of lithium content on Young's modulus and Poisson's ratio of lithiated graphite at different phases. They also plotted the evolution of the interlayer spacing as a function of x_{Gr} . They obtained a global spacing expansion of around 8%, which is close to the result for volume presented by Dahn (1990) [199]. However, the evolution does not show a significant plateau, certainly because of other parameters that could influence the total volume, such as the diameter.

All these examples shows how hard it is to measure the volume expansion of pure silicon or graphite, facing a very low scale phenomenon confronted to many other phenomena and uncertainties (SEI formation, material impurity, indirect measurement of Li content...). This electrochemical approach also suffers from a lack of notation conventions, engendering several uncertain references. For example, the initial volume in relative volume formula is never clearly specified (volume of pure material or volume after a first lithiation and SEI for-

mation?). In addition, when it is used, the state of charge is incompletely described (*i.e.* the minimum/maximum capacities of the cell are not detailed), engendering a misunderstanding of the meaning of 0 and 1. Finally, the volume expansion is expressed in different ways (expansion rate superior to one, percentage superior to zero, indirect parameter such as diameter, etc.), making the data difficult to compare and more subject to mistakes.

Similarly to Vidal (2021) [40], it was decided to take the data from Louli *et al.* (2017) [30] and approximate the curves to global observations revealed in literature (linear for Si and presence of typical plateau for Gr). The curves in Fig. 2.7 plot the related data. Let us notice that this data defines v_γ (related to Si and Gr) and not v_λ (related to Si/C and Gr), the required relative volume. To extend the definition, we have to make an equivalency for the silicon composite.

Thanks to Eq. (2.16), we can link the volume of carbon black to the volume of silicon:

$$V_C = \frac{m_{Si}(1 - B_{Si})}{\rho_C B_{Si}} \quad (2.25)$$

The volume V_C remains constant due to Hyp. 2.B.iv (page 84). Concerning the silicon, we can define two volumes: $V_{Si,0}$, the initial delithiated volume, and V_{Si} , the lithiated volume:

$$V_{Si} = v_{Si} V_{Si,0} = v_{Si} \frac{m_{Si}}{\rho_{Si}} \quad (2.26)$$

Moreover, at any time, the relative volume of silicon composite is defined as:

$$v_{Cs_i} = \frac{V_{Si} + V_{C,0}}{V_{Si,0} + V_{C,0}} \quad (2.27)$$

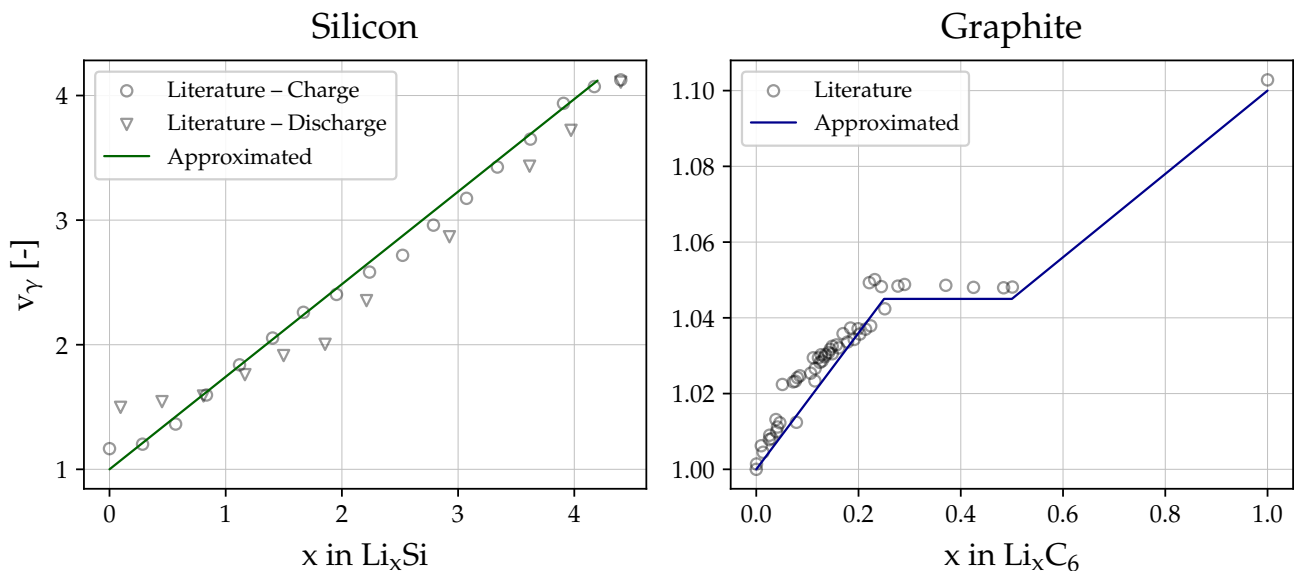


Figure 2.7: Relative volumes of silicon and graphite as a function of lithium content, raw literature data and approximated functions. Literature data based on Beaulieu *et al.* (2003) [42] for silicon and Dahn (1990) [199] and Dahn *et al.* (1991) [198] for graphite.

Where the carbon black volume ($V_{C,0}$) is supposed constant due to Hyp. 2.B.iv (page 84). Then, by injecting Eq. (2.25) and Eq. (2.26) in Eq. (2.27), we get:

$$v_{CSi} = \frac{B_{Si} \rho_C v_{Si} + \rho_{Si}(1 - B_{Si})}{B_{Si} \rho_C + \rho_{Si}(1 - B_{Si})} \quad (2.28)$$

2.3.3.b Lithium content as a function of potential

This relationship is intrinsically linked to a curve type commonly used in electrochemistry: the Open Circuit Voltage (OCV) curve. It represents the potential of a component as a function of its capacity, its state of lithiation, its state of charge or its lithium content.

The CEA already measured several OCV of anode components, extracted from the Anastasia Project performed with the partner Umicore and measured with the device used in Chapter 4. More precisely, this data is expressed as function of the state of charge, considering the maximum as the maximum value reached during experiment. In practice, an OCV curve is obtained by measuring two physical quantities: the potential (with pure lithium as reference) and the charged/discharged capacity of cell component during measurement of potential. In our case, the cell was submitted to a constant current. Hence, the capacity on x-axis has a zero value fixed by the initial state of the component. Thus, the zero value of an OCV curve does not necessarily correspond to a given state of lithiation, so major parameters are missing: the initial and final lithium content of the component that we will note $x_{y,\min}$ and $x_{y,\max}$.

To solve these issues, a point can be noticed: by looking the results of Dahn (1991) [198] and Beaulieu *et al.* (2003) [42], we can approximate the characteristic potential of both silicon and graphite for their full delithiated state, around 1.2 V. This indicates that if an OCV curves presents a potential of 1.2 V, the associated value of capacity/state of charge corresponds to the delithiated state one (and the sub-amount of capacity is a parasitic data, engendered by interaction with other materials during the experiment).

Yet, it is possible that some OCV curve do not present this potential. For example, the available curve for silicon during lithiation has a maximum potential of around 0.86 V (whereas it is expected to be 1.2 V). In fact, the reason is that during the first charge, the very first introduction of lithium within silicon implies a very fast decrease of the voltage, as we can see in Beaulieu *et al.* (2003) [42]. Consequently, for this curve, the zero can be approximated to the fully delithiated state. Furthermore, concerning the maximum lithium contents, they are approximated based on measurements of integrated current during lithiation/delithiation. For the silicon, this value is around 2,650 mAh/g, and for graphite, 358 mAh/g. We can notice that the maximum weight capacity for graphite is quite close from the maximum theoretical value ($C_{Gr,\max,theory} = 369$ mAh/g). However, the value for silicon is quite lower than the theoretical value ($C_{Si,\max,theory} = 4,199$ mAh/g). In practice, this theoretical value is unreachable at room temperature and the maximum reached during OCV is around 3,580 mAh/g. Furthermore, to reach this value, it is necessary to highly lower the material potential (around 5 mV), a value rarely reached in practice (the minimum voltage used in the whole thesis being 10 mV). In addition, the silicon within Si/C is not pure, often covered by a layer of silicon dioxide (SiO_2 , also called "silica"), which also decreases the active amount of silicon. For all these reasons, it was decided to simplify the OCV to values closer to application. It then engendered the following Set of Hypothesis 2.C:

- (i) For the lithiation OCV curve of silicon, the point at lowest state of charge is considered as the fully delithiated state ($x_{\text{Si},\text{min}} = 0$)
- (ii) For the delithiation OCV curve of silicon, the point at $U = 1.2$ V is considered as the fully delithiated state ($x_{\text{Si},\text{min}} = 0$)
- (iii) For the OCV curve of graphite, the point at $U = 1.2$ V is considered as the fully delithiated state ($x_{\text{Gr},\text{min}} = 0$)
- (iv) For the OCV curve of silicon, the point at $U = 0$ V corresponds to a weight capacity of 2,650 mAh/g ($x_{\text{Si},\text{max}} \simeq 2.78$)
- (v) For the OCV curve of graphite, the point at $U = 0$ V corresponds to a weight capacity of 358 mAh/g ($x_{\text{Gr},\text{max}} \simeq 0.97$)

It finally gives the OCV curves showed in Fig. 2.8.

2.3.3.c Potential smoothing

Nevertheless, when it comes to computation of potential, an issue appears at the end of charge or discharge, more precisely concerning the silicon potential. Indeed, looking at Figure 8 in Beaulieu *et al.* (2003) [42] make us confident about the existence of a hysteresis between the lithiation and delithiation OCV curves of silicon. Undoubtedly, at the end of each phase, the potential does not “jump” from a curve to another. Unfortunately, by lack of time, the transition model between both curves was not built on rigorous physics. Instead, a virtual transition between them was made using a home-made “transitional function” ϑ_ζ . It consists in a function whose source and target sets are both equal to $[0, 1]$, defined as:

$$\begin{aligned} \vartheta_\zeta : [0, 1] \times \mathbb{R}_+^* &\longrightarrow [0, 1] \\ (X, \zeta) &\longrightarrow X(1 - X)^\zeta + (1 - X) \left(1 - X^{\frac{1}{\zeta}}\right) \end{aligned} \quad (2.29)$$

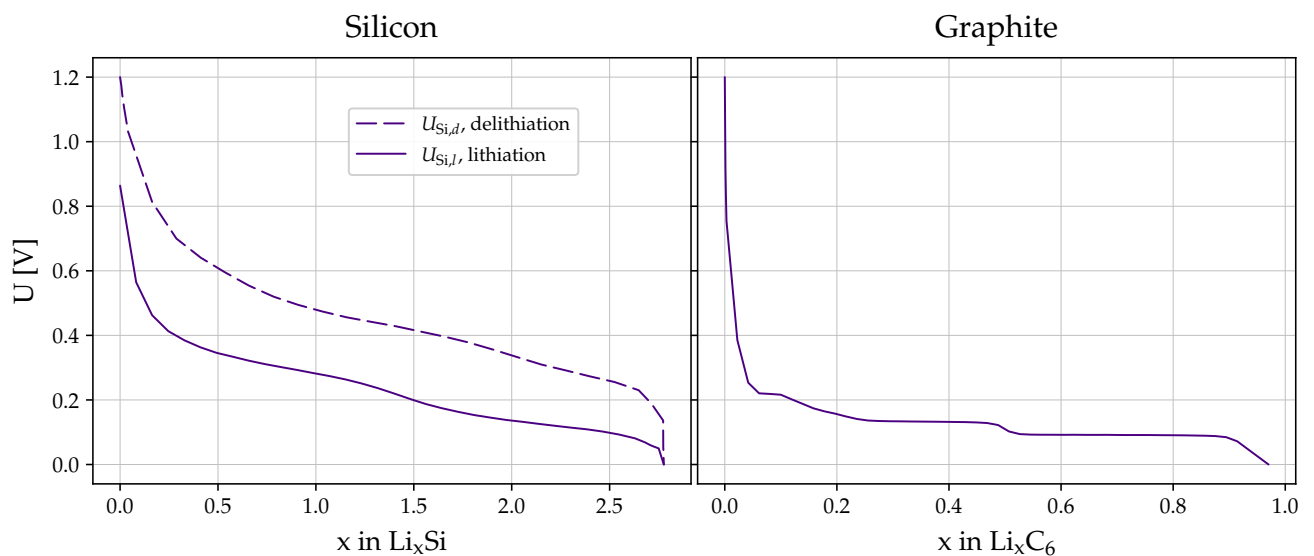


Figure 2.8: OCV curves of silicon ($U_{\text{Si},l}$ and $U_{\text{Si},d}$) and graphite (U_{Gr}).

The advantage of this application the controllability of the smoothness via the “smooth factor” ζ . As Fig. 2.9a demonstrates, several values of ζ enables to create from an instantaneous jump at the end ($\zeta \rightarrow 0$) to and instantaneous jump at the beginning ($\zeta \rightarrow +\infty$), passing by the pure linear transition ($\zeta = 1$). Of course, the terms “beginning” and “end” do not mean anything without clear definition. In our electrochemical application, they correspond to minimum and maximum lithium contents $x_{\text{Si,min}}$ and $x_{\text{Si,max}}$, and the variable X is a linear increase of x between minimum and maximum values $x \in [x_{\text{Si,min}}, x_{\text{Si,max}}]$. Consequently, the transitional OCV curve of silicon is defined via a linear composition of both lithiation / delithiation OCV curves:

$$U_{\text{Si}}(x) = U_{\text{Si},d}(x) \vartheta_{\zeta} \left(\frac{x - x_{\text{Si,min}}}{x_{\text{Si,max}} - x_{\text{Si,min}}} \right) + U_{\text{Si},l}(x) \left[1 - \vartheta_{\zeta} \left(\frac{x - x_{\text{Si,min}}}{x_{\text{Si,max}} - x_{\text{Si,min}}} \right) \right] \quad (2.30)$$

Where $x \in [x_{\text{Si,min}}, x_{\text{Si,max}}]$. For example, by making a cycling between potential 0.1 and 0.6 V, we obtain $x_{\text{Si,min}} = 0.52$ and $x_{\text{Si,max}} = 2.48$. Finally, the potential hysteresis is set through the reversing of ζ depending on the charge/discharge state. For example, for a given input value ζ_{input} superior to 1, we have:

$$\zeta = \begin{cases} \zeta_{\text{input}} & , \text{if charge} \\ 1/\zeta_{\text{input}} & , \text{if discharge} \end{cases} \quad (2.31)$$

As an example, Fig. 2.9b shows the resulting smoothed potential of the anode considering a smooth factor $\zeta_{\text{input}} = 10$, with potential varying between 0.1 and 0.6 V. In practice, the potential range is larger, and the potential varies between 0.01 and 1 V.

2.3.3.d Potential as a function of capacity

Even if the OCV curves may seem not useful at first consideration, they are in reality essential to create a relationship between both lithium contents (x_{Si} and x_{Gr}). To understand this fact, let us make a total capacity balance on all studied materials:

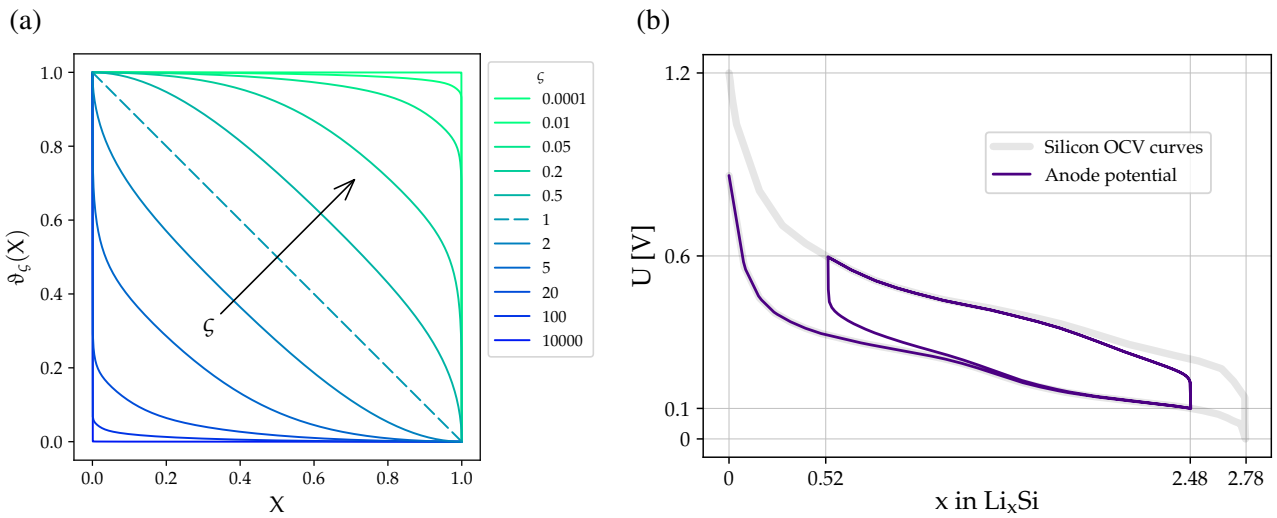


Figure 2.9: Exploitation of transitional function ϑ_{ζ} — **a)** Evaluation of transitional function over several values of smoothing factor ζ . **b)** Example of transitional function for potential smoothing with $\zeta_{\text{in}} = 10$.

$$Q_A = Q_{Si} + Q_{Gr} = m_{Si} C_{Si} + m_{Gr} C_{Gr} = m_{an} A_{Si} \frac{e^- \Lambda x_{Si}}{y_{Si} \eta_{Si}} + m_{an} A_{Gr} \frac{e^- \Lambda x_{Gr}}{y_{Gr} \eta_{Gr}} \quad (2.32)$$

Once again, e^- is the elementary charge, Λ the Avogadro constant and η_y the molar mass of the material y (Si or Gr). The mass m_{an} is the sum of all active materials: $m_{an} = m_{Si} + m_C + m_{Gr}$. By defining the absolute capacity of the anode by:

$$Q_{an} = C_{an} m_{an} \quad (2.33)$$

It comes the following weight capacity of the anode:

$$C_{an} = x_{Si} C'_{Si} + x_{Gr} C'_{Gr} \quad (2.34)$$

With:

$$C'_y = A_y \frac{e^- \Lambda}{y_y \eta_y} \quad (2.35)$$

Where y represents Si or Gr. However, the resolution of Eq. (2.34) is incomplete in itself, because two unknowns are present (x_{Si} and x_{Gr}). This is where the OCV curves are crucial. Indeed, thanks to the potential equilibrium between components stated by Hyp. 2.B.ii (page 84), we have:

$$U_{Si}(x_{Si}) = U_{Gr}(x_{Gr}) \quad (2.36)$$

Fortunately, mathematically speaking, Set of Hypothesis 2.C (page 91) implies that the images of lithiation and delithiation OCV functions of silicon are included in the images of OCV function of graphite. Consequently, we can write the reverse images of the silicon OCV functions and complete Eq. (2.34) that goes to:

$$x_{Si} C'_{Si} + U_{Gr}^{-1}(U_{Si}(x_{Si})) C'_{Gr} - C_{an} = 0 \quad (2.37)$$

To find x_{Si} , a Newton-Raphson's method of root-finding algorithm (from Python library `scipy`) is used, and the potential non-convergence is corrected by the more recent Brent's method (Brent (1973) [200] from Python library `scipy`). Afterwards, x_{Gr} is simply deduced from OCV curve:

$$x_{Gr} = U_{Gr}^{-1}(U_{Si}(x_{Si})) \quad (2.38)$$

2.3.3.e Capacity / Iterative time relationship

The finale step is to link the problem to time, through the anode weight capacity defined in Eq. (2.34). It is basically an incremental relationship depending on the charging phase (charge or discharge):

$$C_{an}^h = \begin{cases} C_{an}^{h-1} + j \Delta t & , \text{if charge} \\ C_{an}^{h-1} - j \Delta t & , \text{if discharge} \end{cases} \quad (2.39)$$

Where j is the constant current per mass unit in mA/g. And thanks to Hyp. 2.B.vi (page 84), the initial value is fixed at $C_{an}^0 = 0$ mAh/g.

2.3.3.f Electrochemical algorithm and final breathing laws

As a global summary of the previous developments, the electrochemical breathing law is based on the following algorithm. It uses weight fractions of silicon within Si/C and within Si/C/Gr, current per mass unit, and minimum/maximum anode potentials to compute the relative diameters of Si/C and Gr and the anode potential.

Algorithm 1: ELECTROCHEMICAL BREATHING LAW ALGORITHM

Input: A_{Si} , B_{Si} , j , U_{min} , U_{max} , Δt , ζ_{input}

- 1 $x_{Si,min} = U_{Si,d}^{-1}(U_{max})$
- 2 $x_{Si,max} = U_{Si,l}^{-1}(U_{min})$
- 3 $C_{an} = \text{Eq. (2.39)}$, x_{Si} found resolving Eq. (2.37), $x_{Gr} = \text{Eq. (2.38)}$
- 4 $v_\gamma = \text{Fig. 2.7}$, $v_{CSi} = \text{Eq. (2.28)}$, $d_\lambda = \text{Eq. (2.10)}$;

Output: d_{CSi} , d_{Gr} , U_{an}

With an anode potential varying between 0.01 and 1 V, this algorithm gives the relative diameters for both silicon composite and graphite displayed in Fig. 2.10 (solid curves). By taking their maximums, these curves finally give us the values that we initially needed in Section 2.3.1.b:

$$\begin{cases} v_{CSi,max} \simeq 1.916 ; d_{CSi,max} \simeq 1.242 \\ v_{Gr,max} \simeq 1.095 ; d_{Gr,max} \simeq 1.031 \end{cases} \quad (2.40)$$

We can consequently deduce the linear volume laws of the diameter using Eq. (2.14), which gives the dashed curves of Fig. 2.10. As expected, the “linear laws” of diameters are not exactly linear due to the cubic relationship with volume.

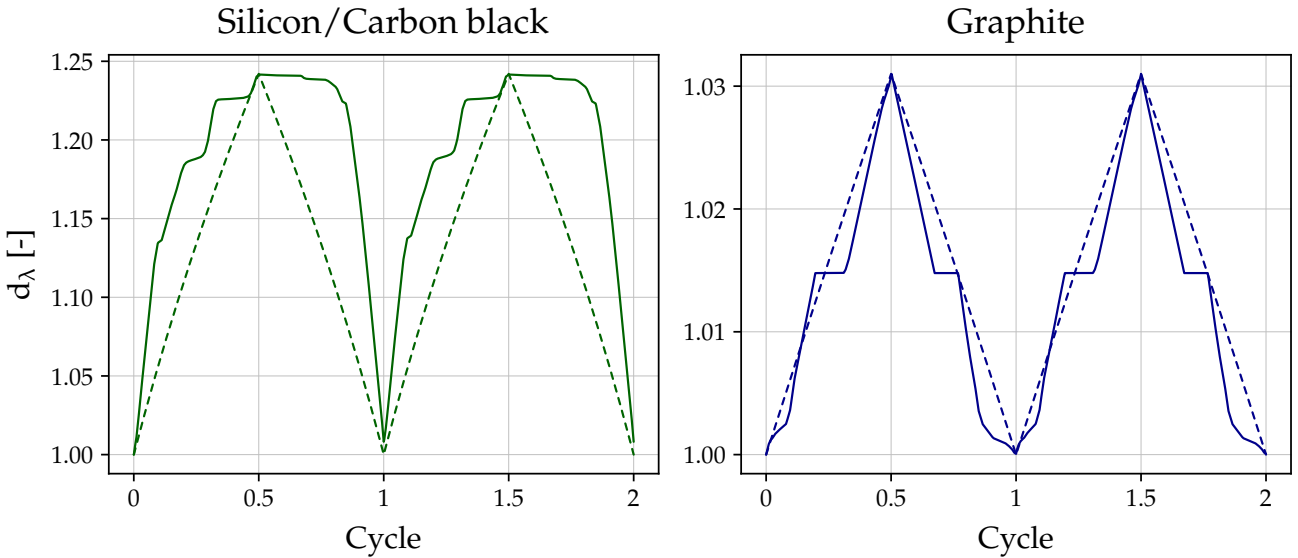


Figure 2.10: Relative diameters of silicon composite and graphite as a function of time (two cycles): electrochemical breathing laws in solid line and linear volume laws in dashed line (the resulting diameter laws are not linear but cubic).

2.3.4 Implementation of virtual irreversibility

The final step of this electrochemical development is the implementation of a virtual irreversibility in the breathing laws. Even it is opposite to Hyp. 2.A.v (page 74), its utility is explained during the results, in Section 3.3.6. The idea is to restrain the breathing to one cycle only and to define an irreversible relative volume $v_{\lambda,irr}$. It gives birth to a “ratio of irreversibility” r_{irr} defined as:

$$r_{irr} = \frac{v_{\lambda,irr}}{v_{\lambda,max} - v_{\lambda}} \in [0, 1] \quad (2.41)$$

As schemed in Fig. 2.11, the new breathing law is defined, during the shrinking phase, as the sum of the initial breathing law and the irreversible breathing law:

$$v'_{\lambda}(t) = v_{\lambda}(t) + v_{\lambda,irr}(t) \quad \forall t \in]F_{cyc}/2, F_{cyc}] \quad (2.42)$$

In other word, whatever if it is linear or electrochemical, the breathing law is changed to:

$$v'_{\lambda}(t) = \begin{cases} v_{\lambda}(t) & , \forall t \in [0, F_{cyc}/2] \\ v_{\lambda}(t) + r_{irr}(v_{\lambda,max} - v_{\lambda}(t)) & , \forall t \in]F_{cyc}/2, F_{cyc}] \end{cases} \quad (2.43)$$

Where we can notice two particular cases:

- When $r_{irr} = 0$, $v'_{\lambda} = v_{\lambda}$
- When $r_{irr} = 1$, $v'_{\lambda} = v_{\lambda,max}$ during shrinking phase

The equivalent form in relative diameter is then:

$$d'_{\lambda}(t) = \begin{cases} d_{\lambda}(t) & , \text{if } t \in [0, F_{cyc}/2] \\ \sqrt[3]{d_{\lambda}^3(t) + r_{irr}(d_{\lambda,max}^3 - d_{\lambda}^3(t))} & , \text{if } t \in]F_{cyc}/2, F_{cyc}] \end{cases} \quad (2.44)$$

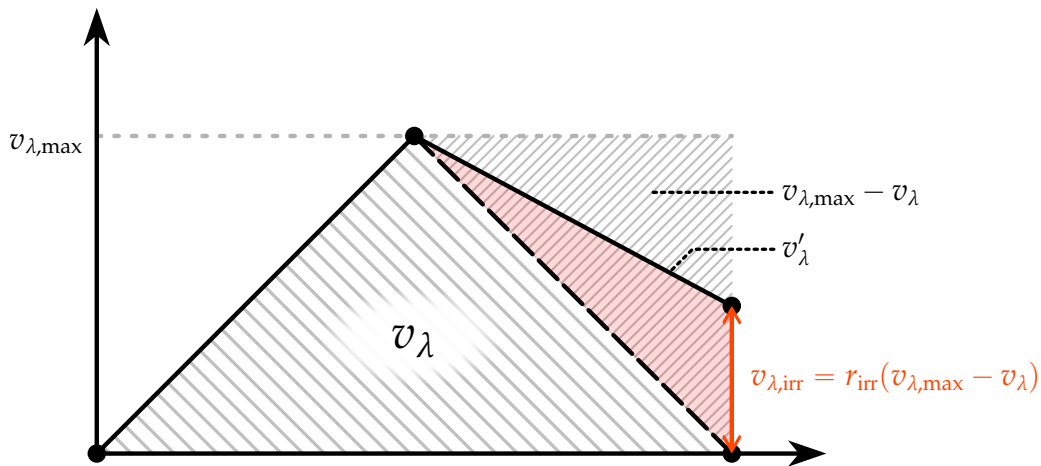


Figure 2.11: Scheme of virtual irreversibility through r_{irr} .

2.4 Parameters of physical evaluation

This section aims to present several dimensionless numbers used to evaluate the physical reliability of DAM or to describe its internal behaviour.

2.4.1 Breathing coefficient

2.4.1.a Introduction to breathing coefficient

The Deltas quantities Δth_{sw} and Δth_{irr} introduced in Section 2.1.1 are interesting to evaluate the raw breathing at electrode scale. However, they miss an important aspect: the transmission of breathing from particles scale to electrode scale. For this reason, it is proposed to reintroduce a notion already introduced in the bibliography of this manuscript: the “swelling coefficient” of Gomadam & Weidner (2005) [60]. In order to diversify the notations, it is proposed to use the Devanagari vowel उ (pronounced [u] using International Phonetic Alphabet notation). As a recall, the volume variation of a breathing porous body is separated into two volume variations:

$$\Delta V_{\text{body}} = \Delta V_{\text{void}} + \Delta V_{\text{solid}} \quad (2.45)$$

Based on this equality, it is proposed here to introduce the “**breathing coefficient**”:

$$\text{उ}_s = \frac{\Delta V_{\text{body}}}{\Delta V_{\text{solid}}} \in \mathbb{R} \quad (2.46)$$

Complementary expressions of this number are possible by exploring the different possible combinations:

$$\text{उ}_v = \frac{\Delta V_{\text{body}}}{\Delta V_{\text{void}}} = \frac{\text{उ}_s}{\text{उ}_s - 1} \in \mathbb{R} \quad (2.47)$$

$$\text{उ}_{vs} = \frac{\Delta V_{\text{solid}}}{\Delta V_{\text{void}}} = \frac{1}{\text{उ}_s - 1} \in \mathbb{R} \quad (2.48)$$

The subscripts have been chosen based on denominator, by considering numerator as body volume variation by default: $s \rightarrow$ body over solid, $v \rightarrow$ body over void, $vs \rightarrow$ solid over void. As an example of interpretation, when उ_s tends towards 1, it means that the volume variation of the body is equal to solid volume variation. In addition, when उ_s tends to 0, it means that the body breathing is null and that the volume variation of solid is fully compensated by the void volume variation. If it tends to 2, it means that the breathing is “balanced”: both solid and void volume variations are equal. However, उ_v is useful to quantify the proportion of breathing that comes from void and उ_{vs} to compare both solid and void volume variations. In a more general way, Table 2.2 guides the interpretation of these numbers.

In the context of electrode breathing, the ideal case would be the “**transfer**” case ($\text{उ}_s = 0$): any solid volume variation is compensated by an opposite void volume variation, and vice versa, implying a null electrode volume variation. The second preferable case is the “**solid breathing**” ($\text{उ}_s = 1$): any solid volume variation is not altered by a supplementary void volume variation. A less desirable case is the “**balanced breathing**” ($\text{उ}_s = 2$): a solid volume variation generates an equal void volume variation. Finally, the extremely unwanted case is the

“**void breathing**” ($\mathfrak{U}_s \rightarrow \pm\infty$): all the electrode volume variation comes a void volume variation. Of course, this case is expected impossible in electrode breathing context, because void is not expected to change by itself.

Limit values	ΔV_{solid} sign	Name	Interpretation
$\mathfrak{U}_s = 0$ $\mathfrak{U}_v = 0$ $\mathfrak{U}_{vs} = -1$	$\Delta V_{\text{solid}} < 0$	Solid transfer	All the solid VV is transferred to the void volume $\Delta V_{\text{solid}} = -\Delta V_{\text{void}}, \Delta V_{\text{body}} = 0 \text{ m}^3$
$\mathfrak{U}_s \rightarrow 1^{+/-}$ $\mathfrak{U}_v \rightarrow +/ - \infty$ $\mathfrak{U}_{vs} \rightarrow +/ - \infty$	/	Solid breathing	All the body VV comes from the solid VV $\Delta V_{\text{body}} = \Delta V_{\text{solid}}, \Delta V_{\text{void}} = 0 \text{ m}^3$
$\mathfrak{U}_s = 2$ $\mathfrak{U}_v = 2$ $\mathfrak{U}_{vs} = 1$	/	Balanced breathing	Solid VV is equal to void VV $\Delta V_{\text{solid}} = \Delta V_{\text{void}}$
$\mathfrak{U}_s \rightarrow +/ - \infty$ $\mathfrak{U}_v \rightarrow 1^{+/-}$ $\mathfrak{U}_{vs} \rightarrow 0^{+/-}$	/	Void breathing	All the body VV comes from the void VV $\Delta V_{\text{body}} = \Delta V_{\text{void}}, \Delta V_{\text{solid}} = 0 \text{ m}^3$

Table 2.2: Breathing coefficient interpretation guides — VV: Volume variation

2.4.1.b Breathing coefficient validity in DAM

In the particular case of the DAM, Eq. (2.45) becomes:

$$\Delta V_{\text{anode}} = \Delta V_{\text{void}} + \Delta V_{\text{particles}} - \Delta V_{\text{overlaps}} \quad (2.49)$$

Where we have $\Delta V_{\text{anode}} = \Delta V_{\text{body}}$. In addition, due to overlapped volume of particles, the particles volume variation exceeds more or less the solid volume variation, which explains the correction $\Delta V_{\text{solid}} = \Delta V_{\text{particles}} - \Delta V_{\text{overlaps}}$. Depending on the problem, it is possible that $\Delta V_{\text{overlaps}} \ll \Delta V_{\text{particles}}$, which gives the approximation of $\Delta V_{\text{solid}} \simeq \Delta V_{\text{particles}}$. Several tests were made on the DAM in order to ensure that this simplification was valid. These tests focused on extreme overlapping configurations corresponding met in Chapter 3. For example, an extreme overlapping configuration occurs when the Young’s modulus E is low, the pressure P is high or the work of adhesion W is high. As a result, Table 2.3 summarizes the volumes proportions of overlaps over anode and particles, captured just after the calendering (pre-relaxation) and just after the relaxation (post-relaxation), for different values of P , E and W . Whatever the configuration, at pre-relaxation state, because each change of parameter P , E or W is made at this state, all the proportions are the same. They indicate that

Contact parameters			Overlaps volumes proportions			
P [MPa]	E [GPa]	W [J/m ²]	Pre-relaxation		Post-relaxation	
			$\frac{V_{\text{overlaps}}}{V_{\text{anode}}}$	$\frac{V_{\text{overlaps}}}{V_{\text{particles}}}$	$\frac{V_{\text{overlaps}}}{V_{\text{anode}}}$	$\frac{V_{\text{overlaps}}}{V_{\text{particles}}}$
–	–	–			< 0.01%	< 0.01%
100	–	–	↑	↑	0.32%	0.47%
–	0.1	–	0.21%	0.31%	0.20%	0.30%
–	–	40	↓	↓	0.01%	0.02%
100	0.1	40			5.14%	3.06%

Table 2.3: Overlaps volume analysis during calendaring and relaxation phases. Two states captured: just after calendaring (pre-relaxation) and just after relaxation (post-relaxation). Five configurations of these states are captured, with different extreme overlapping configurations. By default, $P = P_{\text{ref}} = 0.3 \text{ MPa}$, $E_{\text{CSi}} = 45 \text{ MPa}$ / $E_{\text{Gr}} = 15 \text{ MPa}$, $W = 0 \text{ J/m}^2$.

the overlaps volume represent only 0.21% and 0.31% of anode and particles volumes, respectively. Hence, even after the high compression of calendaring, the overlaps volume is quite negligible. However, the conclusions are different at post-relaxation state. For the reference sample configuration (default values of P , E and W), the overlaps volume proportions go under 0.01%. By creating an extreme overlapping configuration through individual change of P , E or W parameters, the overlaps volume is more predominant, from around 0.02% for highest W to 0.47% for highest P . Yet, the overlaps volume is negligible in all these configurations.

These figures much facilitate the use of breathing coefficient. Indeed, because of overlaps volume negligibility, Eq. (2.49) becomes:

$$\Delta V_{\text{anode}} \simeq \Delta V_{\text{void}} + \Delta V_{\text{particles}} \quad (2.50)$$

Thus, the breathing coefficient does not require taking into account the volume variation of overlaps. Of course, this conclusion is restrained to these particular cases. For example, by a combination of all these extreme overlapping configurations (high P , low E and high W), the overlaps volume reach 5.14% of anode volume and 3.06% of particles volume. It means that, on one hand, the overlaps volume becomes non-negligible at all, and on the other hand, the anode volume becomes lower than the particles volume, which constitutes a physical limit of the DEM to simulate anode breathing. Fortunately, this particularly extreme case is never met in this manuscript.

Another interesting point is related to the DEM accuracy when it comes to particles deformation. DEM does not consider particles deformation, the reason why some volume is lost in particles overlaps. In reality, it can be imagined that the “overlapped” volume is not absorbed in overlap but displaced around the contact point, due to surface deformation. Consequently, part of the volume lost in overlap is in fact already present in the void volume. Theoretically, it reduces the mistake made by measuring the void volume directly from electrode volume and particles volume. Because it remains a minor uncertainty, this aspect is not precisely evaluated in this manuscript.

2.4.1.c Application to DAM

Now that the Eq. (2.50) is verified, it is possible to extend the definition of the breathing coefficient to the specific parameters of the DAM. More precisely, it becomes:

$$\mathfrak{Z}_s = \frac{\Delta V_{\text{anode}}}{\Delta V_{\text{CSi}} + \Delta V_{\text{Gr}}} = \frac{S(th - th_0)}{V_{\text{CSi},0}(v_{\text{CSi}} - 1) + V_{\text{Gr},0}(v_{\text{Gr}} - 1)} \quad (2.51)$$

Where S is the surface of the top plate, th_0 the initial electrode thickness at the beginning of cycling, $V_{\text{CSi},0}$ and $V_{\text{Gr},0}$ respectively Si/C and Gr initial particles volumes at the beginning of cycling. This form presents the advantage to necessitate the initial particles volumes only, rather than measuring particles volumes all along the simulation. It is possible to simplify this expression using volume fraction of Si/C within Si/C/Gr (A_{CSi}^V) defined by Eq. (2.20) in Section 2.3.2.c:

$$\mathfrak{Z}_s = \frac{S \Delta th}{V_{\text{part},0} \left(A_{\text{CSi}}^V (v_{\text{CSi}} - 1) + (1 - A_{\text{CSi}}^V) (v_{\text{Gr}} - 1) \right)} \quad (2.52)$$

Where $V_{\text{part},0}$ is the particles volumes (Si/C/Gr) at the beginning of cycling. In order to simplify the expression, let us introduce the “**reduced surface**” through the archaic Greek letter “sampi”:

$$\mathfrak{r} = \frac{S}{A_{\text{CSi}}^V (v_{\text{CSi}} - 1) + (1 - A_{\text{CSi}}^V) (v_{\text{Gr}} - 1)} \leq S \quad (2.53)$$

This parameter does not represent a physic phenomenon but at least gathers all the necessary sample structure parameters (S and A_{CSi}^V) and breathing control parameters (v_{CSi} and v_{Gr}) in one expression. Then, this only constitutes a mathematical reduction term for breathing coefficient expression. Furthermore, a specific attention should be paid concerning the propagation uncertainty, the same uncertainty addressed in Section 2.2.3 due to random particles' generation. Indeed, as the opposite to S , A_{CSi}^V , v_{CSi} and v_{Gr} which are model input, Δth and $V_{\text{part},0}$ are both random-influenced outputs. Then, the breathing coefficient is defined with the following uncertainty:

$$\mathfrak{Z}_s = \hat{\mathfrak{Z}}_s \pm \hat{u}(\mathfrak{Z}_s) \quad (2.54)$$

Where, as in Section 2.2.3, the hat notations designates the uncertainty parameters (mean/standard deviation):

$$\begin{cases} \hat{\mathfrak{Z}}_s = \mathfrak{r} \frac{\widehat{\Delta th}}{\widehat{V_{\text{part},0}}} \\ \hat{u}(\mathfrak{Z}_s) = \hat{\mathfrak{Z}}_s \widehat{u_{\text{rel}}}(\mathfrak{Z}_s) \end{cases} \quad (2.55)$$

With:

$$\widehat{u_{\text{rel}}}(\mathfrak{Z}_s) = \sqrt{\left(\frac{\widehat{u}(\Delta th)}{\widehat{\Delta th}} \right)^2 + \left(\frac{\widehat{u}(V_{\text{part},0})}{\widehat{V_{\text{part},0}}} \right)^2} \quad (2.56)$$

And where $\widehat{V_{\text{part},0}}$ and $\widehat{u}(V_{\text{part},0})$ are computed from the different initial states of a statistical series.

2.4.1.d Swelling and irreversibility breathing coefficients

When considering volume variations corresponding to thickness Deltas (Δth_{sw} and Δth_{irr}), particular expressions of the breathing coefficient appear. For the Delta of swelling Δth_{sw} , the reduced surface takes a particular form, directly based on the maximum relative volumes:

$$\mathcal{V}_{sw} = \frac{S}{A_{CSi}^V (v_{CSi,max} - 1) + (1 - A_{CSi}^V) (v_{Gr,max} - 1)} \quad (2.57)$$

Then, the breathing coefficient associated to swelling is defined by:

$$\mathfrak{V}_{s,sw} = \mathcal{V}_{sw} \frac{\widehat{\Delta th_{sw}}}{V_{part,0}} \left(1 \pm \widehat{u}_{rel}(\mathfrak{V}_{s,sw}) \right) \quad (2.58)$$

For the Delta of irreversibility Δth_{irr} , the definition depends on the context. Indeed, in the case of Hyp. 2.A.v (page 74), at the end of the cycle, the variation of volume of particles is null ($v_{CSi}(F_{cyc}) = v_{Gr}(F_{cyc}) = 1$), hence this is a non-compatible case for the breathing coefficient. Consequently, its irreversibility definition is only available when irreversibility is implemented within breathing laws. Taking the irreversible breathing law v'_λ defined in Eq. (2.43) and by supposing Hyp. 2.A.v (page 74) (constant swelling amplitude) for v_λ , we get:

$$v'_\lambda(F_{cyc}) = 1 + r_{irr}(v_{\lambda,max} - 1) \quad (2.59)$$

So by replacing v_λ by v'_λ , the reduced surface becomes:

$$\mathcal{V}_{irr} = \frac{S}{r_{irr} \left(A_{CSi}^V (v_{CSi,max} - 1) + (1 - A_{CSi}^V) (v_{Gr,max} - 1) \right)} = \frac{\mathcal{V}_{sw}}{r_{irr}} \quad (2.60)$$

Then, the breathing coefficient associated to irreversibility is defined by:

$$\mathfrak{V}_{s,irr} = \frac{\mathcal{V}_{sw}}{r_{irr}} \frac{\widehat{\Delta th_{irr}}}{V_{part,0}} \left(1 \pm \widehat{u}_{rel}(\mathfrak{V}_{s,irr}) \right) \quad (2.61)$$

Both parameters are important as they are often used in the sensitivity analysis in Chapter 3, based on interpretation guidelines detailed in Section 2.4.1.a.

2.4.2 Mean coordination number

In a packed particles bed, an interesting feature to observe is the amount of contacts occurring within this bed. The most simple and common technique to evaluate the level of contact is to measure the average number of contacts. The DEM software LIGGGHTS easily return the “coordination number” (*i.e.* number of contacts) for each particle. Thus, the chosen evaluating parameter is the “**mean coordination number**” (MCN), which corresponds to the mean value of all coordination numbers:

$$\widetilde{MCN} = \frac{1}{N_{part}} \sum_{i=1}^{N_{part}} CN_i \quad (2.62)$$

Where CN_i is the coordination number of the particle i , *i.e.* its number of contacts. The interpretation of this number is then quite intuitive: the higher, the more contacts between particles, and vice versa.

2.4.3 Inertial number

In the Section 2.1.4 about time step, I specified that the long period of charge/discharge required to choose the time step wisely, in order to avoid an unreasonable computation time. Nevertheless, even with a judicious choice of the time step, this is strictly impossible to reach an acceptable computation time.

To obtain an order of magnitude, let us consider the computation time required to simulate one cycle of the DAM reference sample. In real time, this cycle is equal to one hour (which is actually quite fast in practice). We have:

$$T_{\text{compute}} = \hbar \frac{T_{\text{cyc}}}{\Delta t} \quad (2.63)$$

Where $T_{\text{cyc}} = 1\text{h}$ and \hbar is the time necessary for four cores of the cluster to compute one step of the DAM reference sample. Considering the simulations that have been made for this thesis, the order of magnitude was about one hour of computation for around 20 million steps, which gives an approximated value of $\hbar = 180 \mu\text{s}/\text{step}$. As a consequence, by considering the time step defined in Section 2.1.4 ($\Delta t = 2 \text{ ns}$), the resulting computation time for a real-physical-time simulation would be equal to around ten years, which is obviously impracticable.

Solutions are not abundant to solve this issue. The time \hbar is intrinsic to the computation power and correlated to the complexity of the model (mostly the number of particles). As we saw, the time step Δt is physically constrained by the model. In conclusion, for the DAM reference sample, the only solution to reduce the computation time is to decrease T_{cyc} . The mechanical evolution of the electrode during cycling is quasi-static: inertial effects are negligible, as stated in Hyp. 2.A.vi (page 74). Thus, the cycle period T_{cyc} can be reduced without changing the result as long as the inertia remains negligible in the system. To evaluate the inertia, the “**inertial number**” is particularly useful. Noted \tilde{I} in this manuscript, it was introduced by Combe & Roux (2003) [201] to evaluate the dynamic state of a particles bed submitted to a shear flow. By adapting its formulation to maximise it, it comes:

$$\tilde{I} = \dot{\epsilon} \sqrt{\frac{\max_i \left(\frac{m_i}{D_i} \right)}{P_{\min}}} \quad (2.64)$$

Where $\dot{\epsilon}$ is the shear rate. Three main regimes are defined based on the value of this number: quasi-static ($\tilde{I} < 10^{-3}$), dense ($10^{-3} \leq \tilde{I} \leq 10^{-1}$) and collisional ($\tilde{I} > 10^{-1}$). At the origin, this number is used in shear flow case, as in GDR Midi (2004) [202], da Cruz *et al.* (2005) [203]. Other approaches used this number for packed bed of particles, as in Roux & Chevoir (2005) [204], Agnolin & Roux (2007) [205]–[207] Radjai & Dubois (2010) [208], where the shear rate is also defined as a strain rate. To adapt this number to the DAM, the strain rate is then computed for each step of data save on the disk as:

$$\dot{\epsilon} = \frac{th^h - th^{h-1}}{th^h \Delta t N_{\text{dump}}} \quad (2.65)$$

Where h is the dumping step and N_{dump} the number of time steps between each step of data save on the disk. The value th^h and not th_0 in denominator is taken in order to adapt the inertial number to the new sizes of particles.

In the end, the new cycle period was set such that the inertial number globally remained under 10^{-4} . The resulting value is $F_{\text{cyc}} = 10$ ms. Because it is almost four million times faster than a real cycle at C/5 (10 hours), this cycle period presents a sense only for computation purpose and not physical analysis. All the time results are then expressed in cycles in Chapter 3, and not in time.

2.4.4 Stiffness number

The mean coordination number introduced above is a useful number to evaluate the packing level of a particles bed. Despite this aspect, it presents a lack of information about the level of compression itself. Indeed, a high number of contacts does not necessarily mean a high level of compression. By “level of compression”, it is more rigorous to speak about “stiffness level” of the particles bed. This notion evaluates the ratio between the pressure applied on the particles bed and the rigidity of the particles themselves. For example, reaching a high level of compression of particles with low Young’s modulus will require a lower level of pressure than with particles with a high Young’s modulus. Introduced by Combe (2002) [209], the “**stiffness number**” estimates this ratio, through the following relationship:

$$\tilde{\kappa} = \left(\frac{E_V^*}{P(1 - \nu^2)} \right)^{\frac{2}{3}} \quad (2.66)$$

As opposite to the inertial number where the maximisation was justified by the will of remaining in quasi-static regime, the application of stiffness number to the DAM is more difficult, due to the presence of multiple Young’s moduli and proportions of particles. This is why the formulation of $\tilde{\kappa}$ presents the notation E_V^* and not the usual E . The proposed technique here is indeed to define a volume-fraction-based equivalent Young’s modulus, based on volume fraction of Si/C within Si/C/Gr (A_{CSi}^V) defined by Eq. (2.20) in Section 2.3.2.c:

$$E_V^* = A_{\text{CSi}}^V E_{\text{CSi}} + (1 - A_{\text{CSi}}^V) E_{\text{Gr}} \quad (2.67)$$

Considering figures of Table 2.1, we get $E_V^* \simeq 18.2$ GPa and, more importantly, $\tilde{\kappa} \simeq 1644$. According to Radjai & Dubois (2010) [208] (chapter 8), this value indicates a packing of the DAM reference sample particles bed close to the rigid state ($\tilde{\kappa} \gtrsim 2000$ for a mean coordination number of around 6, slightly more for lower value). By “rigid state”, it means that a variation of pressure leads to a limited deformation of the particles bed. On the opposite, the state more sensitive to pressure and Young’s moduli, *i.e.* the state where mean coordination number is highly influenced by pressure and Young’s moduli, is at $\tilde{\kappa} \lesssim 1000$. Consequently, this first evaluation predicts that two actions will have the most influential impact on the DAM structure:

- The decrease of the Young’s moduli
- The increase of the pressure

The evaluation of these predictions are developed in the sensitivity analysis of pressure and particles rigidity in Section 3.3.3.

2.4.5 Cohesion number

Another relevant number presented by Radjai & Dubois (2010) [208] is the “**cohesion number**” that characterises the intensity of cohesive forces relatively to the confinement forces. Really useful for the stickiness models (JKR and PC laws, see Section 1.2.3.b and Section 1.2.3.c), it is generally defined in three-dimensional space as:

$$\tilde{\eta} = \frac{F_{\text{sticky}}}{4\hat{R}^2P} \quad (2.68)$$

For $\tilde{\eta} \ll 1$, the system is “non-cohesive” and the sticky forces are negligible compared to the forces of confinement due to pressure, and reciprocally for $\tilde{\eta} \gg 1$. Similarly to the stiffness number, an issue appears in the real definition of the radius due to the complex particle size distribution. For this reason, it is proposed here to take the mean radius \hat{R} of the particles bed rather than R . Of course, the definition of the sticky force depends on the model.

For the JKR law (adhesion), the “pull-of” force expressed through Eq. (1.37) is a good order of magnitude to estimate this number. By fixing $R_1 = R_2 = \hat{R}$ in the expression of R^* , we then obtain:

$$\tilde{\eta}_{\text{JKR}} = \frac{3\pi W}{16\hat{R}P} \quad (2.69)$$

For the PC law (breakable bond), it is proposed to extract the normal force from the bond break tensile criterion of Eq. (1.53), by considering a null normal torque. By taking this criterion at the limit ($\sigma = \sigma_{\text{max}}$) and fixing $R_b = \hat{R}$, we get:

$$\tilde{\eta}_{\text{PC}} = \frac{\pi\sigma_{\text{max}}}{4P} \quad (2.70)$$

Chapter 3

DAM results

3.1 Introduction

3.1.1 Simulation overview

Our objective is not only to model the breathing of the electrode, but to understand its mechanical behaviour. More specifically, we want to predict and understand the amplitude of the reversible and irreversible thickness increase of the electrode during the cycling. The DEM offers different modelling options for the contacts. The goal of this section is to determine the impact of each model feature on the predicted breathing of the electrode.

First, the silicon fraction within active material (A_{Si}) is analysed because one of the technological challenges is to increase this fraction as much as possible. Hence, the objective is to state if a compromise point exists between silicon fraction (*i.e.* anode capacity) and breathing. This analysis is detailed in Section 3.3.1, considering both linear and electrochemical breathing laws. Second, because the DAM uses spherical particles, a first technique to simulate the particles with complex shapes is to increase the friction between particles (μ). It is also proposed here, in the same scope, to analyse the extreme case where the particles' rotation is completely blocked ($\omega = 0$ rad/s). This approach is developed in Section 3.3.2. In addition, the pressure applied on electrode (P) is fundamental in electrode context, and it can be also easily compared to experimental measurements. In fact, this parameter is closely linked with particles rigidity (*i.e.* E_{CSi} and E_{Gr}). For this reason, pressure and particles rigidity are similarly analysed under the concept of “stiffness level” in Section 3.3.3. Afterwards, the binder material present in the electrode makes particles cohesive and this certainly contributes to the mechanical behaviour of the electrode during cycling or under pressure changes. Therefore, adding stickiness in the model is the simplest way to take the binder into account. This stickiness can be approached in two different ways: reversibly (attraction can reoccur even after a loss contact) and irreversibly (stickiness is lost after a first lost of contact). In this optic, the adhesion model using JKR law (see Section 1.2.3.b) is used to analyse the reversible stickiness in Section 3.3.4, and the breakable bond model using PC law (Section 1.2.3.c) is used to analyse the irreversible stickiness in Section 3.3.5. Finally, all the previous analysis consider the breathing of particles reversibly (particles diameters come back to their initial value at each cycle). Thus, the final analysis consists in varying the particles breathing irreversibility in order to evaluate how this irreversibility is transferred to electrode level. This is the subject of Section 3.3.6.

As summary, Table 3.1 recapitulates all the DAM simulations with the notations of the sensitivity parameters, the number of values studied by parameter, the series type (pre-calendering, pre-relaxation or post-relaxation), the DEM law used, a brief battery-context interpretation and finally the associated section.

3.1.2 Conventions for the observed variables

3.1.2.a Time

As detailed in Section 2.4.3, the raw computed time has been rescaled and is physically meaningless. It means that a cycling at a C-rate of 1C or C/10 would be the same because the quasi-static configuration of the model makes it independent of the charge/discharge speed. Hence, the reference time unit is the cycle c (one unit of time equals T_{cyc}). In other words, at $c = 1$, $t = T_{\text{cyc}}$, at $c = 2$, $t = 2T_{\text{cyc}}$, etc. Every graph presents the relaxation phase, the cycling phase, or both. The zero time is at the beginning of the cycling phases so that negative values of cycle represent the relaxation phase and positive values the cycling phase (the different phases are defined in Section 2.2.1). A decimal value of time is associated to a fraction of T_{cyc} . The lower value of time depends on the display: when starting at the beginning of relaxation, $c_0 = -0.01$ cycle, and when starting at the beginning of cycling, $c_0 = 0$ cycle.

Parameter	Variable notation	N_{values}	Series type	Contact law	Battery-context interpretation	Section
Si fraction (linear)	A_{Si}	6	PreCal	HM	Self-explanatory	3.3.1
Si fraction (elec. chem.)	A_{Si}	6	PreCal	HM		
Friction/Rotation	μ / ω	4	PreRel	HM	Particle blocking due to non-spherical shapes	3.3.2
Pressure	P	8	PreRel	HM	Pressure on electrode	3.3.3
Particles rigidity	E	10	PreRel	HM	Self-explanatory	
Adhesion (before rel.)	W	8	PreRel	JKR	Reversible stickiness of binder	3.3.4
Adhesion (after rel.)	W	8	PostRel	JKR		
Bonds (before rel.)	st_{max}	9	PreRel	HM + PC	Irreversible stickiness of binder	3.3.5
Bonds (after rel.)	st_{max}	9	PostRel	HM + PC		
Part. irr. (linear)	r_{irr}	6	PostRel	HM	Particles irreversible breathing	3.3.6
Part. irr. (elec. chem.)	r_{irr}	6	PostRel	HM		

Table 3.1: DAM simulations summary — *Part. irr.:* Particles irreversibility, *elec. chem.:* electrochemical, *rel.:* relaxation, *PreCal:* pre-calendering, *PreRel:* pre-relaxation, *PostRel:* post-relaxation, *HM:* Hertz-Mindlin (Section 1.2.1.b), *JKR:* Johnson-Kendall-Roberts (Section 1.2.3.b), *PC:* Potyondy-Cundall (Section 1.2.3.c)

3.1.2.b Thickness

When expressed with raw values (using th notation), the initial value is always set to zero at the lower value of time, as stated in the initial conventions of this manuscript. The displayed thickness is then a thickness variation starting from a reference value, detailed in the caption with the notation th_{ref} . This value can be the calendering thickness $th_{cal} = 50 \mu\text{m}$ or the mean thickness after relaxation. Moreover, the thickness th is always displayed with relative values, expressed with percentages, on the right axis. These relative values corresponds to the ratio of the thickness over reference thickness (th/th_{ref}).

3.1.2.c Standard deviation

As introduced in Section 2.2.3, all results are based on a statistical series that measures the impact of initial particles distribution and positions. In all graphs, the surrounding coloured areas around curves represent the standard deviations at 1σ of the statistical series, with $N_{draws} = 10$. In text, the detailed values with standard deviation (\pm notation) refer to this measured dispersion.

3.1.2.d Per cycle quantities

Some quantities are expressed “per cycle” (one value per cycle). For example, swelling amplitude Δth_{sw} , irreversibility Δth_{irr} and respective breathing coefficients $\mathfrak{F}_{s,irr}^n$ and $\mathfrak{F}_{s,sw}^n$ are only defined cycle after cycle. Hence, the superscript integer n indicates the corresponding cycle index (generally 1, sometimes 2, never more).

3.2 DAM reference sample analysis

Before entering the various sensitivity analyses (Section 3.3), this section aims to analyse the DAM reference sample, in order to observe the basic behaviours generated by the DEM model. It mostly constitutes a point of reference for all the sensitivity analyses of next section (Section 3.3). The following analysis is composed of two different simulations of the DAM set with the parameters of Table 2.1. Each simulation is distinguished by the breathing law: linear in volume or electrochemical (as displayed in Fig. 2.10). As a systematic protocol, the cycling is made on four cycles.

As first result, Fig. 3.1 displays a recurrent behaviour of the DAM submitted to a basic cycling process. As expected considering Eq. (2.64), the inertia of the system is highly correlated with the thickness variation. Indeed, Fig. 3.1a shows the evolution of inertial number during relaxation and cycling phases, parallel to Fig. 3.1b that shows the raw thickness variation. The relaxation is much more dynamic than the cycling phase, with an inertial number reaching $6.8 \times 10^{-3} \pm 1.9 \times 10^{-3}$ and dropping fast to 0 (3.1a.①). This behaviour is synchronized with the particles bed relaxation that leads to a thickness growth of around $5.9 \pm 0.2 \mu\text{m}$ until stabilisation (3.1b.②). During the cycling phase, the inertia clearly depends on the breathing laws. Indeed, with linear volume laws, more stable over time, the inertial number stays approximately constant (due to the constant pressure and almost constant displacement of the top plate), at a value of around 7.2×10^{-5} (3.1a.③). However, with electrochemical breathing laws, the inertia drastically varies depending on the breathing speed,

showing important drops to zero when the breathing almost stops (3.1a.④). Concerning the force on top plate in Fig. 3.1c, it decreases during the relaxation of the particles bed, starting from the calendering pressure of 8.5 ± 0.7 N (3.1c.⑤) until reaching P_{ref} . During the cycling phase in Fig. 3.1d, the PID controller shows an efficient stabilisation work, able to keep the force applied on top plate in a range of $\pm 0.8\%$ of PID input (48 mN) despite the particles breathing. Even for electrochemical breathing laws, the fast variation is efficiently damped by the PID controller. Consistently, the system is slightly over-loaded during swelling and under-pressure during shrinking. Finally, Fig. 3.1e displays the evolution of the mean coordination number \overline{MCN} . Starting from

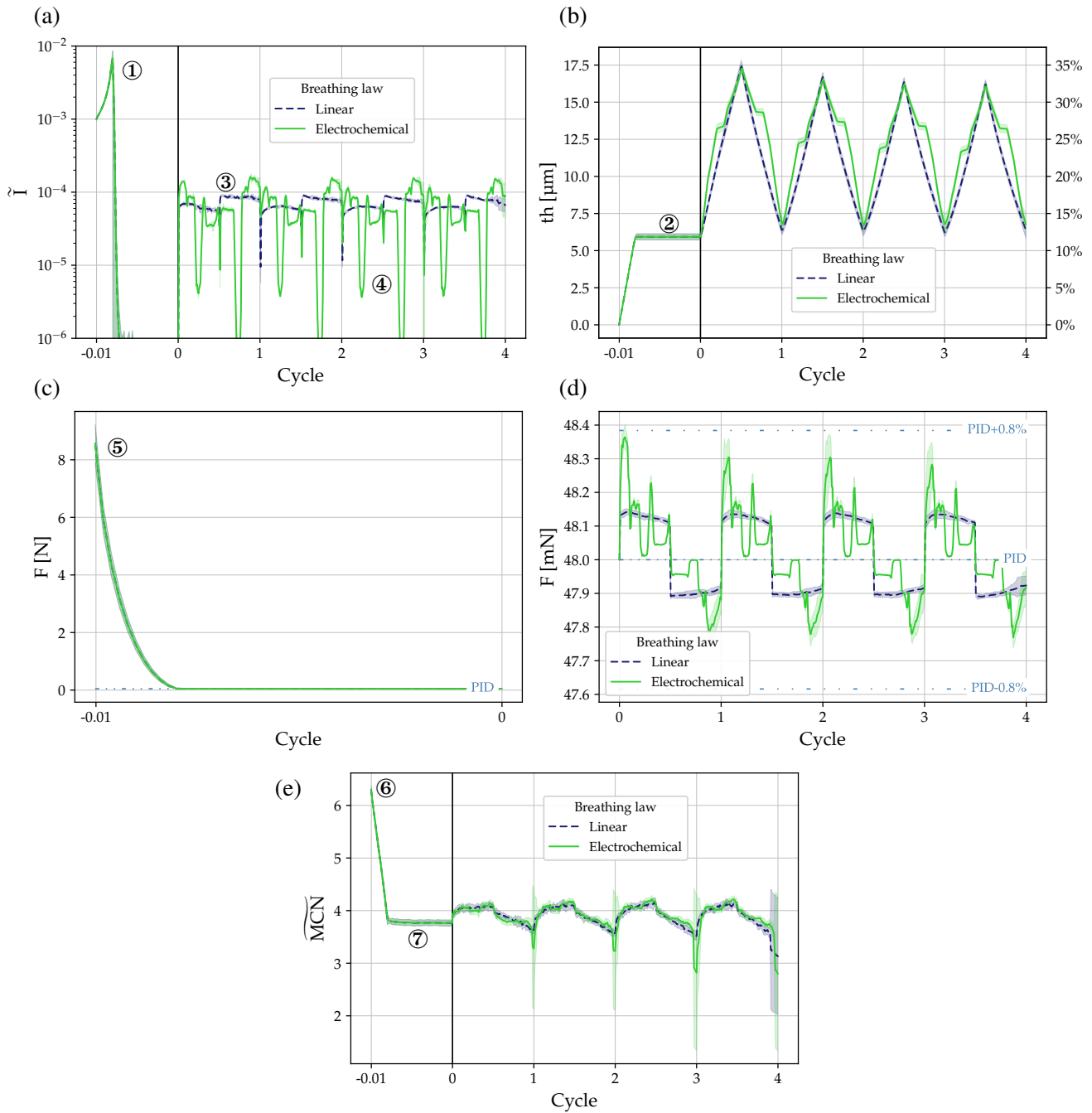


Figure 3.1: DAM reference sample analysis (linear and electrochemical breathing laws) — **a**) Inertial number (relaxation and cycling). **b**) Thickness (relaxation and cycling), $th_{\text{ref}} = 50 \mu\text{m}$. **c**) Force on top plate (relaxation). **d**) Force on top plate (cycling). **e**) Mean coordination number (relaxation and cycling).

the packed particles bed at 6.3 ± 0.1 (3.1e.⑥), the relaxation leads to a mean coordination number of 3.8 ± 0.1 (3.1e.⑦). During cycling, in average, the mean coordination remains quite stable, oscillating around 3.8 ± 0.1 at the rhythm of cycles, which constitute a moderate level of particles packing. It is possible to observe some noisy dispersion of mean coordination at the end of each cycle, suggested by the high standard deviation. This singularity is addressed more in details in Section 3.3.1 and Section 3.3.2.

To complete the analysis, Fig. 3.2 presents the swelling amplitude thickness Delta and breathing coefficient and the irreversibility thickness Delta, as a function of cycles. Concerning the thickness Delta Δth_{sw} , Fig. 3.2a demonstrates the order of magnitude of swelling amplitude captured by the DAM: around $11 \mu\text{m}$ at first cycle (3.2a.①). Whatever the breathing law, this value progressively decreases cycle after cycle, until $9.3 \pm 0.5 \mu\text{m}$ for the lowest point (3.2a.②). The electrochemical breathing law presents lower values of swelling amplitude Δth_{sw} , until a difference of around $0.7 \mu\text{m}$ (between 3.2a.② and 3.2a.③). This suggests an impact of non-linear breathing of particles on reorganisation of particles bed: non-synchronism between Si/C and Gr particles breathing enables a better rearrangement and, then, a better void exploitation (this aspect is further discussed in Section 3.3.6). This “void exploitation” is better evaluated by the breathing coefficient in Fig. 3.2b. First, the resulting curves are strictly similar to swelling amplitude Δth_{sw} , due to the fact that it entirely depends on this parameter in the current configuration. In addition, this presents the range where the DAM evolves in general: between 1.89 ± 0.04 (3.2b.④) and 1.53 ± 0.08 (3.2b.⑤). As a recall of interpretation guides Table 2.2,

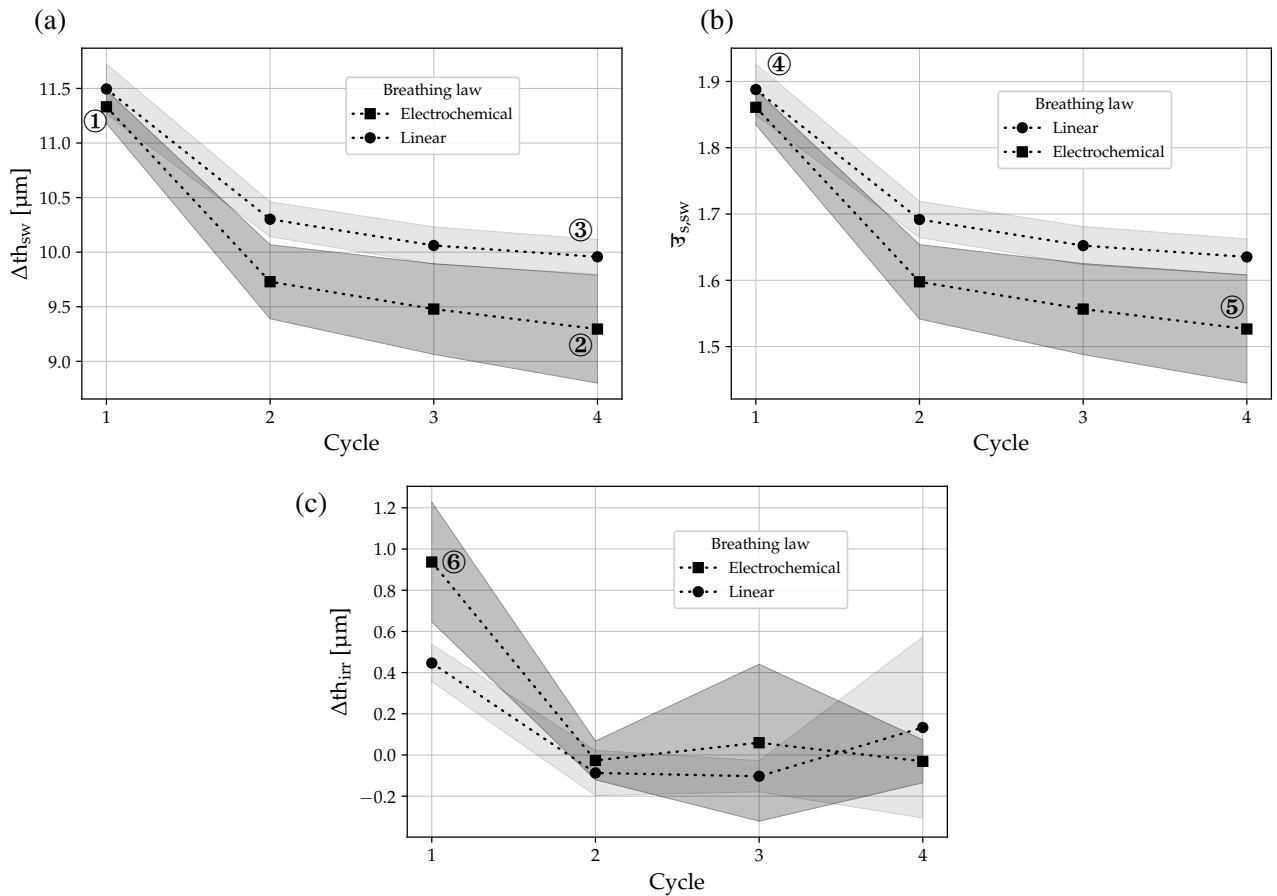


Figure 3.2: DAM reference sample analysis (linear and electrochemical breathing laws) — **a)** Swelling amplitude thickness Delta. **b)** Swelling amplitude breathing coefficient. **c)** Irreversibility thickness Delta.

a value of 2 corresponds to a balanced breathing ($\Delta V_{\text{particles}} = \Delta V_{\text{void}}$) and 1 to a solid breathing ($\Delta V_{\text{anode}} = \Delta V_{\text{particles}}$ and $\Delta V_{\text{void}} = 0$). In other words, the current breathing of the DAM is close to a balanced breathing, which means that the particles volume change generate an almost equal volume change of void. At the lowest breathing obtained with electrochemical law (3.2b.⑤), using the value of $\bar{\alpha}_{s,sw} = 1.53$, the equivalent values $1/\bar{\alpha}_{v,sw}$ and $1/\bar{\alpha}_{v5,sw}$ are respectively equal 0.34 and 0.53 (values not displayed in graphs). In other words, at 3.2b.⑤, 34% of the electrode swelling amplitude comes from void volume variation and the void volume variation corresponds to 53% of the particles volume variation. Thus, we are facing a particles beds that significantly creates extra void volume variation. At last, Fig. 3.2c displays the irreversibility Δth_{irr} as a function of cycles. The highest irreversibility is reached at first cycle with electrochemical law, with a value of $0.9 \pm 0.3 \mu\text{m}$ (3.2c.⑥). Considering the noisy evolution of Δth_{irr} around 0, this graph clearly demonstrates the inability of DAM reference sample, through the use of simple Hertz-Mindlin contact law (detailed in Section 1.2.1.b) with basic contact parameters, in capturing the irreversible breathing.

3.3 Sensitivity analyses

3.3.1 Silicon fraction

This sensitivity analysis is directly initiated by the motivation of the thesis: the addition of silicon fraction within the anode is first and foremost a way to improve the battery weight and volumetric capacity. Consequently, the question about an eventual compromise between capacity and breathing significance has its place in these sensitivity analyses. Of course, in the specific case of the DAM, “capacity” is similar to “silicon fraction”. As detailed in Section 2.3.2.b, the silicon weight fraction within active materials (Si, C and Gr), noted A_{Si} , does not vary between 0 and 1. Indeed, due to the limitation of volume generated by B_{Si} , the silicon weight fraction within silicon composite materials (Si and C), we necessarily have $A_{\text{Si}} \leq B_{\text{Si}}$. In DAM reference sample, we fixed a value of $B_{\text{Si}} = 0.5$, so A_{Si} can go from 0 to 0.5. For numerical reasons, the full Si/C case ($A_{\text{Si}} = 0.5$) led to particles bed instabilities of simulation (maybe due to excessive speed of breathing), so this value was not analysed. Instead, six values from 0 to 0.4 were simulated, first by implementing linear breathing law.

3.3.1.a Linear breathing law

As expected, the silicon fraction induced a higher breathing range, then a higher breathing speed of the electrode. In Fig. 3.3a, inertial number shows this fact by a clear correlation with A_{Si} , where the mean curve for $A_{\text{Si}} = 0.4$ is equal to around 2×10^{-4} compared to around 3.8×10^{-5} for $A_{\text{Si}} = 0.0$. The force is also impacted, with a more pronounced oscillation of PID errors gap, all the more important that the silicon fraction is high, as shown in Fig. 3.3b. Fortunately, the force on top plate is efficiently kept in a range of $\pm 1.4\%$ of PID input. When it comes to raw thickness, as displayed in Fig. 3.3c, the swelling amplitude is clearly impacted by the silicon fraction. Moreover, an amount of irreversibility appears at the end of the first cycle, but at a very low amount (maximum if $1.91 \pm 0.1 \mu\text{m}$ for $A_{\text{Si}} = 0.4$, 3.3c.①). Even if it is correlated to the silicon fraction (the higher A_{Si} , the higher the irreversibility Delta), this amount is not significant enough to catch our attention. Indeed, this amount reaches only a maximum of 5.2% of the swelling amplitude.

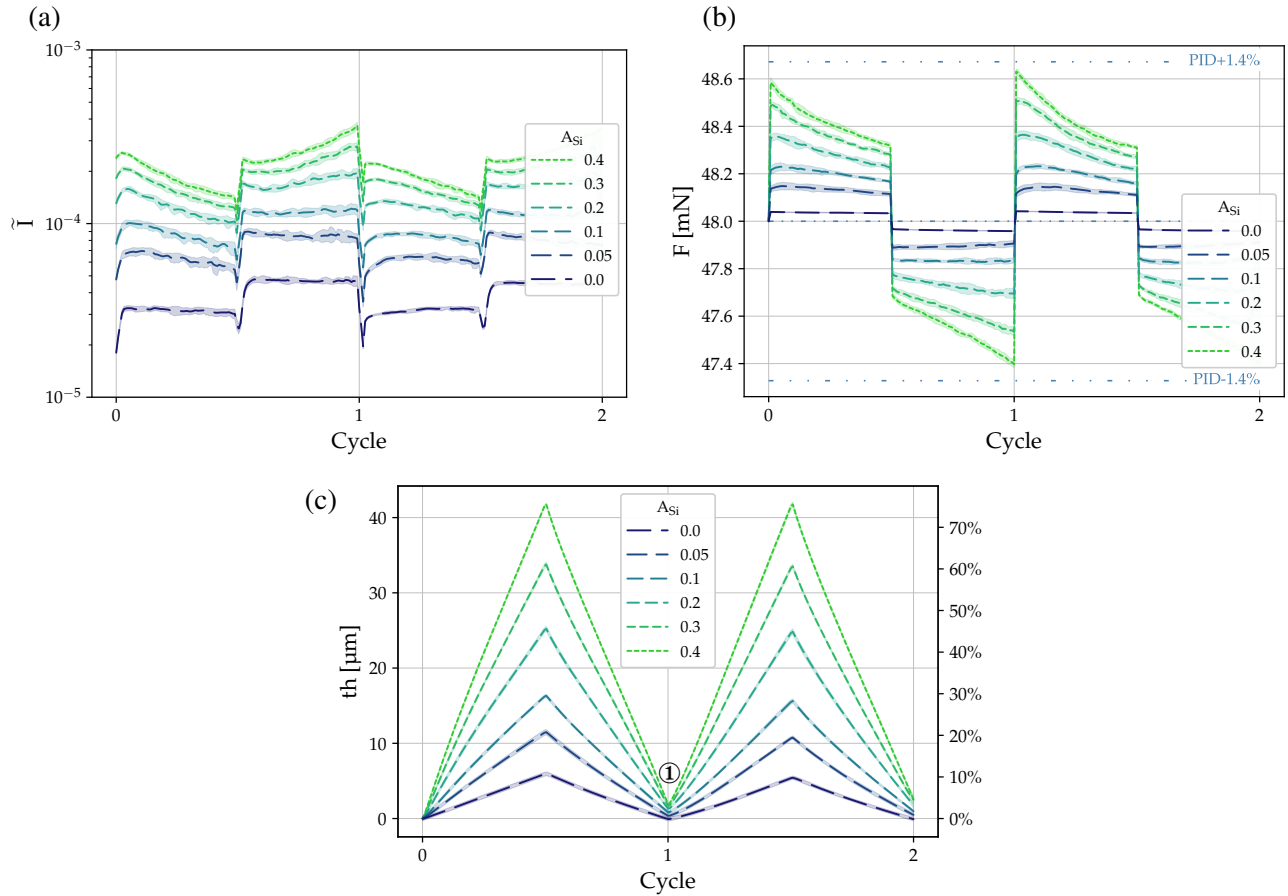


Figure 3.3: Influence of silicon fraction with linear breathing law (6 values set, DAM reference sample for $A_{Si} = 0.05$) — **a**) Inertial number (cycli). **b**) Force on top plate (cycli). **c**) Thickness (cycli), $th_{ref} \simeq 55.3 \mu\text{m}$.

Complementarily, Fig. 3.4a shows the evolution of thickness swelling amplitude Δth_{sw} of the first cycle. It presents an astonishing linearity of thickness swelling amplitude Δth_{sw} with the silicon fraction. The linear regression applied to the curve indeed indicates a matching with a coefficient of determination of $\check{R}^2 = 0.998$, which is a good agreement. On its side, the swelling breathing coefficient indicates a significant reversed evolution, as shown in Fig. 3.4b. Indeed, it decreases with the silicon fraction, from a maximum of 1.88 ± 0.04 for $A_{Si} = 0.05$ (3.4b.①) to a minimum of 1.69 ± 0.01 for $A_{Si} = 0.4$ (3.4b.②). In the DAM reference sample analysis (see Section 3.2), $\mathfrak{F}_{s,sw}$ varies only because of Δth_{sw} , resulting the simple proportionality between Fig. 3.2a and Fig. 3.2b. In the present case, this is different because $\mathfrak{F}_{s,sw}$ also depends on the silicon fraction A_{Si} (see Eq. (2.58) in Section 2.4.1). Thus, the curve of Fig. 3.4b indicates that the increase of silicon fraction (or in more general terms, particles with high breathing range) leads to lower breathing coefficient $\mathfrak{F}_{s,sw}$. By calculating the equivalent breathing coefficients $1/\mathfrak{F}_{v,sw}$, we respectively get the values 0.47 at 3.4b.① and 0.41 at 3.4b.② (values not displayed in graphs). It means that for a silicon fraction of $A_{Si} = 0.05$, 47% of electrode volume variation comes from void volume variation, against 41% at $A_{Si} = 0.4$. This observation manifests in swelling amplitude Δth_{sw} curve in Fig. 3.4a that is not exactly linear but feebly logarithmic: a relative reduction of void volume generation seems to occur as the silicon fraction increases. As a result, a higher proportion of silicon leads to a breathing where particles breathing generates less void volume variation, relatively speaking.

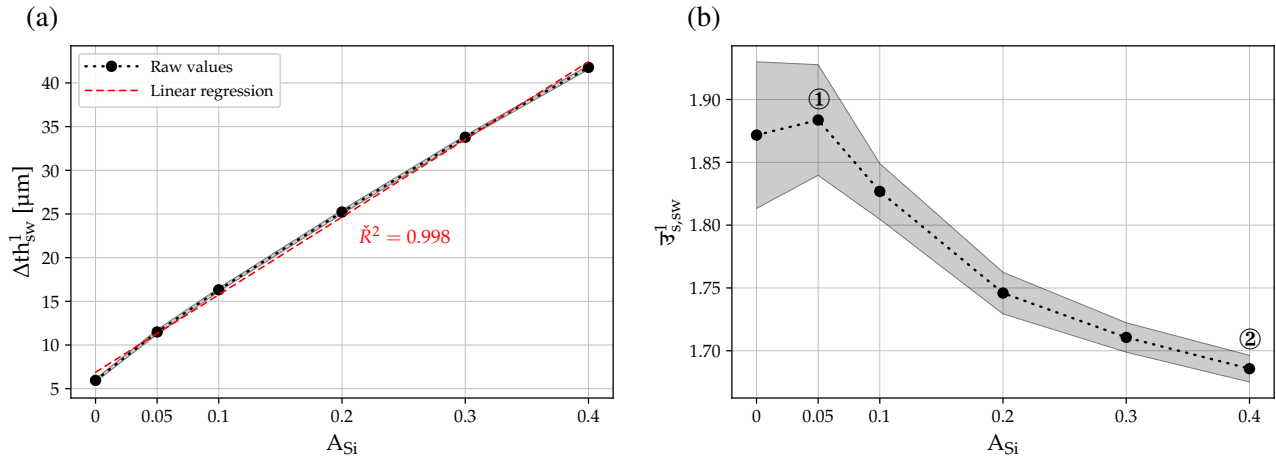


Figure 3.4: Influence of silicon fraction with linear breathing law (6 values set, DAM reference sample for $A_{Si} = 0.05$) — **a)** Swelling amplitude thickness Delta (first cycle). **b)** Swelling breathing coefficient (first cycle).

3.3.1.b Electrochemical breathing law

An extended protocol of this sensitivity analysis is to replace the particles breathing linear volume law by a more realistic electrochemical law for both Si/C and Gr particles. The reason for this change is simple: the balanced breathing ($\overline{\mathfrak{V}}_{s,sw} \simeq 2$) observed above is maybe due to the simultaneous breathing of all particles, as for both Si/C and Gr. Indeed, with linear law, all particles linearly swells and then linearly shrink at each cycle, which constitutes a breathing synchronism. This synchronism is maybe at the origin of this global stable breathing that seems not to reorganise particles. Thus, the idea now is to start from the exact same particles distributions and positions, and to implement electrochemical breathing law (from Fig. 2.10 based on electrochemical algorithm) instead of linear volume law. The main objective at the origin of this protocol is to implement non-synchronous breathing of materials (Si/C and Gr). A sequential and alternating breathing of graphite and silicon particles, resulting from the combination of the material OCV curves, may trigger more microstructure changes compared to the simpler simultaneous and linear growth of all particles.

First, the electrochemical breathing law must be used carefully in the DAM, especially in the case with a high silicon fraction. As observed above, the silicon fraction increases the inertia of the system, and adding electrochemical law also create some local fast breathing speed. More clearly, Fig. 3.5a displays the inertial number with different silicon fractions A_{Si} . Indeed, because particles breath on the exact same ranges ($0 \leftrightarrow v_{CSi,max}$ for Si/C and $0 \leftrightarrow v_{Gr,max}$ for Gr), the non-linearity of electrochemical breathing law necessarily creates local faster breathing. At highest silicon fraction, the maximum point of inertial number is at the end of cycles, reaching for example $9.6 \times 10^{-4} \pm 0.4 \times 10^{-4}$ at 3.5a.①, where the breathing speed is the fastest. Thus, the simulations are still at the limit of quasi-static state. The inertial number is quite coherent with the thickness curves plotted in Fig. 3.5b, where the slope is well synchronised with the associated inertia : the flatter the thickness curve, the lower the inertial number. Moreover, the interesting feature observable in the thickness curve of Fig. 3.5b is the progressive transition of breathing shape between simulations, from the characteristic pyramidal behaviour of graphite for $A_{Si} = 0$ to the asymmetric form of silicon for $A_{Si} = 0.4$. This detail is a perfect illustration of the different proportions of both material between simulations. In fact, this detail is almost the only noticeable difference with linear volume laws. For example, the swelling amplitude remains

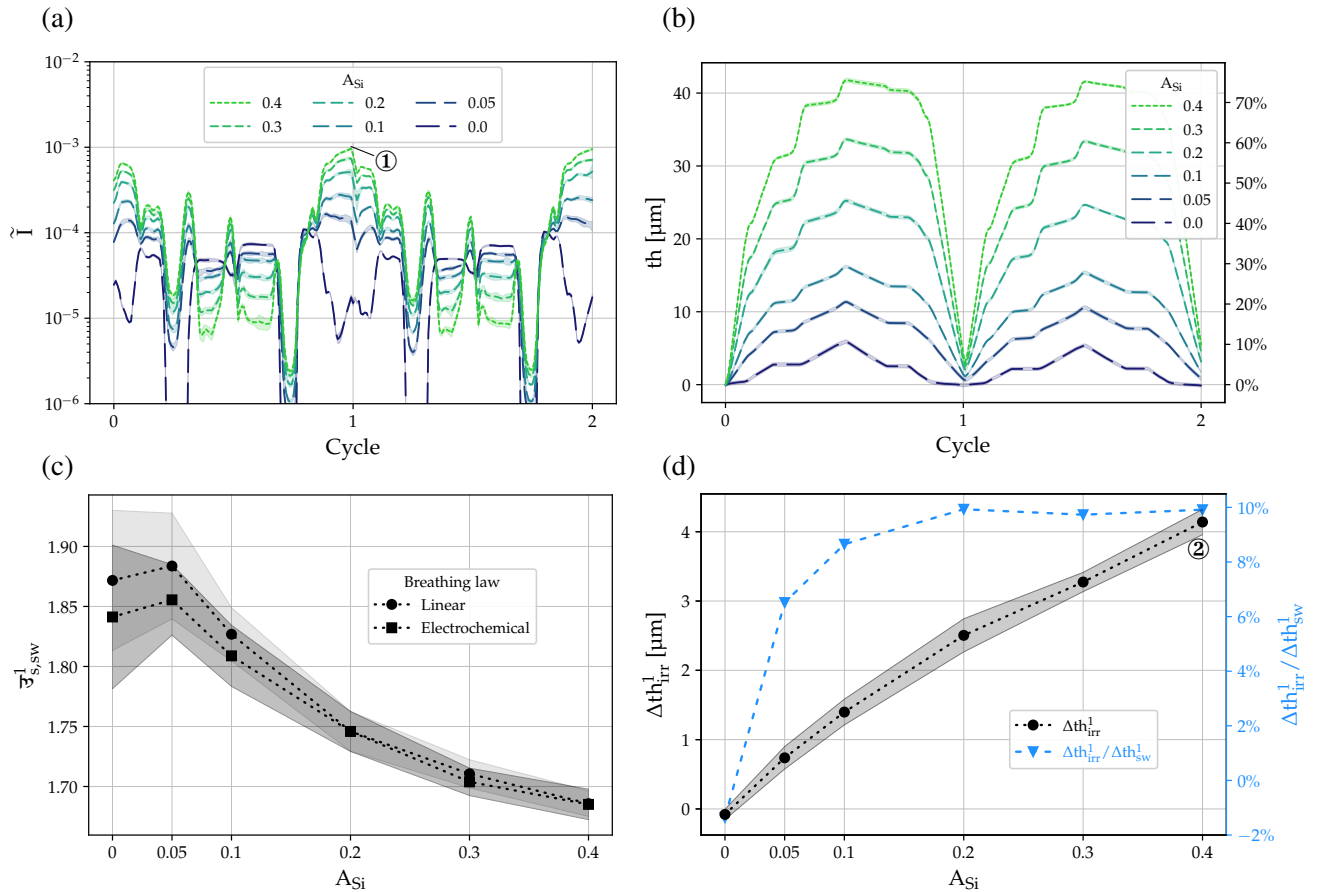


Figure 3.5: Influence of silicon fraction with electrochemical breathing law (6 values set, DAM reference sample for $A_{Si} = 0.05$) — **a**) Inertial number (cycling). **b**) Thickness (cycling), $th_{ref} \simeq 55.3 \mu\text{m}$. **c**) Swelling breathing coefficient (first cycle). **d**) Irreversibility thickness Delta (first cycle), dot markers, left axis. Ratio of irreversibility over swelling amplitude thickness Deltas (first cycle), triangle markers, right axis.

distinctly unchanged, so much that the curve of swelling amplitude Δth_{sw} (not drawn here) is equal to the one related to linear volume law (drawn in Fig. 3.4a). On their side, the swelling breathing coefficients of linear and electrochemical breathing laws are slightly different, but as shown in Fig. 3.5c, the dispersion areas are well overlapped. A noticeable observation appears regarding the irreversibility that, this time, reaches $4.1 \pm 0.2 \mu\text{m}$ for $A_{Si} = 0.4$ (3.5d.②, read on left axis). Moreover, the increase of silicon fraction leads to an increase of the ratio between irreversibility over swelling amplitude Δth (read on right axis in Fig. 3.5d), before reaching a plateau at around 10%. In Fig. 3.5d, we also observe that more void volume variation is irreversibly transmitted to electrode with high silicon fraction. Thus, by comparing Fig. 3.5c and Fig. 3.5d, we can deduce that, as the silicon fraction increases, less void volume is generated, but more is transmitted irreversibly to the electrode.

In addition, the mean coordination number \overline{MCN} displayed in Fig. 3.6 presents strange instabilities, hardly explainable at this stage. These instabilities always manifest at the end of a cycle, as a sudden drop of \overline{MCN} with a very large dispersion (3.6.①), demonstrating the irregular aspect of this phenomenon. The fact that it occurs at any cycle and any sensitivity parameter value, with no clear pattern, suggests arrangement singularity happening randomly. This singular phenomenon is further explored in the next section (Section 3.3.2).

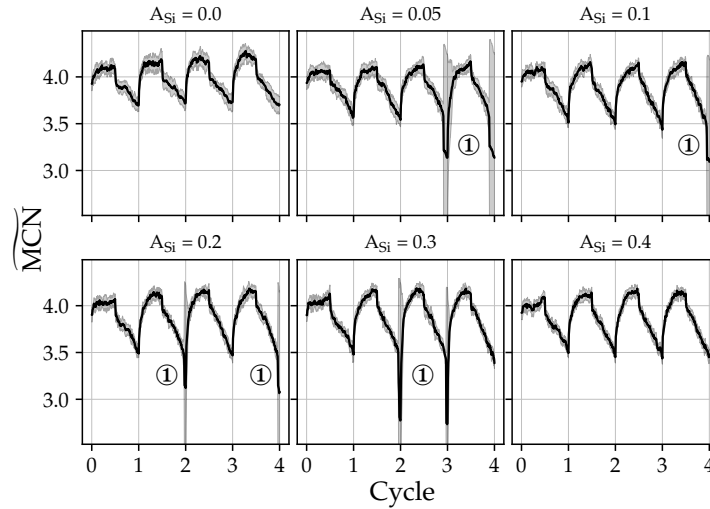


Figure 3.6: Influence of silicon fraction with linear breathing law (6 values set, DAM reference sample for $A_{Si} = 0.05$) — Mean coordination number.

3.3.2 Friction / Rotation

3.3.2.a Standard analysis

As it is detailed in the DAM reference sample analysis in Section 3.2, a Hertz-Mindlin contact law (detailed in Section 1.2.1.b) with basic parameters is not enough to capture a significant variation of swelling amplitude or irreversibility over cycles. It is supposed that the particles are not constrained enough through a contact law that hardly simulates the presence of the binder or complex particles shapes. The first parameter that comes in mind to add more mechanical irreversibility in the model is the friction between particles. As a fundamental parameter of Eq. (1.16), the main constitutive equations of DEM, it is a first way of getting closer of non-spherical particles or binding effects. We can imagine that the higher the friction, the more the particles block one each other due to virtual non-spherical shapes and/or rough surfaces. A comparable method is to control the rotation itself, to the point of removing it completely.

For these reasons, the sensitivity analysis presented here is composed of four sensitivity parameters: two extreme values of friction coefficient ($\mu = 0.05$ or $\mu = 0.4$) in two different cases of particles rotation state (rotation enabled or rotation blocked, *i.e.* $\omega \in \mathbb{R}$ rad/s or $\omega = 0$ rad/s). By “rotation enabled”, it means that particles can freely rotate on all axis. By “rotation blocked”, it means that rotation is removed from dynamics computation, preventing particles to rotate. A sensitivity parameter is then a pair of friction coefficient and rotation state ($\mu / \text{rot.}$). This parameter is set at the end of the calendring, just before the relaxation. The case without friction $\mu = 0$ was not treated here for a reason of behaviour relevancy: without any friction, the particles are free to move between both top and bottom plates, giving birth to a flow of particles through periodic boundaries generated by the particles breathing.

The simulations of this sensitivity analysis are quite stable concerning the dynamics, the force being globally stabilised in a range of $\pm 0.3\%$ of PID input and the inertial number efficiently kept under 10^{-4} , with the highest mean value over cycling phases reached for $\mu = 0.4$ and rotation activated, at $7.4 \times 10^{-5} \pm 0.1 \times 10^{-5}$ (inertial number and force not displayed). The first effect of friction/rotation modification appears within the

relaxation phases, as shown in Fig. 3.7a, where the final thickness is influenced by the friction coefficient. Indeed, the lowest expansion is reached at low value of friction ($\mu = 0.05$) and with rotation enabled, with a final thickness change at $5.8 \pm 0.3 \mu\text{m}$ (3.7a.①). On the opposite, the highest thickness change occurs at high friction with rotation enabled, until $7.5 \pm 0.4 \mu\text{m}$ (3.7a.②). These observations are correlated with the mean coordination number \overline{MCN} curves in Fig. 3.7c, where the friction coefficients are particularly distinguished, with the maximum reached for $\mu = 0.05$ (around 4.0, 3.7c.③) and the minimum reached $\mu = 0.4$ (around 3.0, 3.7c.④, in half-transparent area). The astonishing observation is that the relaxation seems not particularly less influenced by the fact the rotation is blocked or not, whereas it was supposed to have a noticeable impact on particles packing. However, the trend changes when breathing occurs, as plotted in Fig. 3.7b. Both curves for $\mu = 0.05$ are almost merged and do not present any irreversibility. The case for $\mu = 0.4$ and rotation enabled is slightly more significant, with a $1.2 \pm 0.2 \mu\text{m}$ of thickness irreversibility (3.7b.⑤). The behaviour drastically changes by blocking rotation, still with the case for $\mu = 0.4$, where the first cycle generates an important irreversibility of $9.7 \pm 1.5 \mu\text{m}$ (3.7b.⑥). It was initially thought that the high friction, enhanced by the blocked rotation, was creating a stronger global force network maintained after the first swelling. Actually, an observation questions this explanation. Indeed, looking at the mean coordination number \overline{MCN} reveals a divergent facet of the DAM

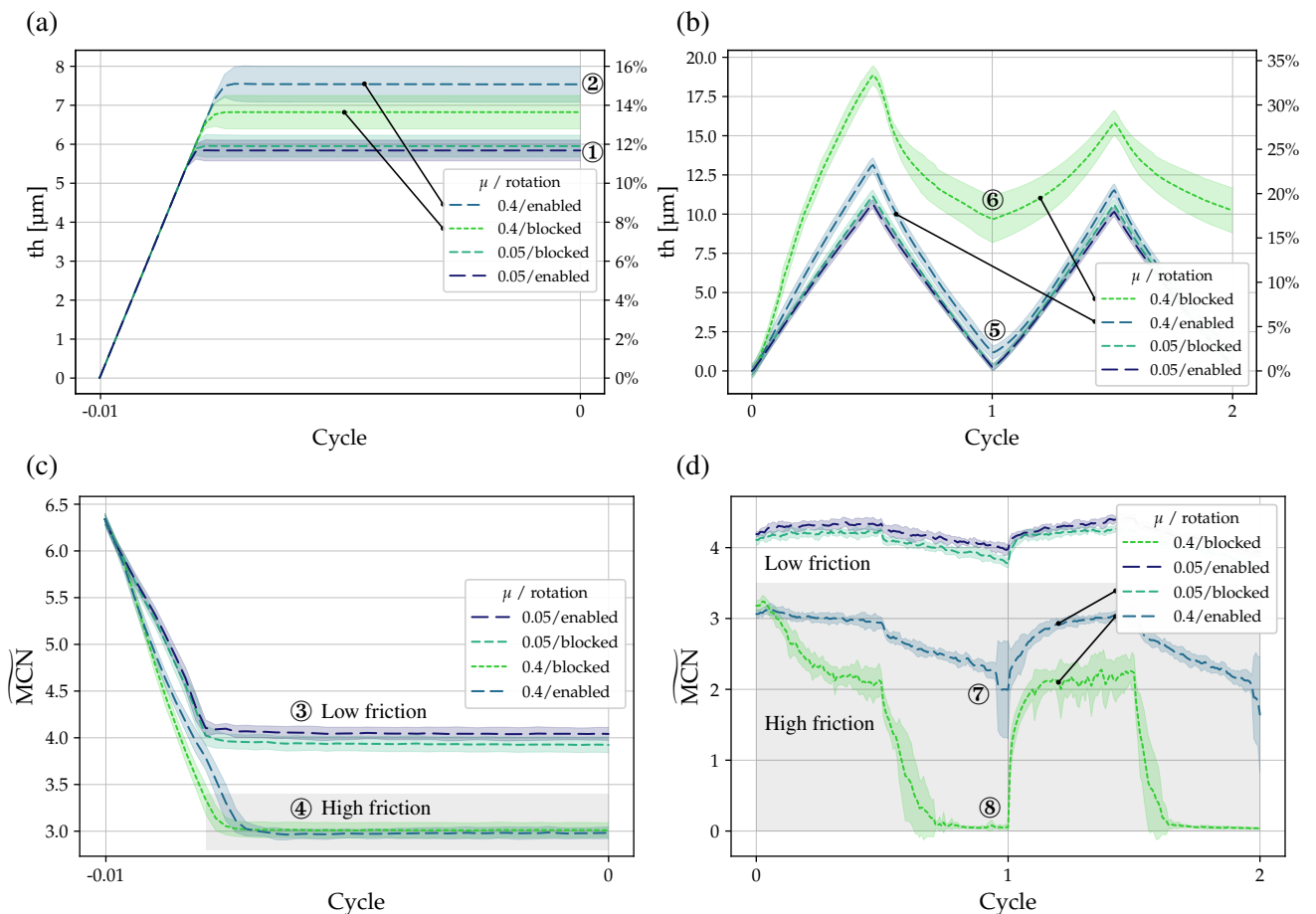


Figure 3.7: Influence of friction/rotation (4 values set) — **a**) Thickness (relaxation), $th_{ref} = 50 \mu\text{m}$. **b**) Thickness (cycling), $th_{ref} \simeq 56.5 \mu\text{m}$. **c**) Mean coordination number (relaxation). Half-transparent area emphasises the curves of high friction. **d**) Mean coordination number (cycling). Half-transparent area emphasises the curves of high friction.

with high friction, as shown in Fig. 3.7d. Both cases at high friction ($\mu = 0.4$), as we saw, begins the cycling with \overline{MCN} almost equal to 3. This value is already not particularly high for a packed particles bed (the order of magnitude introduced in Section 2.4.4 being around 6, the results from DAM reference sample analysis in Fig. 3.1e giving around 4). Moreover, these values radically decrease during breathing, until 2.0 ± 0.7 (3.7d.⑦) for the case with rotation enabled and 0.05 ± 0.04 (3.7d.⑧) for the case with rotation blocked. More precisely, Fig. 3.7d clearly presents a physical singularity: a compressed particles bed with almost zero contact between particles during major part of the shrinking. Such a really low coordination number is easily imagined by an organisation in “pillars” of particles, such that the forces within the network only follows vertical orientations, via the parallel pillars of particles. The exploration of this assumption is the subject of the following section.

3.3.2.b Imaging of force network

To better understand what happens within the particles bed, and also what “pillar” means, Fig. 3.8 displays the forces networks at three different stages of the first breathing of the extreme frictional case ($\mu = 0.4$ and not rotation). Of course, no statistical process is used here, only one simulation has been picked. On the left, for each stage, two views of the particles bed (lateral in y direction and top) displays the contact forces (particle-particle and particle-wall), where a dark colour signifies a strong force and vice versa. On the right, colour maps display the distribution of particle-wall forces on the top plate, with the contrast harmonised for all three stages. The first stage (Fig. 3.8a) corresponds to the middle of swelling phase, the second stage (Fig. 3.8b) to the time just at the beginning of shrinking phase, and the third stage (Fig. 3.8c) to the middle of shrinking phase.

At first stage in Fig. 3.8a, the forces network is quite homogeneous in the x/y plan. The presence of lateral “force thunder lights” witnesses a huge stress in x/y directions. In more appropriate terms, these “force thunder lights” form what we call a “**backbone**”, defined by Agnolin & Roux (2007) [205]–[207] as a “*network of contacting grains that carry forces*”. Hence, instead of “force thunder light”, a more proper term would be “**backbone branch**”. In a complementary way, a particle that is not participating in the backbone structure is called “**rattler grain**”. The remarkable characteristic of the backbone of first stage is its double-layer structure, each layer being compressed against a plate. The presence of an important forces network oriented in x/y directions was predictable as regard to the presence of particles breathing. However, the clear subdivision of this stress into two sub-layers is, for its part, more surprising. We could imagine that these layers would be generated by the z-oriented compression of top and bottom particles by the whole swelling particles bed, but in our case, we have to recall that the system evolves at constant force, the thickness adapted in real-time to keep it stable. This precision is particularly shown by the force map, on the right, where the forces with the top plate are globally well distributed and do not even exceed 3.5 mN. This double-layer force maybe reveals a limitation of the DAM, more precisely its use of two rigid plates as boundaries on z direction (as stated by Hyp. 2.A.viii (page 74) in Section 2.1.2). This strict rigidity in this direction certainly creates a border effect by suppressing a translation degree of freedom for particles in contact with plates, unlike the particles in the middle that can move in z direction. The use of a softer method to simulate plates, such as layers of bonded particles, would have maybe reduced this important border effect.

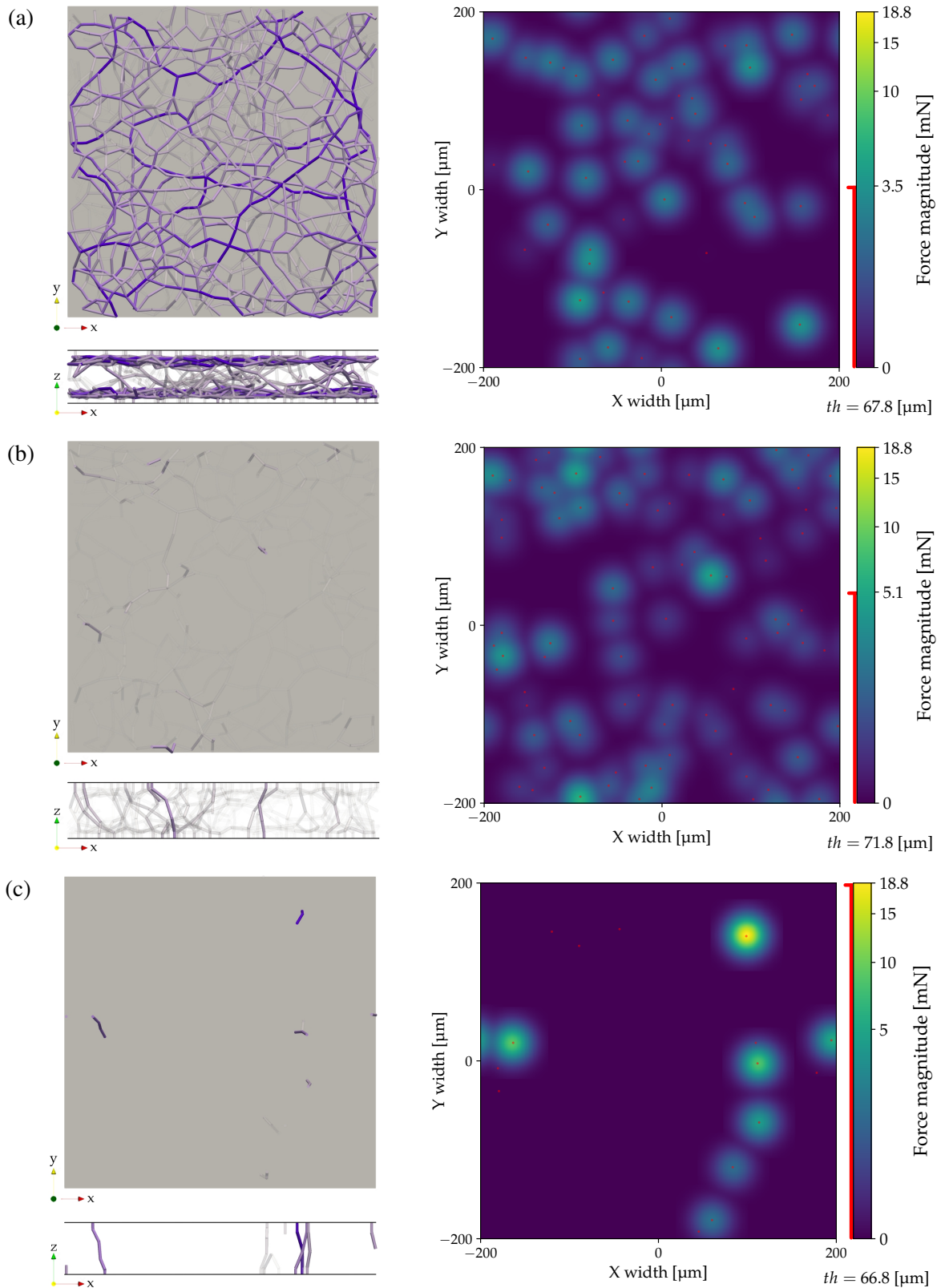


Figure 3.8: Imaging of particles bed forces network over a cycle. Force magnitude includes both normal and tangential components — **Left column)** Lateral (y direction) and top views of forces network (the darker, the stronger). **On the right)** Particle-wall forces maps on top plate (harmonised scale), data processed with Gaussian blur ($\sigma = 10$), colour bar displayed with power norm ($\gamma = 0.4$). **a)** Stage at half of swelling phase, maximum point force on top plate: 3.5 mN. **b)** Stage at the beginning of shrinking, maximum point force on top plate: 5.1 mN. **c)** Stage at half of shrinking phase, maximum point force on top plate: 18.8 mN.

Regarding the second stage in Fig. 3.8b, just at the beginning of shrinking, the first observation is the loss of this double-layer structure. In fact, the reverse occurs: the backbone radically changes from a lateral to a vertical orientation. Even more, the backbone is now subdivided into multiple little backbones, losing its whole-linked structure in favour of multiple individual pillars of force. Now, the vertical forces are stronger, until reaching maximum spots of 5.1 mN. However, because the total force on the top plate is the same, it means that the force distribution is more concentrated into “hot spots”.

In this sense, the third stage in Fig. 3.8c is the extreme manifestation of these “hot spots”: the distribution of forces on top plate is made of only seven spots, including one that carries 40% of the total force (18.8 mN). By the presence of only few strong branches here and there, the left images distinctly show a particles bed that lost all its inner contacts, only formed of rattler particles. This is the reason why, at high frictional case ($\mu = 0.4$ and rotation blocked), the mean coordination number \widetilde{MCN} drops to zero: the high amount of friction enables the creation of single strong branches that support all the top plate force, letting all the other particles free to shrink in an unconstrained and contact-free space. This result is really interesting and questions the way the force applied on electrode is spread within. In real electrode, despite the presence of a binder supposed to maintain a global uniform and cohesive particles bed, the force is maybe carried out by only few backbone branches. This phenomenon would certainly present an impact on electrochemistry, for example by altering the inter-particles conductivity. Of course, this proposition is strictly hypothetical, and it is still difficult to state if the pillars is only an artefact proper to the model (maybe due to the use of rigid plates or spherical particles, for example). The fact remains that the high breathing irreversibility detected with a high frictional case ($\mu = 0.4$ and rotation blocked) is obtained through a numerical behaviour hardly acceptable, due to the drastic global loss of contacts within the particles bed. Hence, using friction to simulate complex shapes of particles or the presence of binder does not seem to be an effective solution. Actually, the main drawback of friction is to be pressure-dependent, because if no force is applied on particles, the simulation of complex shapes or binder is null (exactly what happens when the mean coordination number \widetilde{MCN} drops to down zero). A better way is then to implement a permanent effect of this phenomenon, which is the subject of adhesion or breakable bonds sensitivity analyses (see respectively Section 3.3.4 or Section 3.3.5)

3.3.3 Particles bed stiffness level

This section reintroduces the concept of “stiffness level” presented in Section 2.4.4, evaluated through the stiffness number. As a recall, the stiffness number $\tilde{\kappa}$ evaluates the ratio between pressure and particles rigidity. Moreover, a particles bed with a given stiffness number is supposed to mechanically behaves similarly to another particles bed with the same number, even if both particles beds are submitted to different pressures or have different particles rigidities. Thus, a first intuition would be to analyse only the pressure and to generalise the analysis in terms of stiffness level. However, it is unclear if the concept of stiffness level is compatible with a breathing particles bed. For this reason, it is proposed here to analyse both pressure and particles rigidity, in order to observe an eventual convergence between both approaches concerning the stiffness level.

3.3.3.a Pressure

The pressure applied on the electrode is a key parameter in practice, as it is found to have a noticeable impact on cell performances (see Section 1.1.1), so a sensitivity analysis of pressure to analyse its impact on electrode microstructure seemed evident. For this purpose, eight values were analysed, from 0.1 to 100 MPa, that can be compared to the range used in experimental applications, generally between 0.1 and 10 MPa. In the experiments, cells stop working when the applied pressure exceeds 10 MPa, presumably due to closed porosity of the electrodes. The model permits to explore an order of magnitude above.

First, Fig. 3.9a displays the different curves of pressure during relaxation. They all start at around 54.1 MPa (calendering pressure, 3.9a.①) and efficiently tends to each respective PID input. We can notice that high pressures (60 and 100 MPa) present a quick response time with straight curves, which due to the action of top plate PID controller. At the opposite, the other pressures (lower than the calendering pressure) simply follow the elastic relaxation of particles. One of the precaution when changing the pressure on the DAM is to check once again the inertia. Indeed, the pressure is one of the parameters of the inertial number, so its influence is direct. In this sense, Fig. 3.9b plots the different curves of the inertial number. It clearly

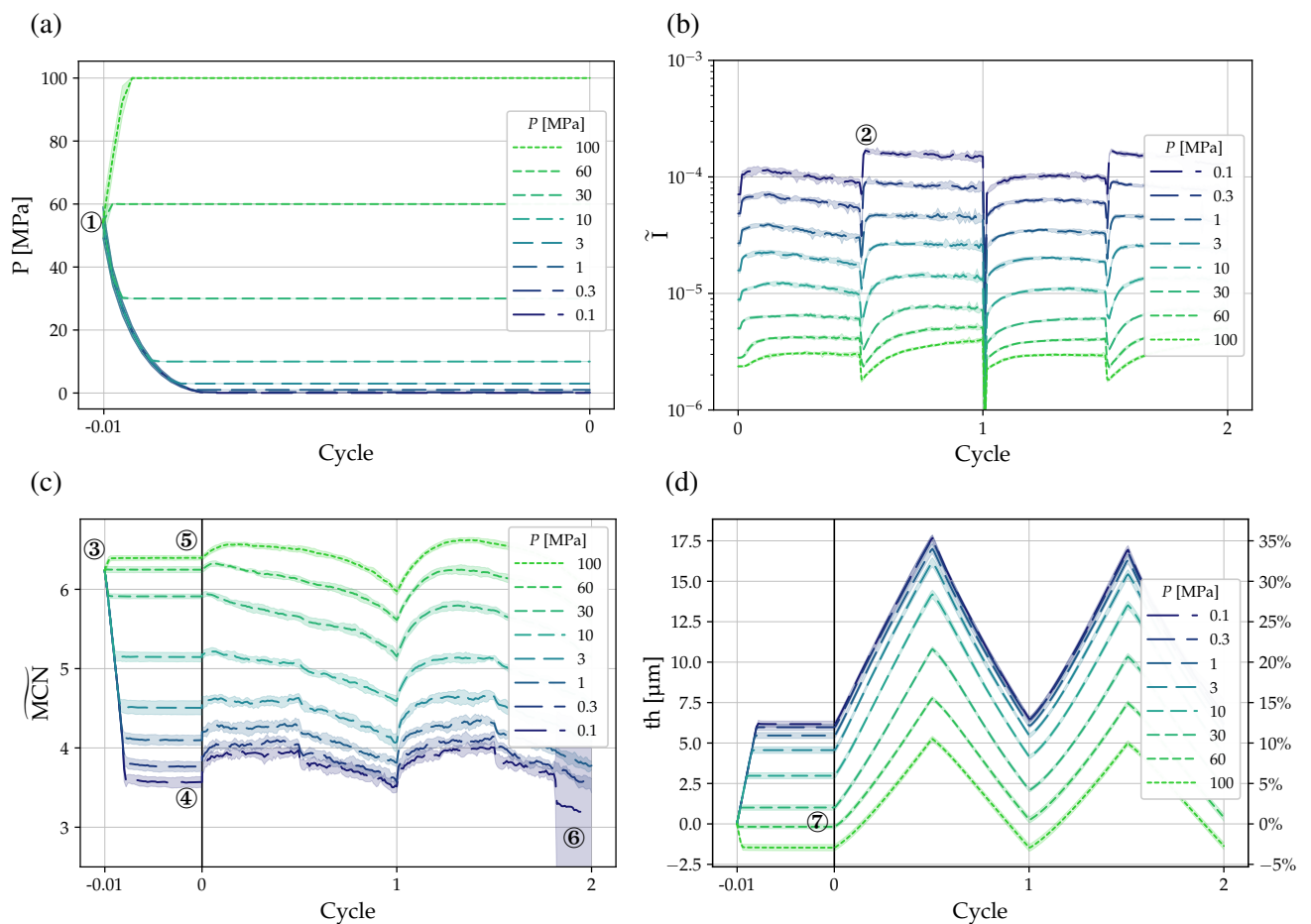


Figure 3.9: Influence of pressure on top plate (8 values set, DAM reference sample for $P = 0.3$ MPa) — **a**) Pressure on top plate (relaxation). **b**) Inertial number (cycling). **c**) Mean coordination number (relaxation and cycling). **d**) Thickness (relaxation and cycling), $th_{ref} = 50 \mu\text{m}$.

changes as the reverse of the pressure, which is coherent with Eq. (2.64). The major doubt on respect of inertia was mainly about the low pressures. Fortunately, the highest curve at $P = 0.1$ MPa does not exceed $1.68 \times 10^{-4} \pm 0.07 \times 10^{-4}$ (3.9b.②). Concerning the mean coordination number \widetilde{MCN} in Fig. 3.9c, the relaxation leads to really different values, positively correlated with the pressure (the higher the pressure, the higher the post-relaxation mean coordination number). Starting at around 6.24 ± 0.05 (3.9c.③), it spreads from 3.56 ± 0.07 at $P = 0.1$ MPa (3.9c.④) to 6.40 ± 0.03 at $P = 100$ MPa (3.9c.⑤). During the cycling, the orders of magnitude remain approximately the same for each pressure. Note that it is possible to observe, once again, the presence of important dispersion at the end of the second cycle (3.9c.⑥). This may be related to the same phenomenon of pillars generation described above in Section 3.3.2.b, due to the lower amount of pressure applied, maybe less susceptible to break these pillars (even if the rotation is activated, some friction is still able to maintain columns of particles). Concerning the thickness itself in Fig. 3.9d, the relaxation leads to reversed behaviour: the higher the pressure, the lower the post-relaxation thickness. A singular relaxation is the one at 60 MPa that remains almost flat (3.9d.⑦), which is consistent with the pressure of calendering. As a recall, the DAM reference sample is built such that the calendering pressure is between 40 and 60 MPa. During the cycling, the different curves follow a quite interesting behaviour that echoes the prediction made in Section 2.4.4: an influential action on DAM would be an increase of pressure. Indeed, all the curves for 0.1, 0.3, 1 and 3 are almost merged, whereas the curves for 10, 30, 60 and 100 distinctly and gradually drops, so most of the change occurs at high pressure.

For a better view, Fig. 3.10a plots the swelling amplitude thickness Delta of the first cycle (left axis). Moreover, in this case, the initial volumes of particles ($V_{\text{part},0}$ in Eq. (2.58)) does not depend on the sensitivity parameter (pressure P), so the swelling breathing coefficient $\mathfrak{B}_{s,\text{sw}}$ is directly proportional to the swelling amplitude Δth_{sw} . The resulting curve is then plotted with a different scale, on right axis. The curve begins with a flat evolution at lowest values of pressure and then quickly drops when the pressure exceeds 10 MPa, which goes exactly in the direction predicted by the stiffness number analysis. However, the order of magnitude of

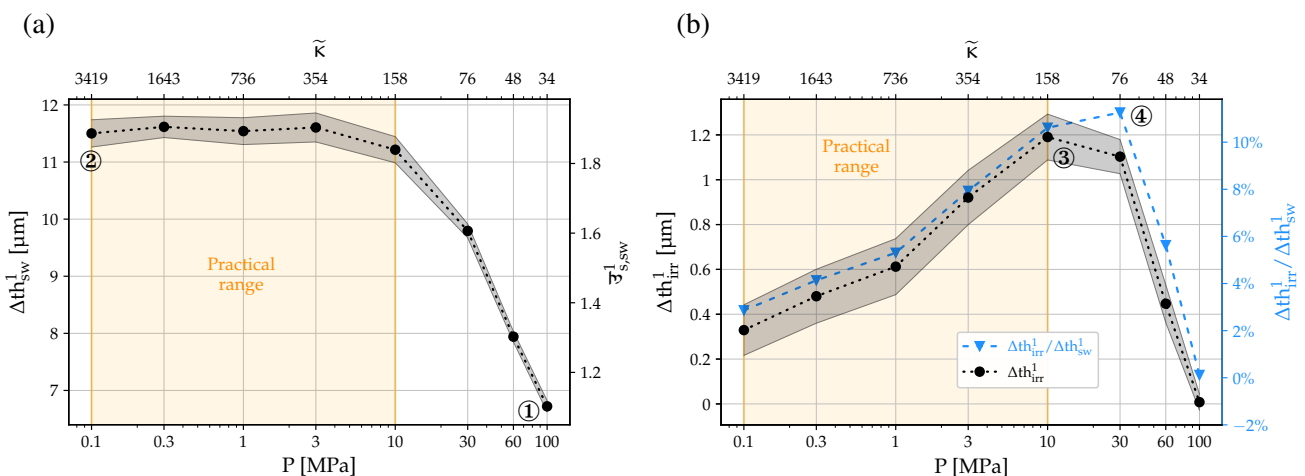


Figure 3.10: Influence of pressure on top plate (8 values set, DAM reference sample for $P = 0.3$ MPa). Rectangular areas represent the common practical range of pressure — **a)** Swelling amplitude thickness Delta and breathing coefficient (first cycle). **b)** Irreversibility thickness Delta (first cycle), dot markers, left axis. Ratio of irreversibility over swelling amplitude thickness Deltas (first cycle), triangle markers, right axis.

the stiffness number, displayed in upper horizontal axis, does not exactly fit the rigidity transition limit stated by Radjai & Dubois (2010) [208], approximately equal to 2000 (not rigid bed below this value and rigid bed below). As a recall, it was detailed in Section 2.4.4 that the state more sensitive to pressure would be at values under 1000. In the current result, the pressure presents a high influence only for value of $\tilde{\kappa}$ inferior to 350. Many factors could explain this difference. For example, the estimations given by Radjai & Dubois (2010) [208] are based on a mono-material particles bed (only one Young's modulus), and also, the mean coordination number \widetilde{MCN} is interdependent to these limits. More importantly, the current result does not display deformation imposed to the particles bed but the particles bed that breathes differently depending on the pressure. Thus, the described behaviour does not correspond to the phenomenon the stiffness number $\tilde{\kappa}$ was evaluated for. By considering the DAM reference sample properties, the stiffness number $\tilde{\kappa}$ states that the electrode submitted to the actual pressure ($P = P_{\text{ref}} = 0.3$ MPa) should be influenced by pressure. Nevertheless, the reverse occurs here: the electrode breathes pressure-independently. Consequently, the limit of 2000 seems not relevant considering the studied breathing behaviour. In any case, the evolution of the swelling amplitude remains coherent with the stiffness analysis, *i.e.* the breathing does not change at higher values of $\tilde{\kappa}$, with a transition limit at around 300 ($\widetilde{MCN} \simeq 4.5$). The most important result in Fig. 3.10a remains the breathing coefficient $\overline{\mathfrak{V}}_{s,sw}$ that clearly presents a volume distribution disparity between levels of pressure, from 1.10 ± 0.02 at $P = 100$ MPa (3.10a.①) to 1.88 ± 0.04 at $P = 0.1$ MPa (3.10a.②). By calculating the equivalent $1/\overline{\mathfrak{V}}_{vs,sw}$, we respectively get 0.1 at 3.10a.① and 0.88 at 3.10a.② (values not displayed in graphs). In other words, for $P = 100$ MPa, the void volume variation is equal to only 10% of the particles volume variation, against 88% for $P = 0.1$ MPa. It demonstrates that the high pressure at for $P = 100$ MPa has noticeably reduced the void volume variation, the electrode close to a solid breathing.

Concerning the irreversibility, the order of magnitude is too low to consider it as significant. However, its evolution, significant as regard to the uncertainty, is worth the analysis. It was intuitively expected that the irreversibility would decrease as much as the pressure would increase. However, we observe in Fig. 3.10b a transition stage at $P = 10$ MPa ($\tilde{\kappa} \simeq 150$), where the absolute maximum reaches 1.2 ± 0.1 μm (③). For the relative maximum (as a proportion of swelling amplitude thickness Delta), the maximum is at $P = 30$ MPa ($\tilde{\kappa} \simeq 80$), with a proportion of 11.2% (④). The interpretation of these figures is developed in the next section (Section 3.3.3.b), because this observation are quite comparable with the particles' rigidity analysis.

3.3.3.b Particles' rigidity

As another fundamental parameter of stiffness level, the particles' rigidity is set in the DAM through the Young's modulus. For this sensitivity analysis, all particles were set to the same Young's modulus ($E_{\text{CSi}} = E_{\text{Gr}} = E$). As a recall, the DAM reference sample considers two distinct Young's moduli ($E_{\text{CSi}} \neq E_{\text{Gr}}$). Ten values were analysed, from 0.1 to 100 GPa. The initial particles distributions and positions used for the current analysis are the same as in the pressure analysis (Section 3.3.3.a).

Concerning the validation of dynamics, the inertia was not clearly correlated to the sensitive parameter and the maximum average value of inertial number was around 7.1×10^{-5} , so this aspect was fulfilled (inertial number graph not displayed). The force was also well stabilised, comprised in a range of $\pm 0.25\%$ of the input PID all along the cycle (force graph not displayed). Concerning the mean coordination number \widetilde{MCN} , displayed

in Fig. 3.11a, the particles Young's modulus presents a clear influence: the more rigid, the lower the mean coordination number. Indeed, changing the Young's modulus from 0.1 to 100 GPa changes the final relaxation value of \overline{MCN} from 6.17 ± 0.03 (3.11a.①) to 3.48 ± 0.08 (3.11a.②). The reduction of Young's modulus improves the particles packing by allowing a lower compression thickness, considering a given pressure. Indeed, when looking at Fig. 3.11b, the thickness evolves similarly as varying the pressure, but reversely: the decrease of Young's modulus leads to a lower relaxation thickness, but also a decrease of amplitude. This also supports the prediction estimated in Section 2.4.4, about the major influence of the decrease of Young's modulus. Indeed, the curves at higher Young's modulus are quite similar, as the opposite to those at lower Young's modulus that exhibits a real influence.

For a better view, Fig. 3.12a presents the swelling amplitude Δth_{sw} of first cycle as a function of Young's modulus. As for pressure analysis, the plot is divided into two parts: a dependent part, between 0.1 and 2 GPa, and independent part, between 2 and 5 GPa. Through these two parts, the breathing evolves consistently with the stiffness number $\tilde{\kappa}$: the higher the value, the less variant the swelling amplitude. In addition, the interesting fact revealed by this figure is the stiffness number corresponding to the limit between both parts: $\tilde{\kappa} \simeq 380$. Even if, once again, a discrepancy appears by taking the limit of 2000 fixed by Radjai & Dubois (2010) [208], this value of transition is really close to the one found during the pressure analysis, for the exact same limit of swelling amplitude variability ($\tilde{\kappa} \simeq 350$). Concerning the breathing coefficient, nothing new particularly appears compared to the pressure analysis, with values going from 1.29 ± 0.01 at $E = 0.1$ GPa (3.12a.①) to 1.88 ± 0.04 at $E = 100$ GPa (3.12a.②). Concerning the irreversibility Δth_{irr} in Fig. 3.12b, here again, the amount reaches an absolute maximum of $1.2 \pm 0.1 \mu\text{m}$ (3.12b.③) at $E = 0.5$ GPa ($\tilde{\kappa} \simeq 150$), which remains quite low. As a result, the curve knows a part of increase and another of decrease around this value, and the limit stiffness number, as before, is shown to be approximately $\tilde{\kappa} \simeq 150$ for the absolute maximum. For the relative maximum (as a proportion of swelling amplitude Δth_{sw}), the maximum is at $E = 0.2$ MPa ($\tilde{\kappa} \simeq 80$), with a proportion of 12.0% (3.12b.④).

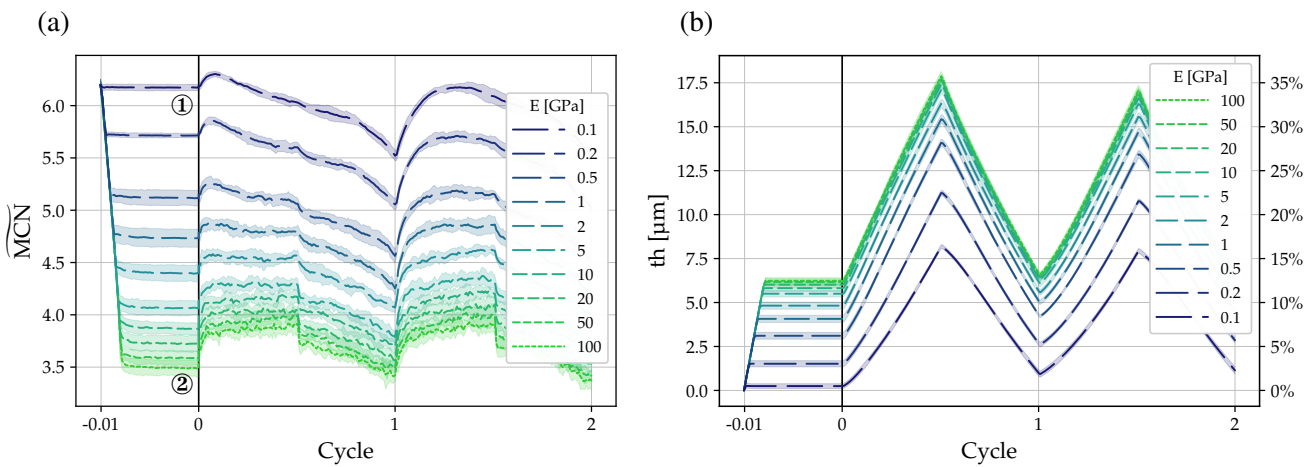


Figure 3.11: Influence of particles' rigidity (10 values set, DAM reference sample for $E = 20\sim 30$ GPa — **a**) Thickness (relaxation and cycling), $th_{ref} = 50 \mu\text{m}$. **b**) Mean coordination number (relaxation and cycling).

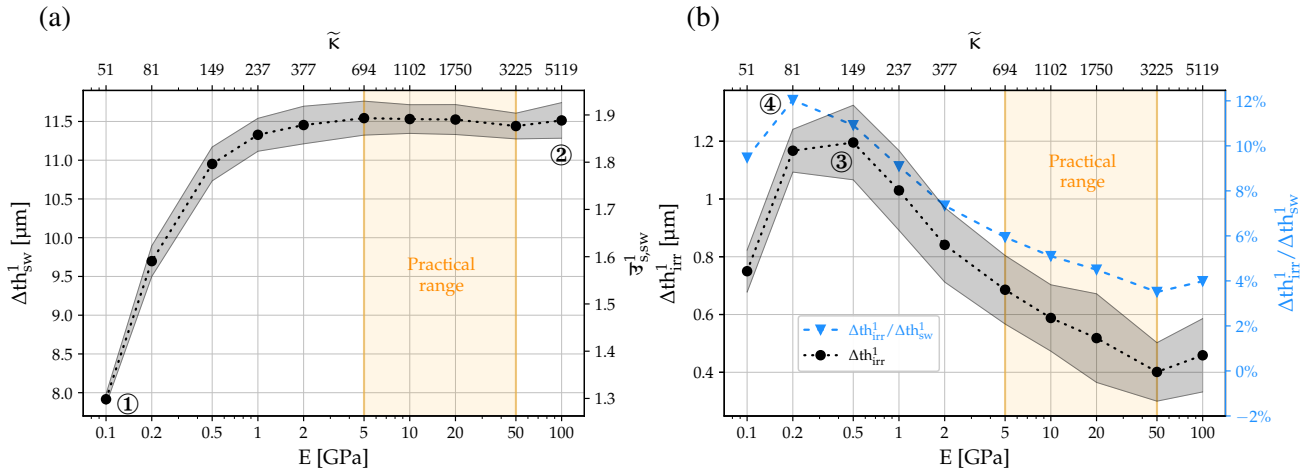


Figure 3.12: Influence of particles' rigidity (10 values set, DAM reference sample for $E = 20\sim 30$ GPa). Rectangular areas represent the common practical range of Young's modulus — **a**) Swelling amplitude thickness Δth_{sw} and breathing coefficient (first cycle). **b**) Irreversibility thickness Δth_{irr} (first cycle), dot markers, left axis. Ratio of irreversibility over swelling amplitude thickness Δth_{sw} (first cycle), triangle markers, right axis.

3.3.3.c Global stiffness level perspective

In a summary, beyond the pressure and Young's modulus taken individually, the key information brought by these sensitivity analyses is the concordance of behaviours considering a stiffness level perspective. The estimation made in Section 2.4.4 seem to be right, and the stiffness number $\tilde{\kappa}$ is maybe an efficient way to evaluate the influence of both pressure and particles rigidity on breathing. In fact, these observations give the impression that the real prediction of the stiffness level impact on breathing mainly lies in the value of $\tilde{\kappa}$. As a good illustration, Fig. 3.13 plots the swelling amplitude Δth_{sw} (from Figs. 3.10a and 3.12a) and irreversibility Δth_{irr} (from Figs. 3.10b and 3.12b) at first cycle as a function of stiffness level. In both cases, the curves match quite well, even the dispersion areas. As a result, as a general indicator of both pressure and particles rigidity, the stiffness number $\tilde{\kappa}$ is consistent to describe the electrode breathing. However, the conventional limit of rigidity ($\tilde{\kappa} \simeq 2000$) seems not adapted for the breathing behaviour. More precisely, the limit of swelling amplitude Δth_{sw} is at around $\tilde{\kappa} \simeq 350$ (reduction below this value and no change above), and the irreversibility Δth_{irr} reaches its absolute maximum at $\tilde{\kappa} \simeq 150$ and its relative maximum (as a proportion of swelling amplitude Δth_{sw}) at $\tilde{\kappa} \simeq 80$, even though the absolute irreversibility is quite low.

Globally, these sensitivity analyses suggest the ability of the stiffness number $\tilde{\kappa}$ in describing breathing material. As far as the author knows, this parameter was not used to evaluate the breathing of a material, so the real rigid limit is still unsure and further application of this parameter to breathing will be necessary to clarify the rigid limit values. For example, by looking at the irreversibility, the variation of rigidity on the DAM seems to reveal the confrontation between two phenomena, whose transition phase occurs at around $\tilde{\kappa} \simeq 100$. The current analysis is insufficient to settle the question.

Finally, when it comes to real application, the rectangular areas in Fig. 3.10 and Fig. 3.12 represent the common practical ranges of pressure and Young's modulus (respectively 0.1~10 MPa and 10~50 GPa). It reveals that they are situated in region where they have a really poor influence on swelling amplitude. For irreversibility, their influence exists, but with a limited amount of result (from 0.4 to 0.8 μm). Hence, with this

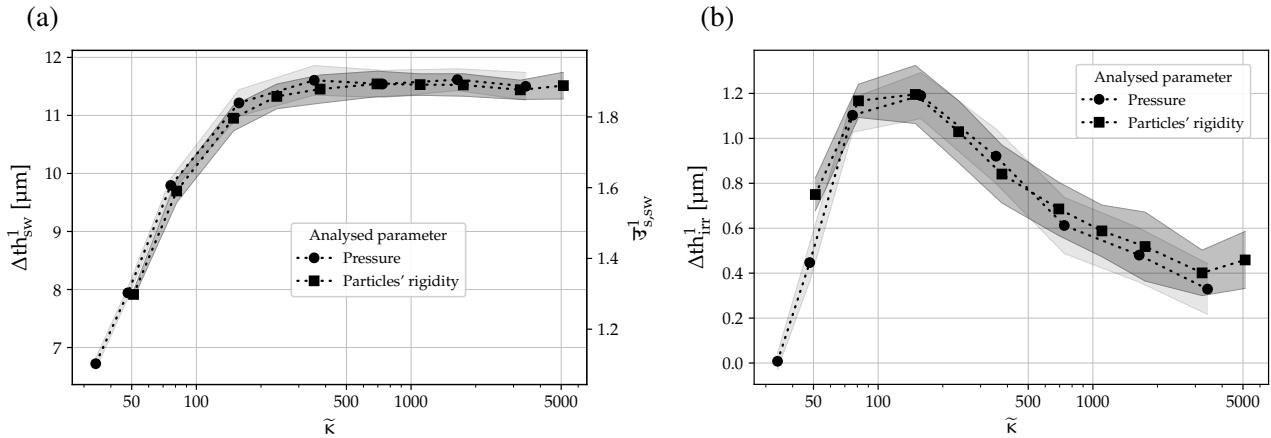


Figure 3.13: Influence of stiffness level (8 to 10 values set, DAM reference sample for $\tilde{\kappa} \simeq 1650$) — **a**) Swelling amplitude thickness Delta and breathing coefficient (first cycle). Results from Figs. 3.10a and 3.12a. **b**) Irreversibility thickness Delta (first cycle). Results from Figs. 3.10b and 3.12b.

view, the stiffness level seems to be a limited key ton control the electrode breathing in practical application. An important point to notice is that these conclusions are stated based on a particles bed with cohesion between particles. An eventual presence of cohesion may impact the breathing behaviour, and its dependency to pressure and/or particles rigidity. Thus, the values of $\tilde{\kappa}$ summarised in this conclusion are only valid in a non-cohesive case. The cohesive remains to be tested.

3.3.4 Adhesion

As discussed in DAM reference sample analysis (Section 3.2) and friction/rotation analysis (Section 3.3.2), the basic Hertz-Mindlin contact law (detailed in Section 1.2.1.b) and the friction fail to capture a realistic breathing, more precisely the irreversibility at first cycle. The hypothesised missing feature is the presence of attraction between particles, quite relevant considering the presence of binder in practical electrode. This attraction would enable the particles bed to store an eventual constrained state (due to calendaring, for example) until it changes to another due to particles breathing reorganisation. In some ways, friction is a form of “state storing method” by blocking particles, but as it is underlined in Section 3.3.2, its action depends on the applied pressure. The current idea is to implement a permanent attraction whose presence is not dependent on pressure. The adhesion between particles, through the use of JKR contact law (detailed in Section 1.2.3.b), is a first way to implement this attraction, as a reversible stickiness between particles (after the loss of contact, stickiness reoccurs).

Technically, it is still hard to estimate the adhesive effect between particles, and especially how this stickiness evolves over time. Indeed, the manufacturing process of an anode may present different steps where stickiness can be more or less enhanced, thinking about the drying or the calendaring. In the protocol proposed here, it is then proposed to study two different configurations of stickiness creation: just after the calendaring (pre-relaxation) or just after the relaxation (post-relaxation). Both versions lead to distinct initial constrained states. The pre-relaxation stickiness configuration is imagined for the case where the calendaring itself, thanks to an important compression, improves the contact of binder between particles and so improve its gluing power. The post-relaxation stickiness configuration if more adapted to simulate the case where, after the relaxation, an additional drying step leads to a reinforcement of the binder strength.

For this sensitivity analysis, eight values of work of adhesion were analysed, between 0 and 40 J/m². The same initial distributions and positions of particles were used in both configurations (pre-relaxation and post-relaxation).

3.3.4.a Pre-relaxation

For this sensitivity analysis, the inertia is globally respected, except for a strange behaviour for $W = 20$ J/m², where the inertial number is much unstable. However, it remains reasonable, with an average value all along cycling at $2.4 \times 10^{-4} \pm 2.7 \times 10^{-4}$ (inertial number graph not displayed). In addition, even if it presents some instabilities for $W = 40$ J/m², the force is globally kept in a $\pm 2\%$ range of PID input (force graph not displayed).

Fairly intuitively, the pre-relaxation configuration of adhesion leads to a different initial state at the beginning of cycling. However, a less expected behaviour occurs during the relaxation, where two groups are distinguished: the non-adhesive case and the adhesive cases. As illustrated in Fig. 3.14a, the first case finished the relaxation at a mean coordination number of 3.75 ± 0.10 (3.14a.①), whereas all other case, even with the lowest work of adhesion, finishes at around 4.79 ± 0.10 (3.14b.②). Thus, the introduction of attraction presents a noticeable impact in particles bed restructuring, even with low amount of adhesion. Of course, a transition may exist between the non-adhesive and adhesive cases, but it was not captured here. Afterwards, this distinction in mean coordination number is maintained all along the cycling, where all the adhesive case follows a similar smoothed evolution of packing level, at the opposite to the non-adhesive case, lower and less stable. Concerning the thickness in Fig. 3.14b, this non-adhesive/adhesive distinction is not present at all, starting with the final thickness of relaxation at around 6.0 ± 0.3 μm (3.14b.③) for all curves. Finally, during cycling, the curves show a significant result: the apparition of an irreversibility at first cycle, all the more important as the work of adhesion increases (arrow 3.14b.④). In addition, this irreversibility is not comparable to the one captured in Section 3.3.2, more precisely the one in Fig. 3.7b (high friction case: $\mu = 0.4$ and rotation blocked). Indeed, the present particles bed of adhesive forces is confirmed to be rightly packed by the mean coordination number \overline{MCN} comprised between 4.3 and 4.8 during cycling. Furthermore, the good stability of mean coor-

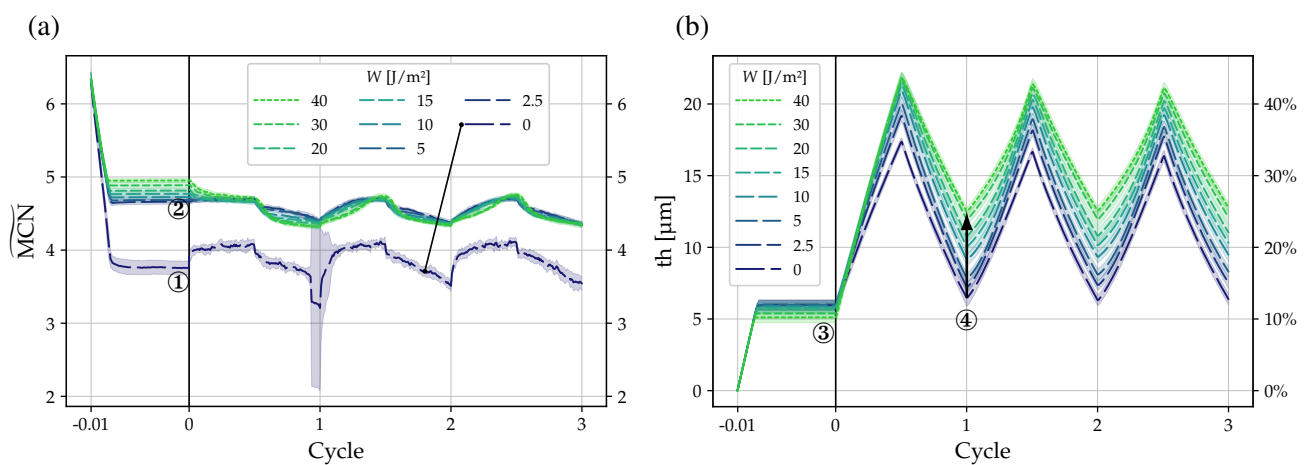


Figure 3.14: Influence of pre-relaxation activated adhesion (8 values set, DAM reference sample for $W = 0$ J/m²) — **a**) Mean coordination number (relaxation and cycling). **b**) Thickness (relaxation and cycling), $th_{ref} = 50$ μm .

dination number when adhesion is present suggests a smoother reorganisation of particles, as opposite to the noisy curve of mean coordination number \widetilde{MCN} when adhesion is absent. Hence, the irreversibility appearing at first cycle is most likely not generated by singular backbone branches generation but by a real structure change homogeneously spread. Of course, the adhesion can generate a mean coordination number that bias the force network interpretation, due to the fact that the rattler particles are certainly glued to the backbone particles. Consequently, rattler particles do not move freely in empty space, which increases the mean coordination number, but still do not participate in the main backbone branches.

To go into deeper analysis, Fig. 3.15a displays the irreversibility Δth_{sw} at first cycle. It explicitly exposes the gradual increase of this quantity as a function of work of adhesion, until reaching a maximum of $7.7 \pm 0.2 \mu\text{m}$ (44.2% of the corresponding swelling amplitude, 3.15a.①). A peculiar behaviour also appears for the swelling amplitude: whereas Δth_{sw} for high work of adhesion is maximum at the first cycle (see x-axis coordinate 1 in

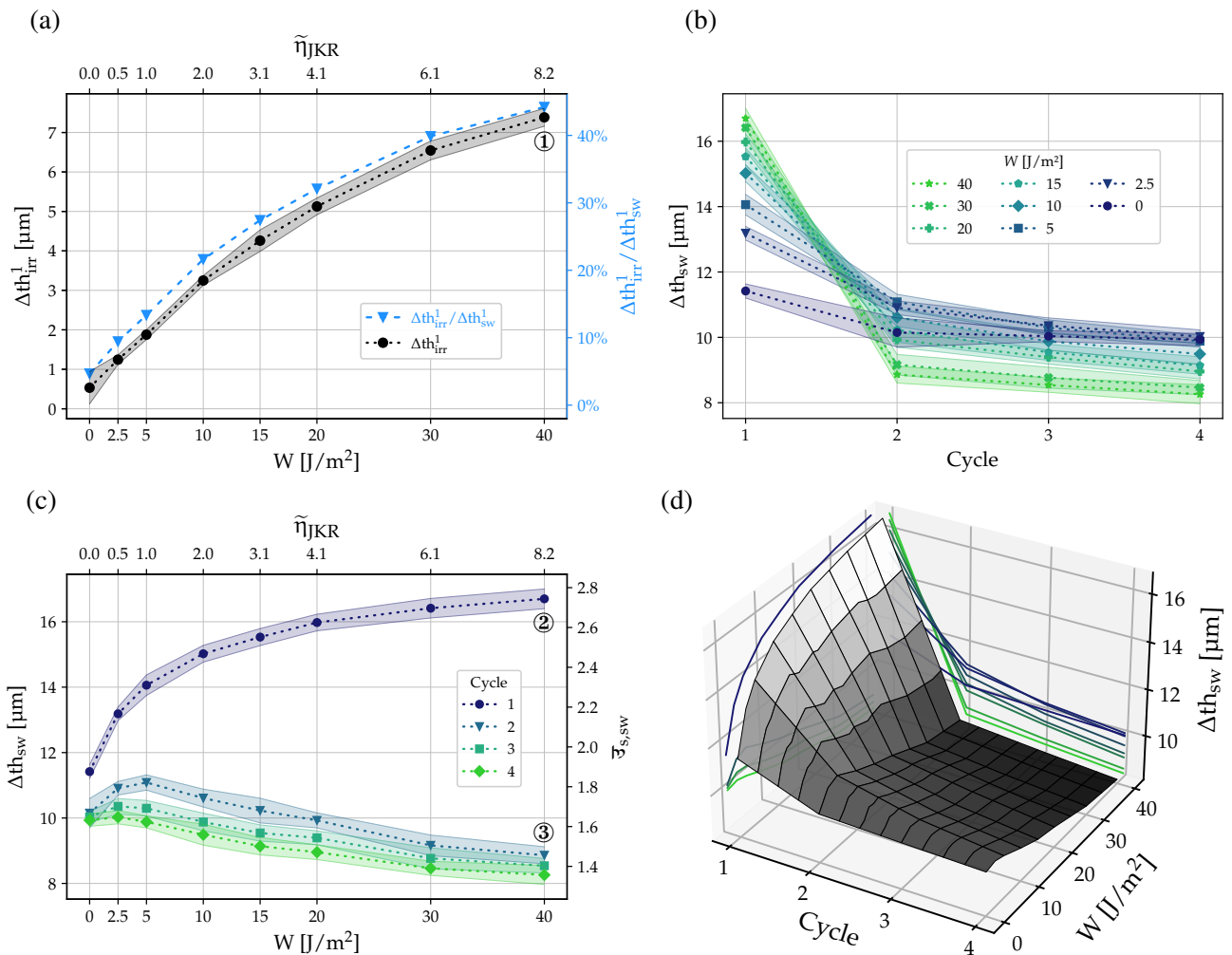


Figure 3.15: Influence of pre-relaxation activated adhesion (8 values set, DAM reference sample for $W = 0 \text{ J}/\text{m}^2$) — **a)** Irreversibility thickness Delta (first cycle), dot markers, left axis. Ratio of irreversibility over swelling amplitude thickness Deltas (first cycle), triangle markers, right axis. **b)** Swelling amplitude thickness Delta (as a function of cycles). **c)** Swelling amplitude thickness Delta and breathing coefficient (as a function of work of adhesion). **d)** Swelling amplitude thickness Delta (as a function of cycles and work of adhesion).

Fig. 3.15b, curve with round markers in Fig. 3.15c), it has then the minimum value for the second cycle (see x-axis coordinate 2 in Fig. 3.15b, curve with triangle markers Fig. 3.15c). The same trend is obtained for the other works of adhesion, to a lesser extent. From the second cycle, Fig. 3.15c draws a variation as a function of work of adhesion with a maximum value. The noticeable information is the situation of the maximum, at $W = 5 \text{ J/m}^2$ that corresponds to a cohesion number of $\tilde{\eta}_{\text{JKR}} \simeq 1$, in other words when the confinement forces are equivalent to attractive forces. A key observation between first and second cycle is the nature of the breathing. As detailed in Fig. 3.15b, the first cycle is a pseudo void breathing ($\Delta V_{\text{void}} > \Delta V_{\text{particles}}$), as proved by the breathing coefficient whose value is always above 2, except for the non-adhesive case. For example, in the most adhesive case ($W = 40 \text{ J/m}^2$), the swelling breathing coefficient reaches 2.77 ± 0.05 (3.15c.②). The corresponding value of $1/\overline{\mathfrak{A}}_v$ is around 0.64 (value not displayed in graphs), which indicates that the void volume variation constitutes around 64% of the electrode breathing. On the opposite, from the second cycle, the breathing is mainly dominated by the solid volume variation. For example, at the highest work of adhesion, the swelling breathing coefficient is about 1.45 ± 0.04 (3.15c.③). Via the corresponding value of $1/\overline{\mathfrak{A}}_v$, we find that the void volume variation constitutes only 31% (value not displayed in graphs). This behaviour gives birth to a permanent reduction of swelling amplitude compared to non-adhesive case, drawn in Fig. 3.15d as the darkest area on the right of the swelling amplitude surface. This darkest area expresses the duality of two phenomena during the breathing of cohesive particles: an increased amplitude at the first cycle that is reversed from the second cycle, compared to the non-cohesive case.

3.3.4.b Post-relaxation

The activation of adhesion after the relaxation was not particularly expected to have a significant impact on breathing, compared to the pre-calendering activation, due to the reversible nature of the stickiness. The results indeed demonstrates a high similarity between pre-relaxation and post-relaxation configurations. More precisely, in Fig. 3.16a and Fig. 3.16b all curves evolves exactly the same as the DAM reference sample during relaxation phases (between -0.01 and 0), since the adhesion is not activated yet. Despite this, immediately at the beginning of cycling phase when adhesion is activated, the adhesive curves come back closely to the curves found in pre-relaxation simulations (respectively Fig. 3.14a and Fig. 3.14b). In addition, Fig. 3.16c and Fig. 3.16d reveal a reduction of irreversibility and swelling amplitude at first cycle. This reduction is all the more important that the work of adhesion is high, until 18% of reduction for irreversibility (arrow 3.16c.①) and 9% for swelling amplitude (arrow 3.16d.②). Despite these differences at first cycle, the breathing globally converges to the same behaviour and presents a similar area of swelling amplitude reduction (as in Fig. 3.15d).

3.3.5 Breakable bonds

The implementation of breakable bonds between particles brings the same features as adhesion, but it considers the gluing phenomenon through an irreversible way. Any attractive contact is definitively lost when the associated bond breaks. As before, an important question is the time when this inter-particles bonds are really generated. Thus, both pre-relaxation and post-relaxation configurations were studied, considering each time the same initial distributions and positions of particles.

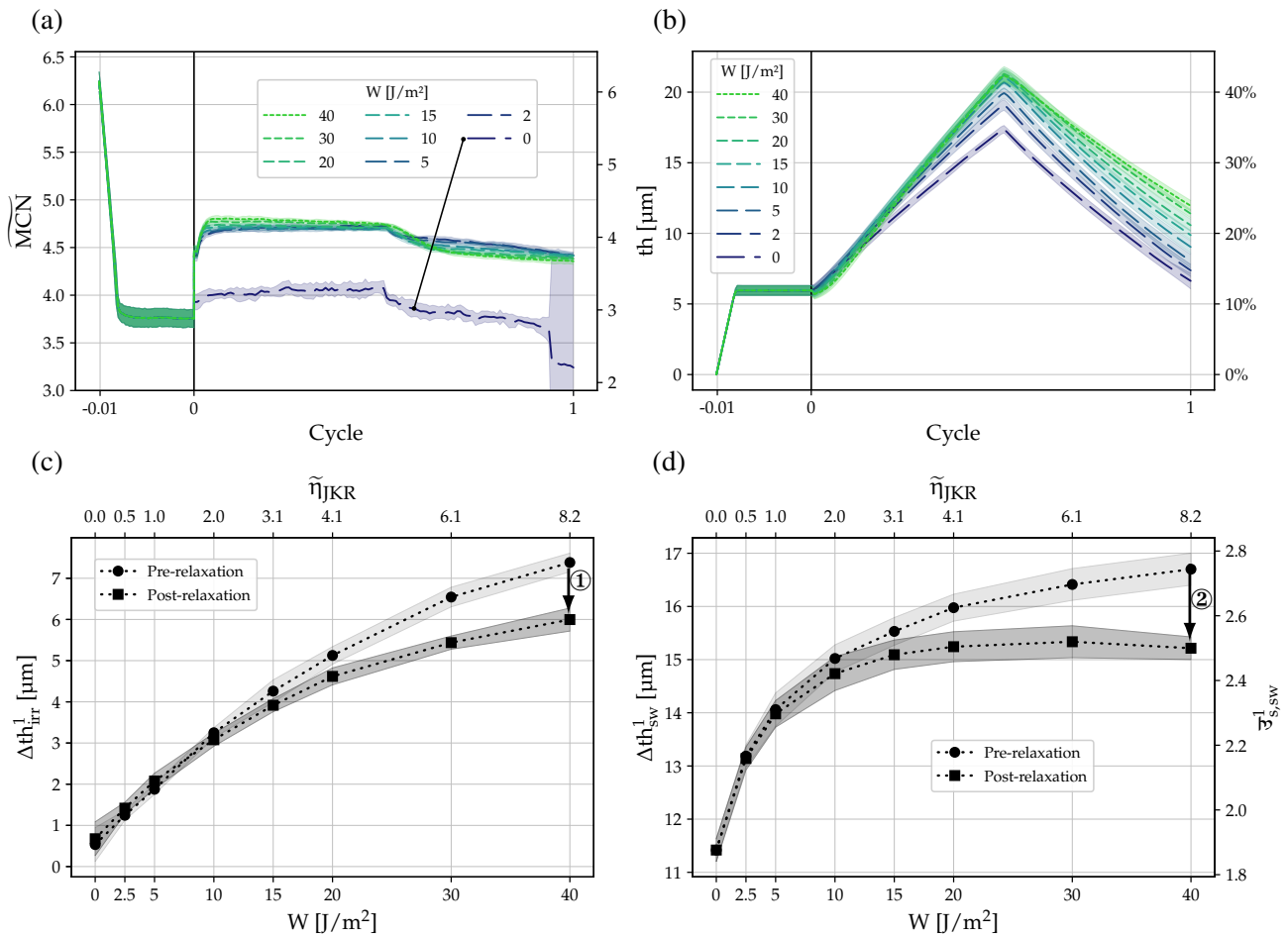


Figure 3.16: Influence of post-relaxation activated adhesion (8 values set, DAM reference sample for $W = 0 \text{ J/m}^2$) — **a**) Mean coordination number (relaxation and cycling). **b**) Thickness (relaxation and cycling), $th_{ref} = 50 \text{ µm}$. **c**) Irreversibility thickness Delta (first cycle, pre-relaxation and post-relaxation activated adhesion). **d**) Swelling amplitude thickness Delta and breathing coefficient (first cycle, pre-relaxation and post-relaxation activated adhesion).

3.3.5.a Pre-relaxation

This sensitivity analysis particularly respects the inertia criterion. The inertial number is even lower with stronger particles bonds, implying a maximum average value of inertial number all along cycling during the non-bonded case, at $7.1 \times 10^{-5} \pm 1.3 \times 10^{-5}$ (inertial number graph not displayed). Nevertheless, the force on top plate was slightly unstable during the first cycle for the strongest bonds cases ($st_{max} = 30, 35$ and 40 MPa), showing some peaks certainly generated by bond breaks. Fortunately, these peaks are maintained in a $\pm 5\%$ PID input range, which remains reasonable (force graph not displayed). When it comes to particles themselves, as for adhesion, the relaxation is quite impacted by the presence of bonds. Looking at Fig. 3.17a, two groups emerge from this first relaxation: distinguished by the final mean coordination number at the end of relaxation. As the opposite of adhesion where two clear groups of non-adhesive/adhesive appeared, they are here distinguished by a limit value of bond strength. For a value of maximum stress from 0 to 15 MPa, the final mean coordination number is around 3.76 ± 0.03 (3.17a.①), whereas from 25 to 40, it is around 5.59 ± 0.02 (3.17a.②). A transitional value appears for $st_{max} = 20 \text{ MPa}$ where the final mean coordination is 5.1 ± 0.2 (3.17a.③). The

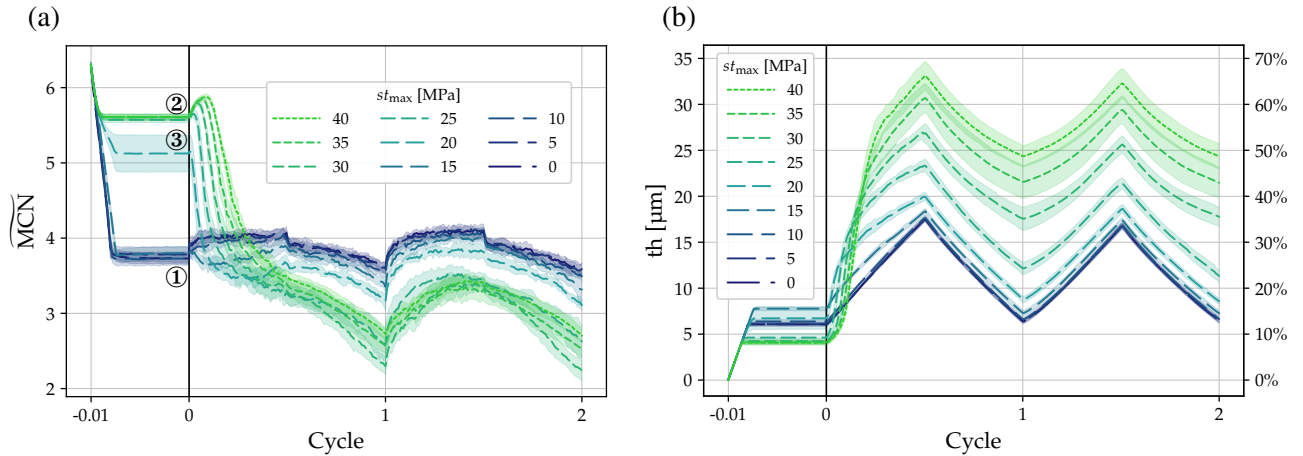


Figure 3.17: Influence of pre-relaxation generated bonds (9 values set, DAM reference sample for $st_{max} = 0$ MPa) — **a)** Mean coordination number (relaxation and cycling). **b)** Thickness (relaxation and cycling), $th_{ref} = 50 \mu\text{m}$.

first group (st_{max} from 0 to 15 MPa) that we can call the “**weak-bonds case**” evolves similarly to a non-bonded case (DAM reference sample, $st_{max} = 0$ MPa): variation of mean coordination number with limited amplitude around 3.9 and triangular variation of thickness with no significant irreversibility, as also shown in Fig. 3.17b. The second group (st_{max} from 25 to 40 MPa) that we can call the “**strong-bonds range**” presents a singular behaviour: at the beginning of cycling phase, the mean coordination number lightly increases before dropping down under values of weak-bonds range, as shown in Fig. 3.17a. After this, the average values of mean coordination remains inferior to the weak-bonds range. By looking at the thickness curves in Fig. 3.17b, it is possible to better understand this behaviour. The curves of strong-bonds range show an initial delay of swelling (smoothed shape at $c = 0$ cycle). This may be due to the strength of bonds that maintain the structure steady, even though all the particle start to swell. Due to the particles swelling, the number of contacts increases within the particles bed, as the jumps of mean coordination number indicates just after 3.17a.②. This increase goes until a critical limit that depends on the value of st_{max} , where a “break chain” engenders successive ruptures of many bonds. At this stage, the delayed electrode swelling radically raises higher than the weak-bonds range.

This characteristic behaviour, in fact, generates a result comparable to the adhesion analysis in terms of thickness Deltas, as shown in Fig. 3.18a: a first drastic swelling amplitude at first cycle, all the more that bonds strength is high, and a reversed trend from the second cycle that, once again, remains constant for the following cycles. To really observe the difference with adhesion, we have to plot it as a function of the sensitivity parameter (here, st_{max}), as in Fig. 3.18b (that should be compared with Fig. 3.15c for adhesion). The curves show a clear distinction of swelling amplitude Δth_{sw} evolution correlated with the bonds’ strength groups. At first cycle, the swelling amplitude is almost independent of the maximum bond stress for weak-bonds range (st_{max} from 0 to 15 MPa). For example, the Δth_{sw} value remains limited at $10.6 \pm 0.3 \mu\text{m}$, with a corresponding breathing coefficient of 1.74 ± 0.04 (3.18b.①). Starting from 20 MPa, the swelling amplitude now depends on the maximum bond stress st_{max} , with a relationship that seems linear. The swelling amplitude Δth_{sw} then increases until $29.0 \pm 1.6 \mu\text{m}$, which corresponds to a breathing coefficient of 4.7 ± 0.3 (3.18b.②). Considering the equivalent $1/\bar{\epsilon}_{v,sw}$, we get the values 0.41 3.18b.① and 0.78 at 3.18b.② (values not displayed

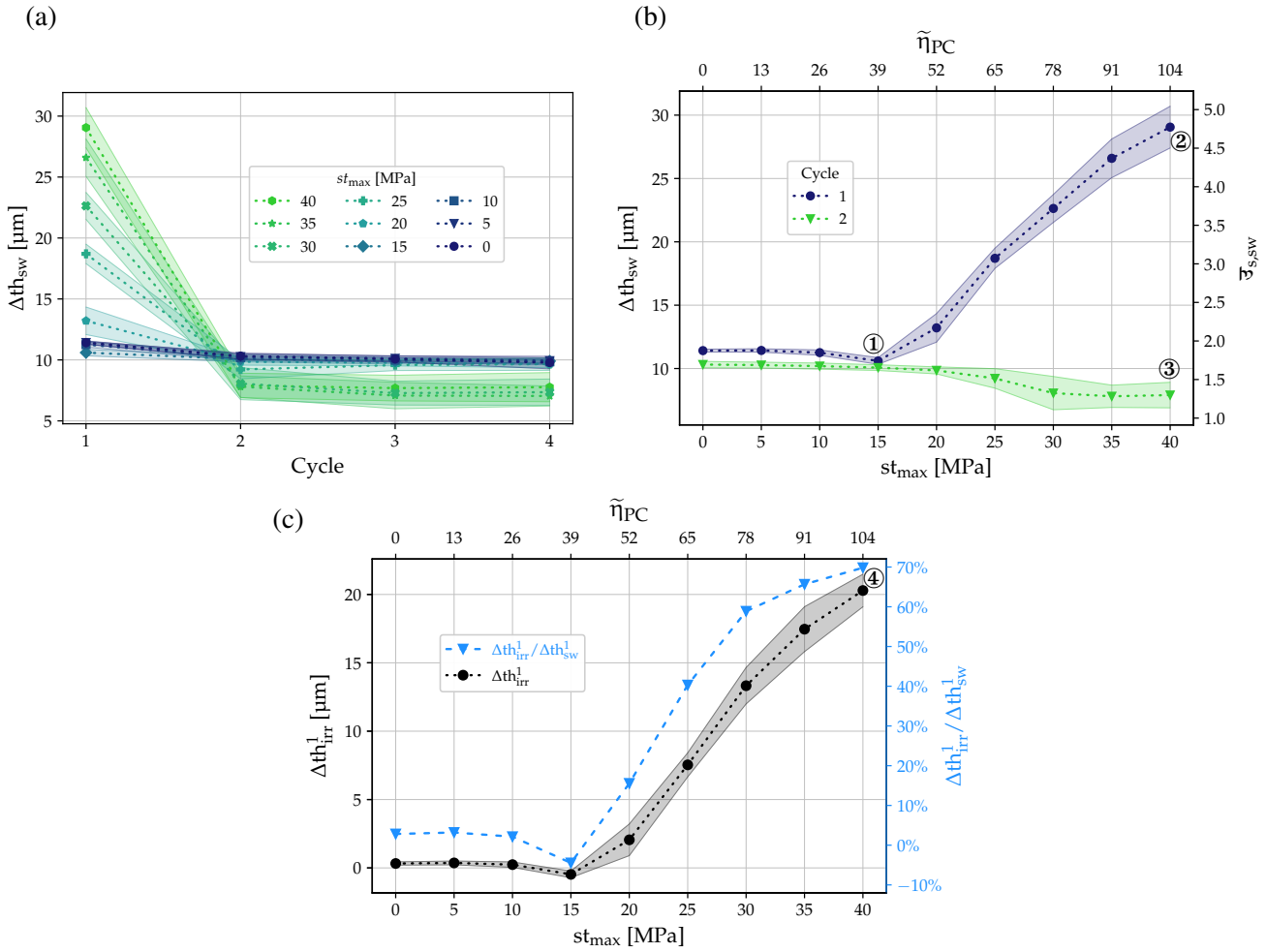


Figure 3.18: Pre-relaxation generated bonds (9 values set, DAM reference sample for $st_{max} = 0$ MPa) – **a)** Swelling amplitude thickness Delta and breathing coefficient (as a function of cycles). **b)** Swelling amplitude thickness Delta and breathing coefficient (as a function of maximum bond stress). **c)** Irreversibility thickness Delta (first cycle), dot markers, left axis. Ratio of irreversibility over swelling amplitude thickness Deltas (first cycle), triangle markers, right axis.

in graphs). It means that at weak-bonds range, the electrode volume variation is composed of around 41% of void volume variation, against 78% at the highest point of strong-bonds case. The other noticeable information is the radical change of breathing from the second cycle. Similarly to adhesion, the trend is now reversed, and the swelling amplitude Δth_{sw} decreases with maximum bond stress st_{max} , however less importantly, until $7.9 \pm 1.0 \mu m$, corresponding to a breathing coefficient of 1.3 ± 0.2 (3.18b.③). The equivalent $1/\tilde{\eta}_{v,sw}$ gives 0.23, so the electrode volume variation is composed of around 23% of void volume variation. Finally, the irreversibility Δth_{irr} at first cycle is well correlated with the swelling amplitude, as shown in Fig. 3.18c. The irreversibility is almost null for the weak-bonds range and linearly increases in strong-bonds range, until reaching $20.2 \pm 1.2 \mu m$ that corresponds to around 70% of the corresponding swelling amplitude Δth_{sw} (3.18c.④). Concerning the cohesion number $\tilde{\eta}_{PC}$ plotted on Figs. 3.18b and 3.18c, it was expected that the limit value of 1 would match with the limit between weak-bonds and strong-bonds ranges ($st_{max} \simeq 15 \sim 20$ MPa). Nevertheless, this is not the case, the corresponding value being at $\tilde{\eta}_{PC} \simeq 40 \sim 50$. In other words, the cohesion forces of bonds have to be around fifty times more predominant than contact forces due to pressure to create a significant impact. However,

this conclusion is questionable. Indeed, the cohesion number $\tilde{\eta}_{PC}$ that is defined in Eq. (2.70) (Section 2.4.5) partially takes into account the maximum stress criterion (only tensile and without torque). This definition may be incomplete to fully describe the cohesive power of breakable bonds. No particular exploration of this number was carried out to detail the question and redefine this number properly.

3.3.5.b Post-relaxation

As the opposite of adhesion, the activation of bonds after the relaxation creates a much distinguished behaviour. First, as shown in Fig. 3.19a, the mean coordination number decreases as a non-cohesive case and the bonded particles bed is constrained to stay at this packing level. Compared to the pre-relaxation configuration, a major difference is the disappearance into two groups (weak-bonds and strong-bonds): all the bonded particles bed behave similarly, with an increase of mean coordination number at the beginning of cycling and a drop below the non-cohesive case (DAM reference sample, $st_{\max} = 0$ MPa). When it comes to thickness in Fig. 3.19b, the difference is not particularly visible at this scale, where we can still notice the presence of swelling delay (smoothed shape at $c = 0$ cycle) that gives birth to important swelling amplitudes and irreversibilities.

In Fig. 3.20a that draws the pre-relaxation/post-relaxation comparison of swelling amplitude Δth_{sw} at first cycle, the shape of the curve for the post-relaxation configuration demonstrates a behaviour closer to the adhesion simulation (compare with Fig. 3.16c curves), with a smoother transition along values of maximum bond stress st_{\max} , rather than a sudden linear increase of Δth_{sw} . Concerning the irreversibility Δth_{irr} at first cycle, the change between post-relaxation and pre-relaxation is quite similar, as plotted in Fig. 3.20b. In addition, even if lowest values of maximum bond stress st_{\max} leads to higher irreversibility in post-relaxation generation of bonds, on the opposite, the highest values of st_{\max} generate less irreversibility at first cycle. For example, at $st_{\max} = 40$ MPa, Δth_{irr} drops from $20.3 \pm 1.2 \mu\text{m}$ to $16.8 \pm 1.1 \mu\text{m}$ between pre-relaxation and post-relaxation configurations (arrow 3.20b.①). Another interesting feature appears at the second cycle, plotted in Fig. 3.20c: the swelling amplitude Δth_{sw} does not decrease any more with the maximum bond stress, it even increases. For

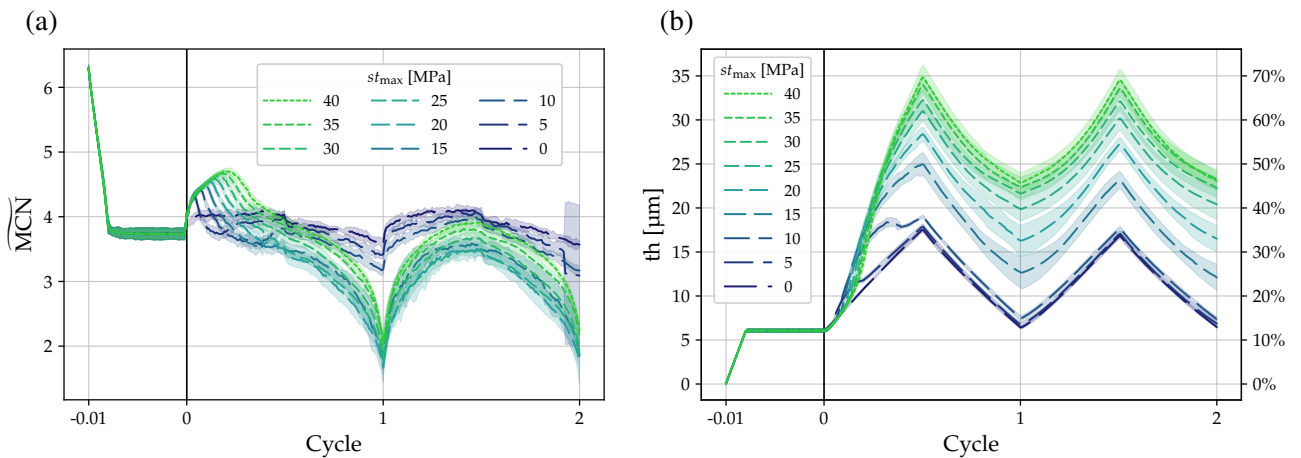


Figure 3.19: Influence of post-relaxation generated bonds (9 values set, DAM reference sample for $st_{\max} = 0$ MPa) — **a**) Mean coordination number (relaxation and cycling). **b**) Thickness (relaxation and cycling), $th_{ref} = 50 \mu\text{m}$.

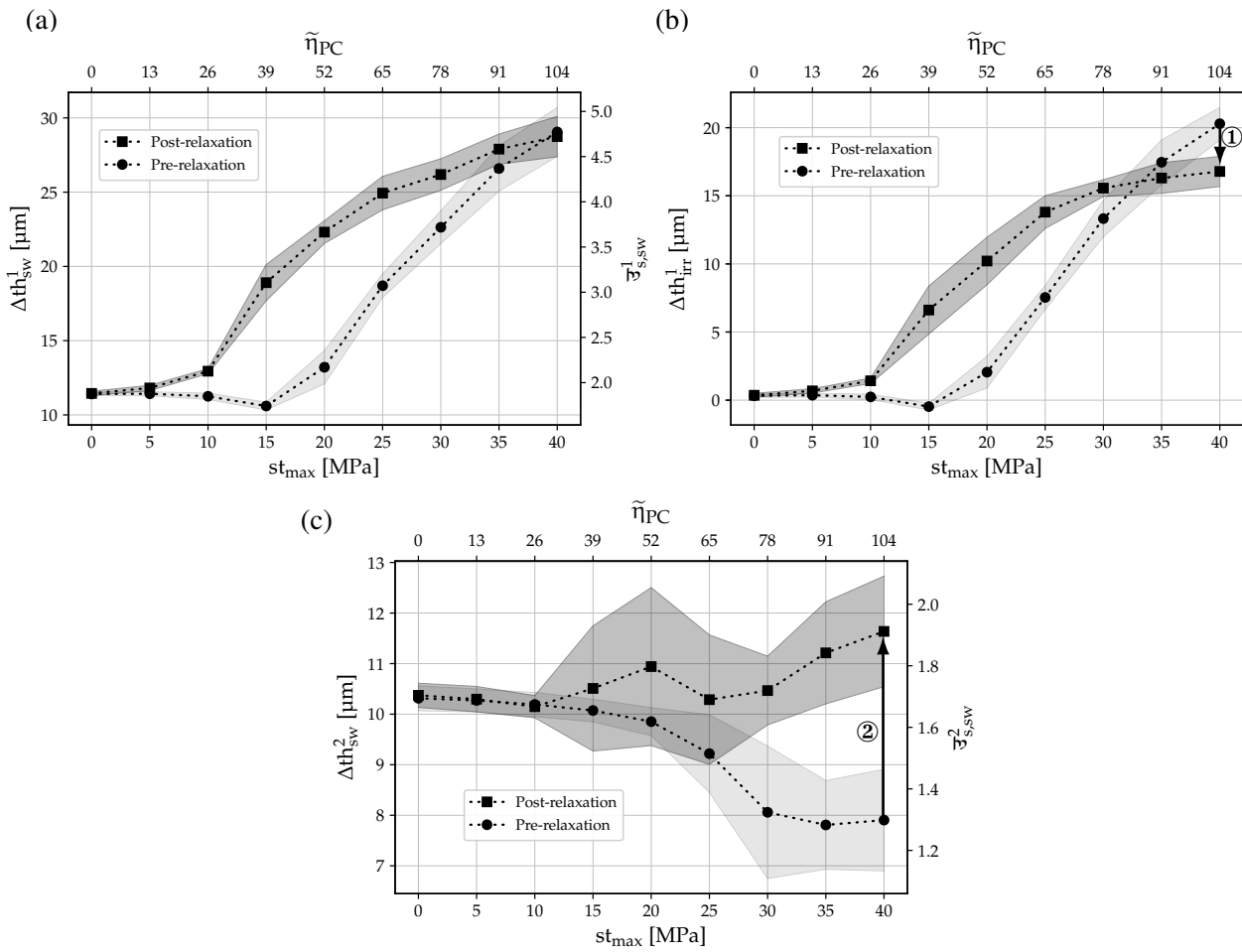


Figure 3.20: Influence of post-relaxation generated bonds (9 values set, DAM reference sample for $st_{\max} = 0$ MPa) — **a)** Swelling amplitude thickness Delta and swelling breathing coefficient (first cycle, pre-relaxation and post-relaxation generated bonds). **b)** Swelling amplitude thickness Delta and swelling breathing coefficient (second cycle, pre-relaxation and post-relaxation generated bonds). **c)** Irreversibility thickness Delta (first cycle, pre-relaxation and post-relaxation generated bonds).

example, at highest maximum bond stress $st_{\max} = 40$ MPa, the swelling amplitude Δth_{sw} goes from 7.9 ± 1.0 μm to 11.6 ± 1.1 μm (arrow 3.20c.②). The respective values of breathing coefficient are 1.3 ± 0.2 and 1.9 ± 0.2 , which corresponds to two distinct breathing regimes (pre-relaxation configuration is close to solid breathing, whereas post-relaxation configuration is close to balanced breathing).

3.3.5.c Pre-relaxation/Post-relaxation deeper comparison

As detailed in Section 3.3.4, when using adhesion between particles, a moderate difference appears between pre-relaxation and post-relaxation activation of adhesion. In the actual use of breakable bonds, the difference between pre-relaxation and post-relaxation is more significant. First, the Figs. 3.21a and 3.21b displays the swelling amplitude Δth_{sw} as a function of both cycles and maximum bond stress st_{\max} . On the left (Fig. 3.21a), the pre-relaxation configuration of bonds creates the sharp peak generated by both weak-bonds and strong-bonds ranges. The interesting fact is the appearance of another reduction of swelling amplitude from the second cycle (dark “canal”), a behaviour similar to the breathing with adhesion (see Fig. 3.15d). On the right

(Fig. 3.21b), the post-relaxation configuration of bonds presents a smoother increases of swelling amplitude at first cycle, with a really closed range. However, the reduction of swelling amplitude from the second cycle disappears and is even increasingly correlated to the maximum bond stress st_{\max} .

In order to deeper understand these differences, the number of bonds is a useful quantity. In this optic, Figs. 3.21c and 3.21d draws the evolution of the number of bonds. As expected, the pre-calendering case presents different numbers of bonds during the relaxation, whereas the post-relaxation presents null curves during this phase. An observation of the pre-relaxation graph, in Fig. 3.21c, enables to better understand the creation of both weak-bonds and strong-bonds ranges: the relaxation creates an important loss of bonds for lower maximum bonds stress. Consequently, at the beginning of cycling, the different simulations start with different numbers of bonds (from 0 to the initial number of bonds). At the opposite, in Fig. 3.21d the post-relaxation case does not present this initial dispersal. Whatever the maximum bond stress, all simulations start at the exact same stage, which explains, at least partially, the disappearance of weak-bonds and strong-bonds ranges. Moreover, the relaxation leads to a less packed particles bed. Consequently, the number of bonds generated is lower than in the pre-relaxation configuration (4740 ± 54 in pre-relaxation, 3.21c.①, against 4046 ± 34 in post-relaxation, 3.21d.②). Both graphs reveal that the first cycle, and more precisely the first swelling, is crucial in the determination of the final bonded particles bed, much more than expected. At the initiation of the use of the breakable bond model, as an intuition based on experimental measurements that presents progressive irreversibility cycle after cycle, it was expected that the loss of bonds would be more progressive along cycles. This does not happen here. Whatever the case, the number of bonds remains almost constant starting from the end of the first swelling. This is all the more visible in Fig. 3.21e, where the proportions of broken bonds is displayed. The dotted areas correspond to the proportions lost during cycles 2, 3 and 4, the clean and light coloured areas correspond to the proportions lost during cycle 1, and the dashed dark correspond to the proportions lost during relaxation. Of course, no dashed dark area appears for the post-relaxation case, because no bond exists during this phase. The facts are clear: the proportions of bonds broken during cycles 2, 3 and 4 are almost negligible next to the proportions of bonds broken during first cycle. As an example, the highest proportion during cycles 2, 3 and 4 occurs with the post-relaxation configuration, at $st_{\max} = 15$ MPa, with $8.1 \pm 2.7\%$, whereas $65.7 \pm 2.2\%$ of total bonds are lost during first cycle (3.21e.③). A major difference between pre-relaxation and post-relaxation configurations are the phase were majorities of bonds are broken. In the pre-relaxation configuration, majorities of lost bonds are broken during relaxation, until $st_{\max} = 15$ MPa where they constitute $65.7 \pm 3.0\%$ (3.21e.④), against $29.8 \pm 3.1\%$ during first cycle. At $st_{\max} = 20$ MPa, the trend reverses with $20.4 \pm 1.5\%$ (3.21e.⑤) lost during relaxation compared to $71.0 \pm 1.7\%$ during first cycle. When it comes to post-relaxation configuration, bonds are in great majority broken during first cycle. Finally, another major difference between pre-relaxation and post-relaxation configuration are the final proportions of broken bonds (respectively dashed and dash-dotted curves). Indeed, the pre-relaxation configuration loses more bonds than the post-relaxation configuration, as in proportions (Fig. 3.21e) as in absolute way (Figs. 3.21c and 3.21d). Whatever the maximum bond stress, the pre-relaxation configuration leads to a less bonded particles bed than the post-relaxation configuration. This fact may explain why the post-relaxation generation of bonds leads to a higher swelling amplitude Δth_{sw} during the first cycle (as in Fig. 3.20a) and the disappearance of the reduced swelling amplitude from the second cycle (dark “canal” in Fig. 3.21a not present any more in Fig. 3.21b).

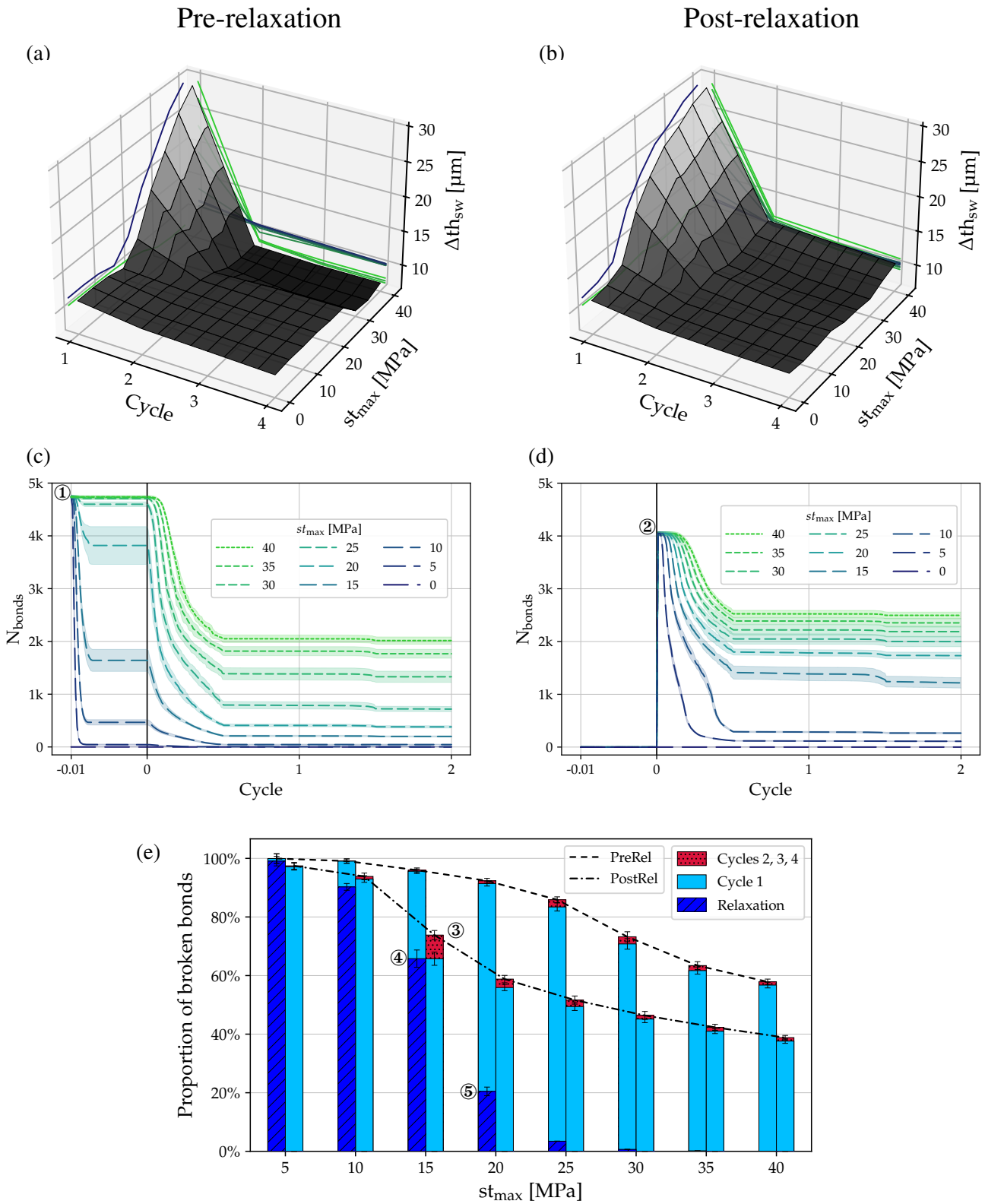


Figure 3.21: Influence of pre-relaxation and post-relaxation generated bonds (9 values set, DAM reference sample for $st_{max} = 0$ MPa) — **a**) Swelling amplitude thickness Δth_{sw} (as a function of cycles and work of adhesion, pre-relaxation generated bonds). **b**) Swelling amplitude thickness Δth_{sw} (as a function of cycles and work of adhesion, post-relaxation generated bonds). **c**) Number of bonds (relaxation and cycling, pre-relaxation generated bonds). **d**) Number of bonds (relaxation and cycling, post-relaxation generated bonds). **e**) Proportions of broken bonds as a function of maximum bond stress, phase in simulation (after relaxation, after first cycle and after four cycles) and bonds activation. For each bar pair, pre-relaxation (PreRel) on the left (dashed curve) and post-relaxation (PostRel) on the right (dash-dotted curve).

3.3.6 Particles irreversibility

All the previous approaches addressed the reversible breathing of particles, with respect of Hyp. 2.A.v (page 74) stated in Section 2.1.2. This last analysis aims to analyse the case where particles would breathe irreversibly. In other words, if an eventual irreversibility occurs at the scale of our particles (due to irreversible electrochemistry, for example), the objective is to evaluate how this irreversibility is transmitted to the electrode scale. To do so, the protocol consists in making a single cycle and applying the virtual irreversibility developed in Section 2.3.4. The protocol is made with six values of r_{irr} , from 0 to 1.

3.3.6.a Linear breathing law

The first observation is the exact same results for all sensitivity parameters during relaxation and the first swelling phase, as Fig. 3.22a shows for inertial number at 3.22a.①. Indeed, the irreversibility parameter only affects simulations at the beginning of shrinking, where each simulation decreases more or less depending on r_{irr} , as the raw thickness graph of Fig. 3.22b explicitly shows. It is possible to notice that for $r_{\text{irr}} = 1$, the inertial number drops to zero (no strain rate), and for lower values of r_{irr} , the inertial number increases due to the increase of the strain rate, until a value of around 8.3×10^{-5} for the DAM reference sample case at $r_{\text{irr}} = 0$ (3.22a.②). Similarly, the force is slightly less precise for lower values of r_{irr} (not shown in graphs). For a better

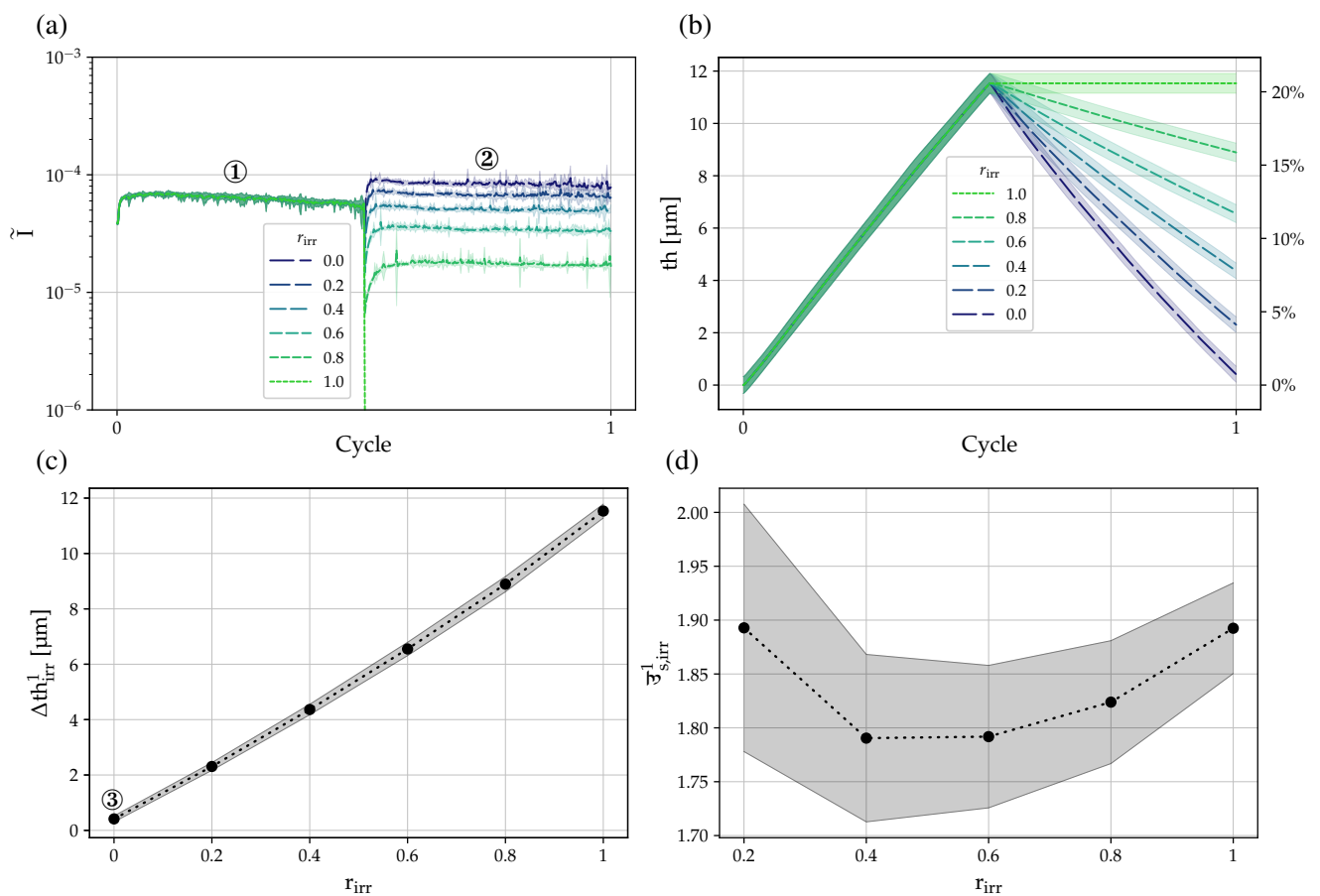


Figure 3.22: Influence of particles irreversibility with linear breathing law (6 values set, DAM reference sample for $r_{\text{irr}} = 0$) — **a**) Inertial number (cycli). **b**) Thickness (cycli), $th_{\text{ref}} \approx 56.0 \mu\text{m}$. **c**) Irreversibility thickness Delta. **d**) Irreversibility breathing coefficient.

view, Fig. 3.22c presents the evolution of the irreversibility Δth_{irr} at first cycle. The evolution is quite linear and a major point to underline is the first one (3.22c.③), corresponding to DAM reference sample. As already concluded in Section 3.2, it recalls that using simple Hertz-Mindlin contact law (detailed in Section 1.2.1.b) with standard parameters is not enough to capture a significant breathing irreversibility. Talking about particles rearrangement, the thickness Δ hardly describe the inner organisation of volumes. To do so, Fig. 3.22d shows the evolution of the irreversibility breathing coefficient. The order of magnitude provided by these curves at least gives us the volume change distribution, thanks to Table 2.2. With a maximum value reached at $r_{\text{irr}} = 0.2$ (1.89 ± 0.11) and a minimum at $r_{\text{irr}} = 0.4$ (1.79 ± 0.07), the system is close to the balanced breathing ($\overline{\mathfrak{V}}_{s,\text{irr}} = 2$, $\Delta V_{\text{solid}} = \Delta V_{\text{void}}$). In fact, the equivalent value of $\overline{\mathfrak{V}}_{vs,\text{irr}}$ are 1.12 and 1.27, which means that the particles irreversible volume variation is about 12% to 27% greater than the void volume variation.

Nevertheless, the interpretation of this result can not go further. If we wanted to extract a sensitivity conclusion from this curve, we would say that the cases $r_{\text{irr}} = 0.4$ and $r_{\text{irr}} = 0.6$ would be the more interesting due to their lower breathing coefficient, because closer to 1 means that all volume change comes from particles only, and even closer to 0 means the void volume variation compensates the particles volume variation. However, the variation of the breathing coefficient for different irreversibility ratios is of the same order of magnitude of the statistical dispersion (area in Fig. 3.22d), so the correlation is more negligible compared the one captured in previous sensitivity analysis.

3.3.6.b Electrochemical breathing law

As for silicon fraction analysis in Section 3.3.1, it is proposed here to make the same simulation by using the particles breathing electrochemical law instead of linear volume law. As a recall, the idea behind this protocol is to implement a non-synchronous breathing of particles (Si/C particles compared to Gr particles). The same initial particles distributions and positions as linear law simulations were used.

As in the previous analysis with electrochemical breathing law in Section 3.3.1.b, a specific precaution is required with this breathing law concerning the inertia of the system. Fortunately, this over-inertia effect seems not noticeable as Fig. 3.23a shows, even for the fast shrinking at $r_{\text{irr}} = 0$ where the inertial number reaches a maximum of $1.7 \times 10^{-4} \pm 0.9 \times 10^{-4}$ (3.23a.①). Concerning the thickness in Fig. 3.23b, the shape is consistent with the breathing laws of Fig. 2.10. It particularly matches with the graphite breathing law due to the higher proportion of this material. We indeed recognise in Fig. 3.23b the characteristic plateaus of the graphite (de)lithiation transition stage $2L \leftrightarrow L$ ($\text{LiC}_{18} \leftrightarrow \text{LiC}_{12}$), at 3.23b.②. However, the desynchronisation of breathing laws does not seem to notably impact the irreversibility. In this optic, Fig. 3.23c displays irreversibility Δth_{irr} for both linear (results from Fig. 3.22c) and electrochemical laws, where the curves are almost merged. The linear law curve seems a little higher, suggesting a higher amount of void volume created. This is consistent with the breathing coefficient displayed in Fig. 3.22d that indicates a higher value for linear laws: because the particles' irreversibility is a common input between both laws, the difference necessarily comes from void volume. However, considering the dispersion areas, the difference between both cases is not particularly significant, even more compared to previous sensitivity analysis.

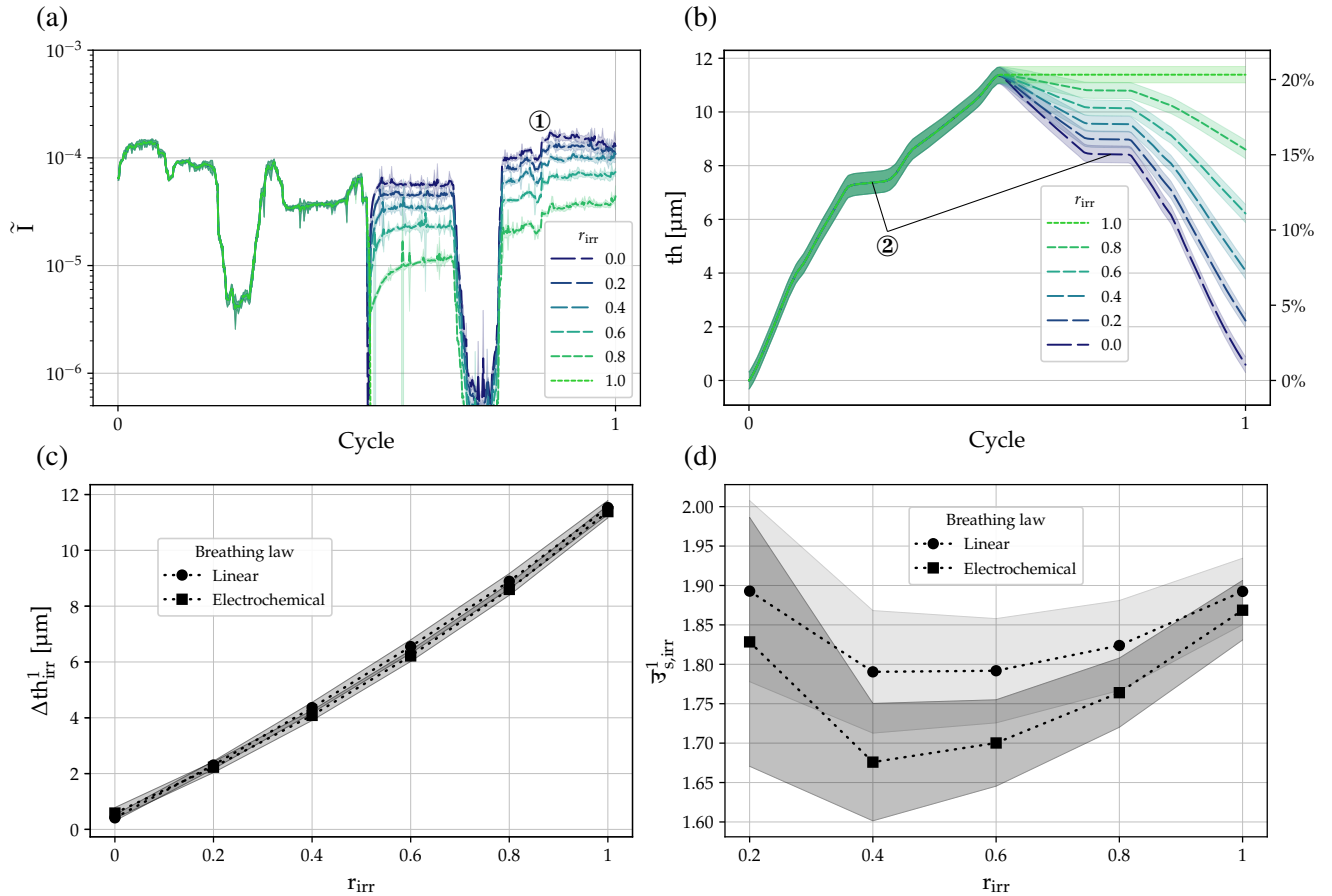


Figure 3.23: Influence of particles irreversibility with electrochemical breathing law (6 values set, DAM reference sample for $r_{irr} = 0$) — **a)** Inertial number (cycli). **b)** Thickness (cycli), $th_{ref} \approx 56.0 \mu m$. **c)** Irreversibility thickness Delta. **d)** Irreversibility breathing coefficient.

As a consequence, this approach of irreversibility transfer from particles to electrode scale presents interesting results. The irreversibility at particles scale is directly transmitted to electrode due to almost linear relationship. Of course, the irreversibility ratio r_{irr} does not explain the role of granular media in generating electrode irreversibility, it is more a fitting parameter. In fact, the key observation appears through the introduction of electrochemical law that brings a supplementary non-synchronism of breathing between both Si/C and Gr particles. Even if the different is slight, the reduction of void volume suggests a different organisation of particles.

3.4 Global analysis

3.4.1 Results summary

The previous section was a detailed review of all the different sensitivity analyses that have been made during this thesis. The current paragraph aims to summarise the main observations, mainly in terms of swelling amplitude and irreversibility. During all above developments, we practically talked about only the first cycle, barely the second one, and never in detail about the next ones. In fact, the current structure of the DAM is

not efficient enough to capture a gradual evolution over cycles. Indeed, most of significant results happened during the first cycle and the states from the second cycle seemed systematically stable. Hence, all the results presented here aims to explain at first cycle, not during next ones. To extend the progressiveness of the model along cycles, a susceptible way would be using the DAM with breakable bonds set with a progressive wear. For example, it is imagined to reduce individually the maximum bond stress of each bond as a function of the past stress it was submitted to.

As an overview of the present chapter results, Table 3.2 draws simplified curves of swelling amplitude Δh_{sw} and ratio of irreversibility Δh_{irr} over swelling amplitude Δh_{sw} , as the orders of magnitude of their maximums (letters A, B, C and D, significations detailed in legend).

The silicon fraction has a direct impact on the swelling amplitude, and even the most important, through a linear variation going up to 40 μm . The Deltas ratio $\Delta h_{irr}/\Delta h_{sw}$ varied singularly, with a fast increase until an asymptotic stabilisation at 10%. The friction and rotation was found to be either non-significantly impacting breathing characteristics or physically non-reliable, due to the creation of “backbone branches” (strong pillars of particles) that let most of the particles floating in empty space, removing any contact between particles. The pressure was detected to diminish the swelling amplitude only at high values, and a maximum irreversibility was detected close to the transition pressure. In fact, the pressure was closely linked to particles rigidity, through the generalised stiffness level that impacts the breathing exactly the reversed way. The adhesion between particles, activated before or after the relaxation, presents a logarithmic-like impact on swelling amplitude, but first generates important irreversibility over swelling amplitude ratio with a similar evolution. Not shown in Table 3.2, adhesion also generates a reduction of swelling amplitude from the second cycle at high values of adhesion, even if these same values generate a huge swelling amplitude at first cycle. The breakable bonds created before relaxation (pre-relaxation) presents a sharp distinction between lower values and higher values of maximum bond stress, with an independence on breathing for lower values and a linear relationship for higher values, giving birth to the highest irreversibilities captured with the DAM, until 70%. The breakable bonds created before relaxation also generated a reduction of swelling amplitude from second cycle, as for adhesion. In addition, creating the bonds after the relaxation (post-relaxation) smooths the transition between low and high values of maximum bonds stress, concerning its impact on first cycle breathing characteristics. This type of bonds generation also erases the reduction of swelling amplitude from the second cycle. Finally, the particles’ irreversibility is not an interesting parameter due to its independence from swelling amplitude. Conclusions are quite intuitive and do not bring real innovative observations, in the limits of the DAM: irreversibility at particles level is directly transmitted to electrode level, without characteristic optimum point.

3.4.2 Manufacturing guidelines for the design of low breathing electrodes

This global analysis enables to draw an estimated portrait of the “optimal electrode” with limited breathing, considering a discrete nature of its structure. It should be composed of particles that breath as low as possible, which is quite obvious and does not really consider the granular aspect. The fact remains that no significant optimal point was captured through the virtual adding of swelling amplitude or irreversibility: the higher swelling amplitude or irreversibility at particles scale, the higher swelling amplitude or irreversibility at electrode scale with linear relationships. Thus, searching a better capacity using silicon necessarily leads to a more

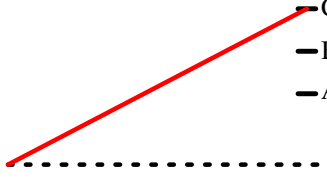

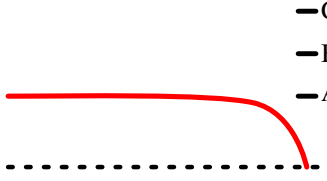
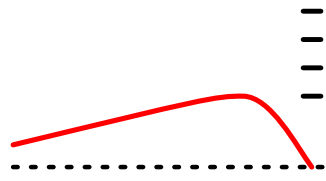
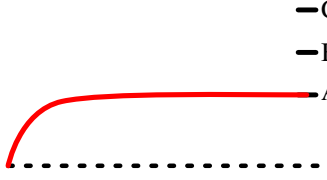
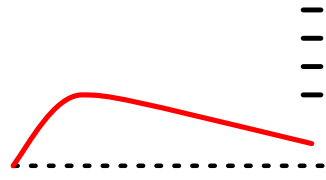
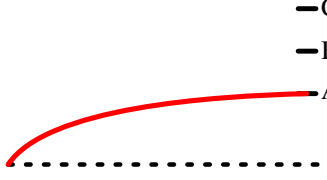
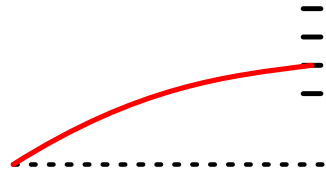
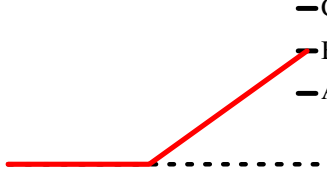
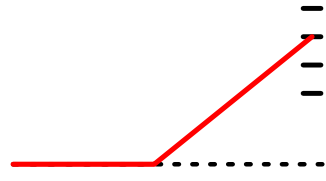
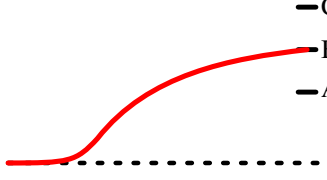
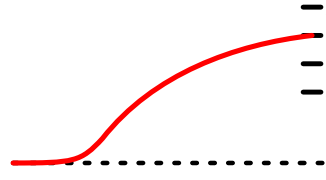
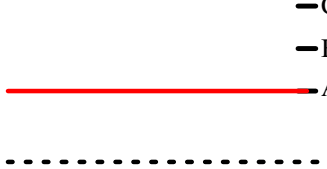
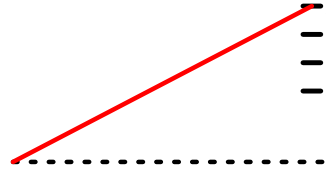
Parameter	Δth_{sw}	$\Delta th_{irr}/\Delta th_{sw}$	Section
Silicon fraction			3.3.1
Friction/Rotation	—	—	3.3.2
Pressure			3.3.3.a
Particles rigidity / Particles bed stiffness level			3.3.3.b
Adhesion			3.3.4
Bonds (PreRel)			3.3.5.a
Bonds (PostRel)			3.3.5.b
Particles irreversibility			3.3.6

Table 3.2: Global analysis of DAM results (graduations represent maximums orders of magnitude) — **Second column**) Swelling amplitude thickness Delta of first cycle (A: 10~15 μm , B: 30 μm , C: 40 μm , DAM reference sample at A). **Third column**) Irreversibility over swelling amplitude thickness Deltas ratio of first cycle (A: ~10%, B: ~40%, C: ~65%, D:~100%, DAM reference sample at around 0%). Prerel: pre-relaxation, PostRel: post-relaxation.

pronounced breathing, without eventual minimised point of swelling amplitude. Furthermore, this “optimal electrode” should be as “soft” as possible, in other words composed of particles as soft as possible and submitted to a pressure as high as possible. However, an attention should be paid on this low rigidity, because a peak of relative irreversibility exists at a stiffness number of $\tilde{\kappa} \simeq 180\sim 350$. The ideal is to reach a value under this range. Finally, the choice of stickiness between particles (through the properties of the binder) depends on the manufacturing process. The ideal configuration is to glue particles as strong as possible before relaxation and anticipate an important swelling of the first cycle. Afterwards, the following cycles are expected to present lower swelling amplitude than without stickiness between particles. However, if this first important swelling and irreversibility is a problem, it is advised to decrease as much as possible the stickiness between particles.

Of course, these guidelines present substantial limits, starting with the fact it is based on a mechanical perspective only, especially on a model certainly incomplete due to its non-negligible structural simplifications. The advised precautions have to be confronted to other fields that closely relates to battery technology, electrochemistry and process engineering being on the front line. For example, it can be underlined that the reduction of stickiness between particles could be counter-productive for the material conductivity, or the increase of pressure can imply a higher packing complexity or a limitation of ions diffusivity within the material.

Beyond composing a proposal for a new modelling approach, the analysis through the DAM is a mechanical contribution, thus partial, to the understanding of electrode breathing.

Chapter 4

Experimental approach

4.1 Experimental needs

As for any modelling approach, a supplementary experimental approach provides a good base to criticise the model. Consequently, it was chosen to give some time of the thesis to this aspect, as an extension of the work already made by Vidal (2021-2023) [40], [52], [210]. Many thickness measurements were made in the work of Delphine Vidal, but some features were never explored before, even considering the literature presented in Chapter 1. After an overview of the work carried out by Delphine Vidal, two main threads were drawn for the current thesis: the impact of pressure (partially addressed in Vidal’s thesis, at constant pressure) and the impact of temperature (not addressed at all in Vidal’s thesis).

Nevertheless, beyond detailing this unexplored approaches, let us have an overview on an important issue concerning the confrontation between simulation and experimental work, which is particularly the case in DEM: “*How to link any simulation parameters to a measurable physical quantity?*”. In this optic, the Table 4.1 summarizes some key parameters, for a macroscopic experimental protocol on one side and for DEM simulation on another side. The parameters that are shared between experiment and model are written in black. However, the parameters written in light colour do not have a direct significance in the opposite column. For example, a contact law has no direct counterpart in the experiment. Reciprocally, the temperature is an accessible and controllable experimental parameter, but its controllability in DEM application is more indirect and does not enter the scope of this thesis. In a nutshell, this reflection raises, once again, the difficulty to establish correlations between a model that transfers a microscopic phenomenon to a larger scale and what it observed experimentally at macroscopic scale. At this stage, the only way remained to make some assumptions in order to unify the microscopic and macroscopic quantities. For example, the intuition about temperature is its impact on the lubrication between particles, by changing the properties of the binder, and so the work of adhesion or the bonds’ fragility within DAM. This aspect of “blurry micro/macro relationships” is discussed in this chapter.

For these reasons, temperature and pressure composed the main threads explored in this experimental approach.

	Experiment (macro-scale)	Model (micro-scale)
Sample parameters	<ul style="list-style-type: none"> → Mass fraction → Particles size distribution → Porosity → Loading → Binder type, quantity, etc. → Mechanical properties 	<ul style="list-style-type: none"> → Mass fractions → Particles sizes → Porosity (indirect) → Loading → Contact laws
Experimental conditions	<ul style="list-style-type: none"> → Pressure → SOC → Temperature 	<ul style="list-style-type: none"> → Pressure → Breathing laws → Temperature dependent contact models
Results	<ul style="list-style-type: none"> → Irreversible swelling → Hysteresis → Void volume changes 	<ul style="list-style-type: none"> → Irreversible swelling → Hysteresis → Void volume change → Local data (coordination number, local pressure fields, etc.)

Table 4.1: Parameters comparison between experimental and model.

4.2 Experimental reference protocol

4.2.1 Pouch cell sample

All the measurements presented in this manuscript are made on a pouch cell sample whose active material (anode + cathode) surface is around 3×3 cm and its initial thickness is about $60 + 80 \mu\text{m}$. The electrodes are surrounded by other packing components: a separator and a pouch bag, composing the final sample, better called “single layer pouch cell”, or more simply “pouch cell”. More precisely, this pouch cell is designed as schemed in Fig. 4.1a.

Three main quantities were real-time measurable for this sample: the pressure, the temperature and the thickness. However, it is highly important to have in mind what thickness is measured. In this sense, Fig. 4.1b presents a cross-section scheme of the sample to detail what is comprised in the measured thickness:

- One layer of anode (bottom medium rectangle)
- One layer of separator (thin solid middle rectangle)
- One layer of cathode (top medium rectangle)
- Two layers of pouch bag (big bottom and top rectangles)

For manufacturing details, the trio of anode/cathode/separator are square layers placed in a heat-sealed pouch bag filled with electrolyte. As for the sizes of anode, cathode and separator, they are respectively

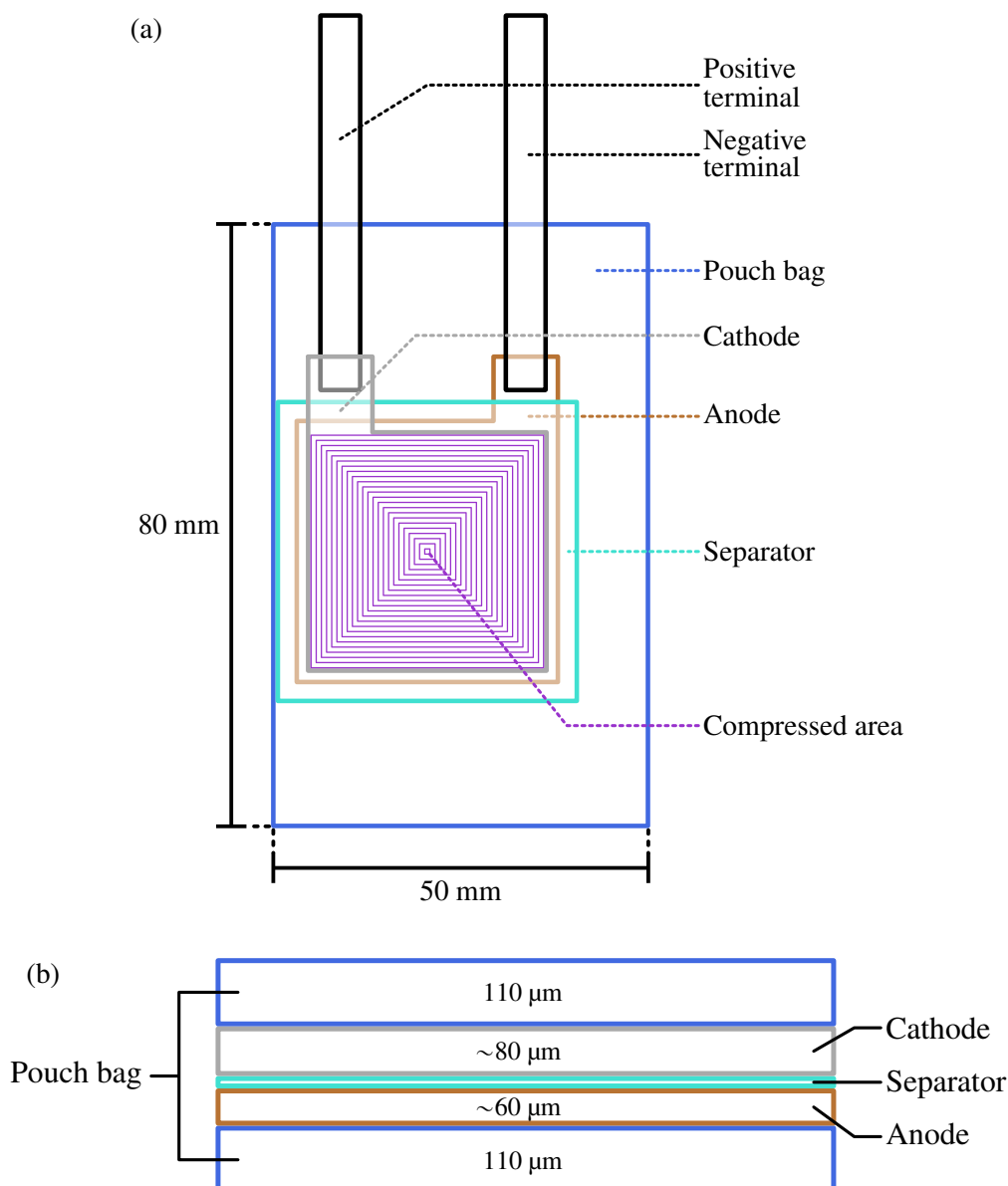


Figure 4.1: Scheme of pouch cell sample — **a**) Full scheme of pouch cell (scale 1:1). Size of compressed area: $32 \times 32 \mu\text{m}$ (same as cathode). **b**) Cross-section scheme (thicknesses relatively at scale with each other). Anode: $\sim 60 \mu\text{m}$, Cathode: $\sim 80 \mu\text{m}$, Separator: $20 \mu\text{m}$, Pouch bag (one layer): $110 \mu\text{m}$.

35 mm, 32 mm and 40 mm square. The cathode active material is NMC622 (Nickel-Manganese-Cobalt, $\text{LiNi}_{0.6}\text{Mn}_{0.2}\text{Co}_{0.2}\text{O}_2$) mixed in the following composition: 92wt% NMC622, 2wt% Super P, 2wt% VGCF, 4wt% PVDF. The Super P improves the electrical contact at short distance, the VGCF (vapour grown carbon fibres) enables a better electrical conduction at higher distance and the PVDF (polyvinylidene fluoride, from Solvay) serves as binder between particles. The mixture is coated on a $20 \mu\text{m}$ thick aluminium collector, for final thickness of dried-calendared ink and collector of $79.8 \pm 2.5 \mu\text{m}$. The anode is a Si/C/Gr blend with the following composition: 95wt% Si/C/Gr (where Si composes 6.4wt% of Si/C/Gr mass), 1wt% Super P, 1.5wt% Na-CMC, 2.5wt% SBR. The SP is similarly used for punctual electrical conduction improvement, Na-CMC (sodium carboxymethyl cellulose) and SBR (styrene-butadiene rubber) are used as binder between parti-

cles. The mixture is coated on a 10 μm thin copper collector, for a final thickness of dried-calendared ink and collector of $57.9 \pm 0.7 \mu\text{m}$. The pairs of cathode/anode chosen for cycling protocols gave final capacity balance ($Q_{\text{tot-}}/Q_{\text{tot+}}$) of 1.10 ± 0.02 . The separator was a PP/PE/PP trilayer (polypropylene/polyethylene/polypropylene, reference 2320 from Celgard), with a thickness of 20 μm and a 48% porosity. The electrolyte was a liquid mixture of solvents EC/DMC/EMC (ethylene carbonate/dimethyl carbonate/ethyl methyl carbonate, 3/5/2) with 2wt% VC (vinylene carbonate) and 10wt% FEC (fluoroethylene carbonate) as additives. Finally, the pouch bag was a trilayered stack of 40 μm thick aluminium foil between polypropylene and polyamide layers of 35 μm with no porosity, for a resulting thickness of 110 μm .

4.2.2 Experimental device: “DForm” test bench and electrochemical apparatus

The DForm bench is a homemade device that was developed to simultaneously measure a pouch bag sample thickness and control the pressure applied. For example, it is capable of measuring a varying pressure while maintaining a constant thickness of the cell, measuring a varying thickness while maintaining a constant pressure. This second process that was used in this study: constant pressure and changing thickness. More precisely, Fig. 4.2 schemes the DForm test bench. The power of compression is initially provided by a step motor ①. The power is transmitted through a pulley system ② to a first lever ③, the latter maintained to the top by a spring ④. The power is transmitted by mechanical leverage to a secondary lever ⑤, the latter compressing a force sensor ⑥ that measures the force applied on the sample with a precision of 1 N. The final pressure is finally applied on the pouch cell ⑦ placed between two anvils ⑧. Its thickness is measured by three linear variable differential transformers displacement sensors ⑨ (only two visible here), with a precision below 100 nm.

The DForm bench measures only mechanical quantities (thickness and force). The thermo-electrochemical quantities (temperature, current, voltage) measurements as well as the cycling control are made by a Biologic VMP3 bench, plugged to the pouch cell via both terminals (positive and negative in Fig. 4.1a). The electrochemical data are pre-processed by a Python-based auto-conversion step (from MPR to CSV format), and a personal Python-based process merges the generated electrochemical data (from VMP3) with the mechanical data (from DForm) to give the final displayable results.

4.2.3 Experimental reference protocol description

As already introduced in Section 4.1, the experimental approach is built on two main threads.

The first thread relies on the observation of an eventual visco-plastic behaviour due to compression on the cell. Delphine Vidal has already measured the impact of pressure, but she did not measure the irreversibility of these compressions, and especially the eventual origins of these irreversibilities. The final fundamental protocol chosen, is the alternation between different levels of pressure with a reference one, in order to observe the impact of punctual compressions at higher pressure.

The second thread is the observation of eventual change of visco-plastic behaviour of the cell during cycling due to temperature. As already introduced before, our first intuition is that the major behaviour affected by temperature is the binder behaviour, that is expected to play an important role in the contacts properties. Bulk particle behaviour is thus supposed to be independent from temperature in the variation range chosen.

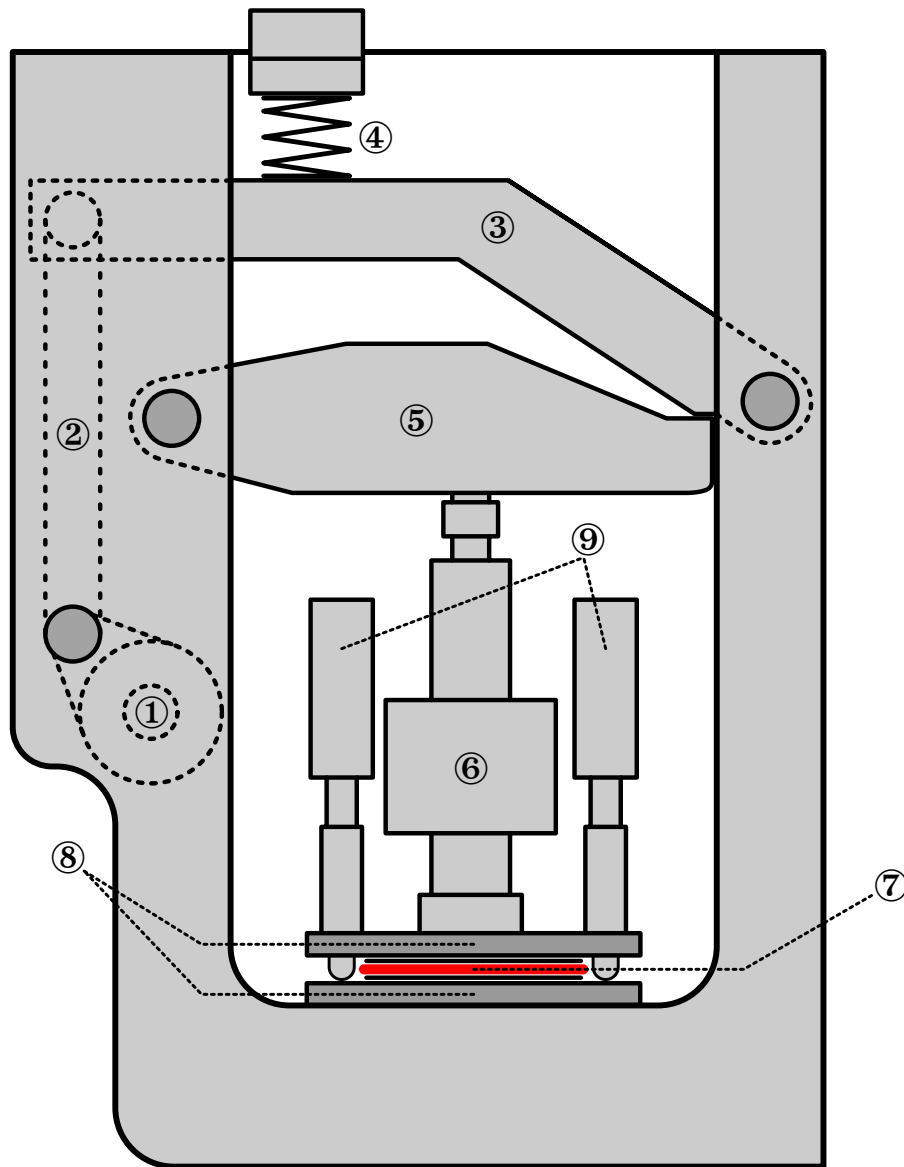


Figure 4.2: Scheme of DForm bench, scale $\approx 1:2$ (with eventual resizing of subcomponents for readability purpose) — ①: step motor, ②: pulley system, ③: primary lever, ④: spring system in traction, ⑤: secondary lever, ⑥: force sensor, ⑦: sample, ⑧: anvils, ⑨: linear variable differential transformers displacement sensors (only two out of three shown here).

The reference protocol is built on the P_{ref} (reference pressure of 0.3 MPa, introduced in Section 2.1.3.a), with a cycling systematically made between 2.5 and 4.2 V. Furthermore, the reference protocol is composed of two parts: the formation part and the cycling part. The formation part is divided into three cycles with gradual C-rates (C/20, C/10, C/5), followed with six cycles at C/5 (even if, generally, the term “formation” designates only the first cycle). The formation phase is submitted to a given pressure P that can change depending on the experiment. The cycling part is made at constant C-rate C/5 and divided into four sub-parts: three cycles under 1 MPa, four cycles under P_{ref} (0.3 MPa), three cycles under 3 MPa and six cycles under P_{ref} (0.3 MPa). All along both parts, the temperature is kept constant, and its value depends on the experiment. It was initially planned to make the reference protocol at three or four different temperatures, but only two (24°C and 61°C) were finally measured.

As summarised in Table 4.2, an experiment is systematically based on the reference protocol and defined through two parameters: the temperature T and the pressure during formation P . Hence, when an experiment is referred with a temperature and/or a pressure, these values respectively refer to these variables.

	Formation			Pressure variation			
Number of cycles	1	1	7	3	4	3	6
C-rate	C/20	C/10	C/5	C/5			
Duration (h)	40	20	70	30	40	30	60
Potential range	← 2.5 ↔ 4.2 V →						
Temperature	← T →						
Pressure (MPa)	← P_{form} →			1	0.3	3	0.3

Table 4.2: *Experimental reference protocol. The duration is estimated from the design capacity. When an experiment is expressed with temperature and/or pressure, each refers to the respective T and P_{form} variables in the table.*

4.3 Anode thickness extraction through modelling

4.3.1 Extraction details and hypothesis

Even if the experimental device presented above generates precise results (precision of 100 nm of displacement sensors), a major drawback is that it measures the whole sample thickness variation (anode, cathode, separator and two layers of pouch bag), whereas only the anode thickness variation is wanted. To simplify the problem, it is possible to state the following Set of Hypothesis 4.A:

- (i) The thickness variation of cathode, separator and pouch bag are negligible compared to the thickness variation of anode

This proposition was used in Delphine Vidal's thesis (2021) [40], but its validity depends on the experimental protocol. To understand this, let us remind that the thicknesses can vary over time due to two origins: electrochemical and mechanical. The objective here is to extract the anode thickness variation (electrochemical and mechanical) via a device that measures the whole sample thickness variation, including cathode, separator and pouch bag. Moreover, the three latter components necessarily present mechanical thickness variation due to pressure. If the pressure applied on the sample was constant (which was often the case in Vidal's thesis), by waiting enough time before cycling to let the system reaching its mechanical stable breathing, the mechanical thickness variation of cathode, separator and pouch bag would have been certainly negligible and Hyp. 4.A.i (page 146) acceptable. However, this is not the case in the reference protocol defined in Section 4.2.3, where the pressure changes over time. For this reason, a deeper understanding of cathode, separator and pouch bag behaviours is necessary to evaluate their participation into sample thickness variation.

— For this purpose, the term “**intermediary**” will systematically be associated to the trio of cathode, separator and pouch bag. —

The aim of this section is then to build a model that estimates the real-time variation of intermediary components (mechanical for cathode, separator and pouch bag, electrochemical for cathode). With a more proper term, the mechanical perspective introduced here is about the “rheology” of components, about the way they deform under a given stress. The methodology follows the process drawn in Fig. 4.3. Before analysing the main reference protocol data (left column), two works of estimation are made: rheological (centre column) and electrochemical (right column). The rheological estimation is based on rheological measurement of intermediary components (cathode, separator and pouch bag). A rheological model is built and parametrised on the measured stress/strain curves. The electrochemical estimation is based on literature, to estimate the electrochemical thickness variation of cathode. Both estimations are joined to estimate each intermediary component thickness variation. The resulting thicknesses variation is finally subtracted from measured thickness variations of reference protocol in order to obtain a better estimation of anode breathing.

To build this estimation works, a new set of hypothesis should be clarified, through the Set of Hypothesis 4.B:

- (i) The **total thickness of pouch cell is composed only of the following components thicknesses: anode, cathode, separator and pouch bag**. The only other component present in the pouch cell is the electrolyte. It designed to fill the pore volume of anode, cathode and separator, and as a liquid, any excess of its volume can be ejected on the borders (out of thickness measurement). This hypothesis is useful to extract the anode component from total pouch cell thickness (Section 4.4.1.a).
- (ii) The **material properties of the cathode are not influenced by its state of charge**. Indeed, as studied in [53], [156], [160], [161], the Young’s modulus of an active material can depend on its lithium concentration. For simplification purpose, it is supposed here that rheological properties of cathode active materials do not depend on their lithium concentration. However, corresponding data for the cathode active material is not common in literature. Hence, this hypothesis is important to determine the rheological equations (Section 4.3.2.c).
- (iii) The **pouch bag rheological properties are supposed not influenced by the contact with electrolyte**. Indeed, at the opposite of cathode and separator that are designed to be soaked with electrolyte, the pouch bag is designed to be impermeable (non-porous and impermeable polymer layer). This is necessary for pouch bag sample preparation (Section 4.3.2.a).
- (iv) The **DForm bench presents a constant error**. When measuring with DForm test bench, it is expected that a parasitic variation of thickness is generated by the device. This parasitic variation is then supposed systematic. This systematic aspect is useful for the definition of cathode, separator and pouch bag thicknesses (Section 4.3.2.a).

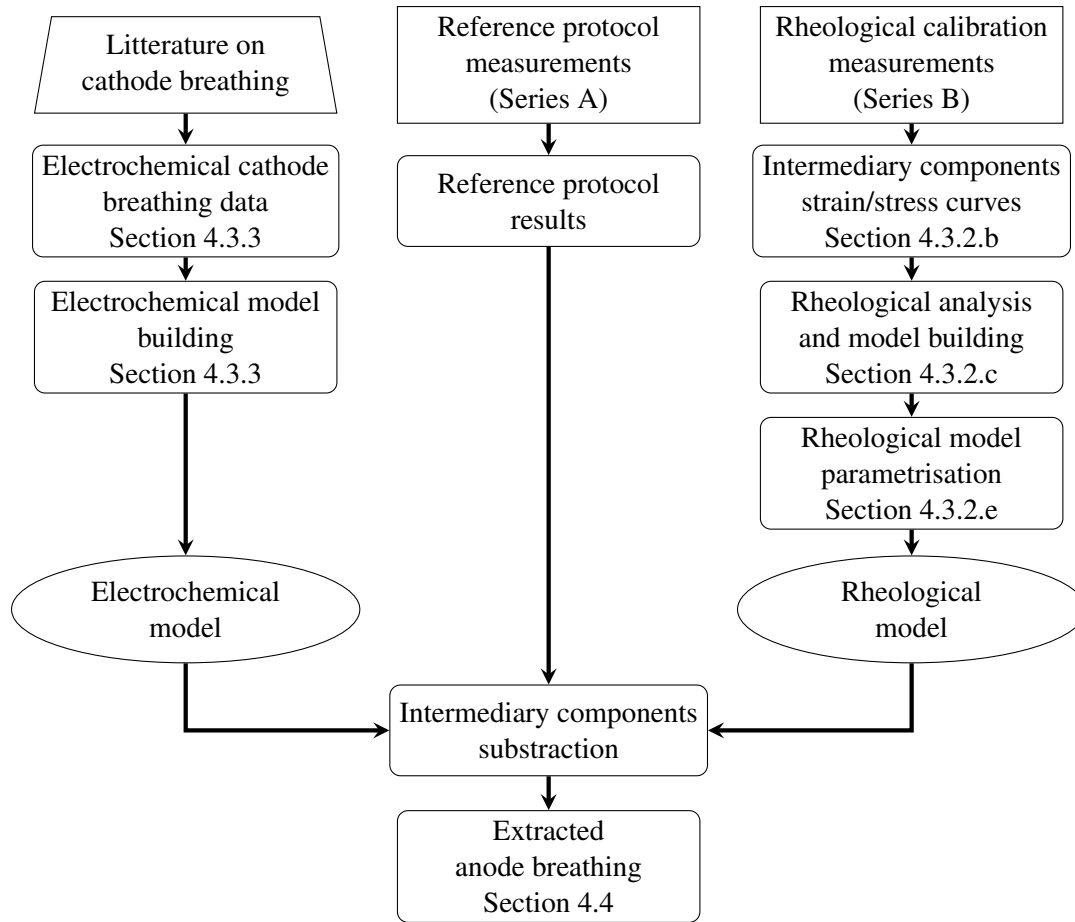


Figure 4.3: Diagram of experimental data estimation of rheological and electrochemical thickness variation of intermediary components (cathode, separator and pouch bag) to extract anode breathing — **Left column**) Cathode electrochemical breathing estimation. **Right column**) Rheological thickness variation of intermediary components (cathode, separator pouch bag) based on Novelisa model. **Center column**) Main measurement corrected by the estimations of cathode breathing and rheological thickness variations to extract anode breathing.

4.3.2 Intermediary components thickness variation due to rheology

4.3.2.a Description of rheological calibration

The objective here is to build a rheological model that predicts the mechanical behaviour of intermediary components under a variable compression, more precisely the solicitation used to characterize the anode behaviour (variable compressions of the reference protocol described in Table 4.2). To feed this understanding, a compression test based on the reference protocol was built.

The rheological calibration consists in a unique and continuous compression test, with a rectangular variation of pressure over time. The values of pressure are based on the reference protocol: 0.3, 1, 3 MPa, and 6 MPa for a supplementary checking value. This pressure pattern is applied on different samples with different compositions, as pictured in Fig. 4.4. It was originally planned to make a unique rheological calibration on the sample B01 to make a global analysis of all intermediary components (B01 being the reference pouch cell sample without the anode). The plan finally changed to a more complex one, in order to extract the behaviour

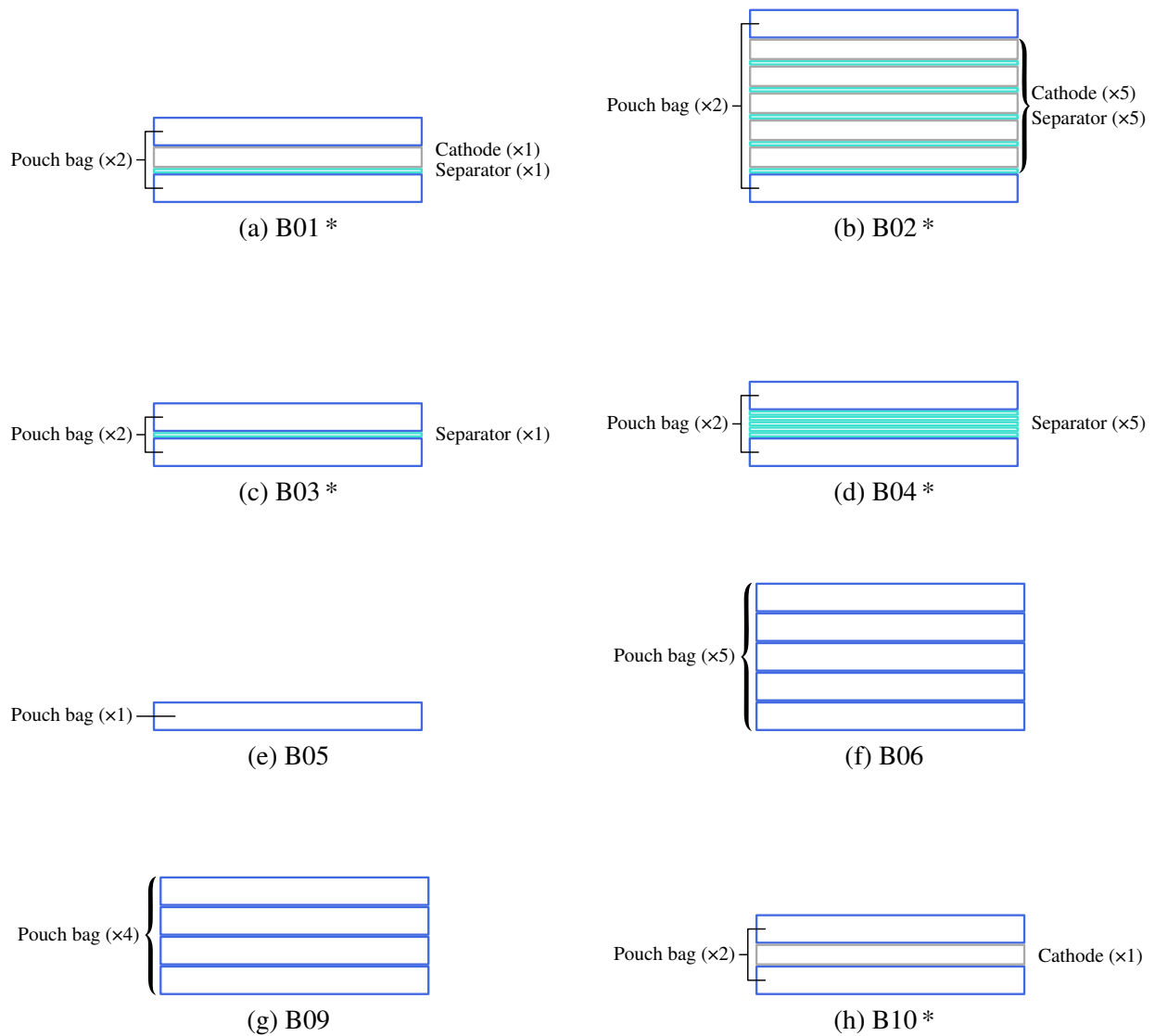


Figure 4.4: Samples used for calibration of the mechanical model of intermediary components. Samples with an asterisk “*” are sealed and contain electrolyte.

of each intermediary component with a better accuracy. For this reason, the samples B02 to 06 were crafted for this purpose. For cathode and separator, the samples were built with pouch bags in order to maintain a contact with electrolyte, because their wet state (soak with electrolyte) were expected to be quite different from their dry state. This is not the case for the pouch bag which is especially designed to be non-porous and impermeable, as stated in Hyp. 4.B.iii (page 147). Thanks to these samples, it is then possible to extract the thickness variations via a system of equations based on total thicknesses that gives the final following solutions:

$$\begin{cases} th_{cat} = \frac{th_{B02} - th_{B01}}{4} - \frac{th_{B04} - th_{B03}}{4} \\ th_{sep} = \frac{th_{B04} - th_{B03}}{4} \\ th_{bag} = \frac{th_{B06}}{5} \end{cases} \quad (4.1)$$

It is possible to detect, in this protocol, a sort of “over-definition”. Indeed, theoretically, only three measurements would have been enough to solve the system, for example by making one sample of only pouch bag and two others with pouch bag + cathode and pouch bag + separator. The idea behind the current protocol is also to get rid of any potential thickness deviation due to parasitic deformation of DForm bench. Thanks to this approach, by supposing the error constant as stated in Hyp. 4.B.iv (page 147), subtracting two twined measurements (*e.g.* B01/B02 or B03/B04) enable to extract the required component and to get rid of the error simultaneously. Concerning the pouch bag, it can be noticed that only the sample B06 is used for thickness extraction. Indeed, the use of sample B05 led to a much noisier curve, and the resulting calibration led to an even poorer prediction of the pouch bag behaviour (using the “muppet tests” in Section 4.3.2.e). Hence, because the total measured thickness in B06 was consequent ($5 \times 110 \mu\text{m}$), it was supposed that the DForm bench error was attenuated enough, then only measurement of B06 was used final parametrisation. The raw thickness extracted from Eq. (4.1) are displayed in Fig. 4.5a.

4.3.2.b Extracted thicknesses of cathode, separator and pouch bag

The application of three equations of Eq. (4.1) provides the three curves of bottom plot of Fig. 4.5a. The results relevantly present similar evolution: successive reductions of thickness as long as the pressure increases, and the presence of an irreversible deformation when the pressure comes back to P_{ref} . A singularity appears in the cathode curves, where an increase of thickness can be observed at the beginning of the first compression (4.5a.①). The most likely hypothesis for this discrepancy is certainly an error amplification. Indeed, in Eq. (4.1), the cathode equation is based on four data sets ($th_{B01}, th_{B02}, th_{B03}, th_{B04}$), the separator on two data sets (th_{B03}, th_{B04}) and the pouch bag on one data set (th_{B06}). Therefore, considering the absolute error of a measurement data set $\hat{u}(th)$ (standard deviation), the final order of magnitude of absolute error is different depending on the component (sum error propagation rule with standard deviations): $\hat{u}(th_{\text{cat}}) = \sqrt{2}\hat{u}(th_{\text{sep}}) = 2\hat{u}(th_{\text{bag}}) = 2\hat{u}(th)$.

Coming back to the data, Fig. 4.5b displays the stress/strain curve of the cathode. Except for the deviation at the beginning of this specific curve, all components follow the same behaviour, so the analysis made here is similar for all intermediary components. The first observation relates to the slopes of relaxation (4.5b.②). Instead of presenting a unique slope, which would be the behaviour of a linear elastic material, the increase of the slope demonstrates a non-constant value of the Young’s modulus. Additionally, the deformation presents a time-dependent part (4.5b.③), which traduces a viscous property. Finally, horizontal viscous parts during decompression, even if they almost reach their asymptotic value, do not come back to initial deformation, sign of a cumulative plastic deformation (4.5b.④). As a result, this quick analysis reveals at least three rheological behaviours that the model has to take into account:

- Non-linear elasticity
- Viscosity
- Plasticity

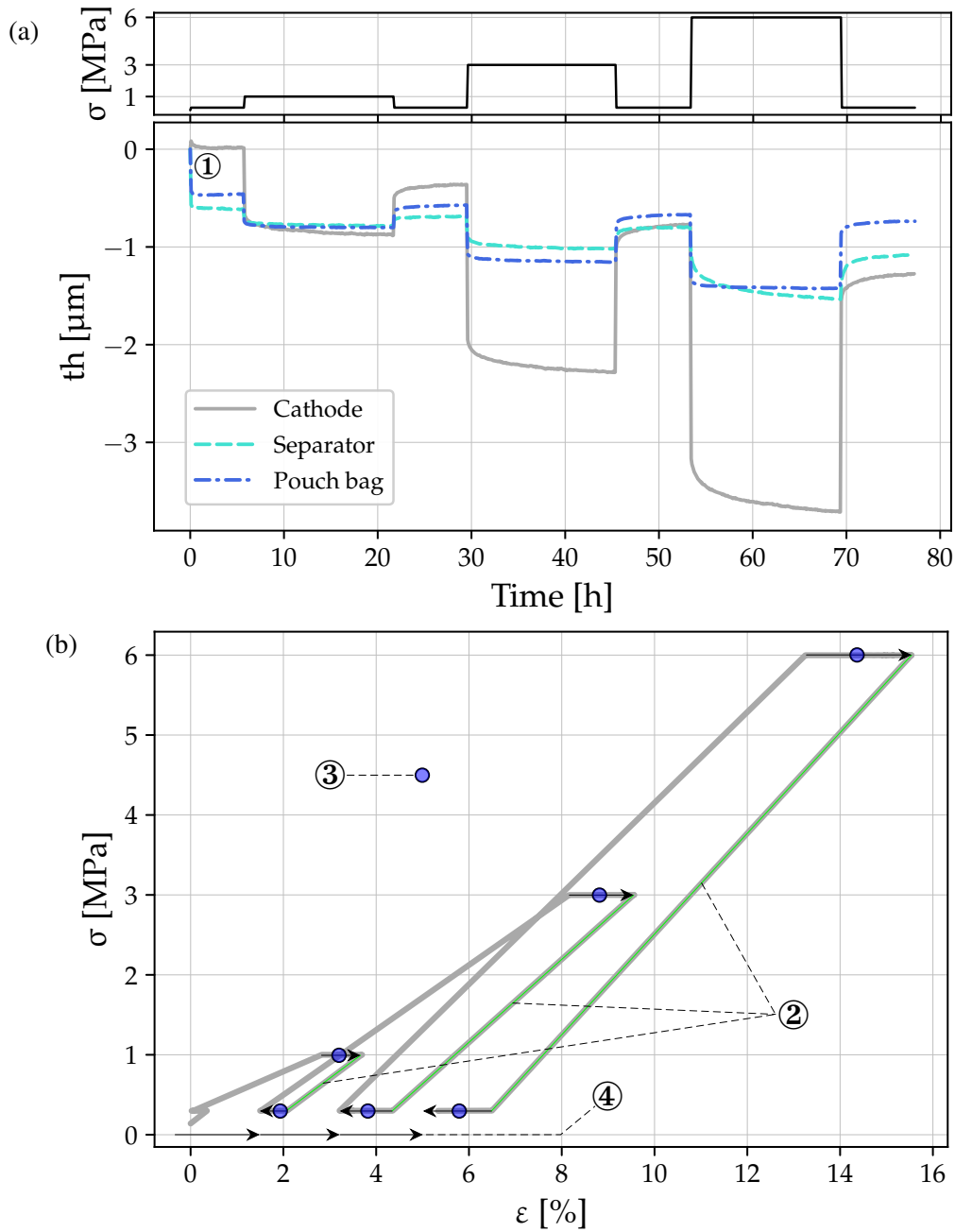


Figure 4.5: Extracted behaviours of intermediary components for rheological calibration — **a)** Top plot: pressure applied on sample; Bottom plot: thickness variations of parallel components deduced from compression tests on samples. **b)** Stress/Strain curve of cathode with rheological characteristics. ②: non-linear elasticity, ③: viscosity, ④: plasticity.

4.3.2.c Rheological analysis and elements deduction

The objective is now to build the rheological model, called “**Novelisa**” in this manuscript. A first step of analysis is necessary to determine the several basic elements of this model.

Concerning the elasticity, the Hooke’s form as in Eq. (1.4) is, of course, the first that comes in mind. However, as previously introduced, the Young’s modulus seems to change dependently to the stress or the deformation. Thus, the elastic compression is not as simple as a linear form, a behaviour that has been already

considered in literature. For example, Mai *et al.* (2019) [56] introduced a porosity-dependent Young's modulus, through the form $E = E_0(1 - \epsilon/\epsilon_0)^n$, where ϵ is the porosity, in order to simulate the hardening of the material when the porosity decreases. In the same philosophy, Liu *et al.* (2020) introduced a non-linear stress/strain relationship via the form $\sigma = E_0 + E_1\epsilon^n$. Finally, Li *et al.* (2022) [211] detail the behaviours of Li-ion battery porous components, known to be softer than the dense material. For example, the NMC and graphite particles see their Young's modulus drop down three or one order of magnitude, and the separator can present a Young's modulus dropping approximately from 1.4 to 0.22 GPa, when used as a battery component material. They consequently reintroduced a semi-empirical porosity-dependent relationship defined as $E = E_0(1 - a\epsilon)^n$, where a and n are two fitting parameters. Consequently, using a non-linear elasticity is common for a model of cell composed of either granular material (cathode) or polymeric (separator and partially pouch bag). Several trials using linear elasticity have been made on the data of Fig. 4.5, but the Young's modulus matching with lower pressures was systematically too low for higher pressures (resulting over-estimated deformations at high pressure). To explain this behaviour, it is supposed that the Young's modulus increasing is due either to variation of pore volumes cathode or polymeric structure change for separator and pouch bag. It was then decided to introduce the following form of non-linear spring, whose Young's modulus is dependent to the irreversible strain (plastic and viscoplastic).

$$\epsilon_e(t) = \frac{\sigma(t)}{E(1 + a_e\epsilon_{irr}(t))^{n_e}} \quad (4.2)$$

Where a_e and n_e are two fitting parameters (setting a_e to zero makes the form come back to the Hooke's law). Through this formulation, the implemented Young's modulus E does not correspond to the bulk material rigidity, but to the sample rigidity without deformation, so the value is expected to be at low order of magnitude. We can then define an "equivalent" Young' modulus dependent to the irreversible strain:

$$E'(\epsilon_{irr}) = E(1 + a_e\epsilon_{irr}(t))^{n_e} \quad (4.3)$$

Where the irreversible strain is defined as the sum of plastic and visco-plastic strains:

$$\epsilon_{irr}(t) = \epsilon_p(t) + \epsilon_{vp}(t) \quad (4.4)$$

Concerning the elastic viscosity, the usual form of damping seemed enough to accurately simulate the time-dependent part, via the form of the damper:

$$\dot{\epsilon}_{ve}(t) = \frac{\sigma(t)}{\eta} \quad (4.5)$$

Concerning the plasticity, this required knowledge that was found in the book "*Mécanique des matériaux solides*" from Lemaitre & Chaboche (1985) [212], where the plasticity is richly treated. In this optic, the plasticity was tackled through two approaches: instantaneous and time-dependent (viscous). Indeed, beyond the usual instantaneous plasticity (occurring during the lighter slopes, opposite to elastic slopes ② in Fig. 4.5b), the temporal evolution during compression at 1, 3 and 6 MPa (see Fig. 4.5a) seems asymmetric compared to the associated relaxation. The presence of a visco-plastic behaviour was suspected. Consequently, the

instantaneous plasticity was introduced via a Ramberg-Osgood equation (based Ramberg & Osgood (1943) [213]), in section 2.1.2 in Lemaitre & Chaboche (1985) [212]:

$$\varepsilon_p(t) = \left\langle \frac{\check{\sigma}(t) - \sigma_{Yp}}{H_p} \right\rangle^{n_p} \quad (4.6)$$

Where σ_{Yp} is the plastic yield stress (minimum stress for a first plastic deformation), H_p and n_p are two fitting parameters. Here, the brackets represent the positive part:

$$\langle y \rangle = \begin{cases} 0 & \text{if } y \leq 0 \\ y & \text{if } y > 0 \end{cases} \quad (4.7)$$

In addition, $\check{\sigma}$ is the highest stress value reached beforehand defined as:

$$\check{\sigma}(t) = \max \left(\sigma(t') \forall t' \in [0, t] \right) \quad (4.8)$$

For the viscous plasticity, an isotropic hardening visco-plasticity was used, more particularly the law proposed in section 4.2.3 in Lemaitre & Chaboche (1985) [212] for the case of successive loads:

$$\dot{\varepsilon}_{vp}(t) = \dot{\varepsilon}_{\text{unity}} \left\langle \frac{\sigma(t) - H_{vp1} \check{\varepsilon}_{vp}(t) - \sigma_{Yvp}}{H_{vp2}} \right\rangle^{n_{vp}} \quad (4.9)$$

Where σ_{Yvp} is the visco-plastic yield stress, H_{vp2} and n_{vp} are two fitting parameters, and $\dot{\varepsilon}_{\text{unity}}$ is a parameter of dimension homogenisation (so that H_{vp2} has the dimension of pressure). Moreover, $\check{\varepsilon}_{vp}$ is the cumulative visco-plastic strain defined as:

$$\check{\varepsilon}_{vp}(t) = \int_0^t \dot{\varepsilon}_{vp}(t) dt \quad (4.10)$$

As a result, the Novelisa model is based on a combination of this fundamental elements. The name is inspired from the resulting NON-linear ViscoELastic ISotropic hArdening (NOVELISA) behaviour the model describes.

4.3.2.d Structure and numerical implementation

The Novelisa model is based on the consideration of four fundamental rheological behaviours: elastic, viscoelastic, plastic and visco-plastic. These behaviours are respectively modelled by the four elements **(A)**, **(B)**, **(C)** and **(D)** drawn in Fig. 4.6. The element **(A)** represents the instantaneous elasticity (non-linear spring), the element **(B)** the viscoelasticity (damper in parallel with non-linear spring), the element **(C)** represents the instantaneous plasticity (slider with non-linear spring) and the element **(D)** represents the visco-plasticity (non-linear damper). Due to the series combination, the total deformation and stress are then defined by:

$$\begin{cases} \varepsilon = \varepsilon_A + \varepsilon_B + \varepsilon_C + \varepsilon_D \\ \sigma = \sigma_A = \sigma_B = \sigma_C = \sigma_D \end{cases} \quad (4.11)$$

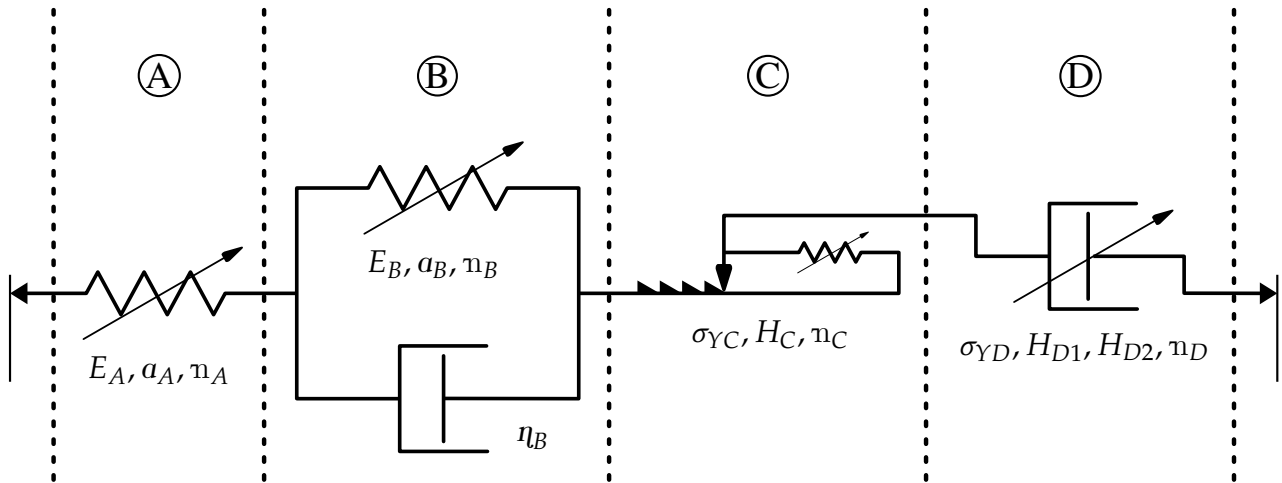


Figure 4.6: Rheological scheme of Novelisa model and fitting parameters. The diagonal arrows represent the non-linear relationship — (A): non-linear elasticity, (B): non-linear visco-elasticity, (C): non-linear plasticity, (D): non-linear visco-plasticity

For the resolution, the evolution over time of σ is already known (pressure as input) but it is not defined through a proper analytical form. Consequently, resolving the evolution over time of ε requires a discretisation of the four following equations, each one related to an element (respectively (A), (B), (C) and (D)):

$$\left\{ \begin{array}{l} \varepsilon_A(t) = \frac{\sigma(t)}{E_A \left(1 + a_A \varepsilon_{CD}(t)\right)^{n_A}} \\ \varepsilon_B(t) = \frac{\sigma(t) - \eta_B \dot{\varepsilon}_B(t)}{E_A \left(1 + a_A \varepsilon_{CD}(t)\right)^{n_A}} \\ \varepsilon_C(t) = \left\langle \frac{\check{\sigma}(t) - \sigma_{YC}}{H_C} \right\rangle^{n_C} \\ \dot{\varepsilon}_D(t) = \dot{\varepsilon}_{\text{unity}} \left\langle \frac{\sigma(t) - H_{D1} \check{\varepsilon}_D(t) - \sigma_{YD}}{H_{D2}} \right\rangle^{n_D} \end{array} \right. \quad (4.12)$$

The equations for strain (A) and (C) are quite explicit at the opposite of strains (B) and (D). After discretisation, the equation for strain (B) is now explicit, but this is not the case for strain (D) that depends on $\check{\varepsilon}_D$. The resolution is then solved by an approximation of the value of $\check{\varepsilon}_D$ based on the previous time step. Finally, the time step can be determined through a sensitivity test, going from a large value and decreasing until the new value does not affect the result any more. After this test, considering the orders of magnitude of rheological parameters, it is found that two minutes is a good compromise between physical reliability and computation time. When computed for experimental result estimation, the time step is reduced to the experimental data set time step, *i.e.* 10 seconds. The resulting algorithm is detailed in Algorithm 2.

Algorithm 2: NOVELISA ALGORITHM

Input: $\sigma[0, h_{\max}]$, Δt , E_A , E_B , η_B , H_C , H_{D1} , H_{D2} , a_A , a_B , n_A , n_B , n_C , n_D , σ_{YC} , σ_{YD}

1 **for** $h = 1$ **to** h_{\max} **do**

$$\begin{aligned}
 2 \quad & \check{\sigma}^h = \sigma^h \text{ if } \sigma^h > \check{\sigma}^{h-1} \text{ else } \check{\sigma}^{h-1}; \quad \varepsilon_C^h = \left\langle \frac{\check{\sigma}^h - \sigma_{YC}}{H_C} \right\rangle^{n_C} \\
 3 \quad & \dot{\varepsilon}_D^h = \left\langle \frac{\sigma^h - H_{D1}\check{\varepsilon}_D^{h-1} - \sigma_{YD}}{H_{D2}} \right\rangle^{n_D}; \quad \check{\varepsilon}_D^h = \check{\varepsilon}_D^{h-1} + \frac{\dot{\varepsilon}_D^{h-1} + \dot{\varepsilon}_D^h}{2} \Delta t; \quad \varepsilon_D^h = \varepsilon_D^{h-1} + \Delta t \dot{\varepsilon}_D^h \\
 4 \quad & \varepsilon_{CD}^h = \varepsilon_C^h + \varepsilon_D^h; \quad \varepsilon_A^h = \frac{\sigma^h}{E_A(1 + a_A\varepsilon_{CD}^h)^{n_A}}; \quad \varepsilon_B^h = \frac{\Delta t \sigma^h + \eta_B \varepsilon_B^{h-1}}{\Delta t E_B(1 + a_B\varepsilon_{CD}^h)^{n_B} + \eta_B} \\
 5 \quad & \varepsilon^h = \varepsilon_A^h + \varepsilon_B^h + \varepsilon_C^h + \varepsilon_D^h
 \end{aligned}$$

Output: ε , ε_A , ε_B , ε_C , ε_D ,

4.3.2.e Parametrisation

To better understand their role in the model, Fig. 4.7 displays a progressive introduction of the rheological elements (A), (B), (C) and (D). First, using the element (A) with a pure linear behaviour gives the reversible rectangular reaction of Fig. 4.7a, where the time-dependency is obviously missing. Adding the element (B) with linear reaction leads to a common Zener model, resulting the curve of Fig. 4.7b. As we can see, the deformation at higher pressure is over-estimated, which is coherent with the non-linear elasticity deduced from Fig. 4.5b. The addition of this non-linearity only appears when plastic and/or visco-plastic deformation occurs, as shown in Fig. 4.7c where the bottom dash-dotted line represents the instantaneous plasticity of element (C). Finally, the element (D) refines the model by smoothing the slopes during compressions at higher pressures, giving the final curve of Fig. 4.7d. Furthermore, Fig. 4.7e draws the evolution of the equivalent Young's modulus E_A' for the cathode. It starts from the initial input value and gradually increases through a succession of instantaneous jump (dependence to instantaneous plasticity), time-dependent progression (dependence to visco-plasticity) and plateaus (no plastic deformation occurs). With a range varying between 45 and 65 MPa, the order of magnitude is quite low, considering the values given by Li *et al.* (2022) [211]. First, we can think that a problem comes from the model parametrisation. In fact, the fitting parameters were set via a Powell minimisation algorithm of mean absolute error between experimental and simulation curves, so it can be imagined that the minimisation gave a fitting result but with physically inconsistent parameters. Nevertheless, this automatic process was manually corrected to obtain the right orders of magnitude. Despite this process, the best Young's moduli required to be that low to obtain the vertical drops of relaxation. As a consequence, suspicions come from the experimental curve itself. As we saw during the uncertainty analysis of Eq. (4.1), the cathode behaviour presents a high accumulated error, so the current fitting is efficient for this curve, but maybe not as accurate as it lets imagines to describe the component generally.

Consequently, an ensuring step is to refine the fitting parameters via what we can call, in a playful way, a “muppet test”. It consists in making a complex pressure variation on a checking sample and testing the Novelisa model on this new measurement, in order to validate or improve the Novelisa model parametrisation. The samples B09 and B10 (Figs. 4.4g and 4.4h) have been made for this purpose. By applying this test,

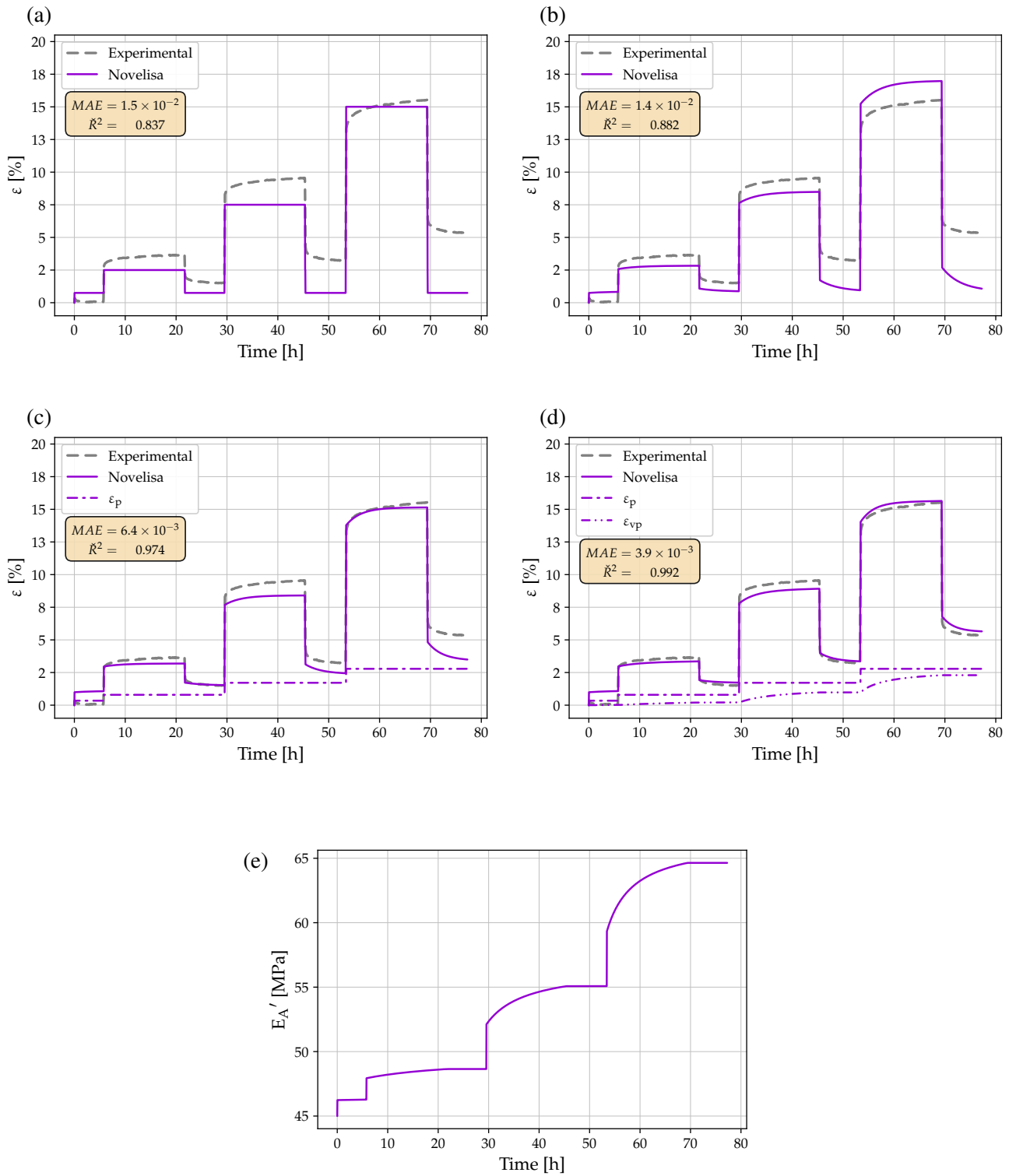


Figure 4.7: Progressive introduction of rheological elements in Novelisa model, example with cathode — MAE: Mean Absolute Error; R^2 : coefficient of determination experiment/model. **a)** Linear elastic model. **b)** Linear elastic/visco-elastic model. **c)** Non-linear elastic/visco-elastic and plastic model. **d)** Non-linear elastic/visco-elastic and plastic/visco-plastic model. **e)** Evolution of equivalent Young's modulus E_A' .

it was systematically noticed that the settings was too soft, and a slight increase of non-viscous elastic or plastic rigidity led to a better match. After the estimation, the fitting was surprisingly good for the sample B09 (Fig. 4.4g) with a coefficient of determination \check{R}^2 of around 0.908 detailed in Fig. 4.8a, which indicates a good fit of the model. The most important observation of this muppet test is the stability of the Novelisa model (at least for this test), *i.e.* its ability to avoid any significant cumulative error that leads to a progressive divergence with experimental result. However, the model is much less matching for sample B10, as presented in Fig. 4.8b, where

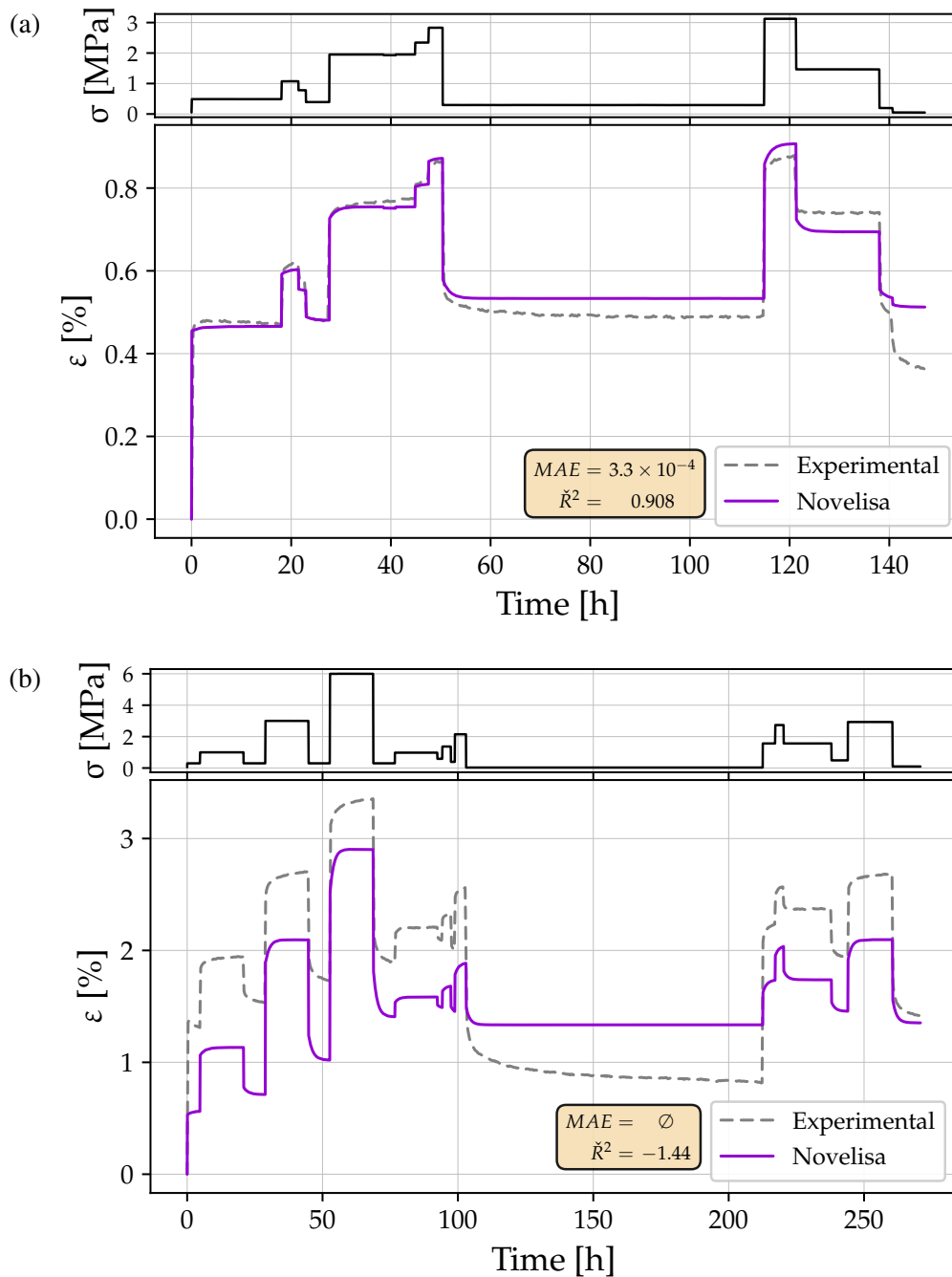


Figure 4.8: Muppet tests after correction of rheological parameters — MAE: Mean Absolute Error, \check{R}^2 : coefficient of determination experiment/model. **a)** Sample B09 (four layers of pouch bag). **b)** Sample B10 (on cathode and two layers of pouch bag).

the negative coefficient of determination witnesses a poor prediction of the Novelisa model. More precisely, its stability and qualitative prediction are quite good, but the real issue appears for order of magnitude of instantaneous deformations, as elastic as plastic. For example, after the succession of several pressure changes at $t \simeq 100$ h, the model highly under-estimates the following relaxation. Another important observation is the discrepancy due initial values. The first deformation at $t = 0$ h is a crucial instant in the prediction of the model. As it can be seen, the initial error leads to a substantial constant error that remains all along the simulation. This makes us realise how difficult it is to precisely set up a model based on indirect measurements of components. The main mistakes of rheological calibration is the limited study of the relaxation behaviours of components (leading to an eventual false prediction of plastic behaviour) and the underestimation of the initial deformation importance in the measurement protocols. The whole parametrisation process lead to the final rheological parameters summarised in Table 4.3

4.3.3 Cathode thickness variation due to electrochemistry

The Novelisa model developed in previous section takes into account only the mechanical deformation. However, it does not take into account the variation of volume due to electrochemistry, more precisely concerning the cathode that is also subjected to electrochemical breathing. As a result, it is proposed here to take into account this aspect, through a simplified model of cathode breathing. Vidal (2021) [40] already made an approximation of this breathing, by taking the data provided by de Biasi *et al.* (2017) [214]. The latter authors reveal a approximately linear change of a NMC unit cell volume from 0 to -2.4% , with the potential (VS lithium) varying from 3.6 to 4.3 V. For simplification purpose, the discrete structure of cathode is not considered here, it is supposed that the volume variation of pure NMC is directly transmitted to thickness change. Because the cathode is not entirely composed of NMC (92%), another factor $A_{\text{NMC}} = 0.92$ limits the volume change to this fraction. Hence, the electrochemical volume variation of cathode is defined as:

Parameter	E_A	E_B	η_B	a_A	a_B	H_C	H_{D1}
Unit	MPa	GPa	TPa.s	–	–	GPa	GPa
Cathode	45	0.3	2	5	5	1	1
Separator	400	1	5	40	10	5×10^{20}	0.6
Pouch bag	100	5	25	40	10	1×10^{12}	10
Parameter	H_{D2}	σ_{YC}	σ_{YD}	n_A	n_B	n_C	n_D
Unit	GPa	Pa	Pa	–	–	–	–
Cathode	4	0	0	10	2	0.7	2
Separator	12	0	0	2	1	0.08	2
Pouch bag	10	0	0	12	1	0.16	2

Table 4.3: Novelisa model final parameters.

$$th_{\text{cat,electrochemical}} = th_{\text{cat},0} A_{\text{NMC}} v_{\text{NMC}}(Q) \quad (4.13)$$

Where $v_{\text{NMC}}(Q)$ is the function defined in Fig. 4.9.

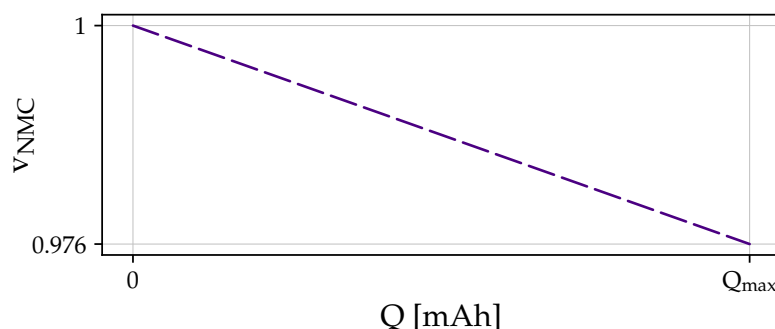


Figure 4.9: Relative volume of NMC622 cathode as a function of capacity. Maximum value of capacity Q_{max} depends on the sample mass. Adapted from de Biasi et al. (2017) [214], Figure 9a^a.

^a © The Journal of Physical Chemistry C. Reproduced under charge-free nature of reuse. American Chemical Society, all rights reserved.

4.4 Results

All the samples used for the following results had the same structure as the reference pouch cell schemed in Fig. 4.1. They have been submitted to different constraints during cycling, in order to analyse the parameters introduced in Section 4.2.3. They follow the description introduced in Table 4.4.

The sample name is composed of the letter A followed by two digits (from 01 to 06). When it is followed by an underscore and a digit, it corresponds to an experiment key. The digit is the index of the experiment. Example: “A01_1” is the experiment number 1 made on the sample A01.

4.4.1 Reproducibility and anode thickness estimation

4.4.1.a Raw data analysis

A first protocol has been made on samples A01 and A02 in order to test the reference protocol reproducibility, by doubling the measurement at room temperature (24°C) and reference pressure (0.3 MPa) during formation. The curves in Fig. 4.10a displays the results of reference protocol, with the three first cycles at C-rates of C/20, C/10 and C/5 (so progressively faster), followed by cycles at C/5 submitted to successive compressions and relaxations. The curves of samples A01 and A02 reveal to be really close. The slight differences of cycling periods certainly comes from the uncertainty of sample capacities, leading to slightly diverging C-rates. These close results are quite ensuring concerning the reliability of the DForm test bench used for the reference protocol. Even during the compressions at 1 and 3 MPa, the thickness changes of both results efficiently follow the same path. Through this first protocol, interesting features already appear. Indeed, we can observe the progressive irreversibility, cycle after cycle, which is particularly present during the first cycle. Hence, two questions raise from these observations:

- **For a given pressure, does a stable breathing exist?** By “stable breathing”, it means a state where the irreversibility is equal to zero and the swelling amplitude is constant.
- **If the stable breathing exists, does the pressure present a memory effect on it?** In other words, by starting from an initial pressure, changing to another one and coming back to the initial one, does it change the initial stable breathing?

In this case, the progression to this eventual stable breathing (maximum at 10.6 μm , 4.10a.①) is interrupted by the compression at 1 MPa. After this first compression, the eventual stable breathing at P_{ref} seems lower (maximum at 10.0 μm , 4.10a.②). During the compression at 3 MPa, the pressure is such that the thickness change tends into negative values, *i.e.* the thickness is lower than its value at the beginning of cycling. After this second compression, the stable breathing at P_{ref} seems once again changed to an even lower amount (maximum at 8.3 μm , 4.10a.③). By consequence, the breathing of the sample seems to keep the history of the temporary compression at higher pressure. Nevertheless, this conclusion is limited by several facts. Firstly, the low number of cycles at P_{ref} limits the real estimation of the asymptotes and makes the evaluation of the stable breathing much less certain. Secondly, we have to remind that these curves are not corrected by application of Novelisa model, so the current thickness change includes all the components, including cathode, separator and pouch bag.

For this purpose, Fig. 4.10b plots the curves of results A01_1 of the full sample (lighter solid line) and the same curve after estimation with Novelisa model, supposed as the real behaviour of the anode (darker solid line) according to Hyp. 4.B.i (page 147) (total thickness composed by anode, cathode, separator and pouch bag). The different predicted behaviours of cathode, separator and pouch bag are plotted in dashed lines (as opposite to anode and cell curves, their initial values are not set to zero to conserve their real change magnitude). As expected, the separator has a limited impact on the global thickness change due to its low thickness. The most

Sample	Experiment key	Protocol description	Protocol aim / Analysed parameter
A01	A01_1	RP, 0.3 MPa, 24°C	Reference results
A02	A02_1	RP, 0.3 MPa, 24°C	Reproducibility test of RP at 24°C
A03	A03_1	RP, 0.3 MPa, 61°C	Influence of temperature
	A03_2	C5, 0.3MPa, 24°C	Test of sample A03 reliability
A04	A01_1	RP, 0.3 MPa, 61°C	Reproducibility test of RP at 61°C
A05	A05_1	RP, 1 MPa, 24°C	Influence of pressure during formation
A06	A06_1	RP, 3 MPa, 24°C	Influence of pressure during formation

Table 4.4: *Experimental protocols summary* — A##: convention of sample name, A##_#: convention of experiment key, RP: Reference Protocol, C5: cycling at C/5. For reference protocol (RP), the pressure indicates the formation pressure (P_{form} in Table 4.2). For simple cycling (C5), the pressure indicates the pressure applied all along the cycling.

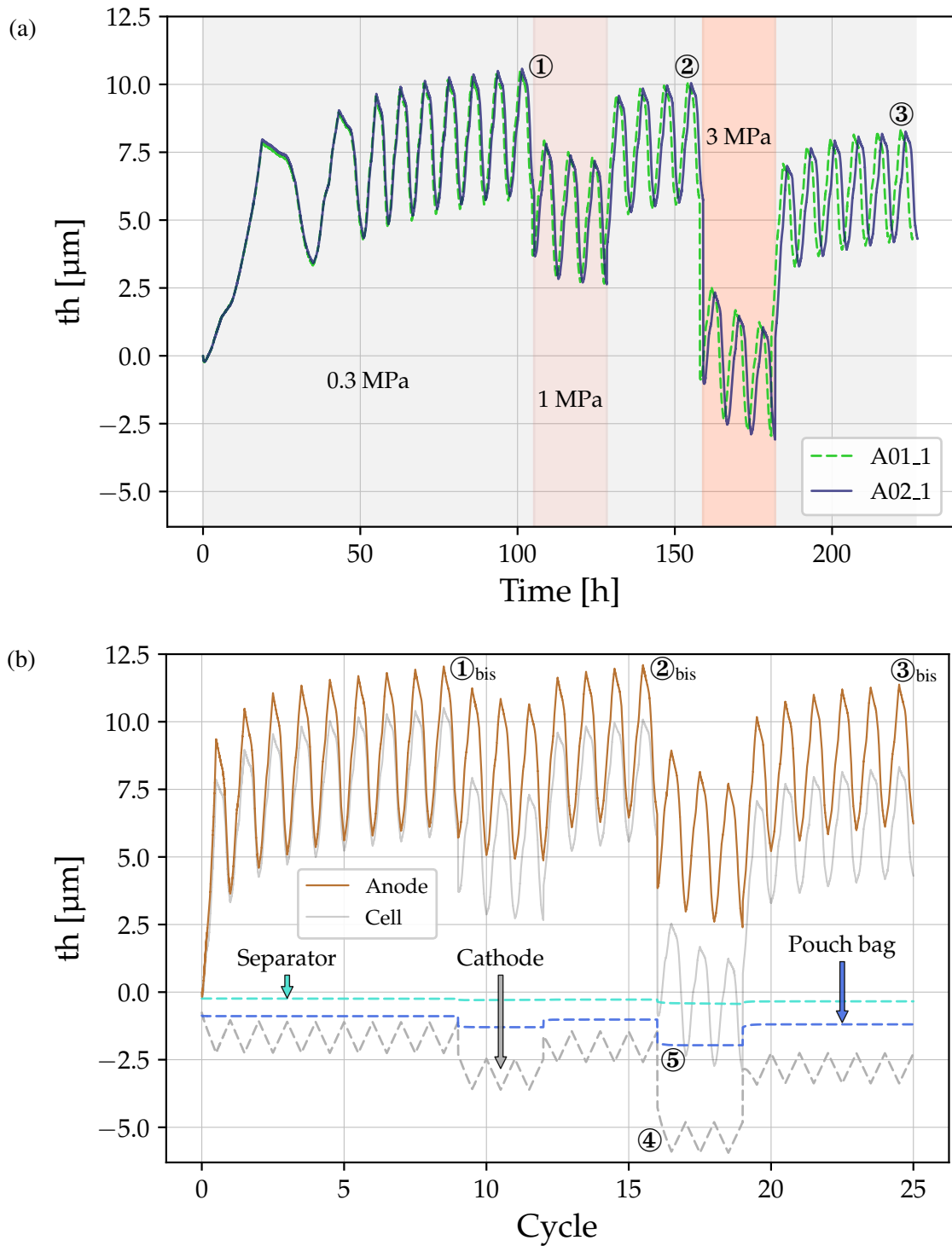


Figure 4.10: Full cell and extracted anode thicknesses — **a)** Reproducibility test of reference protocol (24°C and 0.3 MPa during formation). Thickness correspond to full cell. **b)** Extraction of anode thickness change from A01_1 results with Novelisa model (initial value of new curve in solid line reset to zero after correction).

impacting component is the cathode, predicted to be the softest of the components, engendering a variation of around $5.9 \mu\text{m}$ under a pressure of 3 MPa (4.10b.④). However, even if it was measured to be of higher rigidity, the thickness variation of pouch bag is non-negligible due to its large initial thickness, reaching $2.0 \mu\text{m}$ of thickness change under a pressure of 3 MPa (4.10b.⑤). The resulting thickness change of the anode now shows a more stable evolution. By making the parallel of the highest points in Fig. 4.10a (①, ② and ③), the equivalent points in Fig. 4.10b (①_{bis}, ②_{bis} and ③_{bis}) have less significant amount concerning eventual stable breathing, with respective values of 12.0, 12.1 and 11.4. The history of pressure on the eventual stable breathing at P_{ref} (0.3 MPa) still seems to occur, the previous higher pressures (1 and 3 MPa) reducing the mean breathing value, but once again, the number of cycles makes difficult the estimation of the final stabilised breathing of the anode. Hence, these precise results are incomplete to state if a temporary compression at higher pressure of the breathing anode is able to permanently change its stable breathing, if it exists.

In fact, the difficulty to reach an eventual breathing state for such a breathing system is expected. In her thesis in 2021 [40], Delphine Vidal already made some extended cycling and, depending on the used material, noticed what we can call a “**pseudo-stable breathing**”, *i.e.* a phase where the breathing still deviates but at a constant rate. For example, Fig. 4.11a illustrates three different extend cyclings for different material for cathode (NMC622, NMC811 and LCO) under 0.1 MPa, until 87 cycles. Even after this numerous cycles, all the cyclings still deviate with a more or less linear form, suggesting that the pressure at 0.1 MPa is not enough to obtain a stable breathing. Hence, to state if a stable breathing is likely, a parallel with hydrogen storage can be made. In his review of hydrogen storage using hydrides in 2021 [23], Olivier Gillia noticed that this technological solution presents such a “stabilised densification state” of hydride beds. However, the number of breathing cycles necessary to reach this stabilised state is huge (around a hundred). More precisely, when it comes to dependency to pressure, Galvis Escobar *et al.* (2017) [215] made cycling measurement on a hydrogen storage alloy for different levels of pressure (0.0325, 0.12 and 0.84 MPa). The results are displayed in Fig. 4.11b. It interestingly reveals three different states depending on pressure. At low pressure (0.0325 MPa), the breathing seems to deviate indefinitely (or with a very long time of stabilisation). At high pressure (0.84 MPa), the breathing stabilises at lower volume than the initial volume. Finally, at middle pressure (0.12 MPa), the breathing seems quasi-stabilised around the initial volume. Consequently, considering the anode breathing in Fig. 4.10b, it seems to follow a similar behaviour, so the existence a stable breathing is likely, as long as the right pressure is applied.

4.4.1.b Delta quantities analysis

A deeper analysis of Delta quantities can bring further information on the impact of pressure on the anode.

First, a noticeable point is the different dependencies on pressure changes. The capacity is independent of pressure, following a constant decrease rate over cycles. The particles breathing being mainly dictated by stored capacity, it is then supposed to be also decreasing with the same rate. At the opposite, swelling amplitude and irreversibility are clearly impacted, through the presence of increasing or decreasing peaks when pressure changes, demonstrating a noticeable change of sample shape. Consequently, these important variations of swelling amplitude and irreversibility are more likely to be explained through a particles’ reorganisation rather than a variation of particles breathing (even though, these results are not sufficient to prove it).

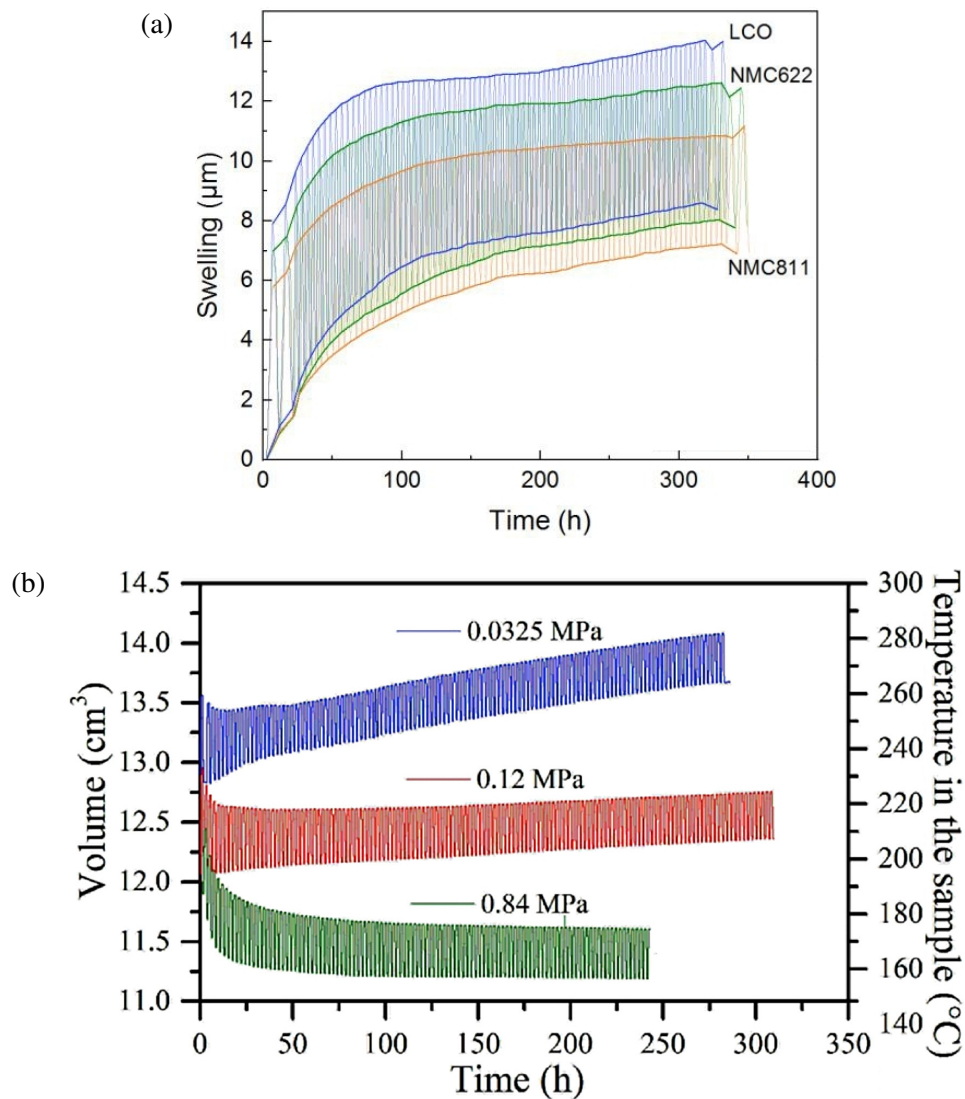


Figure 4.11: Long cycling of battery cell and hydrogen material storage hydride to observe long period of breathing stabilisation — **a)** Breathing of three pouch cells with 6wt% of silicon in anode mass, built with different cathode material: Nickel-Manganese-Cobalt (NMC622 and NMC811), Lithium Cobalt Oxide (LCO). A total of 87 cycles was made under 0.1 MPa. Adapted from Vidal (2021) [40], Figure V-12^a. **b)** Volume and temperature change of hydrogen storage alloy, during hydrogenation-dehydrogenation stages, for three levels pressure (0.0325, 0.12 and 0.84 MPa). Adapted from Galvis et al. (2017) [215], Figure 4^b.

^a © Thesis archives. Open access.

^b © Hydrogen Energy Publications LLC. Reproduced under charge-free nature of reuse. Elsevier Ltd., all rights reserved.

The swelling amplitude Δth is necessarily impacted by the variation of charged capacity per cycle (the less lithiation/delithiation, the less breathing amplitude, and vice versa). To demonstrate it, Fig. 4.12 plots the Deltas quantities of capacity, swelling amplitude and irreversibility as a function of cycles. The clear detail observed here is the similarity of shapes, with a drastic decrease during the three first cycles and a quick stabilisation at an almost constant value. In fact, the “almost” is important in our analysis. The fact that charged capacity decreases during the first cycles is not astonishing, engendered by lithium interface formation during first cycles and decreasingly affected as the C-rate increases. The total capacity indeed decreases from 28.9 mAh (4.12.①) to 23.7 mAh (4.12.②), *i.e.* around 18.0% of initial capacity, in just four cycles. Consequently, a decrease of

the thickness swelling amplitude at the beginning is coherent. However, the precise amount of this decrease is more inconsistent. Looking at the equivalent extreme point of initial decrease, the swelling amplitude Δh_{sw} drops from 9.3 μm (4.12.①_{bis}) to 6.3 μm (4.12.②_{bis}), which represents a decrease of 32.3% (with swelling amplitude at first charge for reference). Hence, at least, it proves that the swelling amplitude thickness Delta is not proportional to the charged capacity per cycle. Indeed, the third graph from the top presents the ratio of charged capacity over swelling amplitude, showing a gradual decrease. Firstly, because it is not constant, both quantities are not proportional. Secondly, the gradual decrease of this ratio suggests that the swelling amplitude is progressively more created by another origin than the capacity loss. In addition, this discrepancy does not only occur during the first cycles. In fact, these curves fit quite well with an exponential law of the form:

$$y(c) = A + Bc + C \exp\left(-\frac{c}{p}\right) \quad (4.14)$$

Where c represents time index in cycles. The resulting fits are plotted in dashed lines in Fig. 4.12, with a particular case for irreversibility thickness Delta where B is set to zero. It results the parameters in the Table 4.5 (experiment A01_1). These fits consequently describe the evolution of these quantities as a succession of two main states: the “formation breathing” and the “pseudo-stable breathing”. The “formation breathing” corresponds to the important drops at the beginning of the cycling, associated to the stabilisation phase of the exponential part. During this stage, the first electrochemical reactions generate the first decomposition products, which leads to an important loss of lithium and so of capacity. According to the values characteristic times p , by considering the common definition at $3p$ (5% of asymptotic value), this phase ends approximately after 2 or 3 cycles. Afterwards, the “pseudo-stable breathing”, as introduced in previous section (Section 4.4.1.a) consists in a phase where the breathing still deviates but at a constant rate. The electrochemistry has stabilised and most of the capacity exchanged is reversible, but not totally, which leads to a slight deviation. This is this deviation the parameter B quantifies. For the capacity, the decrease rate is about 0.03 mAh/cycle, and for the swelling amplitude, the rate is about 0.04 $\mu\text{m}/\text{cycle}$. Concerning the irreversibility, the parameter B was set to zero due to the constant irreversibility captured until the end of the measurement.

Concerning the proposed exponential fit, the introduction of the “pseudo-stable breathing” through the linear component Bc is questionable, because this equation suggests an infinite deviation. It can be imagined that the pseudo-stable breathing certainly leads, after a sufficient number of cycles, to a final stable breathing (swelling amplitude tending to a constant value and the irreversibility to zero). In this case, the infinite deviation due to linear component Bc would not fit any more. Instead, another exponential form with a very long response time would be more appropriate. Nevertheless, considering the number of cycles measured, the linear component Bc seems more adapted and presents the advantage of improving readability, in terms of capacity loss and breathing change per cycle.

These first results demonstrate the difficulty to evaluate the role of particles reorganisation in the variation of breathing behaviour. The presence of a decreasing capacity certainly creates a diminution of swelling amplitude, with a relationship that can be hardly captured through such experimental device. The variations of swelling amplitude and irreversibility, when pressure changes, are the only observations that suggest a real contribution of particles reorganisation, but the assessment of this contribution is still unclear.

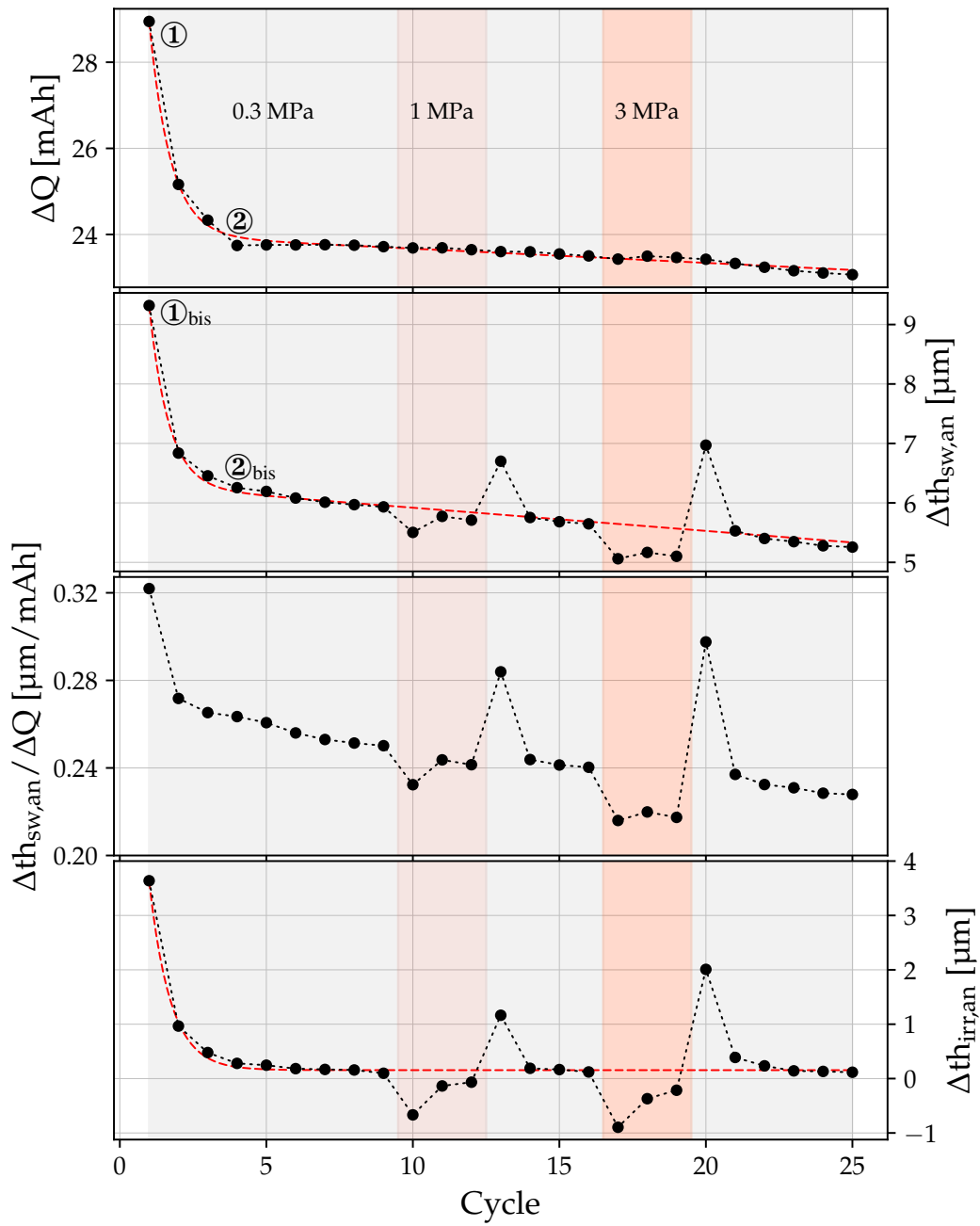


Figure 4.12: Delta graphs of results A01_1 (24°C and 0.3 MPa during formation). Thickness data based on extracted anode thickness (obtained after process described in Fig. 4.3) — **Top graph**) Charged capacity per cycle. **Middle top graph**) Swelling amplitude thickness Delta. **Middle bottom graph**) Ratio of charged capacity over swelling amplitude thickness Delta. **Bottom graph**) Irreversibility thickness Delta. Dashed lines are the fitting exponential functions of form $y(c) = A + Bc + C \exp\left(-\frac{c}{p}\right)$ (values in Table 4.5).

		A01_1				A03_1			
Parameter		A	B	C	p	A	B	C	p
Unit		[y]	[y]/cycle	[y]	cycle	[y]	[y]/cycle	[y]	cycle
ΔQ		24.0	-0.03	19.9	0.72	28.5	-0.19	33.6	0.41
Δth_{sw}		6.3	-0.04	13.7	0.66	5.5	-0.06	6.3	1.61
Δth_{irr}		0.2	0	13.7	0.73	0.2	0	9.3	1.03
		A05_1				A06_1			
Parameter		A	B	C	p	A	B	C	p
Unit		[y]	[y]/cycle	[y]	cycle	[y]	[y]/cycle	[y]	cycle
ΔQ		23.8	-0.02	19.2	0.79	23.6	-0.02	19.4	0.75
Δth_{sw}		5.6	-0.02	6.8	1.02	5.0	-0.02	3.5	1.12
Δth_{irr}		0.1	0	7.1	0.83	0.1	0	2.7	0.72

Table 4.5: Exponential fits of Delta quantities for experiments A01_1 (Figs. 4.12, 4.14 and 4.16), A03_1 (Fig. 4.14), A05_1 (Figs. 4.16 and 4.17) and A06_1 (Figs. 4.16 and 4.17). Unit based on parameter individual unit: for ΔQ , [y] = mAh, for Δth_{sw} and Δth_{irr} , [y] = μm .

4.4.2 Influence of temperature

4.4.2.a Reproducibility and global analysis

The reference protocol was made at room temperature approximately equal to $24.5 \pm 0.5^\circ\text{C}$. For high temperature, the DForm test bench was placed in climatic chamber oven from BINDER (model ED-400), where the temperature was maintained at $61.4 \pm 0.5^\circ\text{C}$. The results reveal a lower reproducibility at this temperature. Indeed, samples A03 and A04 were submitted to the reference protocol at 61°C . The comparison of both thickness curves are displayed in Fig. 4.13. As opposite to samples cycled at 24°C that were well synchronised (see experiments A01_1 and A02_1, Fig. 4.10a), the current cycling periods diverge significantly. Moreover, both shapes reveal a singular shrinking behaviour, absent from the breathing at 24°C . Indeed, after the end of charge, the thickness decreases immediately, whereas for both A03_1 and A04_1 experiments, the shrinking is slightly delayed, which gives this smoother shapes. The fact that it occurs once again reinforce the hypothesis of temperature influence. Furthermore, it was initially planned to make supplementary cycling tests on samples A03 and A04 at 24°C , but both experiments failed (A03 generated an important amount of gas that inflated the pouch bag and A04 potential dropped to negative values at beginning of cycling). It is likely that the cycling at 61°C has damaged the samples.

Despite this bad reproducibility, the impact of temperature can be analysed. As a global summary, Fig. 4.14 displays the whole comparison between experiment A01_1 (24°C) and A03_1 (61°C). By considering the raw thickness change in top graph, the evolution is globally quite similar, with a comparable reaction to pressure

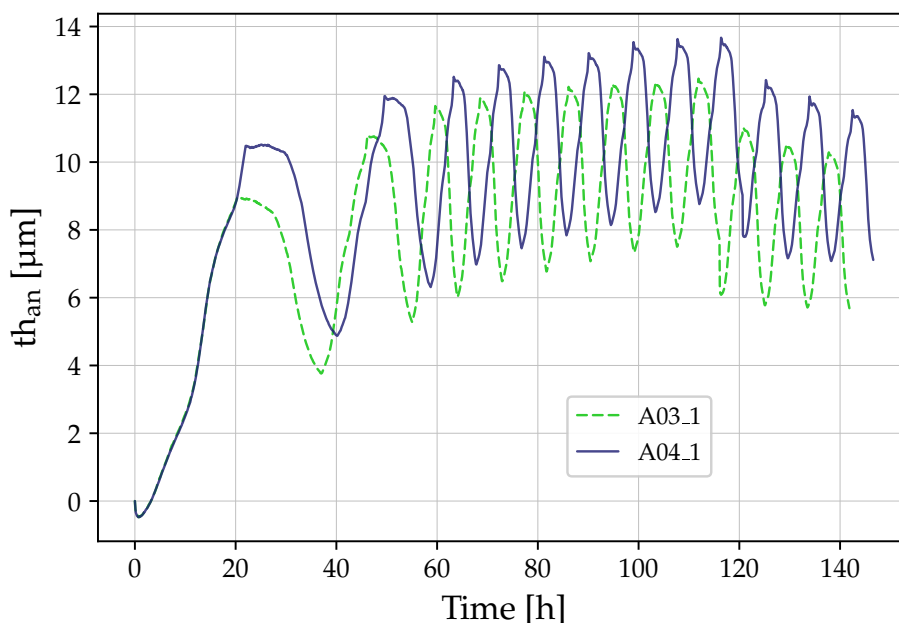


Figure 4.13: *Reproducibility test at high temperature: comparison of experiment A03_1 with A04_1 (both at 61°C and 0.3 MPa during formation), twelfth first cycle including formation. Thickness data based on extracted anode thickness (obtained after process described in Fig. 4.3).*

variation. The first observable difference induced by temperature is the swelling amplitude. Indeed, by looking at the second graph from the bottom, the 61°C swelling amplitude is almost 1.4 μm lower than 24°C, at the 25th cycle (4.14.①). In fact, it mostly comes from a progressive divergence between both curves, as revealed by the exponential fits (with values summarized in Table 4.5). Starting from equivalent initial swelling amplitudes, the breathing at 61°C decreases with a rate of 0.06 $\mu\text{m}/\text{cycle}$, against 0.04 $\mu\text{m}/\text{cycle}$ at 24°C. This higher rate can be partially explained by the decrease of capacity. At 61°C, it begins at a higher value, with 31.3 mAh accessed during the first cycle (4.14.②). However, it quickly decreases, with a rate of around 0.19 mAh lost every cycle (against 0.03 at 24°C, so a factor of around 6). This is coherent with common observations of heated pouch cell: temperature improves the ions' diffusion so enlarges the amount of accessible lithium. However, it shows here that it drastically accelerates the capacity loss, and few supplementary cycles would have probably led to inferior capacity, compared to 24°C.

The other interesting observable feature is the influence of pressure change on capacity, in the 61°C case. Indeed, we can notice a brief increase at the compression at 1 MPa (of around 2.7 mAh, 4.14.③) and more permanent at the compression at 3 MPa (of around 0.7 mAh, 4.14.④). Thus, temperature seems to have increase sample sensitivity to pressure variation, considering an electrochemical perspective.

These impacts on the capacity implies an issue when it comes to the breathing analysis. More precisely, the significant variation of capacity certainly generates a variation of particles breathing. Thus, at the scale the measurement takes place, it is impossible to rigorously quantify the anode breathing variation that comes from particles themselves, as opposed to the variation that comes from their rearrangement. The temperature may have an impact on the particles contact, more precisely on the binder, but the current results are too limited. At least, as the bottom graph in Fig. 4.14 shows, it is suggested that the breathing irreversibility seems poorly impacted by temperature, despite the important reduction of capacity.

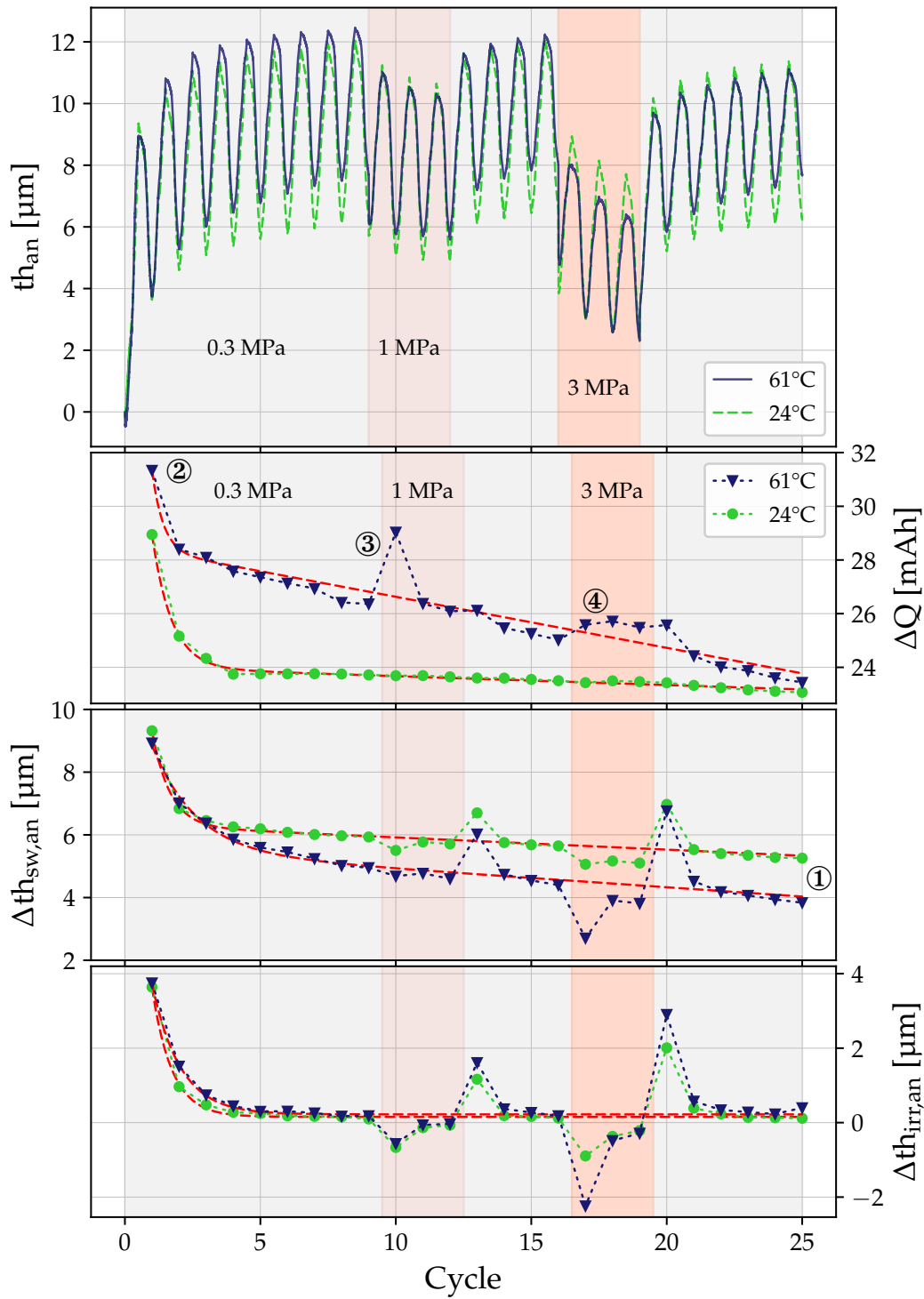


Figure 4.14: Reference protocol at 24°C (A01_1) and 61°C (A03_1), both at 0.3 MPa during formation. Thickness data based on extracted anode thickness (obtained after process described in Fig. 4.3) — **Top graph**) Raw thickness change. **Middle top graph**) Charged capacity per cycle. **Middle bottom graph**) Swelling amplitude thickness Delta. **Bottom graph**) Irreversibility thickness Delta. Dashed lines are the fitting exponential functions of form $y(c) = A + Bc + C \exp\left(-\frac{c}{p}\right)$ (values in Table 4.5).

An important point to note about these results is the way anode thickness has been extracted for the high temperature case. The extraction process (see Fig. 4.3) was made on samples that were measured at 24°C (results of Fig. 4.5a), giving the final rheological parameters in Table 4.3. These rheological parameters were used to extract anode thickness for all cases, even for 61°C case. Nevertheless, these rheological parameters may be different for 61°C. Consequently, an eventual bias due to the incomplete experimental set may have altered the displayed results.

4.4.2.b Singular behaviour of potential for experiment at 61°C

However, these results should be analysed with precaution. Indeed, beyond the bad reproducibility presented above, an electrochemical singularity has been detected in the potential of sample submitted to high temperature (A03). More precisely, in normal functioning, the potential varies between both top and bottom limits of 2.5 and 4.2 V, without any variation at the transition between charge/discharge states. However, during experiment A03_1, the brief pause between charge/discharge states (lasting around ten seconds) was enough for the potential to instantaneously drop by around 0.3 V. It was initially thought that the sample presented a manufacturing defect leading to a current leak. To ensure this, a secondary simple cycling at 24°C has been carried out on sample A03 (experiment A03_2). No potential drop was detected any more. To observe it, Fig. 4.15 draws the potential curve of sample A03, for experimental indexes 1 (61°C, solid line) and 2 (24°C, dashed line). As we can see, at 24°C, the potential perfectly varies between 2.5 and 4.2 V limits (horizontal solid lines). Nevertheless, at 61°C, the potential is globally diminished, more particularly at the transition between charge/discharge states with the sudden drops, whose amplitude are not constant and randomly change over cycles. In addition, during transition from charge to discharge, this drop systematically leads to a smoothed peak (4.15.①). At the opposite, during the transition from discharge to charge, this drop only increases starting from the dropped

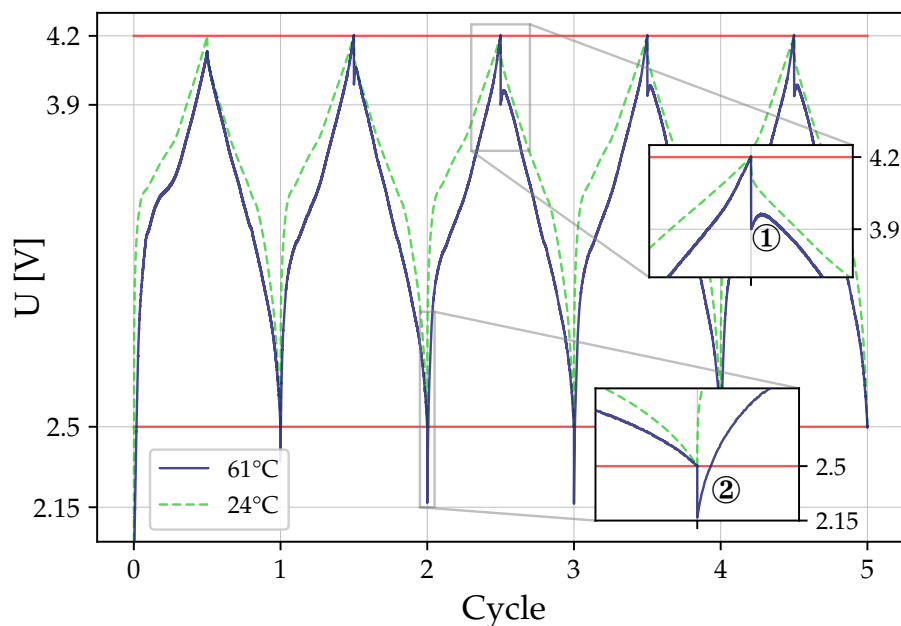


Figure 4.15: Potential singular behaviour at high temperature: potentials of experiments A03_1 (61°C) and A03_2 (24°C), fifth first cycles including formation. Top and bottom horizontal lines correspond to maximum and minimum input cycling potentials (4.2 and 2.5 V).

value (4.15.②). A hypothesis for these behaviours is the electrochemistry doped by temperature that enhances the reactivity between particles. When the current is cut between charge/discharge change, the particles of Si/C and Gr themselves maybe still continue to exchange lithium, leading to a new global potential equilibrium of the cell. Anyhow, the secondary experiment A03_2 demonstrates that the singularity does not come from a global manufacturing defect that made the sample absolutely defective, because it proved to work well after the cycles at 61°C.

4.4.3 Influence of pressure during formation

In order to evaluate the behaviour during the first formation cycles, two additional samples (A05 and A06) were tested under different applied pressure at 24°C. Of course, the pressure is already analysed through the reference protocol itself, but now a particular attention is paid to the pressure during formation. Analysing the behaviour during the formation cycles is interesting since the main irreversibility comes from that period. Hence, it consists in changing the pressure during the first cycles (three formation cycles and six following ones). The objective is to detect if this initial pressure has a permanent impact on the anode breathing. To do so, samples A05 and A06 was submitted to reference protocol with different initial pressures (respectively 1 and 3 MPa, instead of 0.3 MPa for the reference cycling). Unfortunately, a bug occurred for both experiments during the cycling (stop of electrochemical test bench), even though the cycling could be relaunched after this. Consequently, the comparison with experiment at 0.3 MPa (A01_1) is only possible for the first five cycles.

When looking at the Fig. 4.16 that displays experiments A01_1, A05_1 and A06_1 during the five first cycles, we can observe an impact similar to the pressure variation detailed previously: the pressure reduced the raw thickness variation, as observed in the th graph. However, it can be noticed that the shapes of curves are particularly identical and the main difference lies in their amplitudes. The fact remains that the capacities are almost equal and evolve exactly the same, as the ΔQ graph (second from the top) demonstrates. Despite this, the swelling amplitude Δth_{sw} is reversely impacted by pressure, from an initial value at 9.3 μm for 0.3 MPa (4.16.①) to 6.4 μm for 3 MPa (4.16.②). Looking at these first cycles, the swelling amplitudes converge but not perfectly, with distinct asymptotic values depending on pressure, with 6.1 μm for 0.3 MPa (4.16.③) to 4.9 μm for 3 MPa (4.16.④). The irreversibility Δth_{irr} in the bottom graph varies exactly the same, with a reversed impact of pressure that goes from 3.6 μm at 0.3 MPa (4.16.①bis) to 0.8 at 3 MPa (4.16.②bis). In any case, whatever the pressure applied, the irreversibility knows a fast decrease during two first cycle, then the decrease becomes particularly slow. The asymptotic values are not exactly equal to zero, and they seem to decrease when pressure increases.

At the end of Section 4.4.1, we were talking about the necessity of supplementary cycles to eventually reach a stable breathing (constant swelling amplitude and null irreversibility). In this optic, experiments A05_1 and A06_1 have been the occasion to do so by enlarging the total number of cycles to 38. The focus on these two experiments is displayed in Fig. 4.17. In the th graph, key information is the clear distinction between both curves. In fact, both shapes seem quite identical but with an initial irreversibility that maintained their average values distant. Looking at the irreversibility (Δth_{irr} graph), we can see that the irreversibilities at first cycle are equal to 2.2 μm at 1 MPa (4.17.①) and 0.8 μm at 3 MPa (4.17.②), which gives a difference of 1.4 μm . Moreover, this difference is approximately equal to the permanent difference between both curves that we see during the

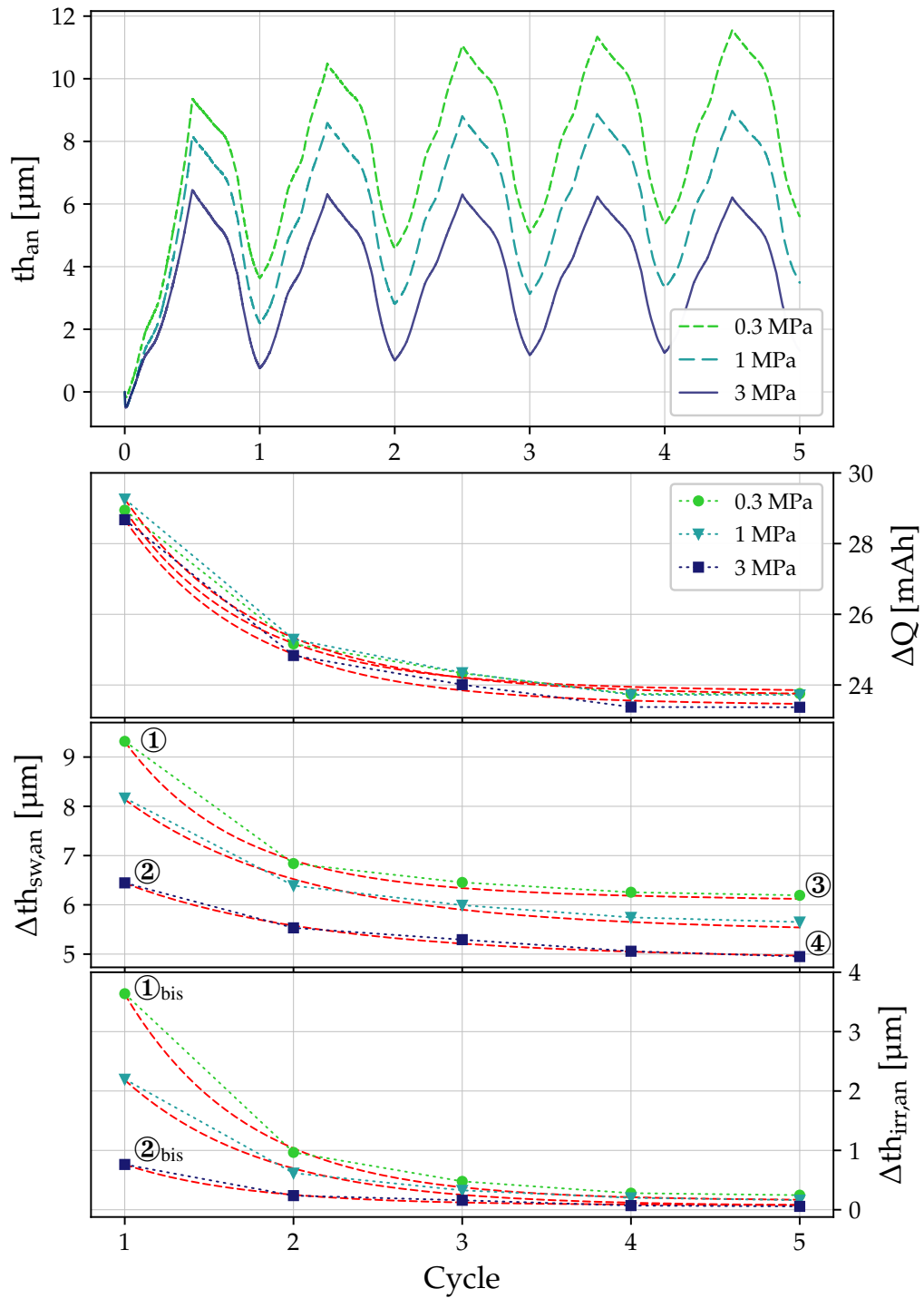


Figure 4.16: Reference protocol at 0.3 MPa (A01_1), 1 MPa (A05_1) and 3 MPa (A06_1), all at 24°C. Thickness data based on extracted anode thickness (obtained after process described in Fig. 4.3) — **Top graph**) Raw thickness change. **Middle top graph**) Charged capacity per cycle. **Middle bottom graph**) Swelling amplitude thickness Delta. **Bottom graph**) Irreversibility thickness Delta. Dashed lines are the fitting exponential functions of form $y(c) = A + Bc + C \exp\left(-\frac{c}{p}\right)$ (values in Table 4.5).

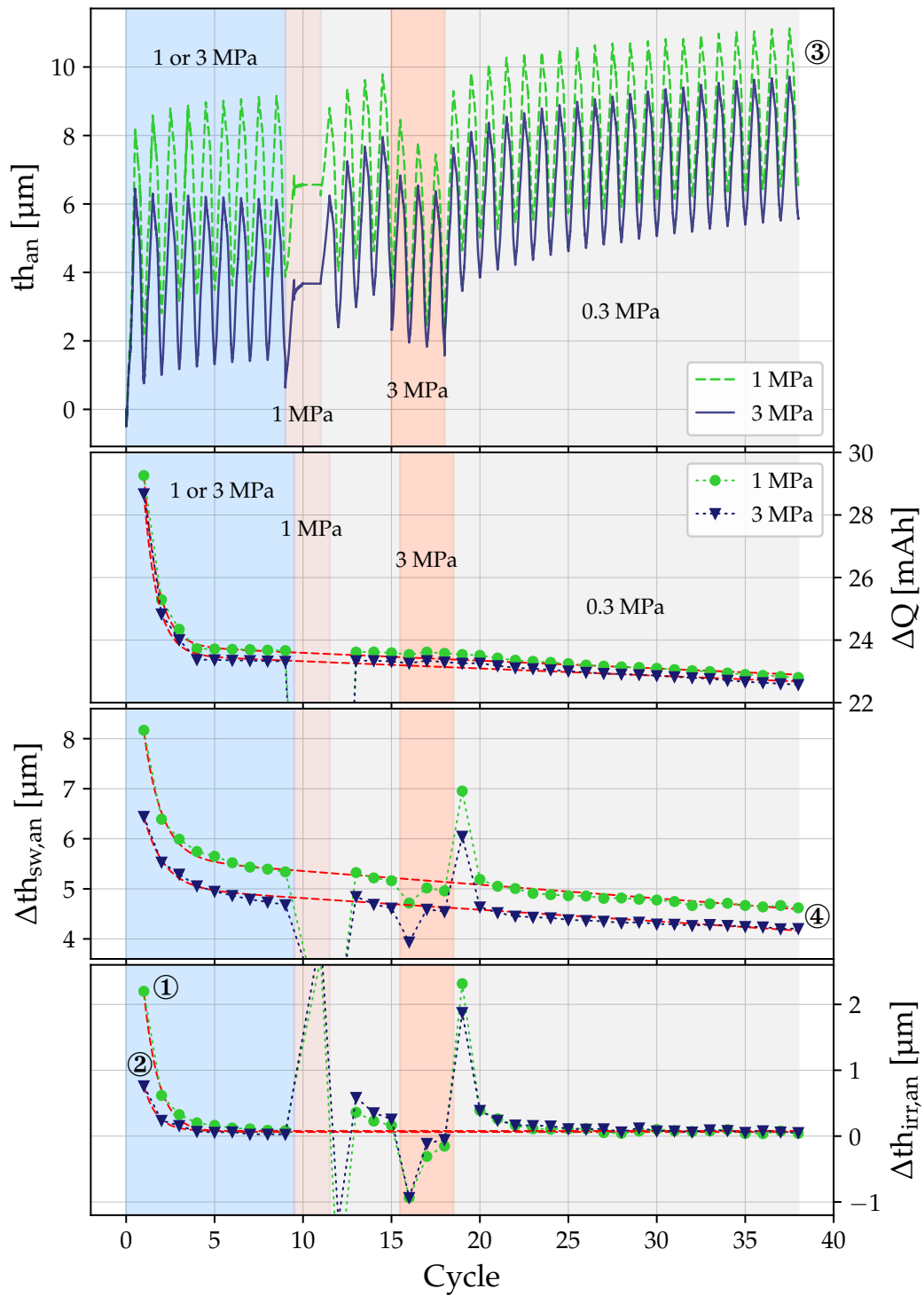


Figure 4.17: Reference protocol at 1 MPa (A05_1) and 3 MPa (A06_1), all at 24°C. Thickness data based on extracted anode thickness (obtained after process described in Fig. 4.3) — **Top graph**) Raw thickness change. **Middle top graph**) Charged capacity per cycle. **Middle bottom graph**) Swelling amplitude thickness Delta. **Bottom graph**) Irreversibility thickness Delta. Dashed lines are the fitting exponential functions of form $y(c) = A + Bc + C \exp\left(-\frac{c}{p}\right)$ (values in Table 4.5).

20-cycles phases at 0.3 MPa (4.17.③). This difference lets think that this first irreversibility has been stamped to the material (plastic deformation) and even a change of pressure cannot compensate it. In shorter terms, the high pressure applied during formation irreversibly seems to change the stable breathing at low pressure during all the following cycles. This constant gap between both curves is also printed to swelling amplitude (Δth_{sw} graph). In both case, it decreases at a constant rate of 0.02 μm per cycle, maintaining a constant difference of around 0.4 μm (4.17.④). Another point to observe is the final state: both curves are still in a “pseudo-stable” breathing, with a constant decrease of swelling amplitude and a non-null irreversibility, even after almost 40 cycles. Consequently, it demonstrates how much difficult is it to reach a stable breathing state (constant swelling amplitude and null irreversibility). However, by looking at the th graph, it is possible to observe a form of stable breathing state for the 3 MPa case, during the cycling formation, where thickness variation oscillates with a decreasing amplitude but around a constant value. Consequently, these results suggest how much the pressure applied on the cell is a key parameter for the state of breathing stability. More importantly, it reveals that the initial pressure applied during formation cycles can play a significant role in the future breathing of a cell.

4.5 Global analysis

4.5.1 Results summary

The results developed above mainly focused on two experimental condition parameters: the pressure and the temperature.

The protocol focused on a cycling at C/5, submitted to the reference pressure of 0.3 MPa with temporary compressions at higher pressures (1 MPa and 3 MPa). It was initially thought that the temporary compressions at high pressure modified the stable breathing, but the number of cycles measured here is too low to really reach an eventual stable breathing. Thus, a temporary compression at high pressure obviously changes the thickness through a clear reduction, but the long term impact on breathing history is much less certain. Even concerning the swelling amplitudes and irreversibility, even if pressure variation to higher level has a temporary impact on them, the permanent impact when pressure comes back to initial pressure is too low to be noticeable. Concerning the capacity, it revealed to be independent of the pressure, considering the levels applied (from 0.3 to 3 MPa). However, the pressure applied during the first cycles seems to play an important role in long term, by creating a permanent breathing behaviour. It suggests the idea that, in order to limit the global amount of breathing, forming the cell under a high pressure will limit the highest thickness change and even the swelling amplitude (but not the irreversibility that remains low but still present).

Concerning the temperature, a heated cell charged a larger range of capacity, but it simultaneously showed a drastic decrease of this quantity over cycles. The swelling amplitude was also decreasing, then it makes the interpretation difficult on the origin of this lowered breathing. Does the temperature create a capacity loss that engenders a limitation of particles breathing, or does it directly impact the particles' rearrangement that leads to a lower swelling amplitude? Unfortunately, the current measurement is not sufficient to quantify both phenomena. In addition, higher temperature seems to generate electrochemical defect, making the cell more

inclined to lose its potential when unused by an external device. However, the limited number of samples makes this conclusion unsure, an eventual defect from the samples themselves is also likely.

4.5.2 Manufacturing guidelines for the design of low breathing electrodes

According to the present results, the portrait of the “optimal cell use” follows two main lines, one in terms of temperature and one in terms of pressure. Concerning the temperature, a probability of swelling amplitude reduction exists thanks to high temperature (around 60°C), but the unclear correlation with capacity loss makes the conclusion uncertain. Still, the objective was mainly to impact the internal microstructure through temperature, not to test an eventual use condition. It is known that high temperature generates accelerated loss of capacity, so it remains a solution to avoid. The pressure is much more interesting, even in terms of temporary action during manufacturing. First, during the life of a cell, the variation of pressure does not generate a significant permanent alteration of breathing. Indeed, coming back to the standard pressure seems enough to recover from this pressure change. Secondly, the level of pressure during the formation cycle determines significantly the future breathing of the cell, in terms of global thickness increase, but also in terms of breathing amplitude. Consequently, most attention should be paid on the pressure applied during the formation cycles, with a preference for high pressure. However, the optimal pressure to apply still remains to be evaluated, even if 3 MPa presented an interesting impact. In summary, the present results dictate the “optimal cell use” as a cell formed under a pressure of 3 MPa (five first cycles) and used under a room temperature.

As a critic reflection, it is obvious that the proposed protocol is not optimal. For example, in Section 4.3.2.a, in the extraction of intermediary components (cathode, separator and pouch bag), it would have been interesting to reduce as best as possible this error propagation by removing, for example, the separators from samples pair B01/B02. In the same section, the Hyp. 4.B.iii (page 147) (non-influence of electrolyte on pouch bag rheological behaviour) is maybe not absolutely certain. A measurement with electrolyte would have been also useful. In addition, in the rheological analysis in Section 4.3.2.c, Hyp. 4.B.ii (page 147) (cathode rheological properties independent of lithium concentration) is known to be not exactly right. A deeper consideration of this aspect would be a plus in the development of the Novelisa model. Finally, the error addressed by Hyp. 4.B.iv (page 147) (systematic error created by the DForm test bench) was maybe not enough considered during the establishment of experimental protocols.

In order to limit the breathing, it is then recommended, during the formation cycles, to submit the cell to the highest possible pressure (tested until 3 MPa).

Chapter 5

Model/Experiment comparison

5.1 Comparison methodology

In summarise, Chapters 3 and 4 respectively presented the results of DAM and experimental approaches separately. The objective here is to cross the results in order to detect possible convergences and divergences, to evaluate the performances of the DAM. To do so, a simulation series has been made with a specific design in order to match as best as possible the experimental parameters, by taking the experimental sample A01 as reference. The DAM sample used in Chapter 3 consequently knew several modifications:

- *Breathing law*: for a matching with experimental results, the choice of electrochemical breathing law instead of linear law is evident.
- *Sample thickness*: the experimental anode (collector excluded) had an initial thickness of 48 μm after relaxation (just before cycling). The DAM was set such that the relaxation led approximately to this thickness ($47.9 \pm 0.3 \mu\text{m}$).
- *Irreversibility matching*: taking into account the conclusions of Section 3.4, it was decided to focus on the adhesion between particles to match experimental breathing irreversibility. Work of adhesion was set such that modelled irreversibility at first cycle was equal to the one found experimentally.
- *Inactive material*: in experimental anode (collector excluded), the active material (Si/C/Gr) composes 95wt% of the total anode material, the remaining proportion being composed by conductor material and binder. In order to simulate the presence of binder within DAM, inactive little particles (not subjected to breathing) were added within the particles' template. These binder particles were set with a higher work of adhesion compared to Si/C/Gr particles, with the following values: 20 J/m^2 for binder-Si/C/Gr contacts and 5 J/m^2 for Si/C/Gr-Si/C/Gr contacts. All other granular parameters were the values of DAM reference sample (see Table 2.1).

In order to complete this comparison, the results of the 1D continuous anode model developed by Vidal (2021) [40], set with the same parameters, are plot on Fig. 5.1. As a summary, Table 5.1 goes over all the parameters settings shared by the three approaches.

Parameter	Value
Proportion of active material (Si/C/Gr) in total anode mass	95wt%
Thickness before cycling	48 μm
Minimum anode voltage	0.01 V
Maximum anode voltage	1 V

Table 5.1: *Model/Experimental comparison settings.*

5.2 Discussions

5.2.1 Results analysis

In both DAM results Chapter 3 and experimental results Chapter 4, the first cycle presents a major significance in the breathing, as in terms of swelling amplitude as in irreversibility. Fig. 5.1 displays four breathing of the first cycle: two using DAM (with and without adhesion), one experimental (experiment A01_1) and one using the continuous anode model (CAM) from Vidal (2021) [40]. The first clear observation about the curves is the difference between their shapes. The experimental thickness change presents a rounded and smoothed curves, as opposite to DAM and continuous model that follow straight and angled paths.

Concerning DAM and CAM models, their shapes are quite similar, with the characteristic plateaus of graphite in the middle of state of charge and the hysteresis generated by silicon breathing. At least, it draws an interesting consistency of the laws implemented within models. The difference between DAM and CAM approaches mainly appear in two details: swelling amplitude and presence of irreversibility. Firstly, the continuous model presents a lower swelling amplitude, with a thickness change at the end of charge $7.5 \mu\text{m}$ ($\sim 15.6\%$, 5.1.①), compared to the DAM without adhesion (“Adh. OFF”) at $9.5 \pm 0.4 \mu\text{m}$ ($\sim 19.6\%$, 5.1.②). The difference is even more important when the adhesion is activated (“Adh. ON”) in the DAM, the resulting curve reaching $12.3 \pm 0.4 \mu\text{m}$ ($\sim 25.6\%$, 5.1.③) at the end of charge. This is coherent with the facts that DAM is able to generate an additional void volume variation due to its discrete nature. This additional void volume affects the second difference between DAM and continuous model, the presence or not of the irreversibility. Whereas the continuous model does not present any irreversibility at the end of discharge, the DAM ends with a $0.6 \pm 0.3 \mu\text{m}$ ($\sim 1.3\%$, 5.1.④) without adhesion and $3.4 \pm 0.2 \mu\text{m}$ ($\sim 7.1\%$, 5.1.⑤) with adhesion. Generally speaking, DAM consequently overestimates the breathing compared to continuous model. In both cases, however, the straight and angled paths of their curves demonstrate how both approaches are sensitive to electrochemical laws, even the DAM that was expected to generate a much smoother breathing due to particles rearrangement. An eventual source of inaccuracy may be the electrochemical breathing laws (developed in Section 2.3.3). The latter are may be too simple to be generalised to all particles, independently of their size or position within the electrode layer.

In fact, both model approaches are complementary when compared to experimental results. The experimental curve presents a swelling amplitude of around $7.8 \mu\text{m}$ ($\sim 16.3\%$, 5.1.①), almost equal to continuous model,

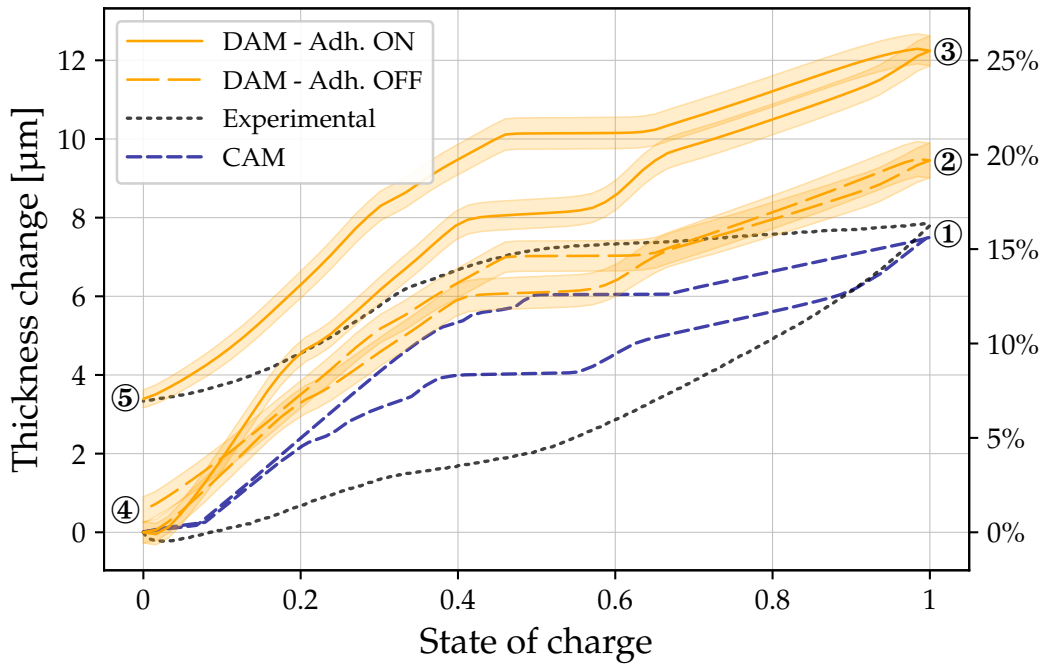


Figure 5.1: Comparison of thickness change between DAM (Discrete Anode Model), experimental and CAM (Continuous Anode Model), first cycle. For DAM results, both cases with and without adhesion (respectively “Adh. ON” and “Adh. OFF”) are displayed. In adhesive case (“Adh. ON”), work of adhesion at 20 J/m^2 for Si/C/Gr-binder contacts and 5 J/m^2 for Si/C/Gr-Si/C/Gr contacts. For experimental results, data is extracted from A01_1 experiment (first formation cycle at 24°C , 0.3 MPa , extracted anode thickness). For continuous anode model, data is computed through the 1D model by Vidal (2021) [40]. Percentage reference thickness: $th_{ref} = 48 \text{ }\mu\text{m}$.

and an irreversibility of around $3.3 \text{ }\mu\text{m}$ ($\sim 6.9\%$, 5.1.⑤), almost equal to DAM with adhesion. This reveals a drawback of the current DAM: to generate a sufficient irreversibility to match the experimental irreversibility at first charge (in this case, through the value of adhesion, “Adh. ON”), it necessitates to overestimate the swelling amplitude. On the opposite, to obtain a more accurate swelling amplitude (by removing adhesion between particles, “Adh. OFF”), the irreversibility almost drops to zero.

Another mismatch of the DAM appears during the following cycles. To observe it, Fig. 5.2 show both thickness change of DAM and experimental measurement during the four first cycles. In addition to the differences that have been already described (different shapes and swelling amplitude), both breathing evolve differently over cycles. In DAM, the first cycle seems to constitute a maximum and the following cycles breath at lower amount with a progressive decrease of the maximum breathing thickness change (decreasing arrow). Furthermore, as already revealed in Chapter 3, the irreversibility is globally non-existent from the second cycle. On the opposite, experimental curve present a gradual increase of maximum breathing point over cycle (increasing arrow), correlated with an irreversibility accumulated cycle after cycle. The interesting detail is the fact that hysteresis of DAM progressively tends to the one drawn by experimental results (cycles 4). Still, the results are not complete enough to precisely conclude about an eventual stabilisation to a common state.

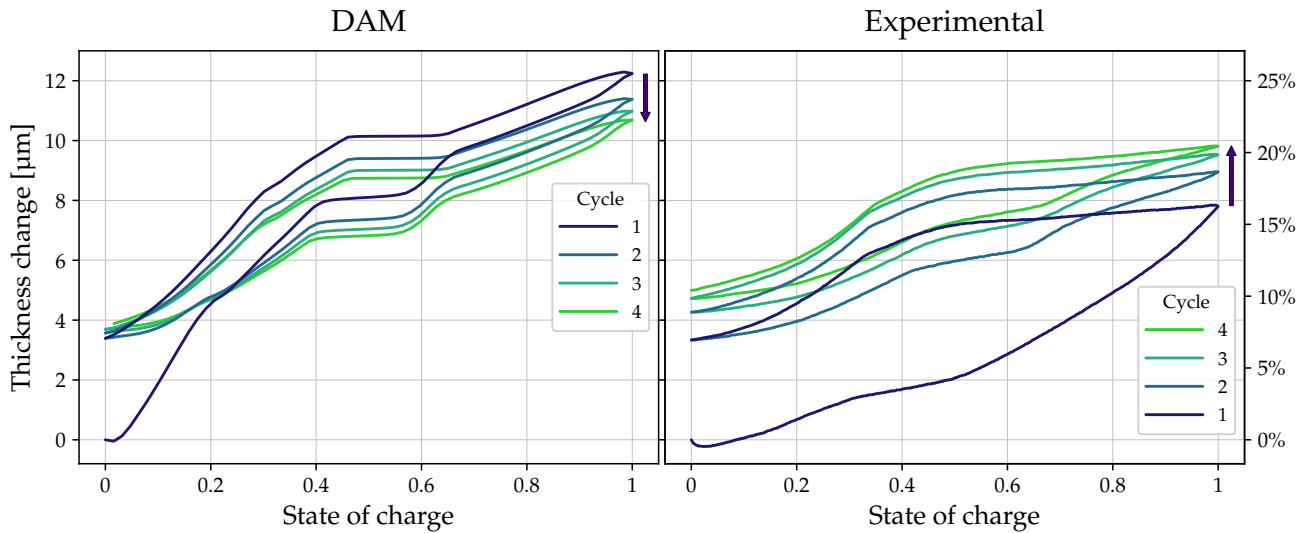


Figure 5.2: Comparison of thickness change between DAM and experimental, four first cycles. For DAM results, adhesion is activated (Si/C/Gr-Si/C/Gr : 5 J/m^2 , Si/C/Gr-binder : 20 J/m^2). For experimental results, data is extracted from A01_1 experiment (first formation cycle at 24°C , 0.3 MPa , extracted anode thickness). Percentage reference thickness: $th_{ref} = 48 \mu\text{m}$.

5.2.2 Hypothesis questionings

At the current stage of development, it is a fact that the DAM is perfectly capable of explaining part of the breathing irreversibility, particularly pronounced at first cycle. However, this first irreversibility is clearly correlated with the swelling amplitude, and it seems difficult to offer both matching irreversibility and swelling amplitude at the same time. Of course, it must be reminded that the current DAM approach was built on strong hypothesis in order to get a tool used to understand more than match. Through the Set of Hypothesis 2.A (page 74), it is obvious that this model does not take into account some phenomena that may play a significant role in electrode breathing, such as active material cracks or lithium diffusion. Indeed, Hyp. 2.A.i (page 74) (spherical particles) clearly limits the deformability of particles or their eventual fracture during breathing. In addition, Hyp. 2.A.iv (page 74) (modelling active materials only) neglects maybe too much the action of binder and conductive materials (even though, it has been roughly introduced in cross comparison, in Section 5.1). Finally, Hyp. 2.A.v (page 74) (constant and reversible breathing of particles) was stated in order to avoid any irreversibility generation due to particles and to capture only the particles bed irreversibility. But is that really true? Of course, this is certainly not the case. As a basic example, even if they were simplified to obtain a reversible breathing, the data provided by Beaulieu *et al.* (2003) [42] and plotted in Fig. 2.7 (silicon graph) reveal a first irreversibility of around 50% at first cycle, which is not negligible at all. Hence, a real question arises about the precise knowledge on how the particles breathe in reality, and in what extent they participate in the progressive accumulation of breathing irreversibility. Furthermore, concerning the difference of shapes between models and experiment, an explanation may come from Hyp. 2.B.iii (page 84) (all particles lithiate and delithiate synchronously, without any delay due to position). In consequence of this hypothesis, all the volume of a given material breathe at the exact same time with the exact same law. Thus, it is not surprising that the global thickness of the DAM follows precisely the electrochemical law, which create the straight and angled curves comparable to CAM results. In fact, all these hypotheses have been already complexified by the team of

So *et al.* (2021-2022) [72], [73], [90]–[92]. Indeed, they already introduced clusters of sub-particles to model active material particles, considered active material and supplementary additives (even if it is a solid electrolyte, the methodology remains equivalent) and implemented an effect of lithium diffusion that creates breathing variation delay and irreversibility. Their simulations demonstrate the importance of considering the complexity of breathing at particles scale, more precisely heterogenous and desynchronised breathing of particles.

In this scope, the next section aims to present some opening perspectives on the DAM, more generally about the discrete modelling of electrode breathing.

5.3 DAM perspectives

Among all the questioned hypothesis, three main threads are susceptible to improve modelling accuracy:

- Breathing heterogeneity
- More complex microstructure geometry
- Progressive contact wear

Breathing heterogeneity and more complex microstructure geometry were roughly approached in order to evaluate their eventual accuracy.

5.3.1 Breathing heterogeneity

This section is an improvement proposal in response to electrochemical hypothesis that have been stated in Set of Hypothesis 2.B (page 84), more precisely Hyps. 2.B.i (page 84) to 2.B.iii (page 84) (homogeneous active material, potential equilibrium within electrode and homogeneous lithiation within electrode layer). By “breathing heterogeneity”, we refer to desynchronisation of particles breathing due to many phenomena, such as lithium diffusion across electrode thickness (especially at high C-rate), self-containment breathing of particles in their own porosity, internal defects depending on particles, etc. So *et al.* (2022b) [73] revealed the presence of incomplete lithiation or delithiation within the active material particles themselves, due to limitation of lithium diffusion (see Fig. 1.14c), so the consideration of this phenomenon is an interesting axis to explore.

As a quick way to consider breathing heterogeneity, a simple modification of electrochemical breathing laws was applied to the DAM simulation displayed in Fig. 5.1 (“Adh. ON” case). It consisted in randomly lowering the breathing law for each particle. Considering a material λ (CSi or Gr), the new breathing law is expressed as:

$$d_{\lambda,\text{reduced}}(t) = \langle d_{\lambda}(t) - d_{\text{red}} \rangle + 1 \quad \in [1, d_{\lambda,\text{max}}] \quad (5.1)$$

Where d_{red} is a reduction factor defined as:

$$d_{\text{red}} = \text{rand}(1, d_{\lambda,\text{red,max}}) \quad (5.2)$$

Where rand is the uniform random function and $d_{\text{CSi,red,max}} = 1.2$ and $d_{\text{Gr,red,max}} = 1.015$. As an illustration, Fig. 5.3 displays the original breathing laws (dashed lines) and two examples of reduced breathing laws (dashed lines). The bottom solid lines represent the minimum breathing laws implemented in the simulation.

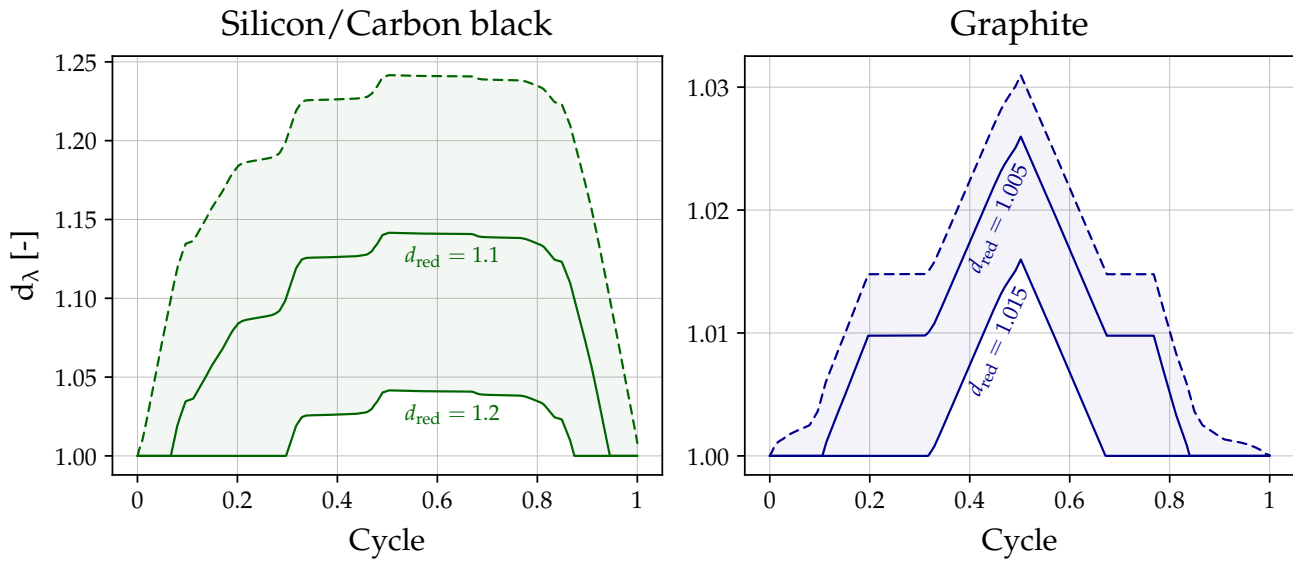


Figure 5.3: Random reduction of breathing laws to simulate heterogeneous breathing of particles — Dashed line: original breathing law. Solid lines: examples of reduced laws with two different reduction factors. Bottom solid lines represent the minimum breathing law implemented.

Of course, this reduction is a rough approximation because it does not create real electrochemical delay of lithiation. At least, this is an easy way to add some random limited and asynchronous breathing at beginning and end of cycle.

The resulting curve is displayed in Fig. 5.4a. On the left graph, the heterogeneous breathing is deactivated and corresponds to the results of Fig. 5.1. On the right side, the heterogeneous breathing is activated for DAM curve. The first observation is the lower swelling amplitude, reduced at an equivalent value of experimental result ($8.0 \pm 0.3 \mu\text{m}$, 5.4a.①). The second main observation compared to case without lithium diffusion/loss is the presence of smoothed breathing at the beginning and end of cycle (5.4a.②), which is in better agreement with experimental measurement in terms of curve shape. However, the DAM result is only changed at the beginning and the end of cycle (area A in Fig. 5.4a), whereas it is similar to the case without heterogeneous diffusion in the middle (area B in Fig. 5.4a). This is coherent with the implemented randomly reduced law: out of grey area (state of charge between 0.4 and 1), all the particles breathe the same way, but in the grey area (state of charge between 0 and 0.4), some particles randomly chosen do not breathe. Consequently, the electrode breathing is more spread over time. The interesting observation is that even if the swelling amplitude is notably reduced, the irreversibility is quite conserved, even if, as a recall, no irreversibility has been implemented in breathing laws. Indeed, it presents an amount of $2.3 \pm 0.3 \mu\text{m}$ (5.4a.③), which corresponds to 28.8% of the swelling amplitude. Compared to the case without adhesion (“Adh. OFF”, left graph in Fig. 5.4a), this is a clear improvement: the swelling amplitude better matches and the irreversibility is more pronounced. We then have kept the irreversibility generated by adhesive granular behaviour and reduced the swelling amplitude to a more realistic value. However, concerning the next cycles, the DAM still meets a regular inconsistency: the gradual decrease of maximum thickness. As displayed in Fig. 5.4b, The maximum point of each cycle decrease over cycles (dark arrow), whereas the reversed is observed experimentally. It still suggests a progressive reorganisation of particles that optimises their positions in initial void volume.

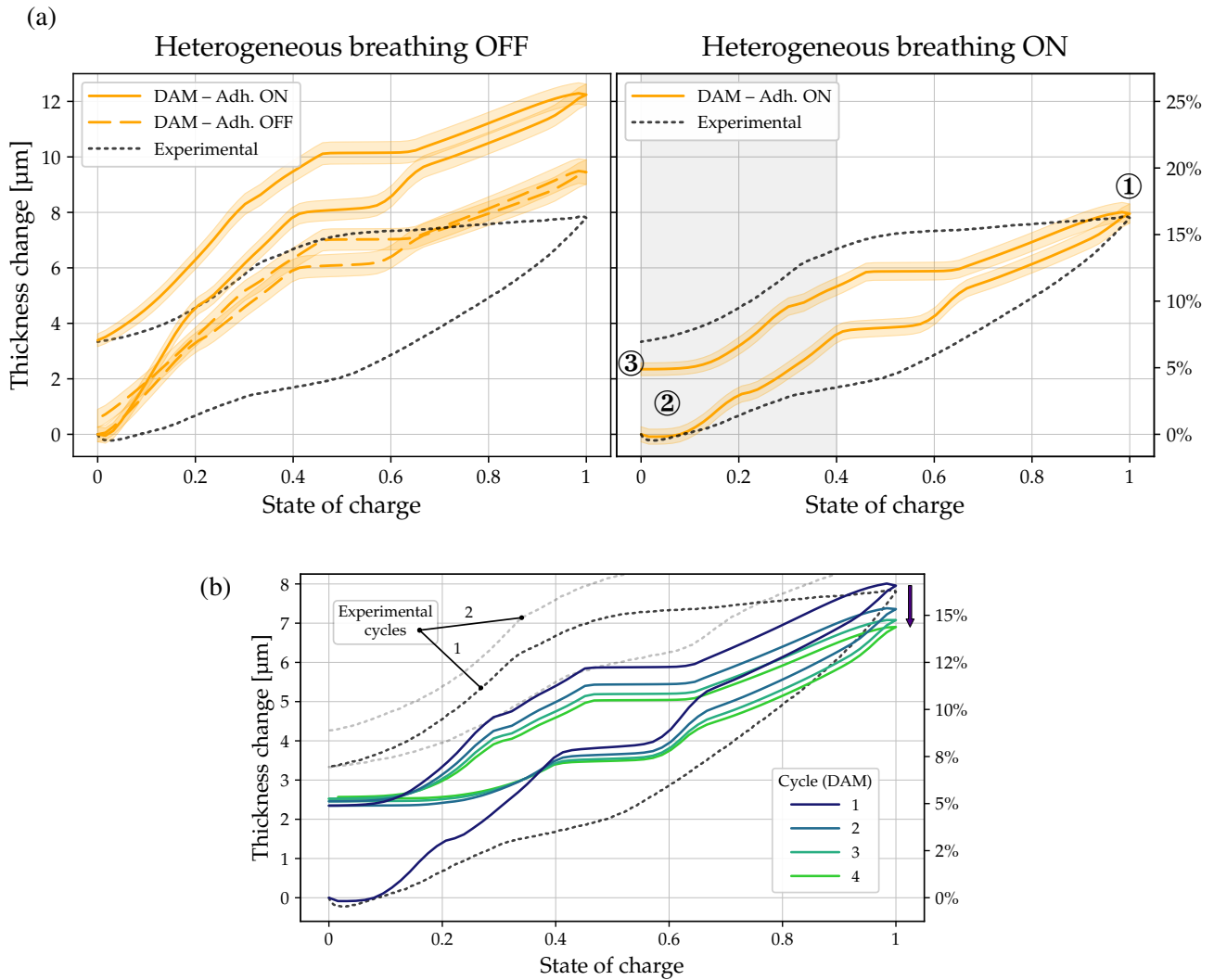


Figure 5.4: Comparison of thickness change between DAM (with and without heterogeneous breathing) and experimental results. When adhesion is activated for DAM (“Adh. ON”), work of adhesion at 20 J/m^2 for Si/C/Gr-binder contacts and 5 J/m^2 for Si/C/Gr-Si/C/Gr contacts — **a)** Comparison without (left) and with (right) lithium diffusion/loss, first cycle. Left graph results correspond to Fig. 5.1. **b)** Comparison of lithium diffusion/loss activation (four cycles) with experimental (first cycle). Gray area corresponds to the state of charge range where heterogeneous breathing occurs most. Percentage reference thickness: $th_{ref} = 48 \mu\text{m}$.

Finally, this simple simulation trick demonstrates the potential of considering heterogeneous breathing of particles. In the preceding sections of this manuscript, this aspect has been addressed only through the differentiation of both Si/C and Gr materials (because each one has its own breathing law), but not through the differentiation of particles themselves. Yet, the consideration of breathing heterogeneity within the electrode layer and within the particles will be of major interest in future researches on electrode breathing. It will certainly be another important key in simulating the granular breathing behaviour, in a complementary way with particles contact properties.

5.3.2 Complex particles shapes

This section is an improvement proposal to the major DEM hypothesis that have been stated in Set of Hypothesis 2.A (page 74), more precisely Hyp. 2.A.i (page 74) (spherical particles). Several methods exist to obtain complex shaped-particles, such a polygonal particle or cluster of sub-particles. However, So *et al.* (2022b) [73] demonstrated the relevancy of using clusters of sub-particles, in order to compute lithium diffusion internal to active material particles.

A first approach to generate a complex shapes anode was carried out. The procedure is described in Fig. 5.5. Starting from an anode cross-section (5.5.1), particles are manually shaped to generate different shapes (five for each material, 5.5.2). The manual shaping follows a two-step process. Firstly, starting from the 2D picture and a 3D sphere, the sphere is manually deformed to fit the projection of the particle. Secondly, the deformed sphere is extrapolated in the third dimension to obtain a credible shape of particle. The generated 3D mesh shapes (5.5.3) are then filled with particles (using a clump command available in the “LIGGGHTS-PFM” version [216]) to generate different templates of clusters (5.5.4). The cluster templates are then directly used in LIGGGHTS as generic particles to give the final microstructure (5.5.5). On the last image, the colours distinguish the different clusters of sub-particles.

By submitting this structure to a similar cycling, as displayed in Fig. 5.6a, the curve is clearly reduced, showing a swelling amplitude of $5.7 \mu\text{m}$ (5.6a.①), as for the irreversibility, lowered to only $1.0 \mu\text{m}$ (5.6a.②). Moreover, the successive cycles displayed in Fig. 5.6b still reveal a progressive reduction of thickness over cycles (dark arrow), as opposite to experimental results. In fact, the reason for the reduction of breathing amplitude comes from the cluster technique used for the simulation. The “multisphere” method used in LIGGGHTS considers each cluster of particles as a rigid solid. It means that the contact between sub-particles belonging to a given cluster is not computed. Instead, the relative coordinates between sub-particles defined by the cluster template (image 4 in Fig. 5.5) are kept constant. By consequence, because of the constant distance between each neighbour particles, any volume change of sub-particles is partially absorbed by the neighbour particles in contact, as schemed in Fig. 5.7. For this reason, part of the implemented breathing is lost and not transmitted to the electrode, resulting in a lower macroscopic breathing.

Despite this breathing reduction, this first trial of clusters instead of spherical particles does not generate a significant change in breathing. As an illustration, Fig. 5.6c displays the first cycle of both approaches, with the cluster approach multiplied to match the highest point of sphere approach. In terms of curves shapes, the major difference between both (coloured area) occurs at the end of the cycle, where the cluster approach even loses its ability to generate significant irreversibility. However, the difference between both curves remain quite limited, suggesting that a more complex implementation of clusters is necessary to improve substantially the ability of the DAM to get closer to the experimental measurements. To do so, two solutions may be interesting. As one solution, still using the “multisphere” method (clusters as rigid bodies), the breathing of a multisphere must be homothetic by adapting the distance between breathing particles. As another solution, mostly used in literature (see Section 1.1.2.b), the clusters of sub-particles must be built based on a breakable bond model .

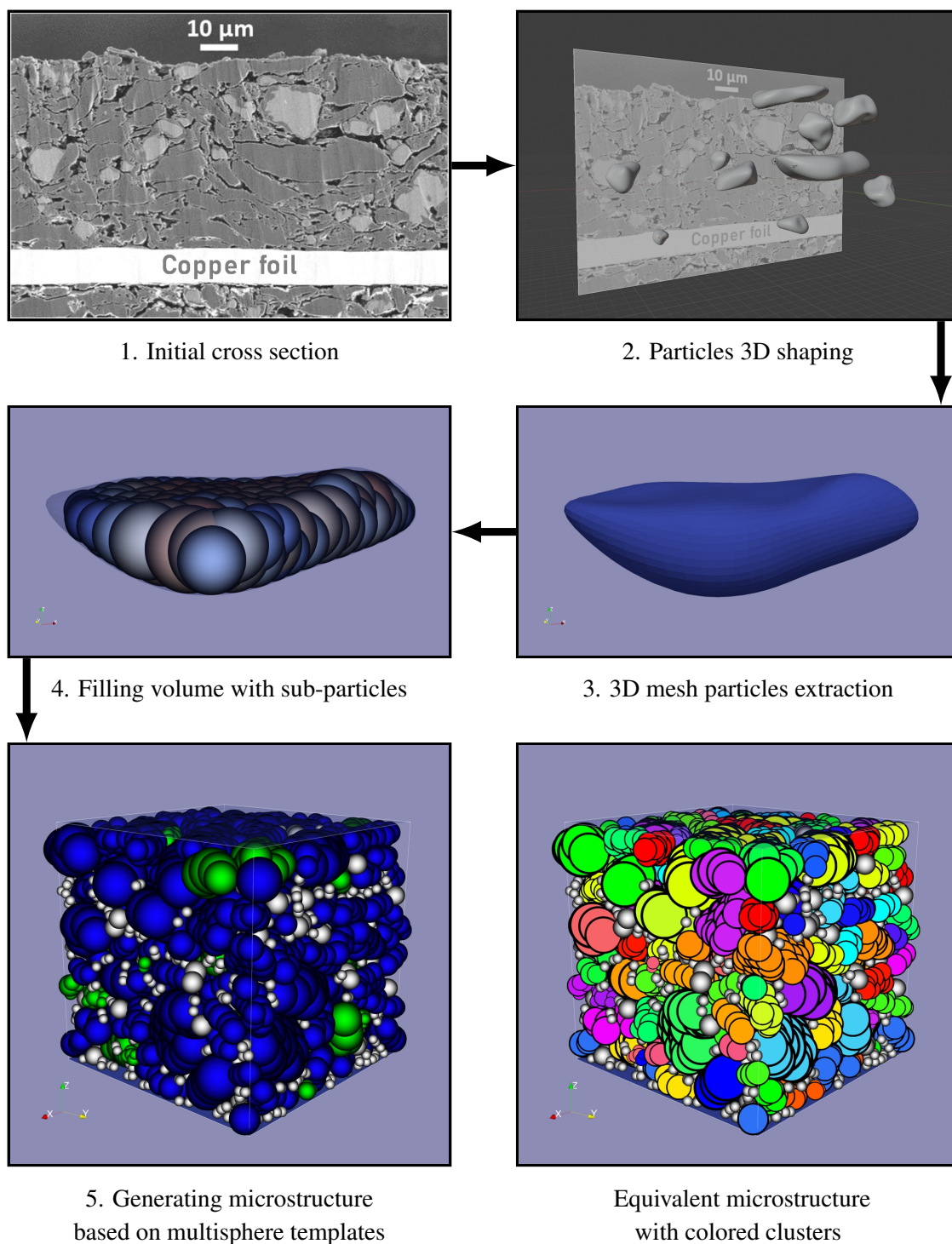


Figure 5.5: Multisphere DAM building steps. Starting from a cross-section image (1), particles are manually modelled in 3D (2) and the resulting 3D mesh particles (3) are filled with sub-particles (4). The final templates (five different per Si/C and Gr) are used to generate the final discrete sample (5), $50 \times 50 \times 50 \mu\text{m}$. The final image is the equivalent microstructure with colours adapted to distinguish individual clusters of sub-particles. White shaded particles correspond to inactive material. Cross-section (first image) extracted from Profatilova et al. (2020) [217], Figure 10^a.

^a © Applied Energy Materials. Reproduced under charge-free nature of reuse. American Chemical Society, all rights reserved.

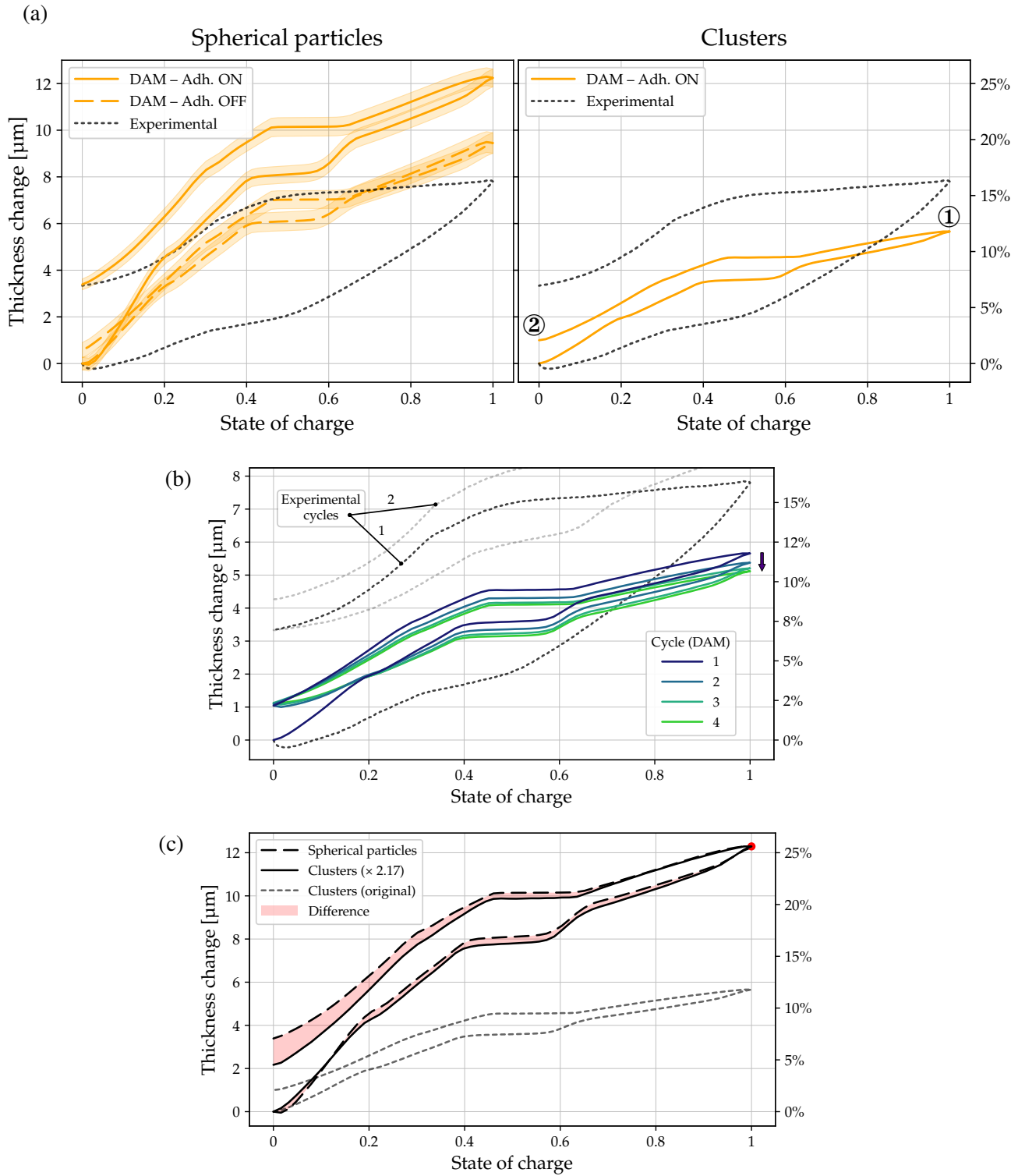


Figure 5.6: Comparison of thickness change between DAM (spherical particles and clusters approaches) and experimental results. When adhesion is activated for DAM (“Adh. ON”), work of adhesion at 20 J/m^2 for Si/C/Gr-binder contacts and 5 J/m^2 for Si/C/Gr-Si/C/Gr contacts. For clusters approach, no statistical process was carried out — **a**) Comparison with spherical particles (left) and clusters (right), first cycle. Left graph results correspond to Fig. 5.1. **b**) Comparison of clusters approach (four cycles) with experimental (first cycle). **c**) Comparison of spherical particles and clusters approaches. Original multi-spheres approach (little dashed line) is multiplied by a factor 2.17 to match maximum point of single-spheres (top coloured dot). Both are from the same simulation and only proportional to within one factor 2.17. The coloured area correspond to the difference between single-spheres and multiplied multi-spheres curves. Percentage reference thickness: $th_{ref} = 48 \mu\text{m}$.

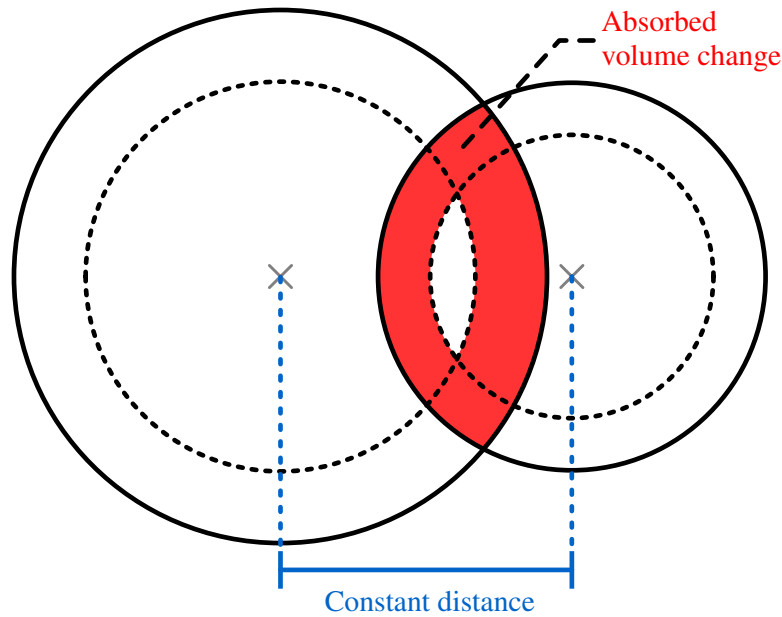


Figure 5.7: Scheme of volume change absorption of two particles belonging to the same cluster.

5.3.3 Discussion about best future axis

The previous sections explored two ways to obtain a better DEM model of electrode breathing: the consideration of heterogeneous breathing and the cluster approach. On one hand, the heterogeneous breathing, implemented with a simple random reduction of breathing law, is able to reduce the swelling amplitude while conserving a reasonable amount of irreversibility. The shape of the resulting curve is also smoother and more consistent with experimental curve. On the other hand, compared to the model heterogeneous breathing, the cluster approach does not prove to be more efficient to model the electrode breathing. Of course, the current technique is limited by the fact that rigid clusters of particles absorb part of the breathing and cannot break. However, the complexity brought by the clusters of particles does not generate a more complex breathing that could explain the DAM divergence with experimental results. Moreover, the cluster approach computational cost is particularly high, so this technique necessitates meticulous optimisation to avoid unnecessary computation consumption. Facing these exploring tests, a future encouraging axis for electrode breathing modelling is the study of particles breathing itself. Still simulated through a granular perspective, it will mainly consist in implementing the space and time non-synchronicity of materials breathing within the electrode. Finally, the third technique to improve DAM accuracy is introduced in the conclusion of Chapter 3 (see Section 3.4.1): the contact wear. As the DAM is not able to generate progressive evolution of breathing along cycles, an eventual solution would be to add of wear condition within contact laws. This option has not been studied during this thesis and remains opened to future explorations.

Conclusions

As final words, this thesis aimed to consider the breathing behaviour of a lithium-ion battery electrode through a granular perspective of the anode media. This work has been motivated by the fact that to gain capacity, silicon is integrated in anode electrode. Silicon has a very high capacity to store lithium, but it exhibits a very high volume increase when lithiated. The main question was about the contribution of the granular microstructure of the electrode to the appearance of two main breathing characteristics: the swelling amplitude (thickness increase during charge) and the irreversibility (difference of thickness between end and beginning of a cycle). The main approach proposed in this manuscript was the use of DEM (Discrete Element Method) to build an electrode model composed of particles that mechanically interact. The global scope was to understand how the breathing of particles (microscopic scale) is transferred to the electrode scale (macroscopic scale), when the battery charges and discharges (respectively lithiate and delithiate for the anode, *i.e.* swell and shrink).

The main objective of the modelling was not to match perfectly the experimental measurements, but to understand in the material and contact properties of particles, what was most susceptible to influence the breathing at electrode scale (Chapter 3). A first analysis stated a case of reference, using simple Hertzian contact between particles, demonstrating that such a contact law was not enough to generate breathing irreversibility (Section 3.2). The second analysis addressed the **silicon fraction** within the particles bed, *i.e.* the proportion of particles with a high breathing amplitude (Section 3.3.1). The swelling amplitude revealed to be particularly linearly correlated to silicon fraction. However, an analysis of volume variation partitions suggested that, at high silicon fraction, the void volume variation was relatively of lower amount compared to low silicon fraction (but it still remained high in absolute perspective). Afterwards, the **friction** between particles and their **ability to rotate** were explored, more particularly their extreme cases, from free rotation with no friction to no rotation with high friction (Section 3.3.2). The results demonstrated no significant influence of these parameters, except for the extreme case without rotation and high friction. In that case, the shrinking of particles led to the generation of distributed “pillars” that held all the force applied on particles bed. As a consequence, most of the contacts between particles disappeared, leading to a singular contactless particles bed. In addition, the pressure and the particles’ rigidity were studied Section 3.3.3. Both quantities revealed to be highly related, as complementary quantities of a more global one: the **particles bed stiffness level**. In other words, increase pressure on the electrode is equivalent to decrease particles rigidity, and vice versa. The only influence of particles bed rigidity on breathing was captured for pressure and particles rigidity out of practical values (more than 10 MPa for pressure and less than 5 GPa for particles rigidity). Hence, according to the model, the particles bed rigidity reveals to be of limited interest to influence the electrode

breathing. As an important detail, these conclusions about particles bed stiffness level have been stated for a particles bed without cohesion. The next analysed contact parameter was the **adhesion** between particles, considered as reversible stickiness between particles (stickiness can be reformed even after a loss of contact). This contact attraction conferred clear ability to the granular media to produce irreversibility during the first cycle of breathing, by increasing the swelling amplitude. The irreversibility was also increased until 40% of the swelling amplitude. This significant result at first cycle is a first proof of the granular media ability to generate irreversibility at electrode scale. Finally, the stickiness between particles was also analysed through **breakable bonds**, considered as irreversible stickiness between particles (a lost sticky contact through a bond is definitively lost). Here again, the attraction was able to generate drastic irreversibility at first cycle, until 70% of the swelling amplitude. However, this time, the breakable bonds required a minimum robustness in order to generate a noticeable influence on breathing (as opposite to adhesion that influenced even at lowest values). A final analysis of **particles irreversibility** was carried out in order to evaluate how a microscopic irreversibility is transferred to macroscopic scale, a transfer that revealed to be quite linear (Section 3.3.6). As a result, all these analyses let think the stickiness between particles present a major role in the breathing transfer from particles to electrode scale. Nevertheless, these conclusions are mainly limited to the breathing first cycle, the other cycles from the second being systematically stable. More detailed conclusions are developed in Section 3.4.

Complementary to the modelling work, an experimental approach was carried out (Chapter 4). It mainly focused on analysis of **pressure variation during cycling**, **pressure during formation** and **temperature** influence on breathing. A particular attention has been paid on the extraction of anode thickness variation from the results, the mechanical device being only capable to measure the full cell thickness (anode + cathode + separator + pouch bag). Globally speaking, no state of “stable breathing” (constant swelling amplitude and irreversibility) has been met, suggesting long asymptotic behaviour before stabilisation (thickness continuously grows cycle after cycle). This observation is stated for the maximum of cycles made, *i.e.* 38 cycles. More precisely, at room temperature (24°C), the results showed to be well reproducible. The variation of pressure during cycling (0.3, 1, 0.3, 3, 0.3 MPa) led to intuitive variation of breathing (the higher the pressure, the less breathing). The variation of pressure also presented a limited history effect on anode breathing, by generating a feeble persistent influence either on cell capacity or on swelling amplitude. In addition, each level of pressure seems to lead to a given average thickness, but the limited number of cycles measured makes the eventual stabilised cycling thickness due to intermediary compressions (1 and 3 MPa) hard to evaluate. At high temperature (61°C), the results presented much less reproducibility, with a high difference of charge/discharge speed, despite the galvanostatic cycling. At 61°C, the cell presented a higher initial capacity than at 24°C (around 3.5%). However, this capacity decreased much faster cycle after cycle than at 24°C (-0.19 mAh/cycle at 61°C against 0.03 mAh/cycle at 24°C). As a result, high temperature led to faster decrease of swelling amplitude, but simultaneously to a lower capacity. As the final tested parameter, the pressure during formation was found to be an interesting key in breathing control. Indeed, the highest pressure during formation (3 MPa during the nine first cycles) did not impact the cell capacity. Most importantly, this higher initial pressure generated a lower initial irreversibility that permanently reduced the thickness change during all the cycling (3 MPa compared to 1 MPa:

around 2.2 μm less, almost the third of the swelling amplitude order of magnitude). Finally, the higher initial pressure systematically reduced the swelling amplitude of around 0.5 μm (1% of initial thickness). Facing these experimental observations, electrode breathing reduction seems most likely to be controlled through pressure. As a first solution, applying a high pressure (3 MPa) during cycling can significantly reduce the breathing, but this remains an *in-operando* constraint. More interesting for a manufacturing perspective, applying a high pressure during the formation cycles (from five to ten first cycles) can permanently reduce the breathing. This conclusion values in terms of global thickness change from initial state as in terms of breathing amplitude at each cycle, and this even if the applied pressure during functioning comes back to a lower pressure (0.3 MPa). Still, these macroscopic observations do not enable a precise evaluation of particles reorganisation contribution to electrode breathing.

A cross-comparison of DEM model and experimental curve was made. It mostly demonstrated that DEM model shared an important discrepancy with continuous model: both approaches generated an electrode breathing highly sensitive to electrochemistry, via the presence of very fast change of thickness variation rate. In measured cell, the breathing is nevertheless more smoothed over time. Two axes were briefly explored with the DEM model to reduce the discrepancy: the breathing heterogeneity and the use of more complex particles shapes (using clusters of sub-particles). The use of complex shapes did not introduce an improvement in reproducing the breathing behaviour. This technique even created an effect of volume absorption because real volume breathing has not been rigorously implemented, resulting in an underestimated electrode breathing. This solution also revealed to be computationally costly. The introduction of heterogeneous breathing of particles generated interesting smoother electrode breathing. It also created a better proportion of irreversibility and swelling amplitude, resulting in a better match with experiment. An eventual third axis consists in implementing wear effect in contact laws between particles, in order to capture a progressive evolution of breathing along cycles. This last axis has not been explored in this thesis.

Considering these observations, the study of heterogeneous breathing of particles but also the implementation of wear effect in contact laws will certainly be preferable to the introduction of higher granular complexity. Concerning the experimental approach, the development of local microscopic measurement of particles breathing will be helpful to better evaluate the mechanical and electrochemical contributions in electrode breathing.

Nomenclature

Table 5.2: Acronyms

Acronym	Definition	
AM	<i>Active Material</i>	Material of electrode participating to lithium storage.
CAM	<i>Continuous Anode Model</i>	Continuous model of anode used in this thesis.
CBD	<i>Carbon-Binder Domain</i>	Mix of binder and electrical conductivity additives (other than active material) within electrode.
DAM	<i>Discrete Anode Model</i>	Discrete model of anode based on DEM, developed and used in this thesis (see Chapter 2).
DEM	<i>Discrete/Distinct Element Method</i>	Computation technique for dynamical interaction between solid particles that move into space (see Section 1.2).
DMT	<i>Derjaguin, Muller and Toporov</i>	Authors of the DMT adhesion theory (see Section 1.2.3.b).
HM	<i>Hertz-Mindlin</i>	Authors of theories used in DEM “HM” law (see Section 1.2.1.b)
JKR	<i>Johnson, Kendall and Roberts</i>	Authors of the JKR adhesion theory (see Section 1.2.3.b).
IPCC	<i>Intergovernmental Panel on Climate Change</i>	Intergovernmental body of the United Nations advancing scientific knowledge about climate change caused by human activities.
PC	<i>Potyondy & Cundall</i>	Authors of the bonded particles model for DEM (see Section 1.2.3.c)
PID	<i>Proportional Integral Derivative</i>	Control loop mechanism for automated system.

Table 1: Text reduced terms

Notation	Definition
C	Carbon black
Gr	Graphite
Li	Lithium
Si	Silicon
Si/C	Silicon/Carbon black

Table 2: Superscripts

Notation	Definition
0	Value at time 0
h	Time step index
n	Cycle index
V	Volumetric

Table 3: Subscripts

Notation	Definition
0	Value at time 0
an	Anode
ap	Apparent
b	Bond property
bag	Pouch bag
cal	Calendering
cat	Cathode
ch	Charge
CSi	Si/C
cyc	Cycle
cont	Contact(s)
d	Delithiation
disch	Discharge

Continued on next column

Table 3: Subscripts (Continued)

e	Elastic
equ	Equilibrium
form	Formation
i/j	Particles pair indices
irr	Irreversibility
k	Sum index
l	Lithiation
max	Maximum value
min	Minimum value
n	Normal
p	Plastic
part	Particle(s)
red	Reduced
ref	Reference
s	Body over solid (for \mathfrak{F})
sep	Separator
sh	Shrinking
stat	Statistics
sw	Swelling
t	Tangential
v	Body over void (for \mathfrak{F})
vp	Visco-plastic
vs	Void over solid (for \mathfrak{F})

Table 5.3: Mathematics

Notation	Operation	Unit
Δy	Variation / Difference	[y]
\dot{y}	Time derivative (first order)	[y] /s
y'	Secondary expression	[y]
\vec{y}	Vector	[y]
$\ \vec{y}\ $	Norm of vector \vec{y}	[y]
$\langle y \rangle$	Positive part (0 if $y \leq 0$, else y)	[y]
y^*	Pair equivalent	[y]
\tilde{y}	Analysis dimensionless number	1
\bar{y}	Breakable bond parameter	[y]
\hat{y}	Mean value	[y]
$\hat{u}(y)$	Absolute standard deviation	[y]
$\hat{u}_{\text{rel}}(y)$	Relative standard deviation	1
\check{y}	Cumulative value	[y]
$\vartheta(y)$	Transitional function	1
C/N	Charge/Discharge C-rate, $N \in \mathbb{N}$	1

Table 5.4: Latin variables

Notation	Definition	Eventual formula
a	Spherical contact radius, m	–
c	Time expressed in cycles, cycle	–
C	Specific weight capacity, Ah/kg	–
CN	Coordination number, –	–
d	Relative diameter, –	$= \frac{D}{D_0}$
D	Diameter, m	–
e	Coefficient of restitution, –	–
E	Young's modulus, Pa	–

Continued on next page

Table 5.4: Latin variables (Continued)

E_V^*	Equivalent volumetric Young's modulus, Pa	$= A_{CSi}^V E_{CSi} + (1 - A_{CSi}^V) E_{Gr}$
F	Force, N	–
g	Swelling coefficient, –	–
G	Shear modulus, Pa	–
H	Fitting parameter, Pa	–
\tilde{I}	Inertial number, –	$= \dot{\epsilon} \sqrt{\frac{\max_i \left(\frac{m_i}{D_i} \right)}{P_{\min}}}$
I/J	Particles pair centres, –	–
J_{Δ}	Moment of inertia, kg/m ²	–
J_{Δ^2}	Second moment of area, m ⁴	–
k	Stiffness, N/m	–
K	Stiffness per area, N/m ³	–
L	Length, m	–
m	Mass, kg	–
M	Torque, kg.m ² /s ²	–
MAE	Mean absolute error, [y]	–
\widetilde{MCN}	Mean coordination number, –	$= \frac{1}{N_{\text{part}}} \sum_{j=1}^{N_{\text{part}}} CN_j$
n	Normal unit vector, –	–
N	Positive integer, –	–
O	Spatial origin, –	–
P	Pressure, Pa	–
Q	Absolute capacity, Ah	–
r_{irr}	Ratio of irreversibility, –	$= \frac{v_{\lambda, \text{irr}}}{v_{\lambda, \text{max}} - v_{\lambda}}$
R	Radius, m	–
S	Surface, m ²	–
t	Time, s	–

Continued on next page

Table 5.4: Latin variables (Continued)

th	Thickness, m	–
T	Temperature, °C	–
U	Electrical potential, V	–
v	Relative volume, –	$= \frac{V}{V_0}$
V	Volume, m ³	–
st_{\max}	Maximum bond stress, Pa	–
W	Work of adhesion, J/m ²	$= \Delta\xi$
x	Stoichiometry, –	–
X	Number between 0 and 1, –	–
Y	Bond size ratio, –	–

Table 5.5: Greek variables

Notation	Definition	Eventual formula
α	Material Si, C, Si/C or Gr, –	$\in \{\text{Si, C, CSi, Gr}\}$
A	Mass fraction (over Si/C/Gr), –	$= \frac{m}{m_{\text{Si}} + m_{\text{C}} + m_{\text{Gr}}}$
A^V	Volume fraction (over Si/C/Gr), –	$= \frac{V}{V_{\text{Si}} + V_{\text{C}} + V_{\text{Gr}}}$
β	Material Si or C, –	$\in \{\text{Si, C}\}$
B	Mass fraction (over Si/C), –	$= \frac{m}{m_{\text{Si}} + m_{\text{C}}}$
γ	Material Si or Gr, –	$\in \{\text{Si, Gr}\}$
δ	Particles overlap, m	–
ΔQ	Cell provided capacity, Ah	–
Δt	Time step, s	–
Δt_c	Critical time step, s	–
Δth_{irr}	Irreversibility thickness Delta, m	–
Δth_{sw}	Swelling amplitude thickness Delta, m	–

Continued on next page

Table 5.5: Greek variables (Continued)

$\Delta\xi$	Interfacial surface energy, J/m ²	$\simeq 2\xi$
ϵ	Porosity, –	$= \frac{V_{\text{void}}}{V_{\text{electrode}}}$
ε	Strain, –	$= \frac{\Delta V}{V_0} \stackrel{1D}{=} \frac{\Delta th}{th_0}$
ζ	Inter-atomic spacing, m	–
η	Damping factor, N.s/m	–
$\tilde{\eta}$	Cohesion number, –	$= \frac{F_{\text{sticky}}}{4\hat{R}^2P}$
$\tilde{\eta}_{\text{JKR}}$	JKR cohesion number, –	$= \frac{3\pi W}{16\hat{R}P}$
$\tilde{\eta}_{\text{PC}}$	PC cohesion number, –	$= \frac{\pi\sigma_{\text{max}}}{4P}$
θ	Particle angle, rad	–
$\tilde{\Theta}$	Adhesion limit number, –	–
$\tilde{\kappa}$	Stiffness number, –	$= \left(\frac{E_V^*}{P(1-\nu^2)} \right)^{\frac{2}{3}}$
λ	Material Si/C or Gr, –	$\in \{\text{CSi, Gr}\}$
μ	Friction coefficient, –	–
μ_d	Dynamic friction coefficient, –	–
μ_s	Static friction coefficient, –	–
ν	Poisson's ratio, –	–
ξ	Surface energy, J/m ²	–
ρ	Density, kg/m ³	–
σ	Tensile stress, Pa	–
σ_Y	Yield tensile stress, Pa	–
ς	Smoothing factor, –	–
τ	Shear stress, Pa	–
χ	Particle position, m	–
ω	Angular velocity, rad/s	–

Table 5.6: Breathing coefficient उ †

Notation	Formula
\mathfrak{U}_s	$= \frac{\Delta V_{\text{body}}}{\Delta V_{\text{solid}}} \in \mathbb{R}$
\mathfrak{U}_v	$= \frac{\Delta V_{\text{body}}}{\Delta V_{\text{void}}} = \frac{\mathfrak{U}_s}{\mathfrak{U}_s - 1}$
\mathfrak{U}_{vs}	$= \frac{\Delta V_{\text{solid}}}{\Delta V_{\text{void}}} = \frac{1}{\mathfrak{U}_s - 1}$
$\mathfrak{U}_{s,sw}$	$= \mathfrak{r}_{sw} \frac{\widehat{\Delta th}_{sw}}{V_{\text{part},0}} \left(1 \pm \widehat{u}_{\text{rel}}(\mathfrak{U}_{s,sw}) \right)$
$\mathfrak{U}_{s,irr}$	$= \frac{\mathfrak{r}_{sw}}{r_{\text{irr}}} \frac{\widehat{\Delta th}_{\text{irr}}}{V_{\text{part},0}} \left(1 \pm \widehat{u}_{\text{rel}}(\mathfrak{U}_{s,irr}) \right)$

† Pronounced [u] (Sanskrit vowel). This specific variable can be also nicknamed “*udan*” (उदन) that means “breathe” / “to breathe out” in Sanskrit.

Table 5.7: Reduced surface \mathfrak{r} †

Notation	Formula
\mathfrak{r}	$= \frac{S}{A_{\text{CSi}}^V (v_{\text{CSi}} - 1) + (1 - A_{\text{CSi}}^V) (v_{\text{Gr}} - 1)} \leq S$
\mathfrak{r}_{sw}	$= \frac{S}{A_{\text{CSi}}^V (v_{\text{CSi,max}} - 1) + (1 - A_{\text{CSi}}^V) (v_{\text{Gr,max}} - 1)}$
$\mathfrak{r}_{\text{irr}}$	$= \frac{\mathfrak{r}_{sw}}{r_{\text{irr}}}$

† Pronounced “sampi” (archaic Greek letter).

Table 5.8: Exotic / Archaic

Notation	Definition
a	Fitting parameter, –
q	Translational acceleration, m/s^2
A	First fitting parameter of exponential fit, [y]
B	Second fitting parameter of exponential fit, [y]/cycle
C	Third fitting parameter of exponential fit, [y]
\mathcal{C}	Particles contact point, –
\vec{d}	Infinitesimal displacement, m
d	Distance between particles centres, m
\hbar	Computation time for one step, s
\bar{i}	Simulation index, –
\bar{j}	Statistical index, –
\dot{j}	Current per mass unit, A/kg –
η	Molar mass, kg/mol
μ	Amount of substance, mol
η	Damping factor, Pa.s
n	Fitting parameter, –
T	Period, s
v	Translational velocity, m/s
α	Angular acceleration, rad/s^2
\check{R}^2	Coefficient of determination, –
\mathfrak{R}_O	Spatial reference benchmark, –
β	Dimensionless damping factor, –
p	Characteristic time, cycle

Table 5.9: Constants

Notation	Definition	Value
e^-	Elementary charge	$1.602\ 176\ 634 \times 10^{-19}$ C
Λ	Avogadro constant	$6.022\ 140\ 76 \times 10^{23}$ mol ⁻¹
m_C	Molar mass of carbon	12.106 g/mol
m_{Si}	Molar mass of silicon	28.085 g/mol

References

- [1] J.-L. Brédas, J. M. Buriak, F. Caruso, *et al.*, “An Electrifying Choice for the 2019 Chemistry Nobel Prize: Goodenough, Whittingham, and Yoshino,” *Chemistry of Materials*, vol. 31, no. 21, pp. 8577–8581, 21 2019. DOI: 10.1021/acs.chemmater.9b04345. Available: <https://doi.org/10.1021/acs.chemmater.9b04345>.
- [2] G. Zubi, R. Dufo-López, M. Carvalho, and G. Pasaoglu, “The lithium-ion battery: State of the art and future perspectives,” *Renewable and Sustainable Energy Reviews*, vol. 89, pp. 292–308, 2018. DOI: 10.1016/j.rser.2018.03.002. Available: <https://www.sciencedirect.com/science/article/pii/S1364032118300728>.
- [3] M. A. Hannan, M. M. Hoque, A. Hussain, Y. Yusof, and P. J. Ker, “State-of-the-Art and Energy Management System of Lithium-Ion Batteries in Electric Vehicle Applications: Issues and Recommendations,” *IEEE Access*, vol. 6, pp. 19 362–19 378, 2018. DOI: 10.1109/ACCESS.2018.2817655.
- [4] M. Armand, P. Axmann, D. Bresser, *et al.*, “Lithium-ion batteries – Current state of the art and anticipated developments,” *Journal of Power Sources*, vol. 479, p. 228 708, 2020. DOI: 10.1016/j.jpowsour.2020.228708. Available: <https://www.sciencedirect.com/science/article/pii/S0378775320310120>.
- [5] M. M. Kabir and D. E. Demirocak, “Degradation mechanisms in Li-ion batteries: A state-of-the-art review,” *International Journal of Energy Research*, vol. 41, no. 14, pp. 1963–1986, 2017. DOI: 10.1002/er.3762. Available: <https://onlinelibrary.wiley.com/doi/abs/10.1002/er.3762>.
- [6] S. M. Abu, M. A. Hannan, M. S. Hossain Lipu, *et al.*, “State of the art of lithium-ion battery material potentials: An analytical evaluations, issues and future research directions,” *Journal of Cleaner Production*, vol. 394, p. 136 246, 2023. DOI: 10.1016/j.jclepro.2023.136246. Available: <https://www.sciencedirect.com/science/article/pii/S0959652623004043>.
- [7] A. Juton and F. Le Berr, “Le véhicule électrifié, une solution d’avenir pour l’automobile ?,” p. 16, 2020. Available: https://eduscol.education.fr/sti/si-ens-paris-saclay/ressources_pedagogiques/le-vehicule-electrique-une-solution-davenir-pour-lautomobile#description.
- [8] “Terres rares, énergies renouvelables et stockage d’énergies,” ADEME, 2019. Available: <https://bibliothèque.ademe.fr/energies-renouvelables-reseaux-et-stockage/492-terres-rares-energies-renouvelables-et-stockage-d-energies.html>.
- [9] F. Beny, S. Canas, M. Chavanne, D. Deutsch, L. Persoz, and A. Tuel, “Synthèse du sixième rapport de synthèse du GIEC,” 2023. Available: <https://theshiftproject.org/article/climat-synthese-vulgarisee-6eme-rapport-giec/>.
- [10] “CLIMATE CHANGE 2023,” IPCC, 2023. Available: <https://www.ipcc.ch/report/ar6/syr/>.
- [11] F. Le Berr, J. Melgar Sossa, C. Ternel, A. Bouter, and F. Badin, “Bilan transversal de l’impact de l’électrification par segment,” ADEME, 2018, p. 23. Available: <https://bibliothèque.ademe.fr/mobilite-et-transport/1267-bilan-transversal-de-l-impact-de-l-electrification-par-segment.html>.
- [12] E. Hache, M. Simoën, and S. Seck Gondia, “Electrification du parc automobile mondial et criticité du Lithium à l’horizon 2050,” 2018, p. 73. Available: <https://bibliothèque.ademe.fr/mobilite-et-transport/3803-electrification-du-parc-automobile-mondial-et-criticite-du-lithium-a-l-horizon-2050.html>.

- [13] H. Mehrjerdi and R. Hemmati, "Coordination of vehicle-to-home and renewable capacity resources for energy management in resilience and self-healing building," *Renewable Energy*, vol. 146, pp. 568–579, 2020. DOI: 10.1016/j.renene.2019.07.004. Available: <https://www.sciencedirect.com/science/article/pii/S0960148119310249>.
- [14] V. Sauvant-Moynot, F. Orsini, and A. Juton, "État de l'art et perspectives des batteries de voitures électriques," p. 25, 2020. Available: https://eduscol.education.fr/sti/si-ens-paris-saclay/ressources_pedagogiques/le-vehicule-electrique-une-solution-davenir-pour-lautomobile#description.
- [15] J. L. Heilbron, *Electricity in the 17th & 18th Centuries: A Study of Early Modern Physics*. University of California Press, 1979, 632 pp. Google Books: U1TLRU1sy8C.
- [16] A. Allerhand, "Who invented the earliest capacitor bank ("battery" of leyden jars)? it's complicated [scanning our past]," *Proceedings of the IEEE*, vol. 106, no. 3, pp. 496–503, 2018. DOI: 10.1109/JPROC.2018.2795846. Available: <https://ieeexplore.ieee.org/document/8303875>.
- [17] "A simple history of batteries - Panasonic Energy Co., Ltd." (2023), Available: <https://www.panasonic.com/global/energy/study/academy/history.html>.
- [18] "Riddle of 'Baghdad's batteries'." (2003), Available: <http://news.bbc.co.uk/2/hi/science/nature/2804257.stm>.
- [19] B. Haughton, *Hidden History: Lost Civilizations, Secret Knowledge, and Ancient Mysteries*. Red Wheel/Weiser, 2006, 272 pp. Google Books: 2dpEDwAAQBAJ.
- [20] A. Volta, "On the electricity excited by the mere contact of conducting substances of different kinds. In a letter from Mr. Alexander Volta, F. R. S. Professor of Natural Philosophy in the University of Pavia, to the Rt. Hon. Sir Joseph Banks, Bart. K.B. P. R. S.," *Philosophical Transactions of the Royal Society of London*, vol. 90, pp. 403–431, 1800. DOI: 10.1098/rstl.1800.0018. Available: <https://royalsocietypublishing.org/doi/10.1098/rstl.1800.0018>.
- [21] A. Volta. "On the Electricity excited by the mere Contact of conducting Substances of different Kinds. In a letter from MR. ALEXANDER VOLTA, F.R.S. Proffessor of Natural Philosophy in the University of Pavia, to the Right Hon. Sir JOSEPH BANKS, Bart. K.B P.R.S.," CNRS. (1800), Available: http://www.ampere.cnrs.fr/ice/ice_page_detail.php?lang=fr&type=role&bdd=koyre_ampere&table=ampere_text&bookId=90&typeofbookDes=Sources&pageOrder=8&facsimile=off&search=no.
- [22] P-F. Lory, B. Mathieu, S. Genies, *et al.*, "Probing Silicon Lithiation in Silicon-Carbon Blended Anodes with a Multi-Scale Porous Electrode Model," *Journal of The Electrochemical Society*, vol. 167, no. 12, p. 120506, 2020. DOI: 10.1149/1945-7111/abaa69. Available: <https://dx.doi.org/10.1149/1945-7111/abaa69>.
- [23] O. Gillia, "Hydride breathing and its consequence on stresses applied to containers: A review," *International Journal of Hydrogen Energy*, 2021. DOI: 10.1016/j.ijhydene.2021.07.082. Available: <https://www.sciencedirect.com/science/article/pii/S0360319921027233>.
- [24] K. Shah, N. Balsara, S. Banerjee, *et al.*, "State of the Art and Future Research Needs for Multiscale Analysis of Li-Ion Cells," *Journal of Electrochemical Energy Conversion and Storage*, vol. 14, no. 2, 2017. DOI: 10.1115/1.4036456. Available: <https://doi.org/10.1115/1.4036456>.
- [25] D. Lyu, B. Ren, and S. Li, "Failure modes and mechanisms for rechargeable Lithium-based batteries: A state-of-the-art review," *Acta Mechanica*, vol. 230, no. 3, pp. 701–727, 2019. DOI: 10.1007/s00707-018-2327-8. Available: <https://doi.org/10.1007/s00707-018-2327-8>.
- [26] A. Aizat Razali, S. N. Norazli, W. S. Sum, S. Y. Yeo, A. Dolfi, and G. Srinivasan, "State-of-the-Art of Solid-State Electrolytes on the Road Map of Solid-State Lithium Metal Batteries for E-Mobility," *ACS Sustainable Chemistry & Engineering*, vol. 11, no. 21, pp. 7927–7964, 2023. DOI: 10.1021/acssuschemeng.3c00057. Available: <https://doi.org/10.1021/acssuschemeng.3c00057>.
- [27] S. Zhang, "Chemomechanical modeling of lithiation-induced failure in high-volume-change electrode materials for lithium ion batteries," *npj Computational Materials*, vol. 3, no. 1, pp. 1–11, 1 2017. DOI: 10.1038/s41524-017-0009-z. Available: <https://www.nature.com/articles/s41524-017-0009-z>.

- [28] L. De Sutter, G. Berckmans, M. Marinaro, *et al.*, “Comprehensive Aging Analysis of Volumetric Constrained Lithium-Ion Pouch Cells with High Concentration Silicon-Alloy Anodes,” *Energies*, vol. 11, no. 11, p. 2948, 11 2018. DOI: 10.3390/en11112948.
- [29] K. Dong, H. Markötter, F. Sun, *et al.*, “In situ and Operando Tracking of Microstructure and Volume Evolution of Silicon Electrodes by using Synchrotron X-ray Imaging,” *ChemSusChem*, vol. 12, no. 1, pp. 261–269, 2019. DOI: 10.1002/cssc.201801969. Available: <https://onlinelibrary.wiley.com/doi/abs/10.1002/cssc.201801969>.
- [30] A. J. Louli, J. Li, S. Trussler, C. R. Fell, and J. R. Dahn, “Volume, Pressure and Thickness Evolution of Li-Ion Pouch Cells with Silicon-Composite Negative Electrodes,” *Journal of The Electrochemical Society*, vol. 164, no. 12, A2689, 2017. DOI: 10.1149/2.1691712jes. Available: <https://iopscience.iop.org/article/10.1149/2.1691712jes/meta>.
- [31] S. Huang and T. Zhu, “Atomistic mechanisms of lithium insertion in amorphous silicon,” *Journal of Power Sources*, vol. 196, no. 7, pp. 3664–3668, 2011. DOI: 10.1016/j.jpowsour.2010.11.155. Available: <https://www.sciencedirect.com/science/article/pii/S0378775310021476>.
- [32] B. Jerliu, E. Hüger, L. Dörner, *et al.*, “Volume Expansion during Lithiation of Amorphous Silicon Thin Film Electrodes Studied by In-Operando Neutron Reflectometry,” *The Journal of Physical Chemistry C*, vol. 118, no. 18, pp. 9395–9399, 2014. DOI: 10.1021/jp502261t. Available: <https://doi.org/10.1021/jp502261t>.
- [33] S. W. Lee, M. T. McDowell, J. W. Choi, and Y. Cui, “Anomalous Shape Changes of Silicon Nanopillars by Electrochemical Lithiation,” *Nano Letters*, vol. 11, no. 7, pp. 3034–3039, 2011. DOI: 10.1021/nl201787r. Available: <https://doi.org/10.1021/nl201787r>.
- [34] F. Ozanam and M. Rosso, “Silicon as anode material for Li-ion batteries,” *Materials Science and Engineering: B, Li-Ion Batteries*, vol. 213, pp. 2–11, 2016. DOI: 10.1016/j.mseb.2016.04.016. Available: <https://www.sciencedirect.com/science/article/pii/S0921510716300435>.
- [35] X. H. Liu, H. Zheng, L. Zhong, *et al.*, “Anisotropic Swelling and Fracture of Silicon Nanowires during Lithiation,” *Nano Letters*, vol. 11, no. 8, pp. 3312–3318, 2011. DOI: 10.1021/nl201684d. Available: <https://doi.org/10.1021/nl201684d>.
- [36] M. N. Obrovac and L. Christensen, “Structural Changes in Silicon Anodes during Lithium Insertion/Extraction,” *Electrochemical and Solid-State Letters*, vol. 7, no. 5, A93, 2004. DOI: 10.1149/1.1652421. Available: <https://iopscience.iop.org/article/10.1149/1.1652421/meta>.
- [37] C. Zhao, L. Liu, X. Qi, *et al.*, “Solid-State Sodium Batteries,” *Advanced Energy Materials*, vol. 8, no. 17, p. 1703012, 2018. DOI: 10.1002/aenm.201703012. Available: <https://onlinelibrary.wiley.com/doi/abs/10.1002/aenm.201703012>.
- [38] N. Boaretto, I. Garbayo, S. Valiyaveetil-SobhanRaj, *et al.*, “Lithium solid-state batteries: State-of-the-art and challenges for materials, interfaces and processing,” *Journal of Power Sources*, vol. 502, p. 229919, 2021. DOI: 10.1016/j.jpowsour.2021.229919. Available: <https://www.sciencedirect.com/science/article/pii/S0378775321004511>.
- [39] J. Mi, L. Chen, J. Ma, *et al.*, “Defect Strategy in Solid-State Lithium Batteries,” *Small Methods*, vol. 8, no. 1, p. 2301162, 2024. DOI: 10.1002/smt.202301162. Available: <https://onlinelibrary.wiley.com/doi/abs/10.1002/smt.202301162>.
- [40] D. Vidal, “Effect of the positive electrode and of mechanical stresses on the cyclability of a Li-ion cell containing silicon-based negative electrode,” Ph.D. dissertation, Université Grenoble Alpes [2018-2020], 2021. Available: <https://tel.archives-ouvertes.fr/tel-03508250>.
- [41] L. Y. Beaulieu, K. W. Eberman, R. L. Turner, L. J. Krause, and J. R. Dahn, “Colossal Reversible Volume Changes in Lithium Alloys,” *Electrochemical and Solid-State Letters*, vol. 4, no. 9, A137, 2001. DOI: 10.1149/1.1388178. Available: <https://iopscience.iop.org/article/10.1149/1.1388178/meta>.

- [42] L. Y. Beaulieu, T. D. Hatchard, A. Bonakdarpour, M. D. Fleischauer, and J. R. Dahn, "Reaction of Li with Alloy Thin Films Studied by In Situ AFM," *Journal of The Electrochemical Society*, vol. 150, no. 11, A1457, 2003. DOI: 10.1149/1.1613668. Available: <https://iopscience.iop.org/article/10.1149/1.1613668/meta>.
- [43] J. B. Cook, T. C. Lin, E. Detsi, J. N. Weker, and S. H. Tolbert, "Using X-ray Microscopy To Understand How Nanoporous Materials Can Be Used To Reduce the Large Volume Change in Alloy Anodes," *Nano Letters*, vol. 17, no. 2, pp. 870–877, 2017. DOI: 10.1021/acs.nanolett.6b04181. Available: <https://doi.org/10.1021/acs.nanolett.6b04181>.
- [44] H. Schmidt, B. Jerliu, E. Hüger, and J. Stahn, "Volume expansion of amorphous silicon electrodes during potentiostatic lithiation of Li-ion batteries," *Electrochemistry Communications*, vol. 115, p. 106738, 2020. DOI: 10.1016/j.elecom.2020.106738. Available: <https://www.sciencedirect.com/science/article/pii/S1388248120300898>.
- [45] X. Li, P. Yan, X. Xiao, *et al.*, "Design of porous Si/C–graphite electrodes with long cycle stability and controlled swelling," *Energy & Environmental Science*, vol. 10, no. 6, pp. 1427–1434, 6 2017. DOI: 10.1039/C7EE00838D. Available: <https://pubs.rsc.org/en/content/articlelanding/2017/ee/c7ee00838d>.
- [46] H. Wen, M. Karulkar, and A. Drews, "In-Operando Measurements of Volume Change of C-Si Pouch Cells," *ECS Transactions*, vol. 77, no. 11, p. 365, 11 2017. DOI: 10.1149/07711.0365ecst. Available: <https://iopscience.iop.org/article/10.1149/07711.0365ecst/meta>.
- [47] V. Müller, R.-G. Scurtu, K. Richter, *et al.*, "Effects of Mechanical Compression on the Aging and the Expansion Behavior of Si/C-CompositelNMC811 in Different Lithium-Ion Battery Cell Formats," *Journal of The Electrochemical Society*, vol. 166, no. 15, A3796, 15 2019. DOI: 10.1149/2.1121915jes. Available: <https://iopscience.iop.org/article/10.1149/2.1121915jes/meta>.
- [48] Y. Zhao, F. B. Spingler, Y. Patel, G. J. Offer, and A. Jossen, "Localized Swelling Inhomogeneity Detection in Lithium Ion Cells Using Multi-Dimensional Laser Scanning," *Journal of The Electrochemical Society*, vol. 166, no. 2, A27, 2 2019. DOI: 10.1149/2.0011902jes. Available: <https://iopscience.iop.org/article/10.1149/2.0011902jes/meta>.
- [49] D. Petz, M. J. Mühlbauer, A. Schökel, *et al.*, "Heterogeneity of Graphite Lithiation in State-of-the-Art Cylinder-Type Li-Ion Cells," *Batteries & Supercaps*, vol. 4, no. 2, pp. 327–335, 2021. DOI: 10.1002/batt.202000178. Available: <https://chemistry-europe.onlinelibrary.wiley.com/doi/abs/10.1002/batt.202000178>.
- [50] K. P. C. Yao, J. S. Okasinski, K. Kalaga, J. D. Almer, and D. P. Abraham, "Operando Quantification of (De)Lithiation Behavior of Silicon–Graphite Blended Electrodes for Lithium-Ion Batteries," *Advanced Energy Materials*, vol. 9, no. 8, p. 1803380, 2019. DOI: 10.1002/aenm.201803380. Available: <https://onlinelibrary.wiley.com/doi/abs/10.1002/aenm.201803380>.
- [51] C. L. Berhaut, D. Z. Dominguez, P. Kumar, *et al.*, "Multiscale Multiphase Lithiation and Delithiation Mechanisms in a Composite Electrode Unraveled by Simultaneous Operando Small-Angle and Wide-Angle X-Ray Scattering," *ACS Nano*, vol. 13, no. 10, pp. 11538–11551, 2019. DOI: 10.1021/acs.nano.9b05055. Available: <https://doi.org/10.1021/acs.nano.9b05055>.
- [52] D. Vidal, C. Leys, B. Mathieu, *et al.*, "Si–C/G based anode swelling and porosity evolution in 18650 casing and in pouch cell," *Journal of Power Sources*, vol. 514, p. 230552, 2021. DOI: 10.1016/j.jpowsour.2021.230552. Available: <https://www.sciencedirect.com/science/article/pii/S0378775321010508>.
- [53] O. von Kessel, T. Hoehl, P. Heugel, F. Brauchle, D. Vrankovic, and K. P. Birke, "Electrochemical-Mechanical Parameterization and Modeling of Expansion, Pressure, and Porosity Evolution in NMC811|SiOx-Graphite Lithium-Ion Cells," *Journal of The Electrochemical Society*, vol. 170, no. 9, p. 090534, 2023. DOI: 10.1149/1945-7111/ace1aa. Available: <https://dx.doi.org/10.1149/1945-7111/ace1aa>.
- [54] D. J. Pereira, J. W. Weidner, and T. R. Garrick, "The Effect of Volume Change on the Accessible Capacities of Porous Silicon-Graphite Composite Anodes," *Journal of The Electrochemical Society*, vol. 166, no. 6, A1251, 6 2019. DOI: 10.1149/2.1211906jes. Available: <https://iopscience.iop.org/article/10.1149/2.1211906jes/meta>.

- [55] Y. Chen, L. Yang, F. Guo, *et al.*, “Mechanical-electrochemical modeling of silicon-graphite composite anode for lithium-ion batteries,” *Journal of Power Sources*, vol. 527, p. 231178, 2022. DOI: 10.1016/j.jpowsour.2022.231178. Available: <https://www.sciencedirect.com/science/article/pii/S0378775322001987>.
- [56] W. Mai, A. Colclasure, and K. Smith, “A Reformulation of the Pseudo2D Battery Model Coupling Large Electrochemical-Mechanical Deformations at Particle and Electrode Levels,” *Journal of The Electrochemical Society*, vol. 166, no. 8, A1330, 2019. DOI: 10.1149/2.0101908jes. Available: <https://iopscience.iop.org/article/10.1149/2.0101908jes/meta>.
- [57] X. Zhang, M. Klinsmann, S. Chumakov, *et al.*, “A Modified Electrochemical Model to Account for Mechanical Effects Due to Lithium Intercalation and External Pressure,” *Journal of The Electrochemical Society*, vol. 168, no. 2, p. 020533, 2021. DOI: 10.1149/1945-7111/abe16d. Available: <https://doi.org/10.1149/1945-7111/abe16d>.
- [58] D. Sauerteig, N. Hanselmann, A. Arzberger, H. Reinshagen, S. Ivanov, and A. Bund, “Electrochemical-mechanical coupled modeling and parameterization of swelling and ionic transport in lithium-ion batteries,” *Journal of Power Sources*, vol. 378, pp. 235–247, 2018. DOI: 10.1016/j.jpowsour.2017.12.044. Available: <https://www.sciencedirect.com/science/article/pii/S037877531731652X>.
- [59] H. Pegel, O. von Kessel, P. Heugel, *et al.*, “Volume and thickness change of NMC811/SiO_x-graphite large-format lithium-ion cells: From pouch cell to active material level,” *Journal of Power Sources*, vol. 537, p. 231443, 2022. DOI: 10.1016/j.jpowsour.2022.231443. Available: <https://www.sciencedirect.com/science/article/pii/S0378775322004529>.
- [60] P. M. Gomadam and J. W. Weidner, “Modeling Volume Changes in Porous Electrodes,” *Journal of The Electrochemical Society*, vol. 153, no. 1, A179, 2005. DOI: 10.1149/1.2136087. Available: <https://iopscience.iop.org/article/10.1149/1.2136087/meta>.
- [61] P. Gudmundson and P.-L. Larsson, “An analytic model for effective mechanical properties and local contact stresses in lithium-ion porous electrodes,” *Extreme Mechanics Letters*, vol. 42, p. 101067, 2020. DOI: 10.1016/j.eml.2020.101067. Available: <https://www.sciencedirect.com/science/article/pii/S2352431620302601>.
- [62] X. Liu, C. L. Martin, G. Delette, J. Laurencin, D. Bouvard, and T. Delahaye, “Microstructure of porous composite electrodes generated by the discrete element method,” *Journal of Power Sources*, vol. 196, no. 4, pp. 2046–2054, 2011. DOI: 10.1016/j.jpowsour.2010.09.033. Available: <https://www.sciencedirect.com/science/article/pii/S0378775310016393>.
- [63] J. Zhu, W. Li, Y. Xia, and E. Sahraei, “Testing and Modeling the Mechanical Properties of the Granular Materials of Graphite Anode,” *Journal of The Electrochemical Society*, vol. 165, no. 5, A1160, 2018. DOI: 10.1149/2.0141807jes. Available: <https://iopscience.iop.org/article/10.1149/2.0141807jes/meta>.
- [64] C. Sangrós Giménez, B. Finke, C. Nowak, C. Schilde, and A. Kwade, “Structural and mechanical characterization of lithium-ion battery electrodes via DEM simulations,” *Advanced Powder Technology*, vol. 29, no. 10, pp. 2312–2321, 2018. DOI: 10.1016/j.apt.2018.05.014. Available: <https://www.sciencedirect.com/science/article/pii/S0921883118302061>.
- [65] C. Sangrós Giménez, B. Finke, C. Schilde, L. Froböse, and A. Kwade, “Numerical simulation of the behavior of lithium-ion battery electrodes during the calendaring process via the discrete element method,” *Powder Technology*, vol. 349, pp. 1–11, 2019. DOI: 10.1016/j.powtec.2019.03.020. Available: <https://www.sciencedirect.com/science/article/pii/S0032591019301871>.
- [66] D. Schreiner, J. Lindenblatt, F. J. Günter, and G. Reinhart, “DEM Simulations of the Calendaring Process: Parameterization of the Electrode Material of Lithium-Ion Batteries,” *Procedia CIRP*, 54th CIRP CMS 2021 - Towards Digitalized Manufacturing 4.0, vol. 104, pp. 91–97, 2021. DOI: 10.1016/j.procir.2021.11.016. Available: <https://www.sciencedirect.com/science/article/pii/S2212827121009148>.

- [67] M. M. Forouzan, C.-W. Chao, D. Bustamante, B. A. Mazzeo, and D. R. Wheeler, "Experiment and simulation of the fabrication process of lithium-ion battery cathodes for determining microstructure and mechanical properties," *Journal of Power Sources*, vol. 312, pp. 172–183, 2016. DOI: 10.1016/j.jpowsour.2016.02.014. Available: <https://www.sciencedirect.com/science/article/pii/S0378775316301227>.
- [68] A. C. Ngandjong, T. Lombardo, E. N. Primo, *et al.*, "Investigating electrode calendaring and its impact on electrochemical performance by means of a new discrete element method model: Towards a digital twin of Li-Ion battery manufacturing," *Journal of Power Sources*, vol. 485, p. 229320, 2021. DOI: 10.1016/j.jpowsour.2020.229320. Available: <https://www.sciencedirect.com/science/article/pii/S0378775320316086>.
- [69] T. Lombardo, A. C. Ngandjong, A. Belhacen, and A. A. Franco, "Carbon-Binder Migration: A Three-Dimensional Drying Model for Lithium-ion Battery Electrodes," *Energy Storage Materials*, vol. 43, pp. 337–347, 2021. DOI: 10.1016/j.ensm.2021.09.015. Available: <https://www.sciencedirect.com/science/article/pii/S240582972100427X>.
- [70] T. Lombardo, F. Lambert, R. Russo, *et al.*, "Experimentally Validated Three-Dimensional Modeling of Organic-Based Sodium-Ion Battery Electrode Manufacturing," *Batteries & Supercaps*, vol. 5, no. 8, e202200116, 2022. DOI: 10.1002/batt.202200116. Available: <https://onlinelibrary.wiley.com/doi/abs/10.1002/batt.202200116>.
- [71] J. Xu, B. Paredes-Goyes, Z. Su, *et al.*, "Computational Model for Predicting Particle Fracture During Electrode Calendaring," *Batteries & Supercaps*, vol. 6, no. 12, e202300371, 2023. DOI: 10.1002/batt.202300371. Available: <https://onlinelibrary.wiley.com/doi/abs/10.1002/batt.202300371>.
- [72] M. So, G. Inoue, R. Hirate, K. Nunoshita, S. Ishikawa, and Y. Tsuge, "Simulation of Fabrication and Degradation of All-Solid-State Batteries with Ductile Particles," *Journal of The Electrochemical Society*, vol. 168, no. 3, p. 030538, 2021. DOI: 10.1149/1945-7111/abed23. Available: <https://dx.doi.org/10.1149/1945-7111/abed23>.
- [73] M. So, S. Yano, A. Permatasari, T. D. Pham, K. Park, and G. Inoue, "Mechanism of silicon fragmentation in all-solid-state battery evaluated by discrete element method," *Journal of Power Sources*, vol. 546, p. 231956, 2022. DOI: 10.1016/j.jpowsour.2022.231956. Available: <https://www.sciencedirect.com/science/article/pii/S0378775322009399>.
- [74] B. Remy, J. G. Khinast, and B. J. Glasser, "Discrete element simulation of free flowing grains in a four-bladed mixer," *AIChE Journal*, vol. 55, no. 8, pp. 2035–2048, 2009. DOI: 10.1002/aic.11876. Available: <https://onlinelibrary.wiley.com/doi/abs/10.1002/aic.11876>.
- [75] J. M. Boac, R. P. K. Ambrose, M. E. Casada, R. G. Maghirang, and D. E. Maier, "Applications of Discrete Element Method in Modeling of Grain Postharvest Operations," *Food Engineering Reviews*, vol. 6, no. 4, pp. 128–149, 2014. DOI: 10.1007/s12393-014-9090-y. Available: <https://doi.org/10.1007/s12393-014-9090-y>.
- [76] Y. Guo, Q. Chen, Y. Xia, J. Klinger, and V. Thompson, "A nonlinear elasto-plastic bond model for the discrete element modeling of woody biomass particles," *Powder Technology*, vol. 385, pp. 557–571, 2021. DOI: 10.1016/j.powtec.2021.03.008. Available: <https://www.sciencedirect.com/science/article/pii/S0032591021001996>.
- [77] C. Schilde, S. Beinert, and A. Kwade, "Comparison of the micromechanical aggregate properties of nanostructured aggregates with the stress conditions during stirred media milling," *Chemical Engineering Science*, vol. 66, no. 21, pp. 4943–4952, 2011. DOI: 10.1016/j.ces.2011.07.006. Available: <https://www.sciencedirect.com/science/article/pii/S0009250911004660>.
- [78] C. Schilde, C. F. Burmeister, and A. Kwade, "Measurement and simulation of micromechanical properties of nanostructured aggregates via nanoindentation and DEM-simulation," *Powder Technology*, vol. 259, pp. 1–13, 2014. DOI: 10.1016/j.powtec.2014.03.042. Available: <https://www.sciencedirect.com/science/article/pii/S0032591014002423>.
- [79] S. Beinert, C. Schilde, and A. Kwade, "Simulation of Stress Energy and Grinding Media Movement within a Wet-Operated Annular-Gap Mill Using the Discrete-Element Method," *Chemical Engineering & Technology*, vol. 35, no. 11, pp. 1911–1921, 2012. DOI: 10.1002/ceat.201200116. Available: <https://onlinelibrary.wiley.com/doi/abs/10.1002/ceat.201200116>.

- [80] M. Jahani, A. Farzanegan, and M. Noaparast, "Investigation of screening performance of banana screens using LIGGGHTS DEM solver," *Powder Technology*, vol. 283, pp. 32–47, 2015. DOI: 10.1016/j.powtec.2015.05.016. Available: <https://www.sciencedirect.com/science/article/pii/S0032591015003939>.
- [81] Y. Li, H. Zhang, Z. Lin, Z. He, J. Xiang, and X. Su, "Relationship between wear formation and large-particle motion in a pipe bend," *Royal Society Open Science*, vol. 6, no. 1, p. 181 254, 1 2019. DOI: 10.1098/rsos.181254. Available: <https://royalsocietypublishing.org/doi/10.1098/rsos.181254>.
- [82] D. Zeng, E. Zhang, Y. Ding, *et al.*, "Investigation of erosion behaviors of sulfur-particle-laden gas flow in an elbow via a CFD-DEM coupling method," *Powder Technology*, vol. 329, pp. 115–128, 2018. DOI: 10.1016/j.powtec.2018.01.056. Available: <https://www.sciencedirect.com/science/article/pii/S003259101830069X>.
- [83] C. Sangrós Giménez, C. Schilde, L. Froböse, S. Ivanov, and A. Kwade, "Mechanical, Electrical, and Ionic Behavior of Lithium-Ion Battery Electrodes via Discrete Element Method Simulations," *Energy Technology*, vol. 8, no. 2, p. 1 900 180, 2 2019. DOI: 10.1002/ente.201900180. Available: <https://onlinelibrary.wiley.com/doi/abs/10.1002/ente.201900180>.
- [84] C. Sangrós Giménez, L. Helters, C. Schilde, A. Diener, and A. Kwade, "Modeling the Electrical Conductive Paths within All-Solid-State Battery Electrodes," *Chemical Engineering & Technology*, vol. 43, no. 5, pp. 819–829, 2020. DOI: 10.1002/ceat.201900501. Available: <https://onlinelibrary.wiley.com/doi/abs/10.1002/ceat.201900501>.
- [85] D. Schreiner, A. Klinger, and G. Reinhart, "Modeling of the Calendring Process for Lithium-Ion Batteries with DEM Simulation," *Procedia CIRP*, 53rd CIRP Conference on Manufacturing Systems 2020, vol. 93, pp. 149–155, 2020. DOI: 10.1016/j.procir.2020.05.158. Available: <https://www.sciencedirect.com/science/article/pii/S2212827120306570>.
- [86] "ARTISTIC project," European Research Council. (2023), Available: <http://www.erc-artistic.eu/>.
- [87] T. Lombardo, J.-B. Hoock, E. N. Primo, A. C. Ngandjong, M. Duquesnoy, and A. A. Franco, "Accelerated Optimization Methods for Force-Field Parametrization in Battery Electrode Manufacturing Modeling," *Batteries & Supercaps*, vol. 3, no. 8, pp. 721–730, 2020. DOI: 10.1002/batt.202000049. Available: <https://onlinelibrary.wiley.com/doi/abs/10.1002/batt.202000049>.
- [88] J. Xu, A. C. Ngandjong, C. Liu, *et al.*, "Lithium ion battery electrode manufacturing model accounting for 3D realistic shapes of active material particles," *Journal of Power Sources*, vol. 554, p. 232 294, 2023. DOI: 10.1016/j.jpowsour.2022.232294. Available: <https://www.sciencedirect.com/science/article/pii/S037877532201271X>.
- [89] B. Charlas, "Etude du comportement mécanique d'un hydrure intermétallique utilisé pour le stockage d'hydrogène," Theses, Université de Grenoble, 2013. Available: <https://tel.archives-ouvertes.fr/tel-01687759>.
- [90] M. So, G. Inoue, R. Hirate, K. Nunoshita, S. Ishikawa, and Y. Tsuge, "Effect of mold pressure on compaction and ion conductivity of all-solid-state batteries revealed by the discrete element method," *Journal of Power Sources*, vol. 508, p. 230 344, 2021. DOI: 10.1016/j.jpowsour.2021.230344. Available: <https://www.sciencedirect.com/science/article/pii/S0378775321008569>.
- [91] M. So, G. Inoue, K. Park, K. Nunoshita, S. Ishikawa, and Y. Tsuge, "Contact model for DEM simulation of compaction and sintering of all-solid-state battery electrodes," *MethodsX*, vol. 9, p. 101 857, 2022. DOI: 10.1016/j.mex.2022.101857. Available: <https://www.sciencedirect.com/science/article/pii/S2215016122002369>.
- [92] M. So, G. Inoue, K. Park, K. Nunoshita, S. Ishikawa, and Y. Tsuge, "Simulation of the compaction of an all-solid-state battery cathode with coated particles using the discrete element method," *Journal of Power Sources*, vol. 530, p. 231 279, 2022. DOI: 10.1016/j.jpowsour.2022.231279. Available: <https://www.sciencedirect.com/science/article/pii/S0378775322002968>.
- [93] P. A. Cundall and O. D. L. Strack, "A discrete numerical model for granular assemblies," *Géotechnique*, vol. 29, no. 1, pp. 47–65, 1 1979. DOI: 10.1680/geot.1979.29.1.47. Available: <https://www.icevirtuallibrary.com/doi/10.1680/geot.1979.29.1.47>.
- [94] R. Hooke, *Potentia Restitutiva, Or of Spring Explaining the Power of Springing Bodies*. London: John Martyn, 1678, 66 pp. Available: <https://www.proquest.com/docview/2240899087/18202145>.

- [95] C. A. de Coulomb, *Théorie des machines simples, en ayant égard au frottement de leurs parties et à la roideur des cordages*. Bachelier, 1821, 395 pp. Available: <http://archive.org/details/thoriedesmachin01coulgoog>.
- [96] H. Hertz. “Ueber die Berührung fester elastischer Körper (Wikipedia archiv).” (1881), Available: <http://archive.wikiwix.com/cache/index2.php?url=http%3A%2F%2Fwww.uni-leipzig.de%2F%7Epwm%2Fkas%2Fafm%2FHertz.pdf>.
- [97] H. Hertz, “Ueber die Berührung fester elastischer Körper,” *De Gruyter*, vol. Band 92, pp. 156–171, 1882. DOI: 10.1515/9783112342404-004. Available: <https://www.degruyter.com/document/doi/10.1515/9783112342404-004/html>.
- [98] H. Hertz, D. E. Jones, and G. A. Schott, *Ueber Die Berührung Fester Elastischer Körper (Miscellaneous Papers - English Version)*, in collab. with Cornell University Library. London: Macmillan, New York, Macmillan and co., 1896, 384 pp. Available: <https://archive.org/details/cu31924012500306/page/n183/mode/2up>.
- [99] J. Boussinesq, *Application des potentiels à l'étude de l'équilibre et du mouvement des solides élastiques*, in collab. with University of Michigan. Gauthier-Villars, 1885, 734 pp. Available: <http://archive.org/details/applicationdesp00bousgoog>.
- [100] A. Love, *A Treatise on the Mathematical Theory of Elasticity*. 1892, vol. 1. Available: <https://hal.archives-ouvertes.fr/hal-01307751>.
- [101] K. L. Johnson, “A note on the adhesion of elastic solids,” *British Journal of Applied Physics*, vol. 9, no. 5, pp. 199–200, 1958. DOI: 10.1088/0508-3443/9/5/307. Available: <https://doi.org/10.1088/0508-3443/9/5/307>.
- [102] K. L. Johnson, K. Kendall, and A. D. Roberts, “Surface energy and the contact of elastic solids,” *Proceedings of the Royal Society of London. A. Mathematical and Physical Sciences*, vol. 324, no. 1558, pp. 301–313, 1971. DOI: 10.1098/rspa.1971.0141. Available: <https://royalsocietypublishing.org/doi/10.1098/rspa.1971.0141>.
- [103] D. Hills, D. Nowell, and J. Barber, “KL Johnson and contact mechanics,” *Proceedings of the Institution of Mechanical Engineers, Part C: Journal of Mechanical Engineering Science*, vol. 231, 2016. DOI: 10.1177/0954406216634121.
- [104] K. L. Johnson, *Contact Mechanics*. Cambridge University Press, 1985. DOI: 10.1017/CB09781139171731. Available: <https://www.cambridge.org/core/books/contact-mechanics/E3707F77C2EBCE727C3911AFBD2E4AC2>.
- [105] K. L. Johnson, “Introduction to Contact Mechanics: A summary of the principal formulae,” in *Fundamentals of Friction: Macroscopic and Microscopic Processes*, ser. NATO ASI Series, I. L. Singer and H. M. Pollock, Eds., Dordrecht: Springer Netherlands, 1992, pp. 589–603. DOI: 10.1007/978-94-011-2811-7_30. Available: https://doi.org/10.1007/978-94-011-2811-7_30.
- [106] C. Thornton and C. W. Randall, “Applications of Theoretical Contact Mechanics to Solid Particle System Simulation,” *Studies in Applied Mechanics*, Micromechanics of Granular Materials, vol. 20, pp. 133–142, 1988. DOI: 10.1016/B978-0-444-70523-5.50023-0. Available: <https://www.sciencedirect.com/science/article/pii/B978044470523500230>.
- [107] P. A. Cundall and O. D. L. Strack, “Modeling of Microscopic Mechanisms in Granular Material,” *Studies in Applied Mechanics*, in collab. with J. T. Jenkins and M. Satake, pp. 137–149, 1983. DOI: 10.1016/B978-0-444-42192-0.50018-9. Available: <https://www.sciencedirect.com/science/article/pii/B9780444421920500189>.
- [108] P. Cundall and R. Hart, “Development of Generalized 2-D and 3-D Distinct Element Programs for Modeling Jointed Rock,” 1985. Available: <https://www.semanticscholar.org/paper/Development-of-Generalized-2-D-and-3-D-Distinct-for-Cundall-Hart/ea9d58874feb816e5c16e264554b0b60daf5f132>.
- [109] P. A. Cundall, “Formulation of a three-dimensional distinct element model—Part I. A scheme to detect and represent contacts in a system composed of many polyhedral blocks,” *International Journal of Rock Mechanics and Mining Sciences & Geomechanics Abstracts*, vol. 25, no. 3, pp. 107–116, 1988. DOI: 10.1016/0148-9062(88)92293-0. Available: <https://www.sciencedirect.com/science/article/pii/0148906288922930>.

- [110] R. Hart, P. A. Cundall, and J. Lemos, "Formulation of a three-dimensional distinct element model—Part II. Mechanical calculations for motion and interaction of a system composed of many polyhedral blocks," *International Journal of Rock Mechanics and Mining Sciences & Geomechanics Abstracts*, vol. 25, no. 3, pp. 117–125, 1988. DOI: 10.1016/0148-9062(88)92294-2. Available: <https://www.sciencedirect.com/science/article/pii/0148906288922942>.
- [111] J.-P. Bardet and Q. Huang, "Numerical modeling of micropolar effects in idealized granular materials," *American Society of Mechanical Engineers, Materials Division (Publication) MD*, vol. 37, 1992.
- [112] Y. Tsuji, T. Tanaka, and T. Ishida, "Lagrangian numerical simulation of plug flow of cohesionless particles in a horizontal pipe," *Powder Technology*, vol. 71, no. 3, pp. 239–250, 1992. DOI: 10.1016/0032-5910(92)88030-L. Available: <https://www.sciencedirect.com/science/article/pii/003259109288030L>.
- [113] Y. Tsuji, T. Kawaguchi, and T. Tanaka, "Discrete particle simulation of two-dimensional fluidized bed," *Powder Technology*, vol. 77, no. 1, pp. 79–87, 1993. DOI: 10.1016/0032-5910(93)85010-7. Available: <https://www.sciencedirect.com/science/article/pii/0032591093850107>.
- [114] C. Thornton, "Coefficient of Restitution for Collinear Collisions of Elastic-Perfectly Plastic Spheres," *Journal of Applied Mechanics*, vol. 64, no. 2, pp. 383–386, 1997. DOI: 10.1115/1.2787319. Available: <https://doi.org/10.1115/1.2787319>.
- [115] L. Vu-Quoc and X. Zhang, "An elastoplastic contact force–displacement model in the normal direction: Displacement–driven version," *Proceedings of the Royal Society of London. Series A: Mathematical, Physical and Engineering Sciences*, vol. 455, no. 1991, pp. 4013–4044, 1999. DOI: 10.1098/rspa.1999.0488. Available: <https://royalsocietypublishing.org/doi/10.1098/rspa.1999.0488>.
- [116] L. Vu-Quoc and X. Zhang, "An accurate and efficient tangential force–displacement model for elastic frictional contact in particle-flow simulations," *Mechanics of Materials*, vol. 31, no. 4, pp. 235–269, 1999. DOI: 10.1016/S0167-6636(98)00064-7. Available: <https://www.sciencedirect.com/science/article/pii/S0167663698000647>.
- [117] N. Maw, J. R. Barber, and J. N. Fawcett, "The oblique impact of elastic spheres," *Wear*, vol. 38, no. 1, pp. 101–114, 1976. DOI: 10.1016/0043-1648(76)90201-5. Available: <https://www.sciencedirect.com/science/article/pii/0043164876902015>.
- [118] A. Di Renzo and F. P. Di Maio, "Comparison of contact-force models for the simulation of collisions in DEM-based granular flow codes," *Chemical Engineering Science*, vol. 59, no. 3, pp. 525–541, 2004. DOI: 10.1016/j.ces.2003.09.037. Available: <https://www.sciencedirect.com/science/article/pii/S0009250903005414>.
- [119] A. Di Renzo and F. P. Di Maio, "An improved integral non-linear model for the contact of particles in distinct element simulations," *Chemical Engineering Science*, vol. 60, no. 5, pp. 1303–1312, 2005. DOI: 10.1016/j.ces.2004.10.004. Available: <https://www.sciencedirect.com/science/article/pii/S0009250904007705>.
- [120] H. P. Zhu, Z. Y. Zhou, R. Y. Yang, and A. B. Yu, "Discrete particle simulation of particulate systems: Theoretical developments," *Chemical Engineering Science*, *Frontier of Chemical Engineering - Multi-scale Bridge between Reductionism and Holism*, vol. 62, no. 13, pp. 3378–3396, 13 2007. DOI: 10.1016/j.ces.2006.12.089. Available: <https://www.sciencedirect.com/science/article/pii/S000925090700262X>.
- [121] C. Kloss and C. Goniva, "LIGGGHTS – Open Source Discrete Element Simulations of Granular Materials Based on LAMMPS," *Supplemental Proceedings*, vol. 2, pp. 781–788, 2011. DOI: 10.1002/9781118062142.ch94. Available: <https://onlinelibrary.wiley.com/doi/abs/10.1002/9781118062142.ch94>.
- [122] C. Kloss, C. Goniva, A. König, S. Amberger, and S. Pirker, "Models, algorithms and validation for opensource DEM and CFD-DEM," *Progress in Computational Fluid Dynamics*, vol. 12, pp. 140–152, 2012. DOI: 10.1504/PCFD.2012.047457.
- [123] C. Kloss, P. Seil, S. Amberger, and A. Aigner, *LIGGGHTS-PUBLIC*, version 3.8.0, 2023. Available: <https://github.com/CFDEMproject/LIGGGHTS-PUBLIC>.

- [124] I. Newton, *Philosophiae naturalis principia mathematica*, in collab. with Smithsonian Libraries. Londini : Jussu Societatis Regiae ac Typis Josephi Streater. Prostat apud plures bibliopolas, 1687, 522 pp. Available: <http://archive.org/details/philosophiaenat00newt>.
- [125] N. V. Brilliantov, F. Spahn, J.-M. Hertzsch, and T. Pöschel, "Model for collisions in granular gases," *Physical Review E*, vol. 53, no. 5, pp. 5382–5392, 1996. DOI: 10.1103/PhysRevE.53.5382. Available: <https://link.aps.org/doi/10.1103/PhysRevE.53.5382>.
- [126] L. E. Silbert, D. Ertas, G. S. Grest, T. C. Halsey, D. Levine, and S. J. Plimpton, "Granular flow down an inclined plane: Bagnold scaling and rheology," *Physical Review E*, vol. 64, no. 5, p. 051302, 2001. DOI: 10.1103/PhysRevE.64.051302. Available: <https://link.aps.org/doi/10.1103/PhysRevE.64.051302>.
- [127] D. Zabulionis, R. Kacianauskas, D. Markauskas, and J. Rojek, "An investigation of nonlinear tangential contact behaviour of a spherical particle under varying loading," *Bulletin of the Polish Academy of Sciences. Technical Sciences*, vol. Vol. 60, pp. 265–278, nr 2 2012. Available: <http://yadda.icm.edu.pl/yadda/element/bwmeta1.element.baztech-article-BPG8-0078-0012>.
- [128] G. Kuwabara and K. Kono, "Restitution Coefficient in a Collision between Two Spheres," *Japanese Journal of Applied Physics*, vol. 26, p. 1230, 8R 1987. DOI: 10.1143/JJAP.26.1230. Available: <https://iopscience.iop.org/article/10.1143/JJAP.26.1230/meta>.
- [129] F. P. Bowden and D. Tabor, *The Friction and Lubrication of Solids* (Oxford Classic Texts in the Physical Sciences). Oxford, New York: Oxford University Press, 2001, 424 pp.
- [130] R. Bradley, "The cohesive force between solid surfaces and the surface energy of solids," *The London, Edinburgh, and Dublin Philosophical Magazine and Journal of Science*, vol. 13, no. 86, pp. 853–862, 1932. DOI: 10.1080/14786449209461990. Available: <https://doi.org/10.1080/14786449209461990>.
- [131] D. Maugis and H. M. Pollock, "Surface forces, deformation and adherence at metal microcontacts," *Acta Metallurgica*, vol. 32, no. 9, pp. 1323–1334, 1984. DOI: 10.1016/0001-6160(84)90078-6. Available: <https://www.sciencedirect.com/science/article/pii/0001616084900786>.
- [132] B. Derjaguin, "Untersuchungen über die Reibung und Adhäsion, IV," *Kolloid-Zeitschrift*, vol. 69, no. 2, pp. 155–164, 1934. DOI: 10.1007/BF01433225. Available: <https://doi.org/10.1007/BF01433225>.
- [133] B. Dahneke, "The influence of flattening on the adhesion of particles," *Journal of Colloid and Interface Science*, vol. 40, no. 1, pp. 1–13, 1972. DOI: 10.1016/0021-9797(72)90168-3. Available: <https://www.sciencedirect.com/science/article/pii/0021979772901683>.
- [134] B. V. Derjaguin, V. M. Muller, and Y. P. Toporov, "Effect of contact deformations on the adhesion of particles," *Journal of Colloid and Interface Science*, vol. 53, no. 2, pp. 314–326, 1975. DOI: 10.1016/0021-9797(75)90018-1. Available: <https://www.sciencedirect.com/science/article/pii/0021979775900181>.
- [135] D. Tabor, "Surface forces and surface interactions," *Journal of Colloid and Interface Science*, International Conference on Colloids and Surfaces, vol. 58, no. 1, pp. 2–13, 1977. DOI: 10.1016/0021-9797(77)90366-6. Available: <https://www.sciencedirect.com/science/article/pii/0021979777903666>.
- [136] V. M. Muller, V. S. Yushchenko, and B. V. Derjaguin, "On the influence of molecular forces on the deformation of an elastic sphere and its sticking to a rigid plane," *Journal of Colloid and Interface Science*, vol. 77, no. 1, pp. 91–101, 1980. DOI: 10.1016/0021-9797(80)90419-1. Available: <https://www.sciencedirect.com/science/article/pii/0021979780904191>.
- [137] D. Maugis, "Adhesion of spheres: The JKR-DMT transition using a dugdale model," *Journal of Colloid and Interface Science*, vol. 150, no. 1, pp. 243–269, 1992. DOI: 10.1016/0021-9797(92)90285-T. Available: <https://www.sciencedirect.com/science/article/pii/002197979290285T>.

- [138] J. A. Greenwood, "Adhesion of elastic spheres," *Proceedings of the Royal Society of London. Series A: Mathematical, Physical and Engineering Sciences*, vol. 453, no. 1961, pp. 1277–1297, 1997. DOI: 10.1098/rspa.1997.0070. Available: <https://royalsocietypublishing.org/doi/10.1098/rspa.1997.0070>.
- [139] K. L. Johnson and J. A. Greenwood, "An Adhesion Map for the Contact of Elastic Spheres," *Journal of Colloid and Interface Science*, vol. 192, no. 2, pp. 326–333, 1997. DOI: 10.1006/jcis.1997.4984. Available: <https://www.sciencedirect.com/science/article/pii/S00219797949845>.
- [140] C. Thornton, *Granular Dynamics, Contact Mechanics and Particle System Simulations* (Particle Technology Series). United-Kingdom: Springer International Publishing, 2015, vol. 24. DOI: 10.1007/978-3-319-18711-2. Available: <http://link.springer.com/10.1007/978-3-319-18711-2>.
- [141] T. Eidevåg, P. Abrahamsson, M. Eng, and A. Rasmuson, "Modeling of dry snow adhesion during normal impact with surfaces," *Powder Technology*, vol. 361, pp. 1081–1092, 2019. DOI: 10.1016/j.powtec.2019.10.085. Available: <https://www.sciencedirect.com/science/article/pii/S0032591019309143>.
- [142] A. J. Kinloch, *Adhesion and Adhesives*. Dordrecht: Springer Netherlands, 1987. DOI: 10.1007/978-94-015-7764-9. Available: <http://link.springer.com/10.1007/978-94-015-7764-9>.
- [143] C. Kittel, *Introduction to Solid State Physics*. Wiley, 2005. Available: <http://archive.org/details/IntroductionToSolidStatePhysics>.
- [144] A. Chokshi, A. G. G. M. Tielens, and D. Hollenbach, "Dust Coagulation," *The Astrophysical Journal*, vol. 407, p. 806, 1993. DOI: 10.1086/172562. Available: <https://ui.adsabs.harvard.edu/abs/1993ApJ...407..806C>.
- [145] E. J. R. Parteli, J. Schmidt, C. Blümel, K.-E. Wirth, W. Peukert, and T. Pöschel, "Attractive particle interaction forces and packing density of fine glass powders," *Scientific Reports*, vol. 4, no. 1, p. 6227, 1 2014. DOI: 10.1038/srep06227. Available: <https://www.nature.com/articles/srep06227>.
- [146] C. Coetzee, "Simplified Johnson-Kendall-Roberts (SJKR) Contact Model - Implementation in PFC," Stellenbosch University, 2020. Available: researchgate.net/publication/346879528.
- [147] J. S. Marshall, "Discrete-element modeling of particulate aerosol flows," *Journal of Computational Physics*, vol. 228, no. 5, pp. 1541–1561, 2009. DOI: 10.1016/j.jcp.2008.10.035. Available: <https://www.sciencedirect.com/science/article/pii/S002199910800572X>.
- [148] C. Thornton, "Interparticle sliding in the presence of adhesion," *Journal of Physics D: Applied Physics*, vol. 24, no. 11, p. 1942, 1991. DOI: 10.1088/0022-3727/24/11/007. Available: <https://dx.doi.org/10.1088/0022-3727/24/11/007>.
- [149] T. Eidevåg, *LIGGGHTS-PUBLIC-JKR*, version 3.8.0, 2020. Available: <https://github.com/eidevag/LIGGGHTS-PUBLIC-JKR>.
- [150] M. Schramm, *LIGGGHTS_Flexible_Fibers*, version 3.8.0, 2023. Available: https://github.com/schrummy14/LIGGGHTS_Flexible_Fibers.
- [151] D. O. Potyondy and P. A. Cundall, "A bonded-particle model for rock," *International Journal of Rock Mechanics and Mining Sciences*, Rock Mechanics Results from the Underground Research Laboratory, Canada, vol. 41, no. 8, pp. 1329–1364, 8 2004. DOI: 10.1016/j.ijrmms.2004.09.011. Available: <https://www.sciencedirect.com/science/article/pii/S1365160904002874>.
- [152] Y. Guo, J. Curtis, C. Wassgren, W. Ketterhagen, and B. Hancock, "Granular shear flows of flexible rod-like particles," *AIP Conference Proceedings*, vol. 1542, no. 1, pp. 491–494, 2013. DOI: 10.1063/1.4811975. Available: <https://aip.scitation.org/doi/abs/10.1063/1.4811975>.
- [153] Y. Guo, C. Wassgren, B. Hancock, W. Ketterhagen, and J. Curtis, "Validation and time step determination of discrete element modeling of flexible fibers," *Powder Technology*, vol. 249, pp. 386–395, 2013. DOI: 10.1016/j.powtec.2013.09.007. Available: <https://www.sciencedirect.com/science/article/pii/S0032591013005846>.

- [154] M. Schramm, M. Z. Tekeste, C. Plouffe, and D. Harby, “Estimating bond damping and bond Young’s modulus for a flexible wheat straw discrete element method model,” *Biosystems Engineering*, vol. 186, pp. 349–355, 2019. DOI: 10.1016/j.biosystemseng.2019.08.003. Available: <https://www.sciencedirect.com/science/article/pii/S1537511019307913>.
- [155] C. Richter, *LIGGGHTS-WITH-BONDS*, version 3.3.0, 2015. Available: <https://github.com/richti83/LIGGGHTS-WITH-BONDS>.
- [156] Y. Qi and S. J. Harris, “In Situ Observation of Strains during Lithiation of a Graphite Electrode,” *Journal of The Electrochemical Society*, vol. 157, no. 6, A741, 2010. DOI: 10.1149/1.3377130. Available: <https://iopscience.iop.org/article/10.1149/1.3377130/meta>.
- [157] V. A. Sethuraman, M. J. Chon, M. Shimshak, N. Van Winkle, and P. R. Guduru, “In situ measurement of biaxial modulus of Si anode for Li-ion batteries,” *Electrochemistry Communications*, vol. 12, no. 11, pp. 1614–1617, 2010. DOI: 10.1016/j.elecom.2010.09.008. Available: <https://www.sciencedirect.com/science/article/pii/S1388248110003929>.
- [158] V. B. Shenoy, P. Johari, and Y. Qi, “Elastic softening of amorphous and crystalline Li–Si Phases with increasing Li concentration: A first-principles study,” *Journal of Power Sources*, vol. 195, no. 19, pp. 6825–6830, 2010. DOI: 10.1016/j.jpowsour.2010.04.044. Available: <https://www.sciencedirect.com/science/article/pii/S0378775310006798>.
- [159] B. Hertzberg, J. Benson, and G. Yushin, “Ex-situ depth-sensing indentation measurements of electrochemically produced Si–Li alloy films,” *Electrochemistry Communications*, vol. 13, no. 8, pp. 818–821, 2011. DOI: 10.1016/j.elecom.2011.05.011. Available: <https://www.sciencedirect.com/science/article/pii/S1388248111002001>.
- [160] L. A. Berla, S. W. Lee, Y. Cui, and W. D. Nix, “Mechanical behavior of electrochemically lithiated silicon,” *Journal of Power Sources*, vol. 273, pp. 41–51, 2015. DOI: 10.1016/j.jpowsour.2014.09.073. Available: <https://www.sciencedirect.com/science/article/pii/S0378775314014827>.
- [161] J.-h. Lee and C. Kim, “Effective modulus of Si electrodes considering Li concentration, volume expansion, pore, and Poisson’s ratio of Li-ion batteries,” *Journal of Mechanical Science and Technology*, vol. 35, no. 5, pp. 2115–2121, 2021. DOI: 10.1007/s12206-021-0427-1. Available: <https://doi.org/10.1007/s12206-021-0427-1>.
- [162] H. Wang, S.-H. Lu, X. Wang, S. Xia, and H. B. Chew, “A review of the multiscale mechanics of silicon electrodes in high-capacity lithium-ion batteries,” *Journal of Physics D: Applied Physics*, vol. 55, no. 6, p. 063 001, 2021. DOI: 10.1088/1361-6463/ac2d64. Available: <https://dx.doi.org/10.1088/1361-6463/ac2d64>.
- [163] M. Zhao, J. Zhang, C. M. Costa, S. Lanceros-Méndez, Q. Zhang, and W. Wang, “Unveiling Challenges and Opportunities in Silicon-Based All-Solid-State Batteries: Thin-Film Bonding with Mismatch Strain,” *Advanced Materials*, vol. 36, no. 4, p. 2308 590, 2024. DOI: 10.1002/adma.202308590. Available: <https://onlinelibrary.wiley.com/doi/abs/10.1002/adma.202308590>.
- [164] E. V. Astrova, V. P. Ulin, A. V. Parfeneva, *et al.*, “Silicon–carbon nanocomposites produced by reduction of carbon monofluoride by silicon,” *Journal of Alloys and Compounds*, vol. 826, p. 154 242, 2020. DOI: 10.1016/j.jallcom.2020.154242. Available: <https://www.sciencedirect.com/science/article/pii/S0925838820306058>.
- [165] S. Song, M. Zhu, Y. Xiong, *et al.*, “Mechanical Failure Mechanism of Silicon-Based Composite Anodes under Overdischarging Conditions Based on Finite Element Analysis,” *ACS Applied Materials & Interfaces*, vol. 13, no. 29, pp. 34 157–34 167, 2021. DOI: 10.1021/acsami.1c07123. Available: <https://doi.org/10.1021/acsami.1c07123>.
- [166] H. Jia, X. Li, J. Song, *et al.*, “Hierarchical porous silicon structures with extraordinary mechanical strength as high-performance lithium-ion battery anodes,” *Nature Communications*, vol. 11, no. 1, p. 1474, 2020. DOI: 10.1038/s41467-020-15217-9. Available: <https://www.nature.com/articles/s41467-020-15217-9>.
- [167] M. Zhao, J. Zhang, X. Zhang, *et al.*, “Application of high-strength, high-density, isotropic Si/C composites in commercial lithium-ion batteries,” *Energy Storage Materials*, vol. 61, p. 102 857, 2023. DOI: 10.1016/j.ensm.2023.102857. Available: <https://www.sciencedirect.com/science/article/pii/S2405829723002362>.

- [168] J.-A. Ruan and B. Bhushan, "Frictional behavior of highly oriented pyrolytic graphite," *Journal of Applied Physics*, vol. 76, no. 12, pp. 8117–8120, 1994. DOI: 10.1063/1.357861. Available: <https://aip.scitation.org/doi/10.1063/1.357861>.
- [169] C. M. Mate, G. M. McClelland, R. Erlandsson, and S. Chiang, "Atomic-scale friction of a tungsten tip on a graphite surface," *Physical Review Letters*, vol. 59, no. 17, pp. 1942–1945, 1987. DOI: 10.1103/PhysRevLett.59.1942. Available: <https://link.aps.org/doi/10.1103/PhysRevLett.59.1942>.
- [170] J. Skinner, N. Gane, and D. Tabor, "Micro-friction of Graphite," *Nature Physical Science*, vol. 232, no. 35, pp. 195–196, 1971. DOI: 10.1038/physci232195a0. Available: <https://www.nature.com/articles/physci232195a0>.
- [171] N. Kumar, A. T. Kozakov, T. R. Ravindran, S. Dash, and A. K. Tyagi, "Load dependent friction coefficient of crystalline graphite and anomalous behavior of wear dimension," *Tribology International*, vol. 88, pp. 280–289, 2015. DOI: 10.1016/j.triboint.2015.03.034. Available: <https://www.sciencedirect.com/science/article/pii/S0301679X15001322>.
- [172] M. Hokao, S. Hironaka, Y. Suda, and Y. Yamamoto, "Friction and wear properties of graphite/glassy carbon composites," *Wear*, vol. 237, no. 1, pp. 54–62, 2000. DOI: 10.1016/S0043-1648(99)00306-3. Available: <https://www.sciencedirect.com/science/article/pii/S0043164899003063>.
- [173] D. R. Lide, "CRC Handbook of Chemistry and Physics," *Journal of the American Chemical Society*, vol. 126, no. 5, pp. 1586–1586, 2004. DOI: 10.1021/ja0336372. Available: <https://doi.org/10.1021/ja0336372>.
- [174] M. B. Peterson and R. L. Johnson, *Friction Studies of Graphite and Mixtures of Graphite with Several Metallic Oxides and Salts at Temperatures to 1000 F*, 1956. Available: <https://ntrs.nasa.gov/citations/19930084859>.
- [175] F. Reusch, D. Umwelttechnik, S. Rudolph, and B. Nitride, "Use of Boron Nitride Coatings with Aluminum Casting Technology," 2015. Available: <https://www.semanticscholar.org/paper/Use-of-Boron-Nitride-Coatings-with-Aluminum-Casting-Reusch-Umwelttechnik/ec1bf77f80971ccc02629284fc5cd2cb7ba45667>.
- [176] A. Angus, L. A. A. Yahia, R. Maione, *et al.*, "Calibrating friction coefficients in discrete element method simulations with shear-cell experiments," *Powder Technology*, vol. 372, pp. 290–304, 2020. DOI: 10.1016/j.powtec.2020.05.079. Available: <https://www.sciencedirect.com/science/article/pii/S0032591020304538>.
- [177] J. Wang, M. Lei, H. Yang, *et al.*, "Effects of coefficient of friction and coefficient of restitution on static packing characteristics of polydisperse spherical pebble bed," *Particuology*, vol. 57, pp. 1–9, 2021. DOI: 10.1016/j.partic.2020.12.013. Available: <https://www.sciencedirect.com/science/article/pii/S1674200121000286>.
- [178] D. Sohn, Y. Lee, M.-Y. Ahn, Y.-H. Park, and S. Cho, "Numerical prediction of packing behavior and thermal conductivity of pebble beds according to pebble size distributions and friction coefficients," *Fusion Engineering and Design*, vol. 137, pp. 182–190, 2018. DOI: 10.1016/j.fusengdes.2018.09.012. Available: <https://www.sciencedirect.com/science/article/pii/S0920379618306379>.
- [179] Y. Feng, B. Gong, H. Cheng, X. Luo, L. Wang, and X. Wang, "Effects of bed dimension, friction coefficient and pebble size distribution on the packing structures of the pebble bed for solid tritium breeder blanket," *Fusion Engineering and Design*, vol. 163, p. 112 156, 2021. DOI: 10.1016/j.fusengdes.2020.112156. Available: <https://www.sciencedirect.com/science/article/pii/S0920379620307043>.
- [180] H. Tangri, Y. Guo, and J. S. Curtis, "Packing of cylindrical particles: DEM simulations and experimental measurements," *Powder Technology*, vol. 317, pp. 72–82, 2017. DOI: 10.1016/j.powtec.2017.03.058. Available: <https://www.sciencedirect.com/science/article/pii/S0032591017302759>.
- [181] S. Ghosh. "Static and Kinetic Coefficient of Friction Reference Table for COF Values of Common Materials," mechGuru. (2011), Available: <https://mechguru.com/machine-design/typical-coefficient-of-friction-values-for-common-materials/>.
- [182] "Coefficient of Friction Equation and Table Chart," Engineers Edge. (2024), Available: https://www.engineersedge.com/coefficients_of_friction.htm.

- [183] “Coefficient of Friction Reference Chart,” Schneider & Company. (2024), Available: <https://www.schneider-company.com/coefficient-of-friction-reference-chart/>.
- [184] “Friction Coefficient of Materials,” Piping Designer. (2024), Available: <https://piping-designer.com/index.php/properties/878-tables/2718-friction-coefficient-of-materials-table>.
- [185] “Coefficient of Friction,” eMachineShop. (2024), Available: <https://www.emachineshop.com/coefficient-of-friction/>.
- [186] K. Takahashi, K. Higa, S. Mair, M. Chintapalli, N. Balsara, and V. Srinivasan, “Mechanical Degradation of Graphite/PVDF Composite Electrodes: A Model-Experimental Study,” *Journal of The Electrochemical Society*, vol. 163, no. 3, A385, 2015. DOI: 10.1149/2.0271603jes. Available: <https://iopscience.iop.org/article/10.1149/2.0271603jes/meta>.
- [187] “Copper,” MIT. (2024), Available: <https://www.mit.edu/~6.777/matprops/copper.htm>.
- [188] Y. Qi, H. Guo, L. G. Hector, and A. Timmons, “Threefold Increase in the Young’s Modulus of Graphite Negative Electrode during Lithium Intercalation,” *Journal of The Electrochemical Society*, vol. 157, no. 5, A558, 2010. DOI: 10.1149/1.3327913. Available: <https://iopscience.iop.org/article/10.1149/1.3327913/meta>.
- [189] X. Yang and D. K. L. Tsang, “Evaluating Young’s modulus of porous nuclear graphite by a novel multi-scale method,” *Journal of Materials Science*, vol. 52, no. 18, pp. 10959–10971, 2017. DOI: 10.1007/s10853-017-1259-3. Available: <https://doi.org/10.1007/s10853-017-1259-3>.
- [190] S. Doddamani and K. M. Kaleemulla, “Indentation Fracture Toughness of Alumnum6061-Graphite Composites,” vol. 1, pp. 40–46, 2016.
- [191] L. B. Freund and S. Suresh, *Thin Film Materials: Stress, Defect Formation, and Surface Evolution*. Cambridge, UK: Cambridge University Press, 2003, 750 pp. Available: <https://doi.org/10.1017/CB09780511754715>.
- [192] M. Otsubo, C. O’Sullivan, and T. Shire, “Empirical assessment of the critical time increment in explicit particulate discrete element method simulations,” *Computers and Geotechnics*, vol. 86, pp. 67–79, 2017. DOI: 10.1016/j.comgeo.2016.12.022. Available: <https://www.sciencedirect.com/science/article/pii/S0266352X16303299>.
- [193] C. Ramírez-Aragón, J. Ordieres-Meré, F. Alba-Elías, and A. González-Marcos, “Comparison of Cohesive Models in EDEM and LIGGGHTS for Simulating Powder Compaction,” *Materials*, vol. 11, no. 11, p. 2341, 11 2018. DOI: 10.3390/ma11112341. Available: <https://www.mdpi.com/1996-1944/11/11/2341>.
- [194] G. F. Miller, H. Pursey, and E. C. Bullard, “On the partition of energy between elastic waves in a semi-infinite solid,” *Proceedings of the Royal Society of London. Series A. Mathematical and Physical Sciences*, vol. 233, no. 1192, pp. 55–69, 1955. DOI: 10.1098/rspa.1955.0245. Available: <https://royalsocietypublishing.org/doi/10.1098/rspa.1955.0245>.
- [195] “Résolution 1 de la 26e Conférence Générale des Poids et Mesures (CPGM),” Bureau International des Poids et Mesures (BIPM), 2018. Available: <https://www.bipm.org/fr/committees/cg/cgpm/26-2018/resolution-1>.
- [196] “Atomic Weight of Silicon,” Commission on Isotopic Abundances and Atomic Weights. (2009), Available: <https://www.ciaaw.org/silicon.htm>.
- [197] “Atomic Weight of Carbon,” Commission on Isotopic Abundances and Atomic Weights. (2009), Available: <https://www.ciaaw.org/carbon.htm>.
- [198] J. R. Dahn, “Phase diagram of Li_xC_6 ,” *Physical Review B*, vol. 44, no. 17, pp. 9170–9177, 1991. DOI: 10.1103/PhysRevB.44.9170. Available: <https://link.aps.org/doi/10.1103/PhysRevB.44.9170>.
- [199] J. R. Dahn, R. Fong, and M. J. Spoon, “Suppression of staging in lithium-intercalated carbon by disorder in the host,” *Physical Review B*, vol. 42, no. 10, pp. 6424–6432, 1990. DOI: 10.1103/PhysRevB.42.6424. Available: <https://link.aps.org/doi/10.1103/PhysRevB.42.6424>.
- [200] R. P. Brent, “Review of Algorithms for Minimization Without Derivatives,” *Mathematics of Computation*, vol. 28, no. 127, pp. 865–866, 1973. DOI: 10.2307/2005713. JSTOR: 2005713. Available: <https://www.jstor.org/stable/2005713>.

- [201] G. Combe and J.-N. Roux, “Discrete numerical simulation, quasistatic deformation and the origins of strain in granular materials,” *Third international symposium on deformation characteristics of geomaterials*, pp. 1071–1078, 2003. Available: <https://hal.archives-ouvertes.fr/hal-00354754>.
- [202] GDR MiDi, “On dense granular flows,” *The European Physical Journal E*, vol. 14, no. 4, pp. 341–365, 2004. DOI: 10.1140/epje/i2003-10153-0. Available: <https://doi.org/10.1140/epje/i2003-10153-0>.
- [203] F. da Cruz, S. Emam, M. Prochnow, J.-N. Roux, and F. Chevoir, “Rheophysics of dense granular materials: Discrete simulation of plane shear flows,” *Physical Review E*, vol. 72, no. 2, p. 021 309, 2005. DOI: 10.1103/PhysRevE.72.021309. Available: <https://link.aps.org/doi/10.1103/PhysRevE.72.021309>.
- [204] J.-N. Roux and F. Chevoir, “Simulation numérique discrète et comportement mécanique des matériaux granulaires,” Jan. 1, 2005.
- [205] I. Agnolin and J.-N. Roux, “Internal states of model isotropic granular packings. I. Assembling process, geometry, and contact networks,” *Physical Review E*, vol. 76, no. 6, p. 061 302, 2007. DOI: 10.1103/PhysRevE.76.061302. Available: <https://link.aps.org/doi/10.1103/PhysRevE.76.061302>.
- [206] I. Agnolin and J.-N. Roux, “Internal states of model isotropic granular packings. II. Compression and pressure cycles,” *Physical Review E*, vol. 76, no. 6, p. 061 303, 2007. DOI: 10.1103/PhysRevE.76.061303. Available: <https://link.aps.org/doi/10.1103/PhysRevE.76.061303>.
- [207] I. Agnolin and J.-N. Roux, “Internal states of model isotropic granular packings. III. Elastic properties,” *Physical Review E*, vol. 76, no. 6, p. 061 304, 2007. DOI: 10.1103/PhysRevE.76.061304. Available: <https://link.aps.org/doi/10.1103/PhysRevE.76.061304>.
- [208] F. Radjai and F. Dubois, *Modélisation numérique discrète des matériaux granulaires*. ISTE, 2010, 464 p. Available: <https://hal.science/hal-00690051>.
- [209] G. Combe, “Mécanique des matériaux granulaires et origines microscopiques de la déformation,” *ETUDES ET RECHERCHES DES LABORATOIRES DES PONTS ET CHAUSSEES - SCIENCES POUR LE GENIE CIVIL*, SI 8 Nov. 2002. Available: <https://trid.trb.org/View/953572>.
- [210] D. Vidal, S. Genies, E. De Vito, M. Tulodziecki, and W. Porcher, “Operando swelling measurement of silicon carbon composite based anode in pouch cell: Effect of external pressure, balancing and anode initial porosity,” *Journal of Energy Storage*, vol. 64, p. 107 174, 2023. DOI: 10.1016/j.est.2023.107174. Available: <https://www.sciencedirect.com/science/article/pii/S2352152X23005716>.
- [211] R. Li, W. Li, A. Singh, D. Ren, Z. Hou, and M. Ouyang, “Effect of external pressure and internal stress on battery performance and lifespan,” *Energy Storage Materials*, vol. 52, pp. 395–429, Nov. 1, 2022. DOI: 10.1016/j.ensm.2022.07.034. Available: <https://www.sciencedirect.com/science/article/pii/S2405829722004044>.
- [212] J. Lemaitre and J.-L. Chaboche, *Mécanique des matériaux solides*, Second edition. Dunod, 1985, 1 vol. (XX-532 p.). ill., couv. ill. en coul.. 25 cm. Available: <https://bibliotheque.utc.fr/Default/doc/SYRACUSE/160322/mecanique-des-materiaux-solides>.
- [213] W. Ramberg and W. R. Osgood, *Description of stress-strain curves by three parameters*, 1943. Available: <https://ntrs.nasa.gov/citations/19930081614>.
- [214] L. de Biasi, A. O. Kondrakov, H. Geßwein, T. Brezesinski, P. Hartmann, and J. Janek, “Between Scylla and Charybdis: Balancing Among Structural Stability and Energy Density of Layered NCM Cathode Materials for Advanced Lithium-Ion Batteries,” *The Journal of Physical Chemistry C*, vol. 121, no. 47, pp. 26 163–26 171, 2017. DOI: 10.1021/acs.jpcc.7b06363. Available: <https://doi.org/10.1021/acs.jpcc.7b06363>.

- [215] A. R. Galvis Escobar, A. Chaise, V. Iosub, B. Salque, J. F. Fernandez, and O. Gillia, "Stress effect on the swelling/shrinking behavior of an AB₂ alloy during hydrogenation cycles," *International Journal of Hydrogen Energy*, Special Issue on The 15th International Symposium on Metal-Hydrogen Systems (MH2016), 7-12 August 2016, Interlaken, Switzerland, vol. 42, no. 35, pp. 22422–22431, Aug. 31, 2017. DOI: 10.1016/j.ijhydene.2017.03.145. Available: <https://www.sciencedirect.com/science/article/pii/S0360319917311096>.
- [216] D. Queteschiner, *LIGGGHTS-PFM*, Department of Particulate Flow Modelling, 2024. Available: <https://github.com/ParticulateFlow/LIGGGHTS-PFM>.
- [217] I. Profatlova, E. De Vito, S. Genies, *et al.*, "Impact of Silicon/Graphite Composite Electrode Porosity on the Cycle Life of 18650 Lithium-Ion Cell," *ACS Applied Energy Materials*, vol. 3, no. 12, pp. 11873–11885, 2020. DOI: 10.1021/acsaem.0c01999. Available: <https://doi.org/10.1021/acsaem.0c01999>.

List of Figures

0	Volumes partition convention scheme	16
1	Mitigation opportunities for scaling up climate action, in terms of greenhouse gas reduction and cost (IPCC, 2013)	20
2	3D scheme of cylindrical battery	23
3	Scheme of battery manufacturing process	24
4	Basic functional scheme of a battery	25
5	Illustration of granular structure of electrode material	26
1.1	Measurement of amorphous silicon structure change during lithiation/delithiation (Beaulieu <i>et al.</i> , 2003)	31
1.2	Cross-sections in two different magnifications of the Si/C anodes harvested from cells cycled (Müller <i>et al.</i> , 2019)	33
1.3	Measurements of breathing/lithiation heterogeneities (Zhao <i>et al.</i> , 2019, Petz <i>et al.</i> , 2021)	34
1.4	Capacity and potential (VS lithium) of graphite and silicon components in Si/Gr electrode during lithiation and delithiation (Yao <i>et al.</i> , 2019)	35
1.5	Operando thickness change measurement on a NMC622 / Si/C/Gr pouch cell (Vidal <i>et al.</i> , 2021)	36
1.6	Scheme of workflow and structure of the multiscale electrochemical-mechanical model (von Kessel <i>et al.</i> , 2023)	37
1.7	Influence of Si/C composite anode capacity on cell voltage and volume variation (Chen <i>et al.</i> , 2022)	39
1.8	Scheme of anode thickness change due to particles (Gr and SiO _x) and porous volumes (Pegel <i>et al.</i> , 2022)	40
1.9	Scheme of thesis main problematic reflections	42
1.10	Discrete microporous electrode sample (Liu <i>et al.</i> , 2011)	43
1.11	Mechanical response of granular cathode during calendaring process (Sangrós Giménez <i>et al.</i> , 2018/2019)	45
1.12	DEM model simulating drying process, including active material and carbon-binder domain particles (Lombardo <i>et al.</i> , 2021/2022)	47
1.13	DEM model simulating calendaring process, including active material and carbon-binder domain particles (Xu <i>et al.</i> , 2023)	48
1.14	DEM model of all-solid-state lithium electrode (So <i>et al.</i> , 2021/2022)	50

1.15	Position of the thesis in current state-of-the-art	51
1.16	Basic schemes of Hertzian contact	54
1.17	DEM scheme of particles mechanical contact	58
1.18	DEM scheme of particles stickiness models	63
1.19	Simple test for Johnson-Kendall-Roberts (JKR) law illustration	69
1.20	Simple test for Potyondy-Cundall (PC) law illustration	70
2.1	Scheme of principal quantities of DAM evaluation: swelling amplitude and irreversibility	73
2.2	Picture of DAM reference sample	75
2.3	Review of material properties (Young's modulus and friction coefficient)	77
2.4	Diagram of simulation phases: calendering, relaxation and cycling	81
2.5	Scheme of simulation "fork" structure configurations	82
2.6	Scheme of multi-sensitivity-analysis tree for statistical analysis	83
2.7	Relative volumes of silicon and graphite as a function of lithium content, raw literature data and approximated functions	89
2.8	OCV curves of silicon and graphite	91
2.9	Exploitation of transitional function ϑ_c	92
2.10	Relative diameters of silicon composite and graphite as a function of time	94
2.11	Scheme of virtual irreversibility through r_{irr}	95
3.1	DAM reference sample analysis (inertial number, thickness, force, mean coordination number)	108
3.2	Particles irreversibility with linear breathing law (swelling amplitude thickness Delta and breathing coefficient, irreversibility thickness Delta)	109
3.3	Influence of silicon fraction with linear breathing law (inertial number, force, thickness)	111
3.4	Influence of silicon fraction with linear breathing law (swelling amplitude thickness Delta and breathing coefficient)	112
3.5	Influence of silicon fraction with electrochemical breathing law (inertial number, thickness, swelling breathing coefficient, irreversibility thickness Delta and irreversibility over swelling amplitude Deltas ratio)	113
3.6	Influence of silicon fraction with linear breathing law (mean coordination number)	114
3.7	Influence of friction/rotation (thickness, mean coordination number)	115
3.8	Imaging of particles bed forces network over a cycle	117
3.9	Influence of pressure on top plate (pressure, inertial number, mean coordination number, thickness)	119
3.10	Influence of pressure on top plate (swelling amplitude thickness Delta and breathing coefficient, irreversibility thickness Delta and irreversibility over swelling amplitude Deltas ratio)	120
3.11	Influence of particles' rigidity (thickness, mean coordination number)	122
3.12	Influence of particles' rigidity (swelling amplitude thickness Delta and breathing coefficient, irreversibility thickness Delta and irreversibility over swelling amplitude Deltas ratio)	123

3.13 Influence of stiffness level (swelling amplitude thickness Delta and breathing coefficient, irreversibility thickness Deltas)	124
3.14 Influence of pre-relaxation activated adhesion (mean coordination number, thickness)	125
3.15 Influence of pre-relaxation activated adhesion (irreversibility thickness Delta and irreversibility over swelling amplitude Deltas ratio, swelling amplitude thickness Delta and breathing coefficient)	126
3.16 Influence of post-relaxation activated adhesion (mean coordination number, thickness, irreversibility thickness Delta, swelling amplitude thickness Delta and breathing coefficient)	128
3.17 Influence of pre-relaxation generated bonds (mean coordination number, thickness)	129
3.18 Pre-relaxation generated bonds (swelling amplitude thickness Delta and breathing coefficient, irreversibility thickness Delta and irreversibility over swelling amplitude Deltas ratio)	130
3.19 Influence of post-relaxation generated bonds (mean coordination number, thickness)	131
3.20 Influence of post-relaxation generated bonds (swelling amplitude thickness Delta and breathing coefficient, irreversibility thickness Delta)	132
3.21 Influence of pre-relaxation and post-relaxation generated bonds (swelling amplitude thickness Delta, number of bonds, proportion of broken bonds)	134
3.22 Influence of particles irreversibility with linear breathing law (inertial number, thickness, irreversibility thickness Delta and breathing coefficient)	135
3.23 Influence of particles irreversibility with electrochemical breathing law (inertial number, thickness, irreversibility thickness Delta and breathing coefficient)	137
4.1 Scheme of pouch cell sample	143
4.2 Scheme of DForm bench	145
4.3 Diagram of experimental data estimation of rheological and electrochemical thickness variation of intermediary component (cathode, separator and pouch bag) to extract anode breathing	148
4.4 Samples used for calibration of the mechanical model of intermediary components	149
4.5 Extracted behaviours of intermediary components for rheological calibration	151
4.6 Rheological scheme of Novelisa model and fitting parameters	154
4.7 Progressive introduction of rheological elements in Novelisa model, example with cathode	156
4.8 Muppet tests after correction of rheological parameters	157
4.9 Relative volume of NMC622 cathode as a function of capacity	159
4.10 Full cell and extracted anode thicknesses (24°C)	161
4.11 Long cycling of battery cell and hydrogen material storage hydride to observe long period of breathing stabilisation (Vidal, 2021, Galvis Escobar, 2017)	163
4.12 Delta graphs of results at 24°C / 0.3 MPa during formation	165
4.13 Reproducibility test at high temperature (61°C)	167
4.14 Reference protocol at 24°C and 61°C (0.3 MPa during formation)	168
4.15 Potential singular behaviour at high temperature (61°C)	169
4.16 Reference protocol at 0.3 MPa, 1 MPa and 3 MPa (24°C)	171

4.17	Reference protocol at 1 MPa and 3 MPa (24°C)	172
5.1	Comparison of thickness change between DAM, experimental and continuous anode model, first cycle	177
5.2	Comparison of thickness change between DAM and experimental, four first cycles	178
5.3	Random reduction of breathing laws to simulate heterogeneous breathing of particles	180
5.4	Comparison of thickness change between DAM (with and without heterogeneous breathing) and experimental results	181
5.5	Diagram of multisphere DAM building steps	183
5.6	Comparison of thickness change between DAM (spherical particles and clusters approaches) and experimental results	184
5.7	Scheme of volume change absorption of two particles belonging to the same cluster	185

List of Tables

1.1	Orders of magnitude of lithium-ion battery energy densities (gravimetric and volumetric, pack level and cell level, 2020, 2030 and 2050)	30
1.2	Review of experimental studies of electrode breathing	32
1.3	Review of modelling studies of electrode breathing	38
1.4	Review of modelling studies on battery using DEM	44
1.5	Values for computation of Tabor limit of studied system	66
2.1	Parameters of DAM reference sample	79
2.2	Breathing coefficient interpretation guides	97
2.3	Overlaps volume analysis during calendaring and relaxation phases	98
3.1	DAM simulations summary	106
3.2	Global analysis of DAM results	139
4.1	Parameters comparison between experimental and model	142
4.2	Experimental reference protocol	146
4.3	Novelisa model final parameters	158
4.4	Experimental protocols summary	160
4.5	Exponential fits of Delta quantities	166
5.1	Model/Experimental comparison settings	176
5.2	Accronymes	191
5.3	Mathematics	193
5.4	Latin variables	193
5.5	Greek variables	195
5.6	Breathing coefficient β	197
5.7	Reduced surface η	197
5.8	Exotic / Archaic	198
5.9	Constants	198

Acknowledgements

As the first words of these acknowledgements, I would like to sincerely thank the first people involved in the process of this thesis: Gwen Snow. This name is a great opportunity to tell the way I found this thesis. When I first started to search for a thesis subject, I began to search through the traditional path, by contacting all the professional people I knew. One day, the traditional being not particularly successful, I told to myself “Fuck it, why not...” and sent a message on the main chat room of the Discord of Morgan of Glencoe, an author and harpist I had been following for few years, an artist I still follow today. The message was simple: “Hey guys, I’m searching for a thesis subject! If you have any contact that could help me, let me know!” (or something like that). On the 3rd December 2020, Gwen Snow replied to my message: “Hi Théo, I know someone in the field that may help you. I send you the contact by private message.”. I did not realise at the time, but this contact was going to lead me to three long, fastidious but beautiful years. Thank you so much, Gwen Snow.

Fast enough, in fact the next day on 4th of December 2020, I sent a message to Emmanuelle Suard, experimental researcher at the ILL (*Institut Laue-Langevin*) in Grenoble, to present my will in making a thesis. She sent an answer back exactly five hours later, listing a number of advices, also proposing to send my CV to her closed contacts. I obviously accepted, quite astonished that my simple ask on Discord, after few clicks, lent me so far. I cannot express all my gratitude to Emmanuelle that was the second link of this wonderful social connection that offered me this opportunity. She also took the time to make me visit the nuclear reactor of the ILL on 15th September 2021, followed by a rich discussion about writing and cinema. Such a brilliant exchange for such a formidable person. Thank you so much, Emmanuelle Suard.

Coming back to my main thread, I received a few days later, on 10th December 2020, a message from a people that was going to become one of my mentors for the three following years, Benoit Mathieu, proposing me a subject on batteries. To be absolutely honest, I was not sure if I was going to like the subject, but any way. I accepted. We quickly made some remote interviews in order to clarify my profile, as the opportunity for me to meet Marion Chandesris, the future laboratory manager at the time. I travelled to Grenoble on 15th January 2021 to meet the team in person, mainly to demonstrate that my engineer profile would fit with a research activity. All happened very well. The administrative hiring was definitively launched. I needed to wait for a few months for the process to conclude, preparing my life in Grenoble, until a date I will hardly forget. The 17th May 2021. An important day for me, as it constitutes the first day of my thesis, as it also composes a key date in my personal construction, for reasons I prefer to keep. I will not be able to detail these three years of intellectual journey, but I will obviously remember all the first times.

The first time I worked in a shared office, with the extraordinary Justine Souteyrand whose ability to think and work, but also her social extravagance hidden in few humble details, inspired so much and still inspire me

today. The first time I attended a doctoral training course, about leadership and team work, on 5th October 2024. The first time I presented my work to the company that funded my thesis, on 30th September 2024. The first time I went to an event as colossal as the OI'INPiades with my dear friend Alexis Martin, an irreplaceable music companion and metalhead from the lab, a talented “social reader” whose I admire his deep empathy. The first time I went to a concert with some colleagues of the lab, to see Magma at the *Théâtre de la Ville* of Valence, on 19th October 2021. The first time I invited a very special person to the restaurant for a very special ask, on the 22nd January 2022. The first time I presented my work on a poster during the LITEN day, on the 6th April 2022. The first time I presented my thesis work to the individual follow-up committee, on 10th June 2022. The first time I went to Hellfest, in Clisson, France, from 17th to 19th June 2022. The first time I presented my work in another country during the Umicore Annual Science days, in Antwerp, Belgium, on 3rd and 4th November 2022. The first time I went in a scientific conference, at ModVal in Duisburg, Germany, from 21st to 24th March 2023. The first time I presented my work during an oral presentation, during EUROMAT conference in Frankfurt am Main, from 4th to 8th September 2024. The first time I submitted an article to publication, on 20th October 2023, published on 5th January 2024. The first time I sent a scientific manuscript as substantial as the one you are reading to a jury.

All these first times composed a wonderful journey, filled of up and downs, of instants of real frustrations but also of pure pieces of joy and love. All the intellectual obstacles were so many opportunities to learn, to reason and to enrich my self-confident in approaching science and art. This would have never happened without all the people I met, and I feel so afraid to forget some as I am writing these lines.

At the origin of this thesis, I thank the Umicore company for funding this work, and of course all the related team involved in the follow-up: Michal Tulodziecki, Jacob Locke, Angelo Mullaliu and especially Duancheng Ma who managed to attend all the meetings. Thank you for their precious discussions and feedbacks. I obviously thank all the people working at the laboratory, for offering me their daily presence and discussions, for their laughs and jokes, for their constant ability during this long routine in recalling me that I am not alone in this vast world. I thank all the PhD students met during the doctoral training courses with whom I shared some pleasant meals, discussions and activities. I would like to particularly thank Marina Callandret, for the precious instant of calm discussions about anything, from social relationships to science philosophy to good food. Her company sincerely helped me during hard times, and it has been a real pleasure to make her discover the world of concert shows (and metal mosh pits). I deeply thank the team Zaza / Eve / Nath / Panda who made me discover the wonderful world of geek convention and board games, thanks to their priceless child's minds. As the continuity of the Discord on which I found this thesis, I would like to send a wave of spangles and happy baby seals to the whole Selkcommunity, for making me discover the world of traditional music, Celtic world, and ability to surpass my own shame to dance *Cochinchine* on the main place of Grenoble at 11pm. Without any doubt, I would like to thank Ilya, for her ability to question the world, ourselves, and first myself. She made me discover so many of my social bias (that I still have to work on), made me realise so many parts of me that I underestimated, for better or worse, so many ways to learn how to become a better person. From the bottom of my heart, Ilya, thank you. For their precious moral support, I sincerely thank the “VH team”, my band of buddies that I know since high school. During these three years, we made memorable soirées, we made

unforgettable new year parties. We also made beautiful travels, in Amsterdam, Netherlands, in the Cévennes, Jura and Corsica in France, celebrating ten years of invaluable friendship. Long life to this band, I rarely love to be so dumb, in a way that I only feel when I am with this gang of stupidity. Love on you, “VH team”, let’s continue being so silly. I also thank all the team of G-OMETRIK association in Tours who made me realise all the complexity of deejing and electronic music, for their pleasant artistic and creative minds. I thank all the people of Le Ciel association in Grenoble for having unveiled me a splendid underground musical place, full of chill and open-mind minds. I thank Guilhem Ginard, for his durable friendship that lasts despite our divergent philosophies, for the intenseness of our pasts, for having converted me to the dark and shining world of metal music (and almost music in general), for all his moral support during difficult psychologic times. I launch a wave of gratefulness and love to my whole family, in particular to my mom, dad, brother and sister-in-law. I would be absolutely nothing without them. Nothing at all. Each time I come back home, they give me reasons, without words, to keep creating, to keep thinking, to keep giving a sense in everything I do. I also thank all people I meet more or less punctually, that I keep in touch with more or less a long time.

I also would like to thank all these musicians whose musical pieces accompanied me during all the writing of this manuscript, by order of appearance: Wegferend, Gustavo Santaolalla, Meshuggah, Thomas Newman, Cissie Redgwick, Igorrr, Yodelice, Joe Bel, Diablo Swing Orchestra, Steven Wilson, Porcupine Tree, Peter Gabriel, Haken, Phenotype, Devin Townsend, Johnny Clegg, Leprous, CLANN, Kalandra, SKÁLD, Vøluspá, OMNIA, Joe Hisaichi, Amenra, Dead Can Dance, Zeal & Ardor, André Schoorlemmer, Hans Zimmer, Hildur Guðnadóttir, Crooked Still, Alexandre Astier, Vandaveer, The Devil Makes Three, Shawn James, Feu! Chatterton, Ilum Sîn, Martyr Defiled, Space Banjo, Sylvaine, Alexandre Desplat, Larkin Poe, The Bones of J.R. Jones, The Dear Hunter, 5keleton, NUANCE., Greg Thomas, Belzebubs, Audiolake, Good Lovelies, Mac Quayle, Daniel Lanois, Woody Jackson, Joan Jett & the Blackhearts, Celkilt, Cécile Corbel, Abigail Washburn.

At last, I wholeheartedly thank my three mentors, Benoit Mathieu, Willy Porcher, and of course Olivier Gillia. Benoit, you have been the person who made me understood that the hardest thing in creativity was not complexity, but simplicity. You also taught me how to think the answer even before asking the question. Willy, with your precious encouragements, you have been a pillar for my self-confident in doing science. You also confronted me to a different way to make science, more realistic and down-to-earth, making me realise how social science was. Olivier, your mind simultaneously creative, child and expert, joined to a fantastic eye for error checking, constituted a robust teaching source on how to be rigour, how to adjust my perception of reality to the right border of my knowledge. To all of you three, I even thank the instants you pushed me on the other side of my limits, despite fatigue and frustrations. I thank your tremendous availability all along the thesis, actually not that common in most doctorates.

As for some discussions we shared, I still maintain some of my ideas about the consideration of the PhD student status, on the lack of underlining how much this experience is so educative and enriching, to the profit of justifying the instants of tiredness and doubts by simple “You are a PhD student, so that’s the way it is”.

To everyone reading these lines: any PhD student has the privilege of living a rare self-rewarding experience, through evident instant of self-questionings and rough psychologic obstacles. You should not justify this situation by the situation itself, this would unavoidably repeat any error of the past, deliberately or not. Instead, if your will is to support them, you should help them realising all what they are actually learning from this present, but also help them find how to detach from these obstacles, by surpassing or avoiding them. Without doubt, this idea may be obvious to many people, and it certainly applies to many other life situations. I leave it to you to appreciate or not. In fact, this piece of advice is more a message to myself, as it constitutes one of the most important life lessons of this thesis, much more than a criticism to my mentors that made an extraordinary job all along these three years.

As conclusive words, I would like to throw a final bottle into the sea, intended to the Cap'tain S. Along these years, after the short instants of laugh and sublime smiles, the silence of the wind became in the same time the source of numerous questions, sometimes of anger against myself, but also of true inspiration. You composed the heart of many of my thoughts, I often imagined your legend crossing the hardest storms, falling but never giving up against this world often cruel.

But this is not your bravery that maintains you course alive, not at all. This is the way you see the best in each people that surrounds you.

I will try my best to transform this philosophy into my own lighthouse at the horizon. As for your future, I wish your travel will lead to the best persons you want to live with, to the best creations you ever dreamt to realise.

On my side, I just finish, right now, one of the creations I am, today, the proudest of. This is certainly not a revolutionary book, maybe not pleasant to read even for the expert people of the related field, I don't really know. But anyway, I can definitively tell you: now that I have it between my hands, yeah. . .

That's right.

That's the hell satisfying.

Fictional epilogue

The last notes, round, warm and peaceful, finished lulling the cottage. Lizilius sustained the vibrating strings of her banjar, with the tips of her fingers, waiting for a deep calm to settle. In front of her, both sisters and brothers Silyo and Greta were captivated by the music coming to its end. Lizilius drew a long breath, before finally opening her eyes. The faces of her guests made her discreetly laugh.

— Wakey, wakey, are you both with me? she gently asked.

Silyo and Greta successively blinked, coming back from their reveries.

— Yeah. . . Yeah, we're here.

While the guests were stretching out their arms, Lizilius placed her banjar next to her.

— Here is all what it is. . . All what I know about the “batteries”, she concluding, mimicking the inverted commas.

— And you did not search further? To know more about these questions? sincerely asked Silyo and Greta.

— No. Of course, not.

— Why “of course”?

Lizilius briefly thought, even if she already had the answer in mind.

— From a perspective, I was not convinced by an important “why” that was supposed to justify why I was searching these answers.

The faces of Silyo and Greta clearly demonstrates their circumspection. Lizilius remarked it and explained.

— I am sure you understand that any act of scientific research is an act of knowledge ambition. Through many centuries of continuous change, science has been a precious source of truth definition. At the time, science constantly tries to remove human emotional bias from the exploring methodology. In fact, its main objective is to answer a one and unique question. . . “How”? How does everything work? We can sometimes make the confusion and ask ourselves “why” such a phenomenon appears like it does, but we still have to think in terms of causality, not in terms of purpose, as a synonym of “how”, to remain in a scientific mind. If we think “why” in terms of spiritual purpose, searching for the reasons of why everything happens, this is more a question of religion, not science. However, there is one version of the “why” that, in my mind, is crucial to make legitimate science: why is that so important to understand even more, every day? In fact, the answer to this question presents a so diversified colours palette that it seems impossible to summarise it to a single sentence.

Silyo and Greta listened attentively, but seemed not convinced. Lizilius kept going, taking a step back in her explanation.

— Would you like an example?

— Yes, yes, of course.

— So...

She gathered her souvenirs and enunciated them.

— His name was Fritz Haber, living during the beginning of 19th century of the Ancient Calendar. In my mind, he is a perfect example of science dilemma. His work in synthesis process of ammonia from nitrogen and hydrogen led to the development of a large-scale synthesis of fertilisers, allowing the production of food for millions of people. He received the Nobel Prize of Chemistry in 1918, one of the most prestigious reward at the time, for the invention of this process. However, in the same time, he was deeply involved in the development of chemical weaponry, proposing during World War I the use of chlorine during trench warfare. He even supervised its initial deployment on the Western Front at Ypres, in Belgium, in 1915. My idea here is not to reveal a wonderful or dark side of science, but to underline the importance of morality in a field that claims to be as far as possible from emotional consideration. As far it is made without moral questionings, science can lead humankind as in the most beautiful and peaceful landscape as in the worst ugly and painful situation.

Lizilius took the time to take a sip from her cup.

— In other words, a science cannot be legitimate without morality, without reflection on the “why” it is carried out.

She let the cup on the bedside table.

— Obviously, the questioning of morality goes hand-in-hand with the principle of “right or wrong”. More precisely, this principle of “right or wrong” is not the one related to objective scientific rigour, but the one related to our empathy. It is the principle related to our ability to state, considering the present knowledge we have at disposal, if the question we want to answer is worth to be answered. It is the principle related to our capacity in determining if the question we want to clarify will be both beneficial to humankind and consistent with our personal values. This is not a “why” of general purpose of the world, of all these phenomena that occur around us, but the “why” of our own actions. For this reason, a legitimate science is a science that both objectively questions the current knowledge and morally questions the axes it explores.

Silyo and Greta appeared more clear-sighted, each one with a stick of licorice between their teeth. Lizilius looked a little more withdrawn, as if she was questioning herself.

— In a way, I wanted to answer these questions about batteries in order to help in solving the big question about climate change. Yet, the more time went by, the more I was asking myself if I was even asking the right questions. I did not even know if I was participating in a blind technosolutionism, maybe more at the service of an economy more than an altruistic purpose. In fact, I was quite convinced that the development of individual electrical vehicles was not a revolution, but a continuation. A continuation of a system in constant research of “more”, of sensational innovation and endless consumption. A continuation of a system that, maybe, did not spend enough time in defining its real fundamental needs, in asking itself “why” it develops all these technologies.

For a few seconds, a spark of nostalgia fizzled in her eyes.

— I admit, these are beautiful words, and I don’t even know if they will help you to answer your own questions. And of course, we should not make the confusion between technology and science. Technology can be a science, or a set of techniques, but science is not necessarily technology. Anyway, these researches

made me realise how much I loved science. Looking at all what it had taught me and everything else it still can teach me, looking at its priceless instants of humour, looking at my writing of tremendous texts with plenty of references of my peers. Also looking at science applicability in art, looking at the bright side of its History, I am definitively convinced in the deep benefit scientific method can offer to humankind. By confronting me to the complexity of technological development, these researches also made me realise the importance of asking ourselves, each one of us, about what we fundamentally need. And . . .

She took back her cup, smiling.

— As a fruit of our collective mind, science should not be exempted from this question.

She finally drank all her cup and exhaled deeply. In front of her, Silyo and Greta took the time to think the words of Lizilius, while chewing they stick of licorice.

— And what about our question? The initial one? they asked again, intrigued.

Lizilius briefly laughed, without offense, then she winked at them.

— If one day you find out, let me know. I would be glad to know the answer.



Things we love give us reasons to move forward.

Things we hate give us reasons to learn.

As for my experience, science always succeeded
in fulfilling both conditions at the same time.
